Integrated Phase-Change In-Memory Photonic Computing



Xuan Li
Wolfson College
University of Oxford

Supervisor: Prof. Harish Bhaskaran

A thesis submitted for the degree of
Doctor of Philosophy

Trinity 2021

This thesis is dedicated to
my dear mother and father
and my dear godmather and godfather
for their endless support
over far distance and time zone

Acknowledgements

Finally I come to the end of my PhD, a craziest period I have ever had in my life. These moments in Oxford is so wonderful and enjoyable that seems not realistic to me with all my supervisors and friends.

First of all, I want to express my deepest thank to my supervisor, Professor Dr Harish Bhaskaran who gave me this precious chance to study on such an exciting topic of integrated photonic computing and storage technology combined with phase change materials and the freedom to explore my own ideas. I don't know what magic power he has to turn a little girl with all fear and dear not to even stand in front of the group to give a presentation to become a researcher like today. Thanks for all the guidances on directions and specific technological problems, inspiring ideas and pushing me out for all the meetings and conferences. Thanks for the infinite optimism on me even after I made so many mistakes, lost so many chances during my PhD that I even lost confidence in myself. It is because of his strong and solid support that I am able to believe in myself and fight back all the obstacles again and again after I was hit down to the floor.

Special thanks go to Professor Dr. Nathan Youngblood, who is my co-supervisor during my first two years of my PhD. His door is always open for my endless all kinds of questions, helping me to establish my research habbits from building setups, establishing new measurement systems, repairing broken wires and writing papers and emails. And I also want to thank Dr. Carlos Rios Ocampo, who supervised my the first months and guided me into the photonic world, took me around MIT and is always willing to collaborate with and guide me. I am also grateful to my colleagues, present and previous group members of Advanced Nanoscale Engineering team: Madhav Kumar, Ghazi Sarwat, Nhlakanipho Mkhize, Qiang He, Zengguang Cheng, Mohd Shahrizal Alias, Benjamin Porter, Gerardo Rodriguez, Sridevi Siddarama, Seongdong Lim,

Zengguang Cheng, Samuel Humphrey, Wen Zhou, Johannes Feldmann, James Tan, Nikolaos Farmakidis, Eugene Soh, Sarolta, Utku Emre Ali, Yu Shu, Samarth Agarwal, Tangsheng Cheng, June Sang Lee, Antonios Mikallou, Hao Luo, Yuhan He, Tara Miline, Mengyun Wang, Luci Bywater, Andriy Moskalenko, Meadhbh O'Connor, Kristian Curtis, for those research or life support, friendship and great moments including puntings, BBQ and lunchtime.

Thanks for friends from Bodle company's help: Clement Talagrand, Graham, Lucky, Peinman Hosseini, and collaborators from IBM, Abu Sebastian, from University of Munster, Professor Wolfram Pernice and from University of Exeter, Professor David Wright and Dr Sanitago Garcia-Cucvas Carrillo, Dr Emanuele Gemo, thanks for the great discussions and inspiring ideas and all your efforts between collaboration projects.

I also want to thank those people behind the scene but gave me great help with fabrication and mechanical systems, Paul Pattinson at the Physics Department cleanroom and Radka Chakalova at Begbroke science park cleanroom. Paul Warron, Chris, Rob as the department IT team and other great department and university officials, thanks a lot for making my life much easier and colorful.

Deep thank goes to my college, Wolfson College and friends there: Wenlei Huang, Siming Ding, Dr Siu Yiu, Zi Yin, Lidingrong Huang, Kai Zhang, Yizhi Wang, Chunsen Bai, Yuting Fu, Yifu Ding, Jingyi Yang, Bohan Chen, Joyce Chou, Victor Wang, Cyrus, Binglun Yin, Saba, Mona, Dr Shuqiu Wang, Dr Kun Peng, to name a few. Thanks a lot for those magic encounters to make us become friends and warm company including gathering, punting, especially thanks for feeding me greatly since I don't know how to cook myself.

I would also express sincere thank to colleagues and friends when I came back to China, to accompany me to have a peaceful and beloved end of this PhD, to compromise those sufferings because of Coronavirus. Thanks to Qingyong Hu, Dr Zhouran Zhang, Dr Shaobo Gao, Wenbo Jing and Jinkun Zhu, Dr Jingjing Zhao, Yunxiu Zeng, Jiajing Liu and Weibin Gui for supporting me and encouraging me during my dark times in my PhD.

Thanks to my parents and godparents, for supporting me every minute overcoming all the restrctions on the whole way not only my PhD but

also my whole life. I finally want to thank myself, for hundreds of times of giving up but then thousands of times of standing up and fighting back again during all those dark time.

”La douleur passe, la beauté reste”

Abstract

In highly-developed societies, easy access to a vast resource of information has gradually become a necessity instead of a choice. People are not only exchanging more information for entertainment, but also relying increasingly heavily on large amounts of data to make decisions. For instance, artificial intelligence relies on an extensive database to have a more precise predictive ability, which is widely used nowadays, such as access control systems using facial recognition, gait recognition or even iris scanning. In the process of diagnosing major diseases, instantaneous access to enormous medical records helps generate a more effective and potent treatment solution quicker. All aspects of people's lives, not just security and health, bring a high demand for a great deal of data processing. In many respects, the performance of data processing is closely related to the quality of people's life.

However, the efficiency of current computing and storage systems is far from adequate to satisfy the abovementioned data processing demands. Moore's law is close to reaching its physical limit, the performance gap between CPU and memory is difficult to bridge, and there is as yet no solution that can simultaneously satisfy the problems of energy consumption and computing performance. People still cannot but suffer when shopping websites crash on Black Fridays.

Fortunately, integrated photonic in-memory computing provides a potential solution to help with the current data processing situation. Photonic processing has high speed and immense throughput volume because of wavelength multiplexing's capability for parallel processing with hundreds or even thousands of channels. Furthermore, the addition of phase-change material to the integrated photonic system makes it possible to process and store data in the same position, eliminating data transport energy consumption. Together with well-established silicon photonics foundry

resources and widespread optical fiber transmission systems, the influence of photonic computing and storage systems will be profound and significant once developed.

This thesis details several milestones on the path towards achieving an integrated phase-change photonic computing system. The research processed through stages covering single device modulation optimization, substrate material investigation, and employing single-device solutions to scale up to a 3 × 3 matrix demonstration system. Every section includes optical or thermal modelling, material calibration, device fabrication and optical measurements.

The first project demonstrated an optically controlled photonic multi-bit memory device with 34 different data storage levels (over 5 bits) in a single memory cell, providing an order of magnitude improvement over previous demonstrations in terms of time and energy consumption. For this stage, numerous methods of optical control and mechanisms behind optical switching are also discussed. Following this up, double-step single-shot modulation was demonstrated to achieve arbitrary data storage level addressing and retrieval without information of former statuses. This work has shown the potential for high-density, low energy cost, and all-optical storage performance through a single device. It pushed the limit of the performance of single devices to their practical maximum by optimizing the controlling method and measuring environment, a milestone for non-volatile integrated photonic memory and computing systems.

Platform investigation was performed after device optimization for a broader range of applications and more practical usage. The phase-change photonic computing devices were transferred from a silicon nitride platform to a silicon platform. A detailed comparison was carried out between the two platforms addressing substrate material, device footprint, switching contrast, energy consumption and switching speed. This substrate investigation follows the path towards, upon the optimization of single devices, achieving a high speed, low energy cost optical computing and storage system.

Finally, a small phase-change optically controlled matrix was demonstrated with 3 × 3 photonic in-memory computing cells that are connected. This matrix was developed for its ability to serve as a matrix fac-

tor to realize easy-programmable, non-volatile in-memory matrix-vector multiplication operations. Its constituent, crucial components were calibrated beforehand, including the single phase-change computing cell's switching contrast and speed, as well as directional couplers and thermal phase shifters to modulate passive splitting ratio and active splitting ratio between different branches, respectively. Moreover, an electrically modulated Mach-Zender interferometer array was added to the photonic matrix to achieve a denser footprint and an automatic weight setting. Two applications were carried out to demonstrate this matrix's functionality: small pattern recognition based on a single perception neural network; and three-dimensional images rotation. This phase-change photonic matrix multiplication core enabled large-scale on-chip non-volatile photonic in-memory computing and demonstrated a capability for solving real problems and tasks in a high speed, low energy consumption manner. This demonstration provides a potential solution to the conflict between an already enormous and still growing data processing burden and the currently overwhelmed available computing and storage systems.

Contents

1 Introduction **3**

1.1 Motivation 3

1.1.1 Comparison between electronic and photonic computing and storage 3

1.1.2 Nonvolativity – Strength added by phase-change materials . . 5

1.1.3 The necessity of platform investigation 7

1.1.4 Towards actual usage – necessary scaling up 8

1.2 Outline and Objectives 8

1.2.1 Objective 8

1.2.2 Layout 9

1.2.3 Statement of originality 11

1.2.4 Key results and new science 11

2 Integrated phase change photonic computing: a literature review **12**

2.1 Comparison of computing platforms 13

2.1.1 Different substrate platforms: an introduction 13

2.1.2 Platform interaction with PCMs 20

2.1.3 Towards large-scale and wider applications 27

2.2 Controlling methods of phase change photonic cells 27

2.2.1 Key demands for modulation/controlling performance 28

2.2.2 Interaction with PCMs 31

2.2.3 Optical controlling methods 31

2.2.4 Electrical controlling methods 33

2.3 Large-scale optical computing implementation methods 35

2.3.1 Key properties in large-scale optical computing 35

2.3.2 Different paradigms to achieve optical computing 36

3 Device preparation and measurement setup **41**
3.1 Device preparation 41
3.1.1 Single device optimization 41
3.1.2 Introducing foundry for large-scale fabrication 46
3.2 Experimental setup 50
3.2.1 Material calibration and passive transmission measurement . . 50
3.2.2 Single device optical switching 52
3.2.3 Matrix measurement: single and multi-wavelength multiplexing 53
3.2.4 Automatic measurement 56
3.2.5 Software preparation assistant to measurement setup 56

4 Optimization of single device optical switching performance **60**
4.1 Backgroud knowledge 61
4.2 Experimental, device and theoretical preparation 62
4.2.1 Experimental Setup 62
4.2.2 Device structure consideration 63
4.2.3 Simulation for Switching Process 65
4.2.4 Mechanism exploration 67
4.3 Experiments 68
4.3.1 5 bits distinguished levels achievement 68
4.3.2 Dual-Pulse, Multi-level Operation 72
4.3.3 Arbitrary Modulation 75
4.4 Repeatability, switching speed discussion 76
4.4.1 Repeatability investigation 76
4.4.2 Switching speed investigation 80
4.5 Conclusion 82

5 Si and SiN platforms performance comparison for computing applications **84**
5.1 Material and device structure comparison 85
5.1.1 Material analysis 86
5.1.2 Mechanism and simulation 87
5.1.3 Device and experimental setup preparation 89
5.2 Demonstration of single pulse modulation on SOI platform 92
5.3 Analysis of dynamic response while switching phase 95
5.3.1 Dynamic response while amorphization 95
5.3.2 Dynamic response while crystallization 97

5.4 Performance comparison . . . 100
5.4.1 Switching speed . . . 100
5.4.2 Switching threshold and energy consumption . . . 101
5.5 Conclusion . . . 103

6 Demonstration of a Large Scale Optical Computing System 105
6.1 Motivation . . . 105
6.2 Mechanism . . . 107
6.3 Development of the matrix structure . . . 109
6.3.1 Single components: design, optimization, and test . . . 110
6.3.2 Weights definition from (-1,1) to the real transmission . . . 117
6.3.3 Experimental setup . . . 117
6.4 Demonstration of the Application . . . 120
6.4.1 Demonstrating 1: Calculation of the 3D rotation matrix . . . 120
6.4.2 Demonstration 2: small pattern recognition . . . 122
6.5 Future optimization . . . 126
6.6 Conclusion . . . 128

7 Conclusion and Outlook 131
7.1 New material exploration . . . 132
7.2 Higher speed, larger scale and lower cost . . . 133
7.3 More efficient computing structures for suitable applications . . . 133
7.4 Challenges to be overcome for larger-scale optical networks . . . 133

8 Publications, patents and conferences 135
8.1 Patents . . . 135
8.2 Publications . . . 135

Bibliography 138

List of Figures

1.1 Classic von Newmann architecture and von Neumann bottleneck. . . 4

1.2 Comparison between electronic and photonic storage 5

1.3 Mechanism of temperature changes during crystalline to amorphous or amorphous to crystalline phase transitions in phase change material GST. T_m is melting temperature for phase change materials and T_x means crystallization temperature. The state of phase change materials change according to the temperature situation of this material. During the amorphization process, this material is firstly heated over its melting temperature and then cooled down rapidly. The weaker covalent bonds break and resonance bonds flip. During the crystallization process, the material is heated over its melting temperature and then cooled down slowly. The material can form ordered structure and becomes crystalline state again. More detailed explanation in [1]. 6

1.4 This figure shows an example of integration of different platforms from [2]. (a) is the cross section view of a SOI-SiN integrated platform. SiN layer is deposited firstly, followed by SOI layer, seperated by a SiO_2 layer. (b) shows the schematic of interlayer coupler between SOI and SiN layer. Waveguide 1 is SOI waveguide and waveguide 2 is SiN waveguide. (c) shows the electric field profile of this coherent taper in (b). 8

2.1 Comparison between different photonic platforms from [3] 12

2.2 SOI fabrication components and available optical components on it from [4] (a) the SOI platform; (b) an arrayed waveguide grating (AWG) on a SOI platform; (c) a hybrid integrated VECSEL and an InP laser source; (d) a Ge PIN photodetector; (e) a thermo-optic phase shifter with implanted heater; and (f) a phase shifter with PIN junction for carrier injection. 15

2.3 A schematic illustration of a SiN platform and the available optical components from [5] (a) The cross-section image of a SiN platform. (b) The stereogram image of a SiN platform. (c) The SEM images of SiN optical components such as strip waveguides and slotted waveguides. 17
2.4 The schematic illustration for an InP platform and available optical components on it adapted from [6]. (a)the schematic illustration; (b)an on-chip laser; and (c) an typical on-chip photodetector for InP platforms. 19
2.5 Different optical components on polymer platforms or polymer hybrid platforms [7]; (a) an assembled polymer-based hybrid integration platform for a colorless optical network unit; (b) a schematic and photograph of a coherent receiver with a polymer-based photodetector array; and (c) a photograph of optical components combined by polymers and other materials: ceramic RF board integrated on the polymer platform; InP-DHBTs for ultrafast driver electronics; polyboard for wavelength tuning and polarization adjustment and electro-optic polyboard for fast light modulation. 21
2.6 (a) The relationship between temperature changes during the phase transitions of the amorphisation and crystallisation process. When a short pulse on a nanosecond timescale with high light intensity is applied to PCMs (red bar in (a)), this material will experience a rapid heating up and rapid cooling down process during the amorphisation process. During the crystallisation process, a longer and less intensive pulse is applied to the material and it will experience a slow cooling process (blue bar in (a)). (b) shows optical properties of $Ge_2Sb_2Te_5$, a widely used type of PCMs and the material used in this thesis. The red solid line represents the real part of refractive index of amorphous GST and the blue solid line represents crystalline GST. The red and blue dashed line represent the imaginary part of refractive index of amorphous and crystaline GST respectively. The green bar is located in the wavelength band which is explored in this thesis, 1400-1600 nm telecom wavelength band. 23

2.7 Refractive indices of different platforms for telecom wavelength range, where black lines and the left y-axis indicate the real part of refractive index and the red lines and right y-axis represent the imaginary part of refractive index. For the polymer platforms, PMMA is used here as an example of commonly used substrates: (a) Si_3N_4 platform; (b) InP platform; (c) Si platform; and (d) Polymer(PMMA) platform. [8]. . . 25
2.8 Mechanism comparison between electrical switching PCM and optical switching PCMs; (a) a mechanism of electrical switching process [9]; (b) typical electrical devices overview [9] (in electrical devices the PCM sits in between two electrodes); (c) typical optical devices overview [10] (in optical devices the PCM sits on the top of a waveguide); and (d) the mechanism of optical switching process [11]. 28
2.9 Different examples of optical switching: (a) optical integrated switching by evanescent coupling in waveguides [10], using the same light path with probe light; (b) optical integrated switching array [12], using separate pump path to improve energy efficiency; (c) a typical measurement setup for integrated optical switching [10]; (d) optical free-space switching using visible laser [13]; (e) a typical measurement setup for free-space switching [14]. 32
2.10 Different examples of electrical switching: (a) electrical heating with the dielectrical material Al_2O_3 as a thermal transfer [15]; (b) electrical switching with conductive PCM as one part of the electrical circuits [16]; (c) nanowire structure to switch the PCM both electrically and optically [17]; (d) graphene heater to switch the PCM on waveguides to improve energy consumption and switching speed [18]; (e) plasmonic structure to switch PCM on waveguides in mixed mode with smallest device size [19]; (f) doped Si waveguide working as a micro-heater to switch PCMs [20]; (g) PIN heater realised by doping the sides but waveguides to operate a thermal heater to switch PCM under low loss propagation situation [21]. 34
2.11 Different optical networks for different functions comparison: (a) programmable optical circuits using MZI phase shifters and splitters [22]; (b) diffractive neural network with compound Huygens' metasurfaces [23]; (c) programmable cascaded MZI network for setting photons phase in quantum technologies [24]; and (d) programmable MZI network mimicking a deep learning neural network [25]. 37

2.12 Different optical neural network computation realization methods: (a) programmable optical circuits using waveguides with directional couplers [26]; and (b) photonic computing design using nanophotonic neural medium [27]. 38

3.1 Device fabrication process. (a)(b) Ebeam pattern transfer and RIE dry etching to have silicon waveguides and grating couplers. (c)Pattern transfer of window for phase-change materials. (d) Deposited phase-change materials on the waveguide using sputtering technology. . . . 42

3.2 Simulated optimization of waveguides and grating couplers. The targetted wavelength is 1550 nm and the targetted mode is TE mode. The boudary condition is perfectly matched layer (PML). Refractive indices are experimentally measured and fit in Oxford. (a)(b)Simulated mode profiles for partially etched waveguides (a) and fully etched waveguides (b). (c) is the XZ view and (d) is the perspective view of the simulation optimization for grating couplers designs. This is a grating coupler structure on the silicon substrate, with varied period and fill factor of this coupler to optimize the transmission performance. The smaller blue cylinder is the fiber core and the bigger blue cylinder is the fiber cladding. The two arrows inside the fiber are the input light source and the two arrows parallel to the waveguide surface are the output coupled light into the waveguide. By varying the period and the fill factor of the coupler, highest output transmission can be found at the signal output port. 44

3.3 Device fabrication process. (a) Pattern designed using python. (b)Fabricated device on SOI platform under an optical microscope. (c)Swept transmission of plain waveguides. 45

3.4 Optimization process for the grating coupler on SOI platform. (a) GDS design of swept grating coupler parameters. (b) AFM measurement of the height of the waveguide. (c) The highest transmission optimized for a single device with two grating couplers. 46

3.5 SEM images of patterns ebeam lithography with PEC correction (a) and without PEC correction(b). 47

3.6 Poor laboratory-based fabrication examples. (a)Broken waveguides when unstable etching is carried out. (b)(c)(d) Broken lines (b), misaligned waveguides (c)(d) caused by ebeam stitching errors. (e) Dirty and ununiform surface with dirt introduced during the whole process. 47
3.7 Foundry fabricated device examples. (a) Fabricated devices with plenty of microring resonators and the corresponding resonances test in (b). 48
3.8 Foundry fabricated device examples. (a) Large-scale matrix devices fabricated by the foundry. 49
3.9 Real setup for single device pump/probe experiment. 51
3.10 Setup for basic transmission and spectrum measurement. (a)Basic setup with tunable laser source and photodetector for data collection. (b)Basic setup with a supercontinuum laser source and OSA(Optical Spectrum Analyser) for data collection. 53

3.11 Single device pump and probe setup. There are two light paths sharing the same fiber channel: the red light path is pump signal path and the green light path is probe signal path. In the probe channel path, the signal is passing through two polarization management paddles and one in-line polarizer. To reduce the fluctuation of the polarization of the probe seed laser, this in-line fiber polarizer is used to pass linearly polarized light while blocking the orthogonal polarization from the randomly polarized probe light source. After that, the signal is split into two parts: 90% of light go into the device through a 3-port circulator and 10% signal goes to a 25 KHz photodetector and then converted from analog signal to digital signal to the computer. This 10% signal works as a monitor of the probe signal. The other 90% of light go through the device and then filted by a tunable filter to avoid noise signal before going into the 25 KHz photodetector. 90% of the signal goes to the 25 KHz photodetector and the rest goes to a ocilloscope directly to record device fast response in nanosecond scale. The sampling speed of the oscilloscope is 4Gb/s. For the pump signal, a tunable attenuator is arranged after the laser source to control the amplitude of the switching power. One EOM (electro-optical modulator) is used then to add the switching pulse shape from an electrical pulse generator. After the EOM, contineous light is converted into rapid optical pulses to switch the device. The signal then passes through an optical amplifier and a tunable filter to obtain high amplitude optical pulses without noise. And then the pulses go through a polarization management paddle because the grating couplers of the device is polarization-sensitive. After going through the device, the final status of the signal is recorded by a high-speed photodetector (1GHz). . . . 54

3.12 Matrix pump and probe setup. The pump line is in red and the probe line is in blue. In the pump line, the polarization management paddle is added before the EOM because EOM is polarization-sensitive. After the EOM, 90 % of the signal goes into the matrix and 10 % of the signal goes to the monitor. EDFA is then used in the pump line to amplify the pump signal to switch phase change materials. The VOA after EDFA is added to completely close this pump path during the computing process. After VOA, there is a 50-50 optical combiner to combine probe line and pump line to the optical matrix. This combiner can be replaced by a optical switch. A demultiplxer is then used to split different wavelength signals to different computing channels of the matrix. One VOA and one polarization management paddle is used before the matrix in each branch to encode input signal and maximize the input power. DWDM ITU-T channel (Dense Wavelength Division Multiplexing International Telecommunication Union Telecommunication Standardization Sector) C36 (1548.51 nm), C34(1550.12 nm), C32(1551.72 nm) is selected to be the computing wavelengths. For the probe line, a supercontinuum source is used to provide multiple wavelengths for wavelength multiplexing computing. Since this supercontinuum laser is from 400 nm to 2000 nm, a splitter after the laser source is used to split near infrared light and visible light. A bandpass filter is then used to filter a wavelength band around 1550 nm. After that the probe signal is sent to 50-50 splitter to the matrix. This matrix setup also has three electrical control parts: a electrical pulse generator to shape the optical switching pulses; a microcontroller to control VOAs to encode input signals and electrical pins to control the phase shifter array in different PCM blocks. Please read Chapter 6 for more detailed explanations for the function of the phase shifter array. 55
3.13 Real setup for matrix with wavelength multiplexing functionality. . . 57
3.14 Labview interface for automatic measurement (1). 57
3.15 Labview interface for automatic measurement (2). 58
3.16 Labview interface for automatic measurement (3). 58
3.17 Schematic for the software strcuture for the matrix measurement system. 59

4.1 Structure of tested devices in experiments. The schematic on the top is the cross-section of the functional material area (the cross-section position is with a red dashed line highlighted in (b)). On the Si_3N_4 partially etched waveguides, there is a 10 nm GST covered by a 10 nm Indium Tin Oxide (ITO) capping layer. (a) An optical image of the device used for multi-level experiments. The device with 50/50 Y splitters combines two simple straight waveguides: the left waveguide works as a reference waveguide, the right waveguide has functional material deposited on it with zoomed-in figure (b). (c)An SEM image of a simpler device structure also used in this experiments with only one straight waveguide. (d) An SEM image of PCM on the waveguide with 30 degrees tiled capture angle. 64

4.2 Simulation for different power and corresponding temperature distribution, transmission contrast and estimated crystalline area of a device. (a) shows the transmission contrast between amorphous and crystalline state, as the crystalline area becomes bigger and bigger because of the increasing programming power. The transmission change is normalised to the initial transmission state of the device. The crystalline area is normalised to the whole area of the phase change material in this simulation. (b) shows the corresponding temperature distribution on the GST cross-section on the waveguide with sending different programming power pulses. The area filled with dark red color is the area where the temperature went over 890 K. This area is defined as crystalline area because the melting temperature of GST is 890 K, the area over 890 K (filled with dark red color in Figure (b)) is expected to be melt and switched to a crystalline state after cooling down to room temperature. (c) Mode profiles on the cross-section for both crystalline state (c) and amorphous state (d). 66

4.3 Schematic of switching process. Two light waves go through the waveguide with opposite directions: pump pulses (from right to left on the plot) and probe continuous light (from left to right on the plot). Rectangular pulses (programming pulses) are used for amorphization and double-step pulses (erase pulses) are used for crystallization. 69

4.4 Multi-level performance with the dual-pulse programming method. (a) The transmission response of one iteration of 34 individual levels achieved by monotonically increasing the amplitude of the programming pulses. The length of the PCM device used is 4 μm. The transmission change is normalised to the initial transmission state of the device. (b) After 10 write and erase cycles, the average transmission of each individual level and standard deviation are recorded in (b). The transmission change is normalised to the initial transmission state of the device. (c) Histogram plots the difference between the desired transmission level and the actual transmission level (b). A red line shows Gaussian fits to the error distribution in this plot. The error rate is normalised to the average value of each specific device level. . 71

4.5 Transmission performance of final states of a PCM photonic device using different double-step programming methods. (a) A schematic of the experiment where the double-step programming pulse trailing end varies in both amplitude and time. (b) The transmission performance of a PCM device with increasing amplitude modulation. Once the relative amplitude exceeds 0.2 of the first pulse, recrystallization starts to occur much more rapidly because the temperature is now over crystalline temperature. The inserted figure is the total deviation distribution of different levels caused by amplitude modulation. (c) Transmission performance of PCM devices for double-step programming pulses using time width modulation of the trailing end. The increasing of the time width leads to more area of GST being amorphized. The inserted figure is the total deviation distribution of time width modulation. The transmission change in (b) and (c) is normalised to the initial transmission state of the device. The error rate is normalised to the average value of each specific device level. . . . 73

4.6 Temperature changes ((a)(b)) because of the two different modulation methods variation and the corresponding transmission contrast changes ((c)(d)). (a)(c) Changes of amplitude variation method. (b)(d) Changes of time width variation method. 74

4.7 (a) Schematic of the physical mechanism for the dual-pulse programming and recrystallization processes. The temperature change in the upper plot illustrates the dynamics of the material while pulses are added. An ERASE pulse is needed to reach the initial state after each programming pulse. (b) Temperature changes and schematic of the method to achieve single-pulse double step programming. The initial high amplitude portion of the double-step pulse with the duration of 50 ns serves to erase the memory of former states by bringing the PCM above its melting temperature before recrystallization. 75
4.8 Arbitrary modulation using the time width modulation method. (a) Multiple double-step programming pulses (upper figure) of random durations are sent to the device and the corresponding transmission performance (lower figure). The device can switch to a certain transmission level without knowing the previous state of the device. (b) Transmission performance and standard deviation distribution of random programming with duration modulation. The inserted plot is the error bar distribution of different levels.The transmission change in (a) and (b) is normalised to the initial transmission state of the device. The error rate is normalised to the average value of each specific device level. 77
4.9 Arbitrary modulation using the arbitrary programmed amplitude of the second step of pulses. (a) Transmission levels and standard deviation distribution of random amplitude programming. (b) Error bar distribution of levels in the left plot. The transmission change in (a) and (b) is normalised to the initial transmission state of the device. The error rate is normalised to the average value of each specific device level. 78
4.10 The relationship between confidence intervals and the number of distinguished levels. 79
4.11 Cooling time test between amorphization and recrystallization pulses. Cooling time is the delay between two programming pulses when the device recovers to a stable state after the phase switch. As the cooling time increases, the GST transmission can saturate to a stable value because of the thermo-optical effect. 81

5.1 Optical refractive indices of both amorphous and crystalline states of Si, SiN, and GST materials measured by ellipsometry: (a) real part and (b) imaginary part of refractive indices respectively. 87
5.2 The simulation of eigenmode profiles and propagation mode profiles of the fundamental TE mode inside Si and SiN waveguides with GST. Eigenmodes in waveguides describe electromagnetic fields that are invariant in their intensity profile as they propagate along the fibre [28]. The 2D eigenmode profiles of Si waveguides with amorphous (a) and crystalline GST (b) and their SiN counterparts (c) and (d) are shown, with a significant electrical field distribution change because of GST. The propagation modes are guided along the propagation direction and depends on the waveguide structure as shown in (e)-(h). (e) and (f) illustrates simulated propagation profiles of the fundamental TE mode with 4 μm amorphous (e) and crystalline GST (f) on top of the waveguide. (g) and (h) are SiN counterparts. Light as an electromagnetic wave can have different formats within the waveguide, such as TE mode (E field is perpendicular to the propagation direction) and TM mode (E field is perpendicular to the propagation direction). . . 88
5.3 The design of the device and fabricated device static performance. (a) A schematic of the applicable device and (b) cross-sectional view of phase change photonic devices on silicon substrates. (c) The optical image of a GST photonic device. GST is highlighted by the red dashed square. (d) Transmission spectrum comparison between a straight waveguide, a waveguide with amorphous GST and thermal annealed crystalline GST, normalized by the transmission of the straight waveguide. 90
5.4 SEM images of different lengths of GST on top of waveguides. (a)1 μm GST. (b)2 μm GST. (c)4 μm GST. (d)6 μm GST. 92

5.5 Single pulse amplitude modulation for GST amorphization on Si waveguides. (a) Pulses shapes (red curves) and corresponding transmission changes (blue curves) with pulse amplitude modulation for amorphization/programming and crystallization/erasing. (b)In a longer time scale, independent multilevel states with pulse amplitude modulation. (c) Total deviation distribution of different levels of programming pulse amplitudes. The standard deviation of different levels is 0.687%. (d) Separate errorbar distribution for each level of programming pulse amplitudes. The transmission change in (a),(b) and (d) is normalised to the initial transmission state of the device. The initial transmission state shows big fluctuation in (d) and even shows lower transmission than the initial crystalline state. There are two possible reasons. Firstly, the initial state may not be fully crstalline state but get more crystallization during the switching process. Secondly, the crystallization pulse may damage the device a bit and the small switching energy cannot guarantee to fully crystalline the device during each switching process. The error rate in (d) is normalised to the average value of each specific device level. 94

5.6 Double step modulation for crystallization process. (a) Pump pulses (red curves) and corresponding transmission changes (blue curves) with different second step time width modulation. From light color to dark color, the time width of the second step of crystallization pulses increases, and the corresponding transmission contrast changes increase. The transmission change is normalised to the initial transmission state of the device. 95

5.7 Double step modulation for crystallization process. (a) Arbitrary second step time width modulation. The upper plot is the different time widths of programming pulses, and the lower plot is the corresponding transmission changes. (b) Total deviation distribution of different levels of programmed second step time width. The standard deviation of different levels is 0.3%. (c) Total deviation distribution of different levels of randomly programming second step time width. The standard deviation of different levels is 0.9%. The transmission change in (a) is normalised to the initial transmission state of the device. The error rate in (b) is normalised to the average value of each specific device level. 96

5.8 The mechanism investigation of the amorphization process through both simulations and experiments. (a) Temperature distribution maps from the top view for a 4-μm-long GST on top of a 500 nm Si waveguide and 1.3 μm SiN waveguide with an amorphization pulse with a 10mW amplitude and a 20ns duration. The position with the highest temperature is labelled with a black dot. (b) The simulation demonstration of the relationship between pump power and temperature changes for both Si and SiN devices. The pulse duration is fixed at 20 ns while the amplitude varies from 2 to 10 mW with the step of 2. (c) (d) are experimental transmission response of thermo-optical effect taken with a high-speed photodetector to the pump pulse changes: amplitude variation (c) and time width variation (d). The transmission change in (c) and (d) is normalised to the initial transmission state of the device. . 98

5.9 Mechanism investigation of crystallization process through experimental demonstrations. (a) Recordings of crystallization pulses with the variation of time width of the second step and (b) device corresponding transmission readout. This modulation method is double-step crystallization time width modulation with a fixed first step of 25 ns and 300-600 ns for the second step time width variation. The pulse power in (a) is normalised to the range of (0,1) to show the relationship between the peak amplitude and the second step pulse. The transmission change in (b) is normalised to the initial transmission state of the device. 99

5.10 (a) Dead time (definition from [10]) comparison for both Si and SiN devices. The modulation methods of amplitude modulation and time width modulation are also compared. The data of SiN devices is from [10] for comparison. (b) is zoomed-in dead time comparison between these two modulation methods on Si waveguides in order to emphasize the difference. 100

5.11 Relationship between switching parameters (including the substrate materials and the length of phase change material GST), optical transmitted contrast between states, and energy consumption. Phase change photonic devices with 2 μm (length along propagation direction) applicable GST and 4 μm applicable GST are depicted with a solid line and dashed line separately. (a) is three-dimensional maps for switching parameters and corresponding transmission contrasts for 2 μm and 4 μm devices separately. (b) The relationship between transmission contrasts and the duration of pump pulses varied from 5 ns to 100 ns and the length of the device is between 2 μm and 4 μm. (c) The correlation between energy consumption and the choice of substrates (Si or SiN) and duration of pulses. Notably, the length of GST is 4 μm on Si and 5 μm on the SiN device from [11]. The duration of pulses varies from 20 ns to 100 ns. Every data point is on average of 300 repeated measurements. The transmission change in (b) and (c) is normalised to the initial transmission state of the device. 102

6.1 Optical hardware acceleration in a typical CNN neural network . . . 107

6.2 Optical image of an 8 $\times$ 8 photonic phase change matrix. In this figure, phase change material devices are deposited on each block of the matrix shown in the inserted figure, working as the weight $G_{11} - G_{nn}$. Different input signals $X_1 - X_n$ can be input into different branches with the amplitude encoded with information. The output signal $Y_1 - Y_n$ is the matrix multiplication results as shown in Equation 6.1. . . 108

6.3 Outlook of foundry-aided matrix chip. Different blocks have different functions. 110

6.4 An image of a phase change photonic matrix and enlarged images of critical single components in the matrix. (a) 10 nm thin film of phase change material (GST here) on top of the waveguide. (b) Directional couplers that couple light from the bus row waveguides to single block and from block back to the bus column waveguides. (c) The outlook of the whole phase change photonic matrix. (d) Crossings inside the photonic network, and (e) thermal phase shifter in each block for adjusting the splitting ratio for different blocks. 111

6.5 Schematic of calculated splitting ratio of directional coupler according to Equation 6.2 112

6.6 Calibration of directional coupler coupling ratio. Directional couplers with different coupling gap: 300 nm (a), 350 nm (b), 400 nm (c), 450 nm (d) with coupling length variation from 1 μm to 10 μm is fabricated and measured. The extiction ratio, coupling ratio and fitting coupling ratio curve are shown in this figure. 113
6.7 Calibration and optimization of the crossing bar structure. (a) Calibration devices used in the optimization process. One calibration device is composed of one MZI with four identical crossing bars on one arm of it. (b) A enlarged plot of one crossing bar. (c) Measurement result of extinction ratio of different crossings with variation of MMI length. (d) Measurement results of transmission per crossing bar of different crossings with the variation of MMI lengths. 115
6.8 Performance of phase shifters of Row 1, Colomn 1,2 and 3 in the matrix. (a) Power concentrates on device of Row 1 Column 1 (black star point). (b) Power concentrates on device of Row 1 Column 2 (red star point) and Row 1 Column 3 (blue star point). 116
6.9 Different components in the matrix experimental setup calibration before the real experiments. (a) The output of supercontinuum laser after notch filter (black), EDFA (red) and mux (blue). (b) Response of different photodetectors. (c) Response of different outputs of the multiplexer. (d) The response of specific multiplexer channels used in the matrix experiments. 118
6.10 Hardware realization of rotation matrix demonstration using rotating a three dimensional cube as an example. (a) The initial photonic matrix state and corresponding cube outlooking in a coordinate system. (b) The state of photonic matrix and corresponding cube outlooking after 90° x axis rotation. (c) The state of photonic matrix and corresponding cube outlooking after 90° y axis rotation. (d) The state of photonic matrix and corresponding cube outlooking after 90° z axis rotation. . 121
6.11 Schematic of matrix multiplication application: single layer perceptron neural network. Red highlighted part is carried out by the phase change photonic matrix hardware. Others are calculated by computer. 123
6.12 Input background signal (a) and targeted patterns that need to be recognized from the background (b). 124

6.13 Step 1: weights setting step. (a) 3 × 3 phase change matrix used to carry out matrix computation in this application. (b) Randomly generated targeted patterns and corresponding digital matrix that will be programmed as weights. 124
6.14 Step 2: Input signal encoding step. The input signals are divided into 3 × 3 blocks and flattened to 1 × 9 vectors before sending to the matrix. And then the moving window goes through the whole matrix so that all the background pixels are encoded and input to the matrix. 125
6.15 Hardware computation results of pattern recognition. (a) Targeted patterns. (b) Hardware computation (in yellow) and software computation results (in blue) comparison of the whole background plot. (c) Heat map of computation results. (d) Original input plot with the red highlighted square of recognized patterns' positions, which agrees with the targeted pattern shapes. 127
6.16 Schematic of wavelength multiplexing computation. (a) is the single wavelength computation mode. (b) is the wavelength multiplexing mode. There are 3 parallel computing channels in each input waveguide in this plot. 128
6.17 Scaling up simulation.(a) Single device block design of directional couplers. (b) Single device block design of one directional coupler and one ring resonator. (c) Simulation of estimated scaling up limit on the condition of current photodetector sensitivity with the above two structures. 129

Nomenclature

AFM Atomic Force Microscope

AIST $Ag_3In_4Sb_{76}Te_{17}$ phase change alloy

CW Continuous wave

DWDM Dense Wavelength Division Multiplexing

EBL Electron Beam Lithography technology

EDFA Erbium-doped fibre amplifier

EOM Electro-optical modulator

FDE Finite Difference Eigenmode

GaAs Gallium Arsenide

GST $Ge_2Sb_2Te_5$ phase change alloy

InP Indium Phosphide platform

ITU – T International Telecommunication Union Telecommunication Standardization Sector

MMI Multimode Interferometer or Multimode Interference Coupler

MZI Mach-Zehnder Interferometer

NIR Near Infrared

OSA Optical spectrum analyser

PCM Phase Change Material

PD Photodetector

PLC Planar Lightwave Circuit platform

PMMA Poly(methyl methacrylate): positive photoresist

RIE Reactive ion etching

SEM Scanning Electron Microscope

Si Silicon platform

SiN Silicon Nitride platform

SiO_2 Silicon Dioxide

SOI Silicon on Insulator substrate

TE Transverse Electric polarised light

Chapter 1

Introduction

1.1 Motivation

1.1.1 Comparison between electronic and photonic computing and storage

The development of electronic computing systems began with the invention of the first transistor in 1947. The introduction of electronic computing and storage systems, such as personal computers, mobile phones and cloud computing servers, have resulted in dramatic changes to everyday life. Electronic information systems have largely served to enhance the accessibility, propagation, processing and storage of information, meaning that an increasing number of people are now able to utilise an ever-growing amount of information. Indeed, people are receiving, exchanging and digesting a broader range of information than ever before, and they are doing so anywhere and at any time. Of course, all these information-related activities lead to the development of more information within global information systems. In fact, according to statistics, the volume of information doubles every two years and shows the potential for exponential growth. Further, in accordance with Moore's law, the data storage density had been growing at a similar speed to the data generation speed until recent years, although the physical limits of nanomanufacturing will restrict its development steping forward.

Von Neumann architecture is a classic computer architecture developed by John von Neumann in [29]. As shown in Figure 1.1, This document describes that an electronic digital computer should have these components: a processing unit, a control unit, a memory, an external storage and input and output mechanisms. The problem of this structure is that the total signal processing speed of a computer depends on the data transport bandwidth and speed between the memory and the processor. This

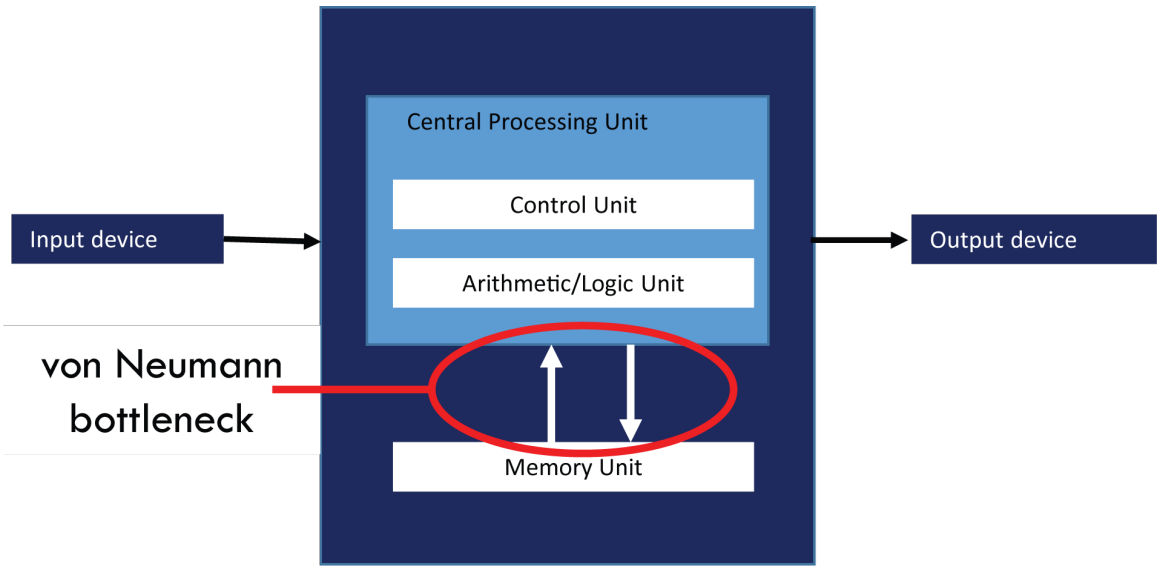


Figure 1.1: Classic von Newmann architecture and von Neumann bottleneck.

data transition adversely restricts the whole performance of a computer. This is the well-known problem: von Neumann bottleneck.

In light of the limitations associated with electronic systems, photonic computing systems appear to represent a promising alternative that should allow modern technologies to overcome the bottleneck caused by the mismatch between the increasing data size and the limited capacity of data-processing technologies. Figure 1.2 shows the comparison between electronic systems and photonic systems for the consideration of computing applications. Firstly, from the density perspective, dominant manufacturers such as TSMC and Intel have been able to downscale technology nodes from 45 nm and 32 nm to 7 nm and 5 nm. However, as the sizes of semiconductors have been decreasing, they have moved increasing close to reaching their physical limits.

Alternative solutions such as three-dimensional CMOS structures and vertically integrated electronics have been developed, but they are insufficient to serve as permanent solutions to the problem caused by the intrinsic physical bottleneck. The photonic data storage system, on the other hand, has a high density because of availability of the full wavelength spectrum for information storage and high parallelism with wavelength and mode multiplexing.

Concerning energy consumption, electrical systems have numerous problems such as crosstalk, current leakage, parasitic components of devices, and so on, while these factors have fewer significant influences on photonic systems. Taking computing speed into consideration, conventional von Neumann computing system structure means that the central processing unit and memory are separated from each other, resulting

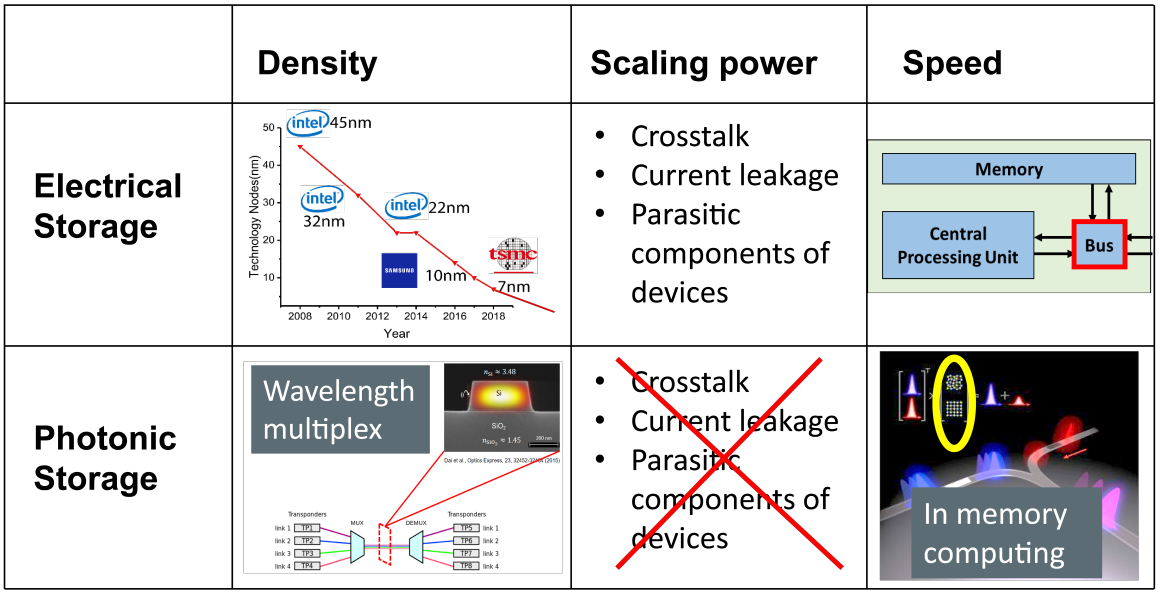


Figure 1.2: Comparison between electronic and photonic storage

in data communication between them taking up to 75% of the total energy consumption of the system. However, with the addition of phase-change materials, a photonic computing system can achieve in-memory computing functionality with which computing and storage can be processed simultaneously to reduce energy consumption on a large scale. All of these aforementioned reasons explain why photonic computing has been the subject of intense investigation in recent years. And thus photonic computing becomes the main topic the author wishes to address in this thesis and pursue in a future academic career.

1.1.2 Nonvolativity – Strength added by phase-change materials

Phase-change materials can enable in-memory computing thanks to having the property of non-volativity. Phase change materials can switch between two different states, amorphous and crystalline, according to temperature conditions, as bonding between the different atoms form or break as the temperature changes. Figure 1.3 illustrates the mechanism of phase transitions of phase change materials, taking GST as an example. The natural or as-deposited state that phase-change materials are in is amorphous state. After being heated by external means (either electrical, photonic, or thermal methods), the temperature exceeds their melting temperature, thereby becoming liquid. After a fast enough cooling process, the temperature drops below crystallization temperature, and the cooling time should be sufficiently brief so that a

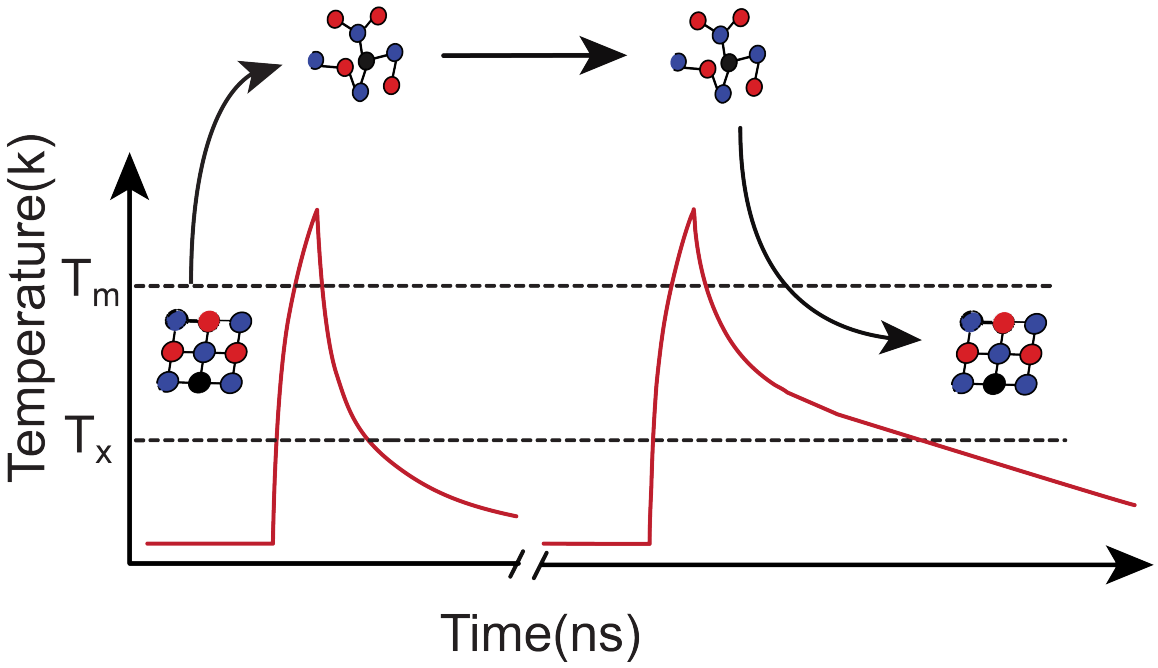


Figure 1.3: Mechanism of temperature changes during crystalline to amorphous or amorphous to crystalline phase transitions in phase change material GST. T_m is melting temperature for phase change materials and T_x means crystallization temperature. The state of phase change materials change according to the temperature situation of this material. During the amorphization process, this material is firstly heated over its melting temperature and then cooled down rapidly. The weaker covalent bonds break and resonance bonds flip. During the crystallization process, the material is heated over its melting temperature and then cooled down slowly. The material can form ordered structure and becomes crystalline state again. More detailed explanation in [1].

regular crystalline structure cannot be generated, thus causing the material to assume an amorphous state. In the event of an extended cooling duration, the material will have enough time to form an ordered crystalline structure before the temperature drops below the crystallization temperature, forming a crystalline state. Both of these states remain stable under room temperature and pressure for more than ten years [30]. This sustained maintenance of state without the intervention of an extra source of energy is defined as non-volatility.

Complimentary data storage cells in an electrical memory such as DRAM (Dynamic Random-Access Memory) and SRAM (Static Random-Access Memory), on the other hand, are volatile because they need a continuous supply of electricity to keep their transistors on. This feature makes these cells suitable for computing because of the high modulation speed. For photonic computing, the state of phase-change materials can be changed towards either amorphous or crystalline states by accumulated integrated light. Therefore, it is volatile, but after the targeted state of resistance has been achieved, it can be maintained without static energy consumption. Consequently, one can easily change the state of a device with specific switching parameters and keep the new state without the need for extra energy input. This is why phase-change materials can help photonic systems to realize both information storage and information computing in a photonic manner.

1.1.3 The necessity of platform investigation

The Si platform as a universal platform has been used for decades for CMOS fabrication among many different applications, including mobile phones, personal computers, and embedded systems. Different photonic platforms have a variety of properties that are suitable for a range of applications. Unfortunately, no photonic platform is currently capable of integrating all the advantages like silicon platforms in electronics. Thus, to develop a future all-photonic data processing system, making use of features from all different platforms and combining them during fabrication is a likely trend for the near future. Figure 1.4 shows a recent work demonstrating a three-dimensional photonic chip structure that combines Si and SiN platforms where adiabatic tapers are used to vertically route light [2]. In light of this, it is likely that a viable phase-change photonic integrated system combining different platforms will soon appear. Applications for different platforms then need to be carefully arranged to make maximum use of all platforms.

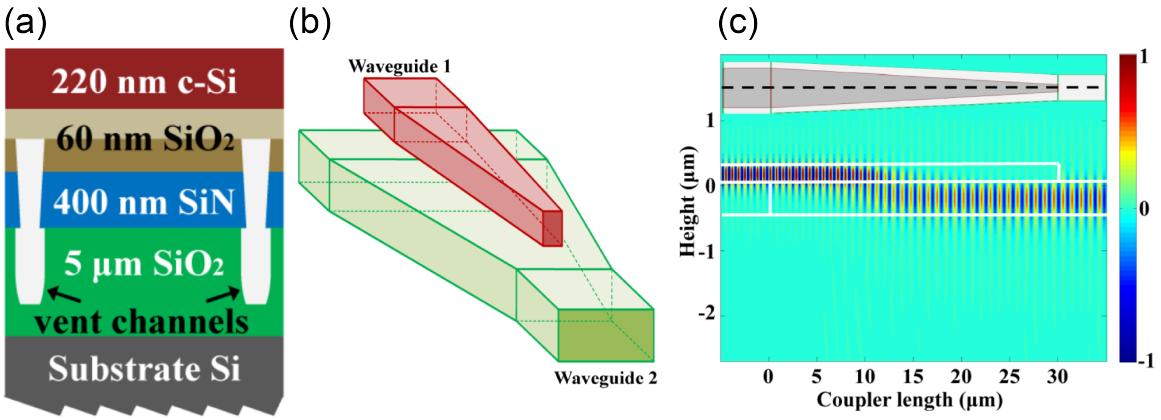


Figure 1.4: This figure shows an example of integration of different platforms from [2]. (a) is the cross section view of a SOI-SiN integrated platform. SiN layer is deposited firstly, followed by SOI layer, seperated by a SiO_2 layer. (b) shows the schematic of interlayer coupler between SOI and SiN layer. Waveguide 1 is SOI waveguide and waveguide 2 is SiN waveguide. (c) shows the electric field profile of this coherent taper in (b).

1.1.4 Towards actual usage – necessary scaling up

So far, the photonic computation and storage are still at a stage that single devices are being explored, while matrix scale investigation remains lacking. However, to apply photonic computing and storage to practical applications, scaling up for a single device is crucial. In this thesis, the performance of the photonic matrix is thus extensively explored. As expected, many problems exist when the focus of research switches from a single device to a matrix, for example, the loss control of the whole matrix. For this problem, a similar total power is inadequate for switching the single element in a matrix as compared with switching an independent photonic element. But although there are plenty of technical problems that need to be overcome, the advantages of the optical system mentioned before, in the first section, such as high speed and parallel processing, are not insignificant. As a result, developing a photonic computing system is nonetheless of great importance.

1.2 Outline and Objectives

1.2.1 Objective

This thesis focuses on developing phase-change photonic computing and storage area through single device optimization, substrate comparison and large-scale matrix demonstration. Considering contemporary popularity of mobile devices and

integration with data centers, all subsequent experiments are based on integrated photonics for further system miniaturization and future integration with electronics. Aiming at broad, practical applications of optical data processing systems, this thesis firstly delves into a detailed review of existing research into single devices, including the comparison of different modulation methods and an investigation into their respective mechanisms. The single device performance optimization contributes to the precise control of proposed devices, and improve their data storage density as well as their time and energy efficiency. After single device optimization, transfer of methods to photonic platforms constitutes another part of the work since the interactions between phase-change materials and photonic devices on different platforms form the foundation for satisfying all the demands posed by different applications. The comparison of platforms encompasses assessing their respective substrate materials, intrinsic physical properties, device functionality performance, energy consumption, and speed, the complete and thorough investigation of which will be a guide in the future when considering applications on a particular platform. Being application-oriented and as a proof of concept, the research focus will turn to large-scale matrix lab demonstrations to show the capabilities of optical computing and storage as a functional computational core, using in-memory computing architecture. Ultimately, this new computing-storage methodology aims to solve problems generated by the von Neumann bottleneck.

1.2.2 Layout

The content of this thesis is structured following this layout:

- **Chapter 2** reviews existing up-to-date research into integrated phase-change photonics, current photonic platform comparison, and different large-scale photonic system realization methods. In depth of all of these lead to a better understanding of these research topics, their drawbacks, and the necessity for and the importance of developing these projects of this thesis.

- **Chapter 3** contains the device preparation and measurement setup for different experiments in the succeeding chapters. Specifically, this chapter describes how to develop a single device on a new platform, including optimization of photonic devices for the best transmission, choice of different photonic components for different research purposes, and PEC methods to obtain correct nanofabrication devices with critical dimensions. The limits of laboratory fabrication

for large-scale matrices will also be addressed here. Subsequently, it gives the introduction of foundry fabrication for large matrices, which includes detailing transferable and scalable pattern programming. And finally, the specific parameters and fabrication steps of phase-change photonic chips are featured in this chapter, namely electron beam lithography, reactive ion etching, sputtering, and thermal evaporation.

For the experimental setup section, this manuscript describes the setup for single device measurement and matrix multi-channel simultaneous measurement for both single wavelength and wavelength multiplexing measurement, including photonic circuit arrangement and crucial equipment introduction and calibration. Crucially, this manuscript develops the automatic measurement system for automatic device array spectrum measurement and automatic phase-change material status setting process, with the help of automatic two-scale stage mover and Labview programming.

- **Chapter 4** explores the modulation method of single-phase change photonic cell and extends the storage density of a single device to 34 levels, much more than the storage density of electronic transistors: 2 levels. It also achieved the precise and repeatable control of distinguished levels. The results of this chapter have been peer-reviewed and published in [31].

- **Chapter 5** includes the experimental investigation of silicon and silicon nitride platforms for phase-change integrated photonics, including the investigation of material optical properties, the device structure comparison, and the device performance. The silicon platform uses a double-step modulation method demonstrated on the silicon nitride platform in the previous chapter. This illustrated that the modulation method is a universal method that is suitable for different platforms. The results of this chapter have been peer-reviewed and published in [32].

- **Chapter 6** describes the demonstration of a small phase-change photonic computing system that can carry out matrix multiplication. This chapter includes the matrix components preparation, the measurement process of single devices and matrices. The results of this chapter have been peer-reviewed and published in [33].

- **Chapter 7** discusses about possible future improvements based on achievements in this thesis.

All the results recorded in Chapter 4, 5 and 6 were obtained by the author during experiments carried out in Oxford. The fabrication of the matrix chip in Chapter 6 is designed by the author and carried out by Cornerstone Foundry. Moreover, the results found in these chapters lead to patents and publications listed in Chapter 8.

1.2.3 Statement of originality

This thesis manuscript is an original contribution written by the author independently and thoroughly. It consists of an original literature review, innovative findings and procedures carried out during nine academic terms as part of the DPhil studies at the University of Oxford. The exception is that Cornerstone Foundry did the fabrication of the matrix. As mentioned in the above context, this exception is a necessary step that laboratory fabrication facilities cannot carry out. Thus the foundry help is introduced in order to accomplish this work. All the relative foundry technologies are mature and standard on the market. This fabrication is not a central point of the results presented and aims only to accelerate the project progress.

1.2.4 Key results and new science

The main findings of this manuscript – optimization of single photonic device performance, investigation of different photonic platforms for computing and storage applications and demonstration of small functional system application – are described in Chapters 4, 5, and 6, supported by software and hardware preparations presented in the other chapters. The key results and new science included in this manuscript are listed in the followings:

- Demonstration of 34 levels in 1 photonic memory cell: world record at that time and became the cover page of Optica.
- Demonstration of double-step single pulse to control phase-change photonic memory cell efficiently, fast and reliably.
- Analysis and comparison of different photonic platforms for phase-change photonic computing and storage applications.
- Demonstration of photonic hardware matrix multiplication computation core with a 3×3 matrix.
- Demonstration of a software assistance system for automatic photonic matrix controlling and measurement.

Chapter 2

Integrated phase change photonic computing: a literature review

Optical on-chip systems are still in the early stages of development and not as well-explored as electrical systems. Thus, photonic platforms cannot yet handle all the optical functionalities and satisfy all the user demands in the same manner as electrical silicon platforms. To describe the background of integrated phase change photonic computing as clearly and thoroughly as possible, and explain the purpose of the research detailed herein, this chapter is divided into three sections: a comparison of integrated computing platforms; addressing the controlling methods of phase change in photonic cells; and a discussion of large-scale computing systems. This literature review aims to summarize the current state-of-the-art technology, and discuss critical problems and their corresponding innovative solutions for further development.

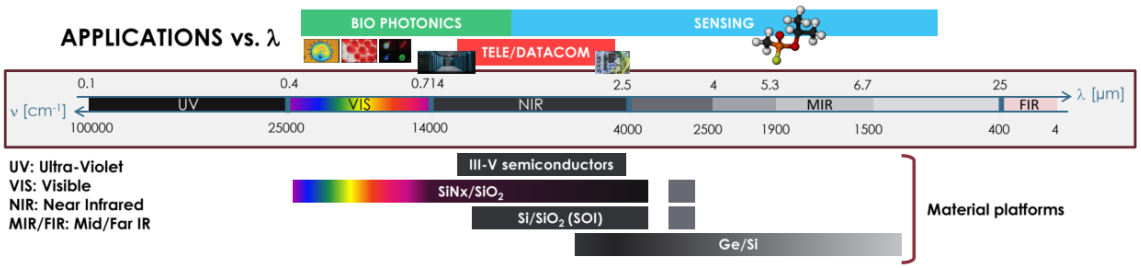


Figure 2.1: Comparison between different photonic platforms from [3]

2.1 Comparison of computing platforms

2.1.1 Different substrate platforms: an introduction

Currently available and widely used platforms in the market include Si, SiNx, III-V semiconductors, Lithium Nitride and polymers [3, 7, 34–37]. The relationship between platforms and wavelength range and applications is shown in Figure 2.1. A fully integrated computing system features numerous interlinked blocks including active devices (such as electro-optical modulators, semiconductor optical amplifiers, and photodiodes) and passive devices (such as directional couplers and arrayed waveguide gratings). All of these devices are important in an optical system, but not all the platforms have sufficiently advanced analogous optical components.

Table 2.1 shows the basic comparison between different platforms in regards to optical components. Three widely used platforms are listed in this table, namely SOI/silica platform, SiN platform and InP/GaAs platform. For SOI/silica-on-silicon platforms, waveguide core is fabricated by silicon, with silica or air working as a cladding layer [4, 38]. In SiN [39] platforms, waveguides are fabricated in SiN material with a silica or air cladding layer. InP/GaAs platforms provide desirable optical properties that silicon or SiN platforms lack such as a direct bandgap and nonlinearity [37, 40]. As can be seen from Table 2.1, all of these three types of platforms have developed passive basic or composite building blocks such as waveguide crossings, Y-Branch splitters, directional couplers, multimode interference couplers (MMI) and arrayed waveguide gratings. Basic building blocks that need nonlinear materials such as electro-absorption modulators, semiconductor optical amplifiers exist on InP/GaAs platforms among these three types of platforms [37]. PIN-doped, N-doped or P-doped waveguides on InP and silicon platforms enable the accessibility of active building blocks such as carrier injection modulators and distributed Bragg reflectors [37, 41]. Thermo-optic modulators, normally achieved by adding metal heaters, are available on all platforms [39, 42–44]. Photodiodes, normally available in Germanium and Germanium alloys, are compatible to both silicon platforms and GaAs platforms [41, 45]. The SiN platforms only support passive devices with easier fabrication processes and lower costs. However, when it comes to the computing applications that this thesis focuses on, as will be shown, different platforms have their own sets of advantages and disadvantages.

To supplement shortages of integrated electronics in areas such as multiplexing, bandwidth, processing speed and intensity, integrated photonics has been developed, primarily in bio-photonics, sensing systems and data communications. Bio-photonics

is often within visible and mid-infrared wavelength ranges [46–48] and use SiN platforms while its sensitive wavelengths covers a wide range of applied wavelengths, from visible to far infrared. Meanwhile, bio-applications rely heavily on Ge/Si and diamond platforms [49, 50] in the mid and far infrared wavelength ranges. Telecom data processing, on the other hand, is based on near infrared and can use platforms based on III-V semiconductors, SiN/SOI and Ge material.

Table 2.1: Maturity of optical components developed on different platforms. (For the sake of fairness of the comparison, hybrid platform devices are not in the comparison scope of this table. More references and detailed explanations are in the main text.)

Components \ Platform	SOI/Silica[4, 38]	SiN[39]	InP/GaAs[37, 40]
Waveguide crossing	✓	✓	✓
Y-Branch splitter	✓	✓	✓
Directional coupler	✓	✓	✓
Multimode interference coupler	✓	✓	✓
Arrayed waveguide grating	✓	✓	✓
Thermo-optic modulator[39, 42–44]	✓	✓	✓
Carrier injection modulator[37]	✓		✓
Distributed Bragg reflector [41]	✓		✓
Semiconductor optical amplifier[37]			✓
Electro-absorption modulator[37]			✓
Photodiode [41, 45]	✓		✓

SOI/Silica platform

Silicon platforms, such as SOI (silicon on insulator), are some of the most popular platforms because of their suitability for complementary metal-oxide-semiconductor (CMOS) electronics. Optical data transport, from tele-optical fibre communication to interconnections between Si electronic chips, raises further demand for both production and long-term development of silicon-based platforms [51].

A schematic illustration of a typical SOI platform is shown in Figure 2.2 (a). The intrinsic bandgap of silicon gives it transparency in the telecom wavelength range, which enables the development of optical computing systems compatible with other optical components and with the CMOS fabrication process. This compatibility also gives it further capability for the cost-effective integration of System on Chip (SoC)

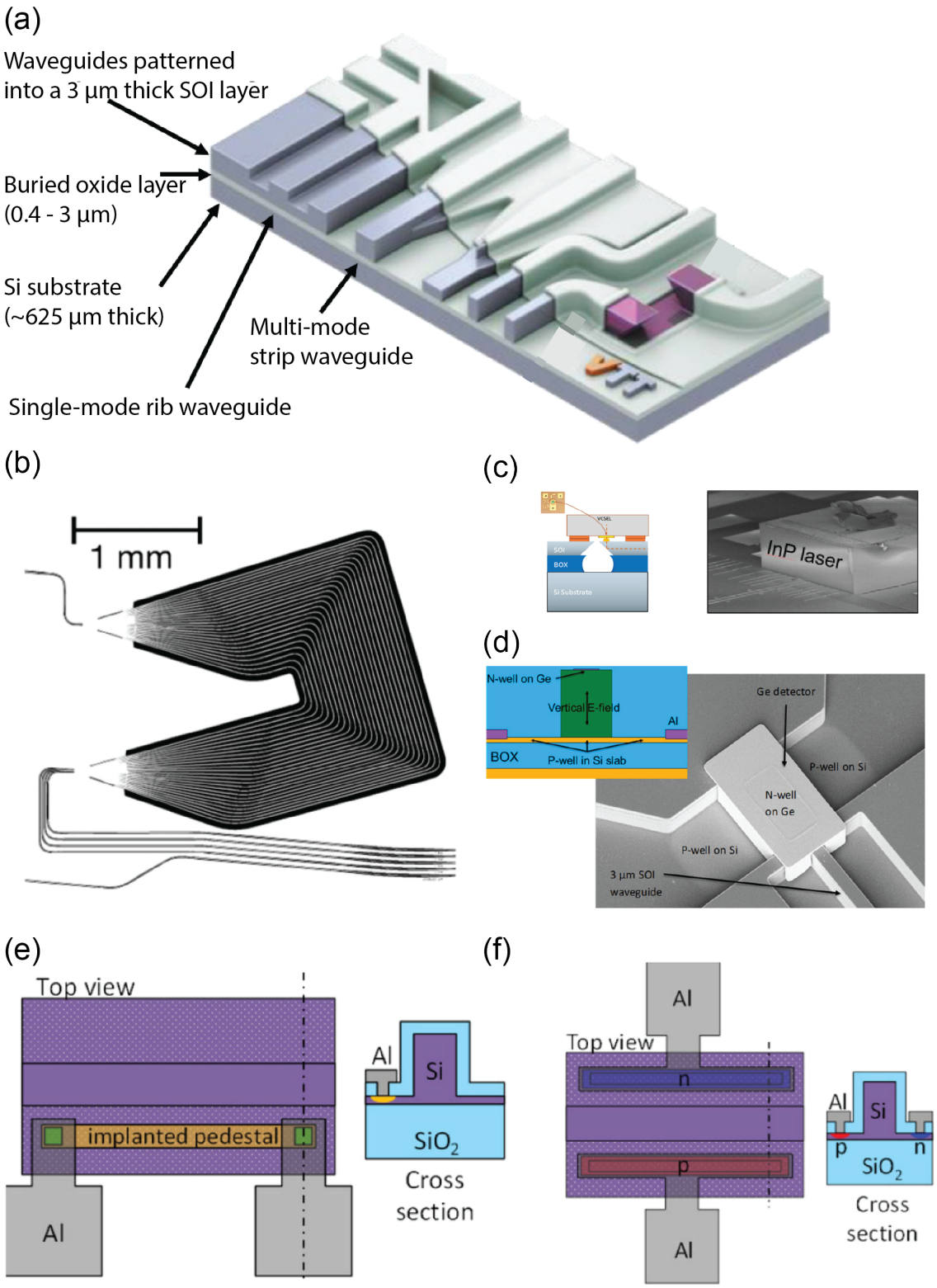


Figure 2.2: SOI fabrication components and available optical components on it from [4] (a) the SOI platform; (b) an arrayed waveguide grating (AWG) on a SOI platform; (c) a hybrid integrated VECSEL and an InP laser source; (d) a Ge PIN photodetector; (e) a thermo-optic phase shifter with implanted heater; and (f) a phase shifter with PIN junction for carrier injection.

and System in Package (SiP) designs. Additionally, the high refractive index contrast of SOI platforms provides them with a compact physical footprint, enabling optical components to scale down to the micrometer level instead of the previous millimeter scale [52]. Moreover, active optical components such as carrier depletion modulators (Figure 2.2(e))can be added onto SOI platforms through ion implantations, thus enabling electrical-optical conversion [53]. Optical on-chip lasers (Figure 2.2(c)) and on-chip photodetectors (Figure 2.2(c)) can be made available on SOI platforms in a hybrid manner, for example with an InP film. Large thermal conductivity and thermo-optic coefficients also make it advantageous in accommodating thermally driven optical components. In this way, many critical optical components have been developed on this platform, not least high-speed modulators (Figure 2.2(e)), couplers, multiplexers and demultiplexers (Figure 2.2(b)). All of them contribute to a flexible and functional all-optical computing system.

There are disadvantages to a SOI platform for computing applications. Significant thermal conductivity accelerates the thermal dissipation, and as a consequence, it reduces cooling time and improves computing speed. However, on the other hand, it can generate problems relating to optical computing processes. During passive data computing that only requires low optical signals, thermal stability and thermal isolation are needed. However, during processes with active weights settings that need energy accumulation to switch the state of the PCM, high thermal conductivity makes it difficult to accumulate energy. Crucial components for integrated optical systems such as on-chip InP lasers, amplifiers, and on-chip Ge photodetectors need further development to be integrated onto SOI platforms. While denser footprints may bring lower costs, they are nonetheless associated with a higher demand for quality and lower tolerances during fabrication. This makes it difficult to yield repeatable performances in large computing systems with regard to research and design, thereby pushing fabless commercial fabrication models to a more quickly developed iteration. The typical propagation loss of silicon is 1-3 dB/cm with a minimum bending radius of 5 μm [3]. The refractive index of silicon is noted in Figure 2.7, but to reiterate, The effective refractive index for a silicon waveguide is typically 2.35 for a wavelength of 1550 nm [54].

SiN platform

SiN is a CMOS compatible platform, and its broadband nature gives it a wider range of functions that cover wavelengths from the visible to the mid-infrared. Therefore, applications such as signal sensing and processing, telecom data transport, and biophotonics can be developed extensively on this platform [3]. Low loss makes it

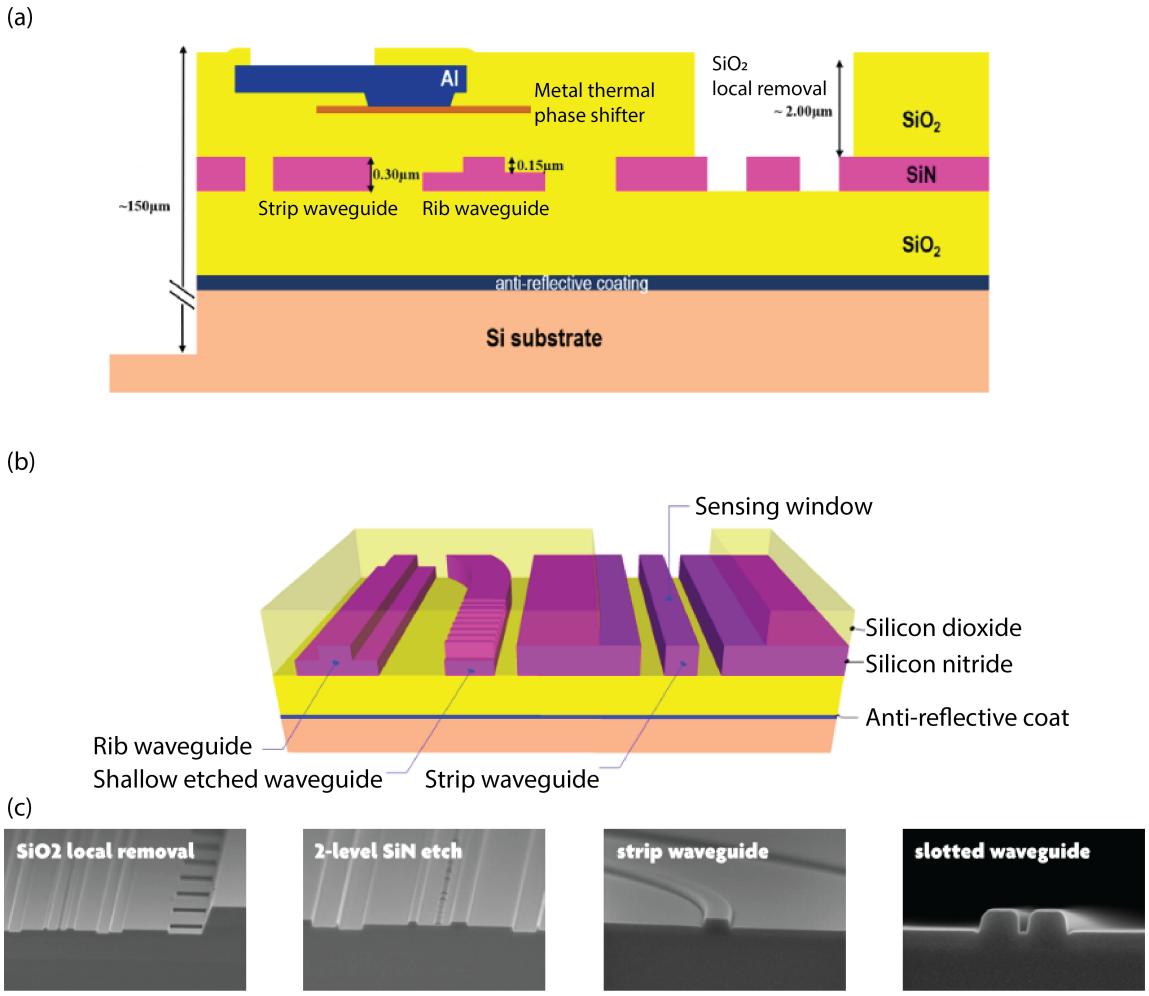


Figure 2.3: A schematic illustration of a SiN platform and the available optical components from [5] (a) The cross-section image of a SiN platform. (b) The stereogram image of a SiN platform. (c) The SEM images of SiN optical components such as strip waveguides and slotted waveguides.

suitable for quantum computing which only uses single photons, while the low confinement in the Si_3N_4 gives it low propagation loss down to 0.02 dB/cm [3, 55], simultaneously leading to a bigger footprint, over twice the width of typical silicon waveguides. This bigger footprint contributes to it having greater tolerances and stable fabrication. Thus, this platform has advantages such as a short fabrication period and lower foundry costs.

However, the typical bending radius for SiN platforms is much bigger than that of SOI platforms. Figure 2.3, below, shows a schematic illustration of a standard SiN platform layout. It can be seen that many passive optical components have been integrated into this platform but also that there is a lack of active optical components because SiN dielectric based photonic platforms do not support them, whether they are optical sources, amplifiers or photodetectors as shown in Table 2.1. As a result, the integration of large-scale optical on-chip systems is challenging. With smaller thermal conductivity, Si_3N_4 accumulates energy more easily compared to SOI platforms, but heat dissipates from them with markedly more difficulty. According to [32], the heat dissipation of Si_3N_4 platforms is approximately 4 times harder compared with SOI platforms. If energy accumulation is required(as instanced in existing research that enough energy is needed for switching PCM on waveguides [32]), this property leads to slower energy transfers but higher energy accumulation efficiency on SiN platforms. Another characteristic feature of SiN compared to other platforms is its small non-linear coefficients. This is a useful property since it means that higher power can be guided through the waveguide, though it would be a disadvantage if non-linearities are needed.

InP platform

Thanks to a great deal of time invested in the development from the production of the first on-chip InP laser [6], InP platforms can integrate all kinds of active and passive optical components including lasers, amplifiers, modulators, multiplexer/demultiplexers and detectors. Added to this, it can work in the near and mid-infrared wavelength range. The flexibility in application is the biggest advantage of this platform and provides it with much potential for further development of all-optical versatile systems on one chip. Figure 2.4 shows a schematic illustration of InP platform components including lasers (Figure 2.4(b)) and photodetectors (Figure 2.4(c)).

However, InP substrates are not compatible with the CMOS fabrication process, which leads to difficulties in developing hybrid optical and electronic systems. InP platforms are also limited to small wafer scales (presently of the order of 6 inchs) unlike

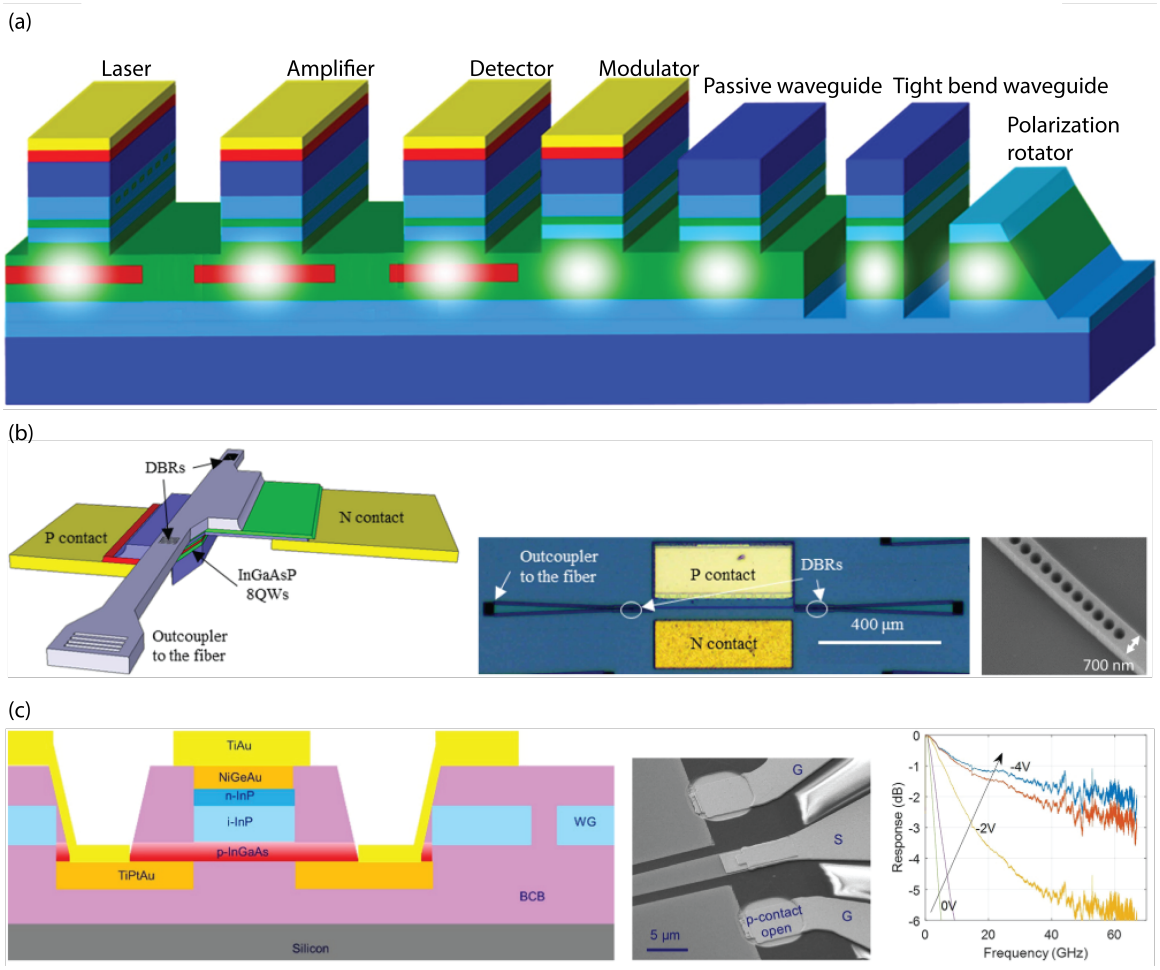


Figure 2.4: The schematic illustration for an InP platform and available optical components on it adapted from [6]. (a)the schematic illustration; (b)an on-chip laser; and (c) an typical on-chip photodetector for InP platforms.

Si platforms, due to the more fragile properties of the material used. Furthermore, this necessary material is more expensive than its silicon counterparts. Intensive research has been conducted, investigating the potential in combining InP and Si platform methods [56–58], to take the advantage of their collectively excellent active components performance, CMOS compatibility, and low costs.

Polymer platforms

Started as an alternative to the dominant platforms, namely InP and silicon, the polymer platform was developed due to its unique properties. These include a combination of large thermo-optic coefficient and low thermal conductivity, easy and cost-effective manufacture, and being capable of integrating active components (e.g. InP lasers) and accumulating low loss passive components (e.g. waveguides, thermo-optic tunable modulators, and arrayed waveguide gratings. Not only this, but it easily combines thin-film-based optical components and Ge-Si photodetectors, and is suitable for on-chip optical fiber attachments [7, 59, 60]. Polymer platforms also have potential in bio-sensing, DNA detecting, and flexible or wearable devices applications [61–64]. However, a relatively low refractive index reduces its potential in device miniaturization and highly compact optical systems. Figure 2.5 shows the integration of different polymer platforms of active or passive optical components.

It can be seen clearly from Table 2.1 that while most of the platforms are suitable for telecom data processing related applications, there is no platform that can cover all the wavelength ranges that are suitable for all applications. This means that a combination or integration between different platforms is needed to have sufficient optical components with optimized performance, and good packaging is important to enable the combination of all platforms and interfaces with electronics [65, 66]. Comparing different platforms gives us an opportunity to take advantage of the specific properties of different platforms to develop highly compact, cost effective, and high-performance optical computing systems. For this thesis, the focus is the applications of data computation and storage at a wavelength of 1550 nm with on-chip phase change photonics on SiN and SOI platforms. These will be discussed and compared in the following chapters.

2.1.2 Platform interaction with PCMs

After acquiring a general understanding of different platforms, researchers started to combine PCM and different photonic platforms to have photonic devices with

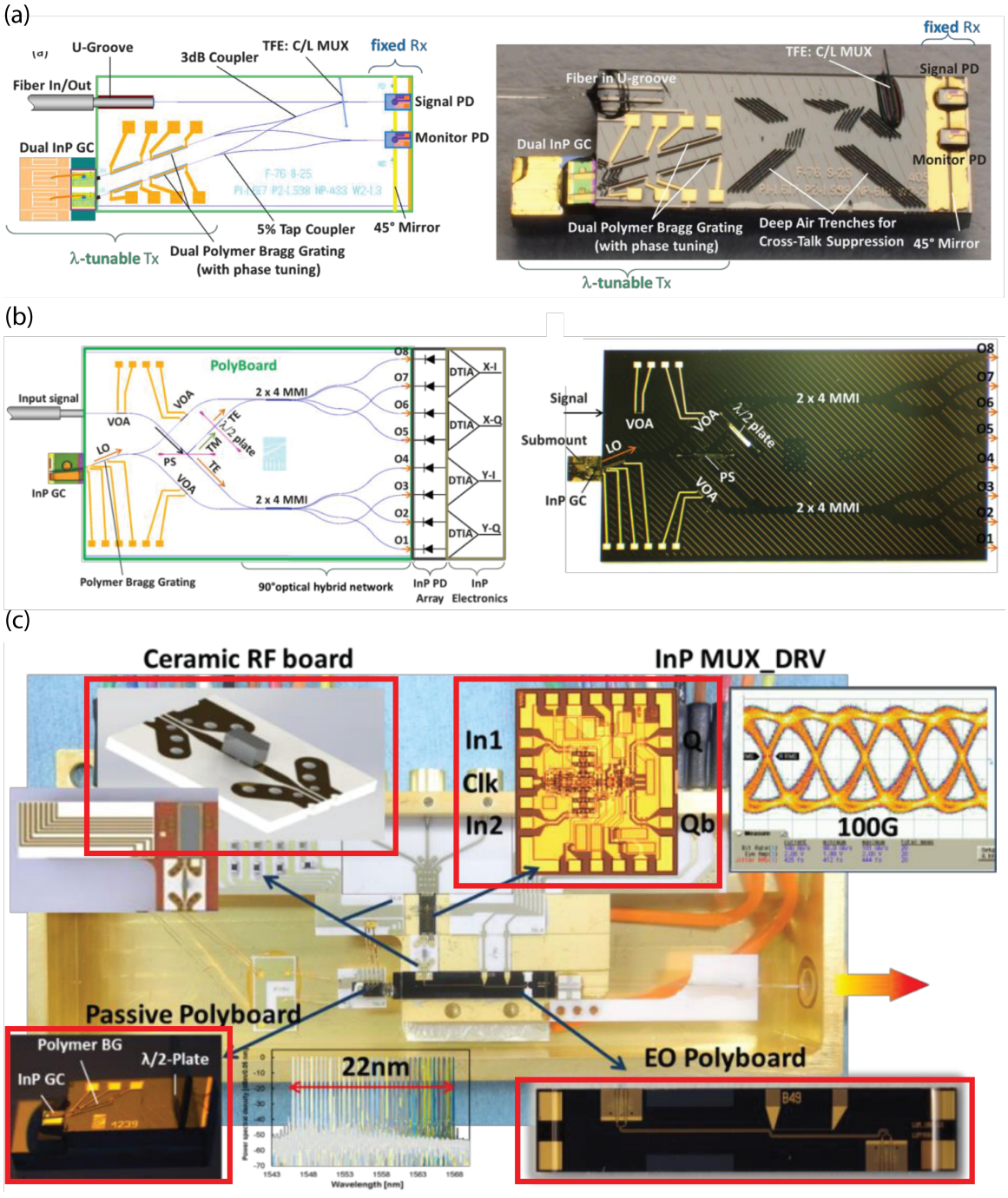


Figure 2.5: Different optical components on polymer platforms or polymer hybrid platforms [7]; (a) an assembled polymer-based hybrid integration platform for a colorless optical network unit; (b) a schematic and photograph of a coherent receiver with a polymer-based photodetector array; and (c) a photograph of optical components combined by polymers and other materials: ceramic RF board integrated on the polymer platform; InP-DHBTs for ultrafast driver electronics; polyboard for wavelength tuning and polarization adjustment and electro-optic polyboard for fast light modulation.

excellent functionalities as mentioned earlier. This is because of their advantages in adding active components to passive circuits, non-volatility for energy efficiency consideration, and the unique in-memory computing feature, amongst others.

Introduction to PCM

There have been different definitions of the term PCM for the duration of its usage. Initially the term was used for fast phase changes [67–70], namely, materials that can change from a solid to liquid state (e.g., water) are labelled "phase change materials" [71]. This feature was used for work into energy storage and release during the phase transition from solid to liquid states [72]. However, for this thesis, the definition of PCM is restricted instead to that of an alloy of different metals that can switch between different states (namely, amorphous and crystalline states), and maintain stability in each state if the external environment does not change [73]. The research of fast phase changes and, subsequently, huge non-volatile changes in optical or electrical properties started in the 1970s [74]. Here, the switching condition is related only to the temperature of the material. Table 2.2 shows the melting and crystallization temperatures of different PCMs as defined for this thesis. The absolute temperature and relative temperature differences between melting and crystallization points determine the difficulty of modulating the status of these materials. The materials can be heated by methods such as direct heat [75], electricity [76], optics [10], magnetic [77], or other forms of energy transfer. It then transitions to a liquid state after its temperature exceeds its melting point and when slowly cooled down, allowing the atoms enough time to shift, it will form the energetically preferred crystalline phase [78]. If the cooling rate is high enough, it will instead become amorphous, as shown in Figure 2.6. The proportions of crystalline and amorphous parts can be tuned to achieve multi-level states extending to either fully amorphous or fully crystalline states [10]. This kind of mixed state, together with the significant optical changes in telecom wavelength range (green color range shown in Figure 2.6), enables the possibility for multilevel storage for recording different information. Moreover, the switching between states is reversible, flexible and easy to control [79]. Taking advantage of this property, plenty of applications such as in digital storage [80, 81] (i.e.Blue-Ray discs [82], and CD/DVD [83]), displays [84], and phase change electrical memories [84], have been demonstrated.

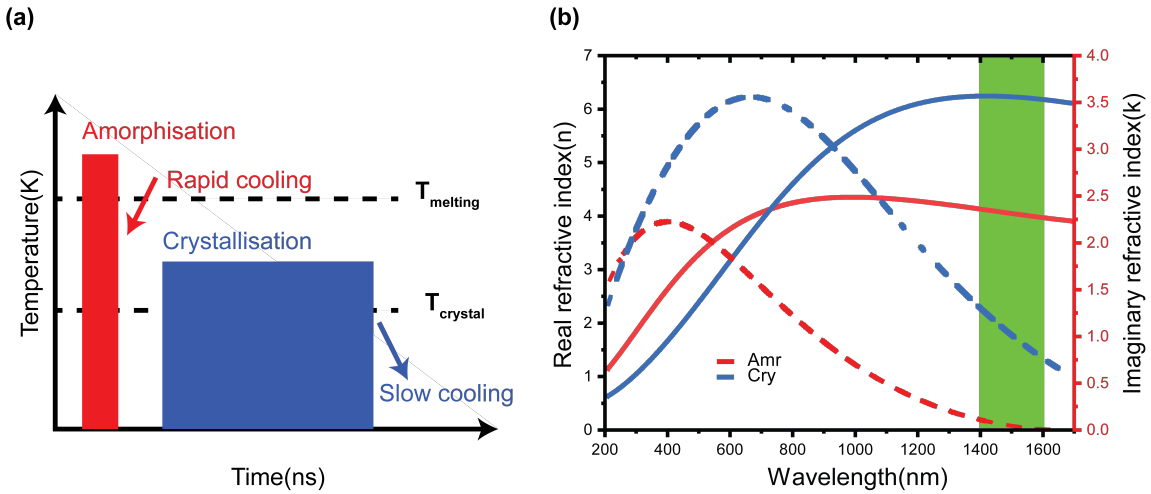


Figure 2.6: (a) The relationship between temperature changes during the phase transitions of the amorphisation and crystallisation process. When a short pulse on a nanosecond timescale with high light intensity is applied to PCMs (red bar in (a)), this material will experience a rapid heating up and rapid cooling down process during the amorphisation process. During the crystallisation process, a longer and less intensive pulse is applied to the material and it will experience a slow cooling process (blue bar in (a)). (b) shows optical properties of $Ge_2Sb_2Te_5$, a widely used type of PCMs and the material used in this thesis. The red solid line represents the real part of refractive index of amorphous GST and the blue solid line represents crystalline GST. The red and blue dashed line represent the imaginary part of refractive index of amorphous and crystaline GST respectively. The green bar is located in the wavelength band which is explored in this thesis, 1400-1600 nm telecom wavelength band.

Table 2.2: Melting temperature and crystallization temperature of different PCMs

PCM	$T_{melting}$ (℃)	$T_{crystallization}$(℃)	Reference
$Ge_2Sb_2Te_5$ (GST)	600	100-150	[85]
AgInSbTe	535	110	[86]
Sb_2S_3	550	270	[87]
Sb_2Se_3	611	183	[88]
Sb	630.6	150	[89]
$GeSe_4$	692	165	[90]
GSST	627	314	[91]

Platform interaction with PCMs

Figure 2.6(b) shows the optical properties of a typical PCM GST ($Ge_2Sb_2Te_5$). Photonic processing has been investigated for a long time since the first on-chip laser

was produced in the 1970s [6]. However, it was only much later, in 2015, that PCMs started to be used as a photonic material to enable optical integrated memory [10], which led to extensive exploration into the SiN and Si platforms. Figure 2.7 (a) and (b) show the optical properties of these two latter platforms, from which it can be discerned that in the wavelength range that is of interest to the research herein (the telecom wavelength range), GST has a large contrast in both real part of refractive index n and imaginary part of refractive index k, and a significant difference in n across the two platforms. Si has a much greater refractive index compared to both GST and SiN, these two being similar in this aspect. This also means that there is a bigger mismatch between Si and PCMs when compared with other platforms, leading to a stronger confinement of light and, thus, a denser footprint. The differences between SiN platform and PCMs are not as great.

PCMs, including GST, AIST and recently heated Sb_2S_3, have been investigated on SiN platforms [92] for a long time. Because of the difference in both thermal conductivity and optical absorption properties [32], it is preferable to use SiN instead of Si platforms. At the very beginning people started phase change photonics on SiN and it proved to be convenient since such devices can have smaller insertion loss and propagation loss [84]. It is better to use this platform from an energy cost consideration, while tolerance during fabrication also makes the final results more stable between devices. For example, studies have been conducted in adding PCM to rings and enabling high on-off switching ratios [93]. The repeatable micro-ring resonators built into the SiN platform with a high-quality production process, along with high transmission, facilitated excellent performance. Similarly, plenty of optical components have been developed, including modulators, accumulators [94], memory arrays [95], and computing cores [12], all of which are on SiN [16, 96] platforms. Equally important is that it is suitable for large-scale usage because of its high tolerance during manufacture.

For Si platforms, since the medium has a higher refractive index, in contrast to PCMs [32], they can confine light more efficiently thus leading to a smaller footprint. In addition, because plenty of active optical components have been demonstrated to be viable on silicon platforms (Table 2.1), PCMs are easier to transfer to different applications when combined with other powerful optical components such as high speed modulators [84, 97, 98], doped Si heaters [20, 21] and so on.

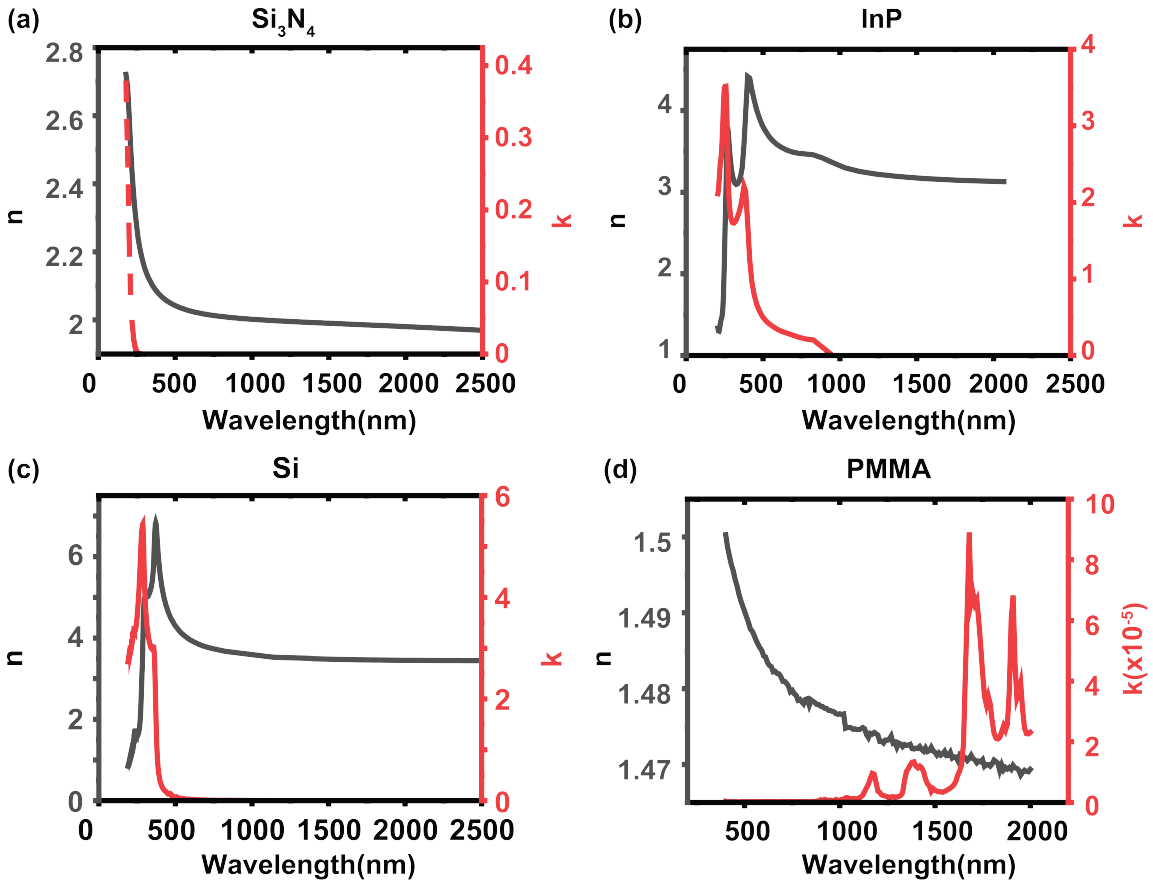


Figure 2.7: Refractive indices of different platforms for telecom wavelength range, where black lines and the left y-axis indicate the real part of refractive index and the red lines and right y-axis represent the imaginary part of refractive index. For the polymer platforms, PMMA is used here as an example of commonly used substrates: (a) Si_3N_4 platform; (b) InP platform; (c) Si platform; and (d) Polymer(PMMA) platform. [8].

Table 2.3: Melting and crystallization temperature of different polymer substrates

PCM	$T_{melting}$ (℃)	Reference
PDMS	-40	[99]
PMMA	160	[100]
PC	145	[101]
PET	255	[102]
PVC	115	[103]
PEI	340	[104]

However, before the commencement of the research that will be presented here, there were no SiN and Si comparisons for PCM applications, and several important considerations were lacking in existing studies, most notably energy consumption, and switching speed and contrast, which is crucial for the further development of phase change integrated photonics. It is for this reason that systematic research was carried out in the directly related DPhil study, wherein the experimental investigation the differences among various platforms served as inspiration for further study, including this continuation.

For InP platforms, concerted efforts are yet to be made into their advancement in combination with PCMs, though it is worth exploring. It is transparent in telecom wavelengths band and with its refractive index, it can provide a small footprint [105], added to which, it has the intrinsic capacity for optical components with non-linear properties such as on-chip lasers[106–109]. Non-linear functionality is vital in neural networks for optical machine learning, while on-chip lasers and photodetectors are also necessary for the integration of optical systems.

Similarly, little work has been done covering polymer platforms in conjunction with PCMs, though in this instance, it is because polymers generally cannot sustain the high switching temperatures that PCMs require [110, 111]. The typical melting temperatures for different PCMs and polymers are shown in Tables 2.2 and 2.3, respectively, which demonstrates their incompatibility. Smart methods are needed to be able to combine PCMs with polymer substrates. Nevertheless, further research is valuable in this area since polymers have been heavily studied with respect to medical or human interaction applications such as bio-detection or wearable devices [46, 112–114], which can be a large market for PCM-assisted photonic computing tools.

2.1.3 Towards large-scale and wider applications

Without a doubt, for the large-scale fabrication of optical circuits to be realised, commercial foundry assistance is essential, as instanced by the popular Multi-Project Wafer(MPW) services [115]. After MPW was enabled, this field has gained enormously in its development because of increasingly lower costs and a more stable and reversible performance for large-scale optical circuits [116], as compared to prototyping in university facilities.

For large-scale applications, the energy consumption in the photonic circuitry is imperative since it will rapidly accumulate if not carefully treated, thus becoming a huge burden on the system. The energy costs include propagation loss because of the platform material, bending loss of rings, and the connection loss in cascaded structures, with a majority loss resulting from sidewall roughness and bending loss. Consequently, several techniques were applied to improve the energy efficiency, such as using unique design waveguides or optimizing power distribution manners [117–119]. High loss across the system naturally leads to suboptimal footprint and data density, problems that have been alleviated by the development of components that supply energy on chip in the whole system such as on-chip amplifiers and lasers.

It is important to take the wavelength cover range and completeness of the system into consideration, as a good system should be flexible and adjustable for as many applications and functionalities as it can deliver. In this way, telecom data processing is compatible with long distance optical information transmission. However, a great many applications such as bio-detection and human-machine interaction related computation require a mid- or far- infrared wavelength range [50, 120–123] and to cover all of these ranges on a single chip or a standard process, combining platforms is a method worth looking into more deeply on the development path.

2.2 Controlling methods of phase change photonic cells

The state of PCMs is easy to change, as long as the temperature of the material goes over its melting temperature so that the bonding between different molecules is broken and it can be either amorphised or crystallized depending on the rate of cooling. Advantages and disadvantages of different controlling methods, such as electrical switching or optical switching methods were investigated, and the following details the results and subsequent discussions.

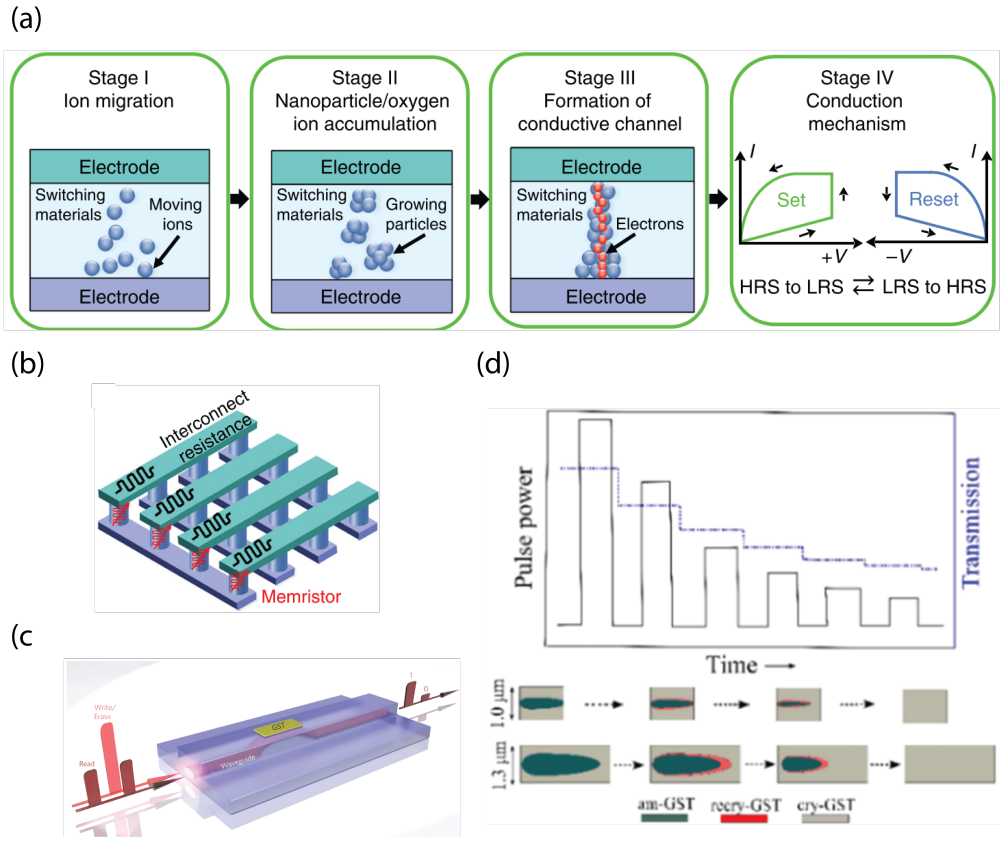


Figure 2.8: Mechanism comparison between electrical switching PCM and optical switching PCMs; (a) a mechanism of electrical switching process [9]; (b) typical electrical devices overview [9] (in electrical devices the PCM sits in between two electrodes); (c) typical optical devices overview [10] (in optical devices the PCM sits on the top of a waveguide); and (d) the mechanism of optical switching process [11].

2.2.1 Key demands for modulation/controlling performance

Stability of status after switching

One reason that the state of a device must be stable is because that it is crucial to develop multilevel devices rather than 0/1 state transistors similar to what are still widely used in electronics worldwide, and their stability is the foundation of realizing multilevel storage and computation. To improve the performance of computing tools, individual devices, onto which several bits were integrated, were developed for this study, serving to increase the data density and thus optimize the integration of devices and the computing density per chip. Therefore, it is very important that each state of a device capable of achieving multiple states must be stable, for them to be distinct and recognizable while keeping overall energy consumption low. This stability includes thermal, electrical, and magnetic stability as well as against other

forms of environmental interference.

Performance with multilevel switching

The aim of developing optical modulation methods in this thesis is to reduce and ultimately annul the current disadvantages of optical systems as compared to those transistors or new electronic formats of storage and computation based on electronic systems. Transistors as a well refined and fundamental electronic component have evident advantages after several decades of optimization, which extends to a nanoscale footprint (technique nodes can go down to 1 nm in the lab and 5 nm in large-scale fabrication, as achieved by TSMC and Samsung in 2020 [124].

On the contrary, there are disadvantages for optical components that need more work to be solved. To begin with, the footprint of photonic circuitry is large, since typical waveguides are about 500 nm for Si and 1-2 μm for SiN, and this is not to mention crucial components such as MZI and rings, which can be as much as over 200 μm in diameter. Another problem comes from fabrication tolerance, wherein a difference of 20 nm in thickness will have a substantial effect on the waveguide confinement mode and the roughness of sidewall confers a high demand for quality throughout the fabrication process. Third, energy consumption is relatively high for PCMs since they rely mainly on temperature changes to switch between different states [1] while electronics make use of the conductive filament's expansion [81, 125, 126]. Although research has been done on directly breaking the bonds between different atoms to switch PCMs using femtosecond laser bursts [127–130], it is still in the early stages of development.

Transistor-based electronic systems have been optimised thanks to generations of researchers throughout the years, but by contrast, optics seems to lose their advantages if the optical device is only one binary device. This current disparity necessitates finding breakthrough points from other areas, such as accommodating more bits in one cell to improve computing or storage density. In addition, other attempts such as wavelength multiplexing are needed to take full advantage of photonic computing, and therefore have the potential to gain compatibility compared to the current tried and tested electronic computing tools. Multilevel platforms will be increasily useful when it comes to large-scale optical circuits with high integration at the system level and the more components that are integrated, the higher the computing density it will be capable of, and more so with multilevel components compared against transistors. This is because the size or density of physical devices increases linearly while the storage volume increases exponentially.

Reversible identical status realization

Another key aspect for controlling is reversible switching. Compared to the 0/1 transistor, multilevel devices have less error tolerance, but there are two options to mitigate this reduced tolerance: conformation of the exact state of the device after each switch occurs; or improve the reversible switching performance to make sure that the same performance using identical switching parameters can be achieved. A popular method in use is Write and Verify when the device is in specific states. Electrical devices previously underwent much drifting, prior to the implementation of optimized device structures [131]. However, in the optical domain, it has been noted that the phase change photonic devices are intrinsically drift-free [132]. Even better, the optical devices can reversibly switch to the same state without problem or further modification, something which is very hard to achieve in the electronic domain. Thus, it is inherently difficult to have clear, easily-distinguishable, and easily-controlled phase change electronic switching or detecting devices. As a consequence, the argument in favour of further development on these functions from an optical approach with photonic devices is compelling, as will be demonstrated further as part of this thesis, and high-density data storage will be shown with good reproducibility in Chapters 4 and 5.

Fast speed and cyclability for the training process

Considering specific applications that are targeted in this thesis, devices need to have the capability to, very rapidly, switch hundreds and thousands of times between different states. For example, in the training process of kernel weights in convolutional neural network, the device states need to be modulated very frequently, while in the training process of online learning networks, the device states need to be modulated rapidly and in real-time. Currently, cycles between switching actions can last as little as a few picoseconds [94], which is comparable to current electrical transistor switching speed (several GHz). However, the cool-down time between continuous pulses is on the scale of nanoseconds [79] which delays the system modulation taking effect. Naturally, different switching methods have different physical limits. Figure 2.8 (as below) shows the different mechanisms of switching PCMs via both electrical methods (Figure 2.8 (a) and (b)) and optical methods (Figure 2.8 (c) and (d)). For optical switching, the PCM itself has limits for switching speed since the switching mechanism needs thermal accumulation to heat up this material over its melting point as well as dissipation, and these processes are generally comparatively slow. For electrical switching, the mechanism is the formation of a conductive filament so the temperature changes do not matter. Other switching methods, such as using

femtosecond lasers, are used to directly break the bonds between different atoms but they are not detailed here.

For electrical switching, because the formation and severing of the conductive filament is relatively simple, it is never difficult for electronic devices to achieve high switching cyclability. Figure 2.8 shows the mechanism of both electrical switching and optical switching. In the electrical domain, the growth of the conductive filament and thus the on/off switching between these two states decides whether the device is conductive or not. Only a very small amount of material is required to form a connection point, which can still lead to a large switching contrast with regards to electrical resistance. However, in the case of optical switching, the area of evanescent coupling material decides the absorption of light, as it is shown in Figure 2.8 (c), which means that a smaller transmission contrast results in a narrower switching on/off window. Worse yet, and conversely, larger switching areas lead to lower cyclability and slower switching speed. Despite that, this particular feature can help to generate more stable and distinguishable multilevel states.

2.2.2 Interaction with PCMs

Since PCMs have a large contrast in both electrical resistance and optical absorption between amorphous and crystalline states, a wealth of researches exist concerning this property, including studies into optical versus electrical switching, optical and electrical measurement, exploring optimized modulation methods, and information recording methods in optical computing systems with PCMs. As is expected, different switching methods are chosen in accordance with the different properties of the materials and their applications. For example, in some instances optical switching is chosen because it has substantial capability for absorption in the pump wavelength range during the process of being switched. In addition, some PCMs are electrically conductive while others are not, leading to different electrical switching mechanisms (electrical field switching or joule heating switching).

2.2.3 Optical controlling methods

To optically switch a PCM, high rates of absorption in near-infrared wavelength range are needed. Amorphous states absorb much less light than crystalline states. As a consequence, crystallization process is a much harder process than amorphization process. Regardless, PCMs can work on both thin film meta-surfaces for free-space optics and attached to waveguide for integrated photonics, which are shown in Figure

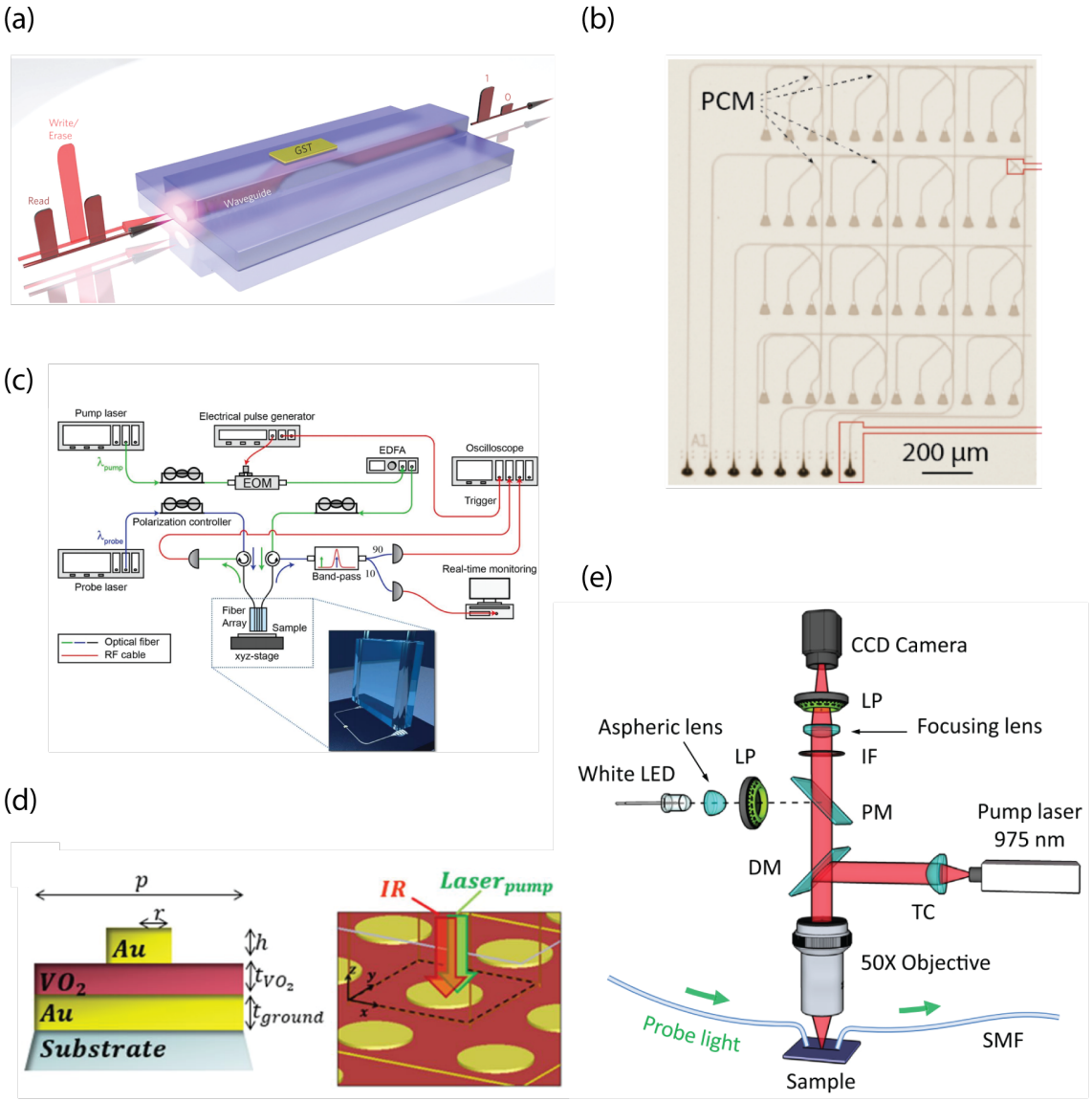


Figure 2.9: Different examples of optical switching: (a) optical integrated switching by evanescent coupling in waveguides [10], using the same light path with probe light; (b) optical integrated switching array [12], using separate pump path to improve energy efficiency; (c) a typical measurement setup for integrated optical switching [10]; (d) optical free-space switching using visible laser [13]; (e) a typical measurement setup for free-space switching [14].

2.9 (a) and (b) respectively. Free-space lasers are used frequently in switching PCM [13, 14, 133, 134] (mostly in the visible wavelength range), introducing the notable advantage of higher energy efficiency since PCM has greater ability for absorbing light in the visible wavelength range. However, free-space switching has certain disadvantages, such as a complicated setup (shown in Figure 2.9(e)) and the need for extra access at the top of the optical chip (shown in Figure 2.9(d)) which limits further integration of larger optical systems combined with electronics. Integrated switching with optics is widely used [12, 32, 135, 136] because of the easily repeatable measurement setup (shown in Figure 2.9(c)) and controllable evanescent coupling. Femtosecond lasers have also been explored for reducing switching energy cost [137], even though it will increase the size and complexity of future optical chips to reserve room for integrated switching circuits. In certain specific situations, volatile switching is used instead of non-volatile, such as using phase shifters to modulate the transsmission of a light path [14] (realized by a thermo-electrical cooler), and using probe power as a source for volatile modulation [132].

2.2.4 Electrical controlling methods

DC voltage and RF electrical pulses are usually used for crystallization and amorphization, respectively [138], since amorphization process lasts on a nanosecond timescale, much faster than crystallization process, which can last for hundreds nanoseconds to several seconds [31]. There are plenty of electrical switching methods such as formatting electrical circuits to switch under particular circumstances and those developed from more complicated structures, for instance, plasmonic structures, nanowires, doped Si heaters, or sandwich structures with different conductive pads, shown in different figures in Figure 2.10. Crystallization can be achieved via continuous heating by thermal conductive heaters [15, 16] (shown in Figure 2.10(a)), though it lacks the property of fast switching, meaning that it cannot realize amorphization either easily or quickly. Conductive PCM can also work as one part of the electrical circuit to realize phase transitions (shown in Figure 2.10(b)). A doped Si heater has been used to electrically switch PCM GST to work as a heating resistor [20] (shown in Figure 2.10(f)) while in another study, a PIN heater was applied as a resistive heater that also alleviate the loss influence of doped silicon [21] (shown in Figure 2.10(g)). Other research has explored using graphene thin film for thermally switching the material [18] (shown in Figure 2.10(d)) but showed limitations due to a difficult fabrication process. Also, nanowire GeTe has been used to have a large electrical resistance contrast [17] , lower thermal conductivity and thus smaller modulation voltage and

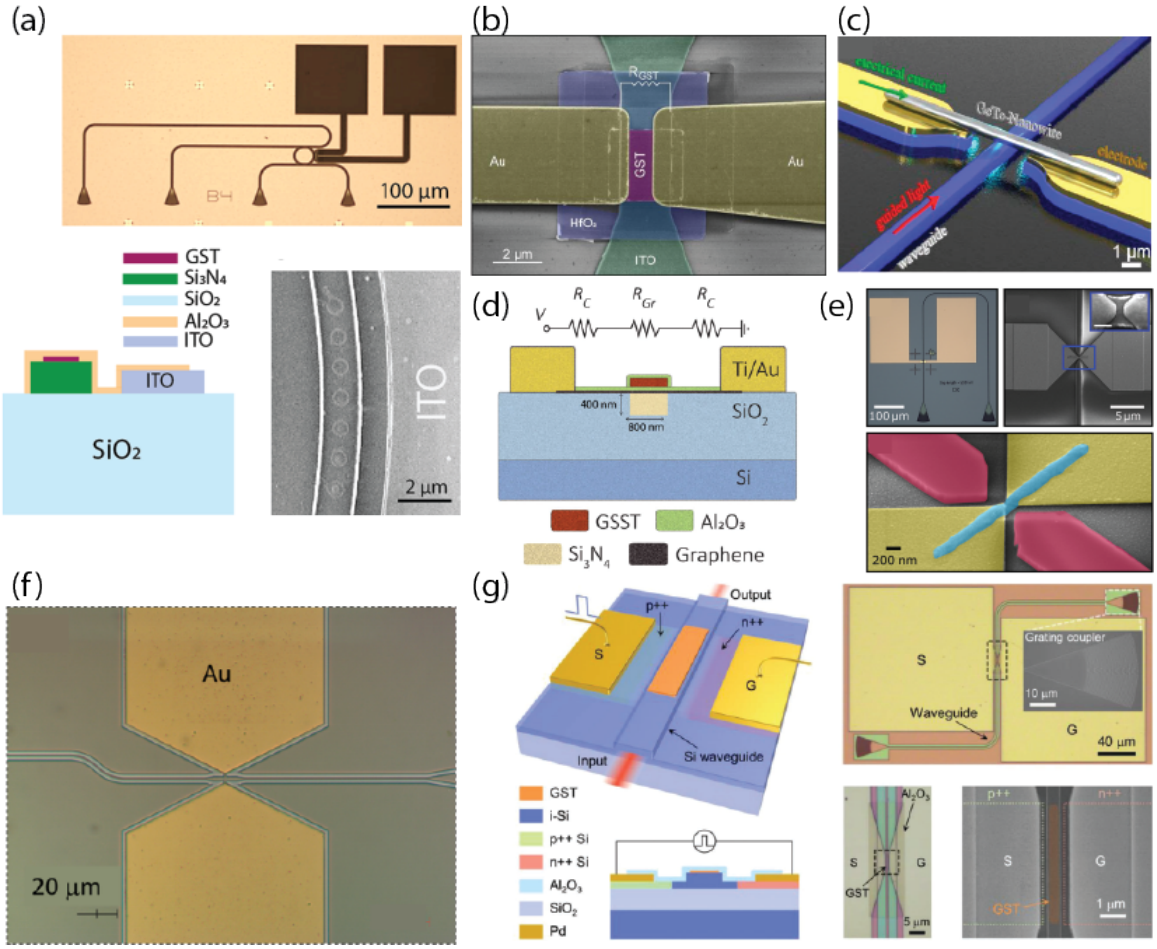


Figure 2.10: Different examples of electrical switching: (a) electrical heating with the dielectrical material Al_2O_3 as a thermal transfer [15]; (b) electrical switching with conductive PCM as one part of the electrical circuits [16]; (c) nanowire structure to switch the PCM both electrically and optically [17]; (d) graphene heater to switch the PCM on waveguides to improve energy consumption and switching speed [18]; (e) plasmonic structure to switch PCM on waveguides in mixed mode with smallest device size [19]; (f) doped Si waveguide working as a micro-heater to switch PCMs [20]; (g) PIN heater realised by doping the sides but waveguides to operate a thermal heater to switch PCM under low loss propagation situation [21].

smaller power consumption (shown in Figure 2.10(c)). Subsequently, a plasmonic sturcture was also explored for mixed mode modulation to further reduce device size and energy consumption [19] (shown in Figure 2.10(e)). Volatile controlling normally happens in real-time active modulation applications such as phase shifters for which VO_2 PCM is frequently used thanks to its low crystallization temperature (68 ℃) [139, 140].

2.3 Large-scale optical computing implementation methods

2.3.1 Key properties in large-scale optical computing

Before the innovation of optical circuits, the development of large-scale electrical circuits gave excellent examples of the performance criteria for large-scale circuits, irrespective of modes. Most of these criteria are suitable for assessing the performance of large photonic circuits in computing. Among the key properties used in a large-scale matrix are stability, aggregate loss from the large-scale optical circuits, and density.

Stability

Stability is a fundamental consideration when accounting for the increasing density of devices on a chip. The first obstacle towards obtaining adequate stability is the heat dissipation resulting from the switching or computing processes of different devices when dealing with parallel functions. The temperature of the device must go over melting temperature or crystallization temperature for the phase transitions, as the table 2.2 shows. Heat may thus build up from PCM absorption during the switching process, the increasing number of parallel channels, or the frequent pump power accumulation over a short time frame. The state of the PCM itself is stable and will hardly be affected by small variations in environmental conditions, but stability of optical signals in the waveguide is easily affected and will vary as temperature changes. This is because the Si platform is highly thermally conductive and easily influenced by the environment, and so its refractive index changes with background temperature accordingly.

Loss

The second consideration is the loss when it comes to larger matrices, particularly when combined with different devices. Loss can be caused by PCM absorption, as well as optical components (e.g. crossings and directional couplers), from modulation

doping, waveguide propagation and the splitting between columns and rows within a large-scale optical network. In this thesis, where grating couplers were used for light coupling from optical fibres to on-chip waveguides. Only 4% energy was coupled into the integrated matrix, thus highlighting another source of energy loss. If specific energy optimization methods such as fiber-to-chip couplers [141] or edge coupling can be used, the energy efficiency will be further improved.

Broadband consideration

To make use of wavelength multiplexing, wavelength bandwidth is another important consideration since it is preferable to have a broadband matrix. It is limited by grating couplers, waveguide propagation profiles, and the bandwidth of directional couplers. The wider the wavelength bandwidth is, the more channels that be accommodated in the optical matrix, and consequently, the higher computation density and computation speed that can be achieved. Additionally, to make full use of different platforms to cover more wavelength ranges and applications, three dimensional structures [142] can be incorporated to combine different substrates, as well as vertical coupling between different layers.

2.3.2 Different paradigms to achieve optical computing

Optical circuits are suitable for actualizing information processing because they are superior to electronic counterparts in three aspects: high parallelism; low heat dissipation; and linearity.

First of all, high parallelism: different from electronics, optical signals can propagate in the same channel as long as just one of the optical properties is different, whether it is wavelength [143, 144], mode [145–147] or phase [148–150]. Secondly, low heat dissipation: heat generated from integrated photonic chips mainly comes from the absorption of photonic waveguides, which can reduce to 3.6 dB/cm in silicon waveguides [151]. For electronic counterparts, heat dissipation depends on joule heating of specific electrical circuits. Heat sinks have become almost necessary for modern integrated circuits such as CPUs, GPUs. Furthermore, optical signals can undergo multiplication through optical waveguide interactions, addition through optical branches without unpredictable energy consumption compared with electronics. All of these unique properties indicate the excellent potential for optical circuits in the future of information processing, especially machine learning and artificial intelligence in which matrix multiplication calculations play a substantial role.

Optical systems haven been intensively studied, due in no small part to a long history in tele-communication systems, in which large-scale arrays are indispensable

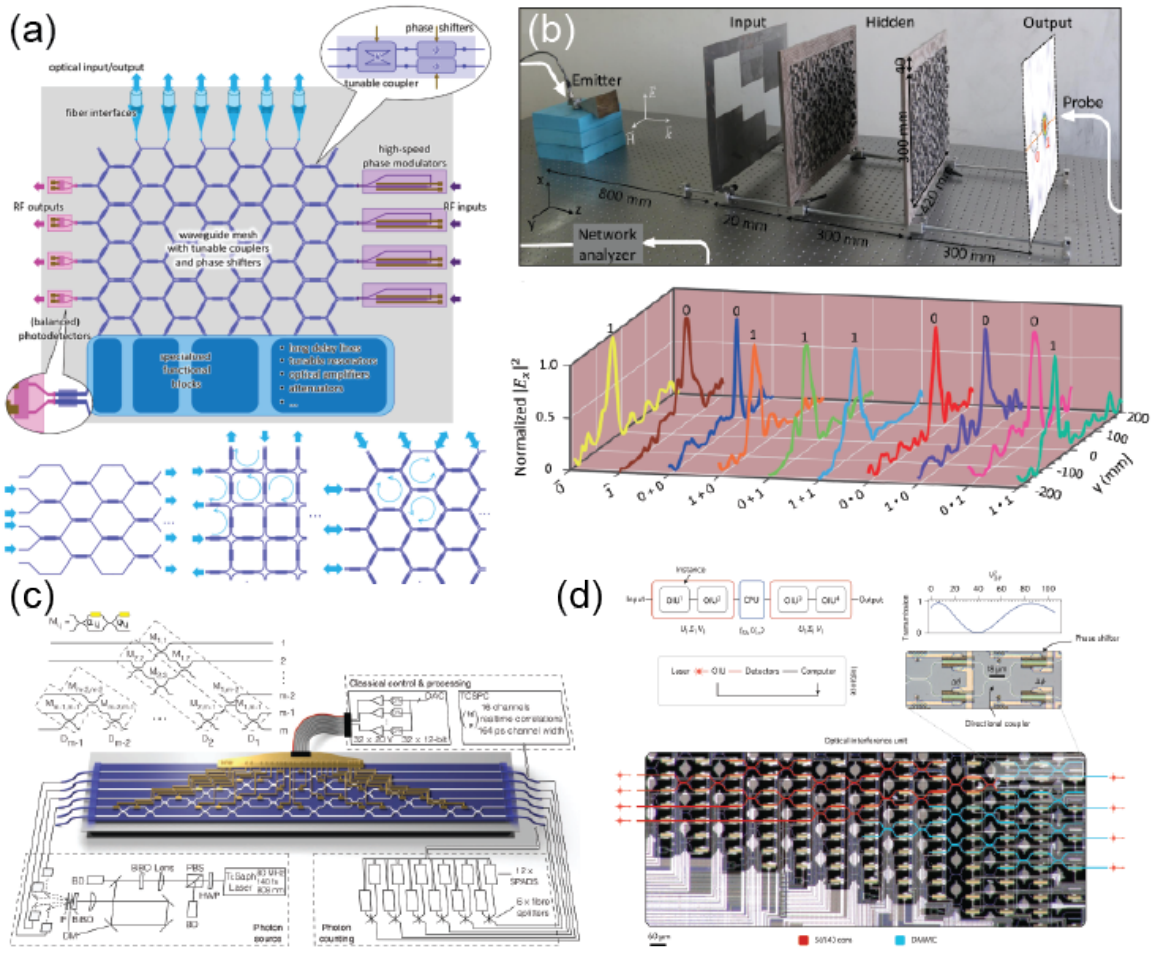


Figure 2.11: Different optical networks for different functions comparison: (a) programmable optical circuits using MZI phase shifters and splitters [22]; (b) diffractive neural network with compound Huygens' metasurfaces [23]; (c) programmable cascaded MZI network for setting photons phase in quantum technologies [24]; and (d) programmable MZI network mimicking a deep learning neural network [25].

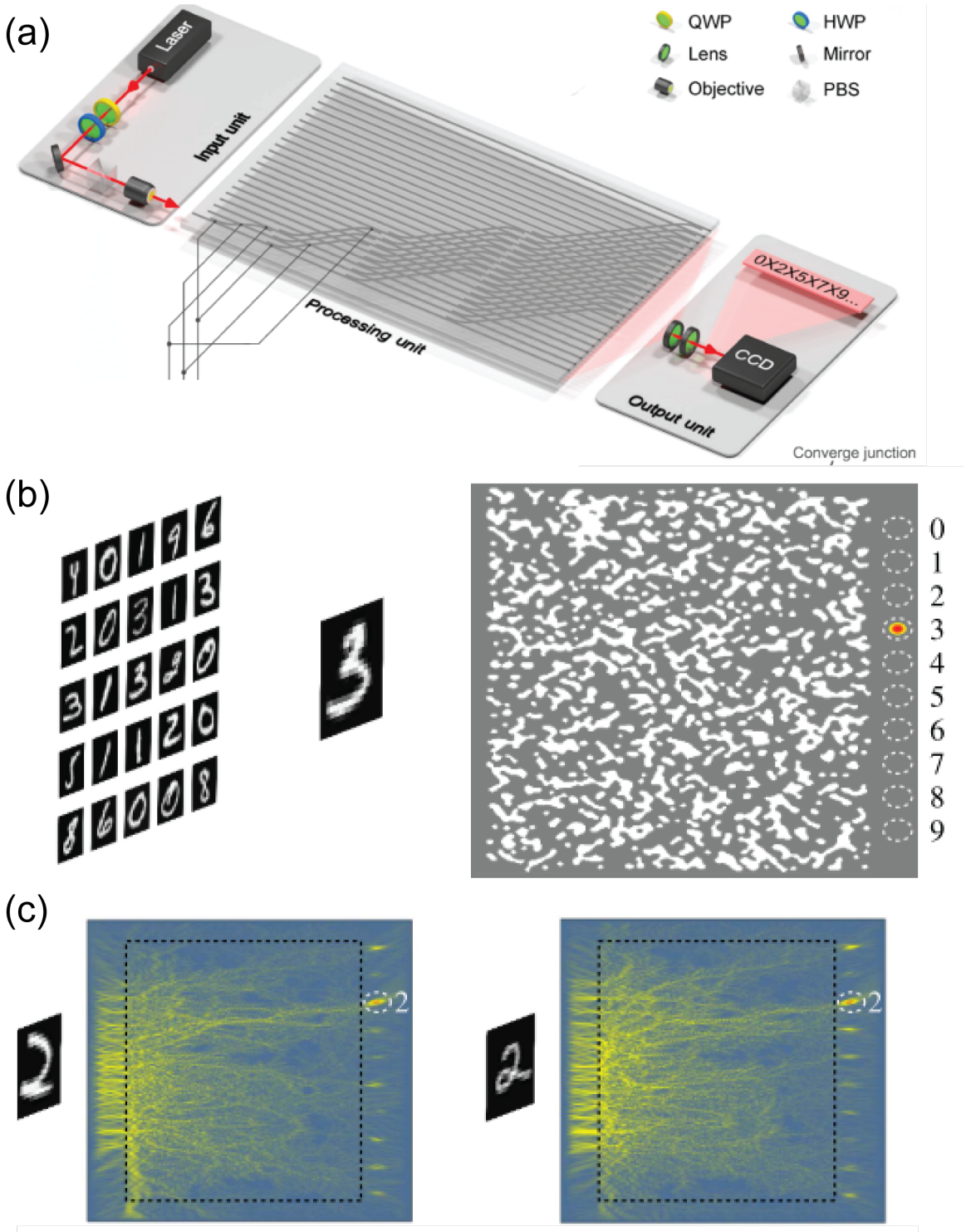


Figure 2.12: Different optical neural network computation realization methods: (a) programmable optical circuits using waveguides with directional couplers [26]; and (b) photonic computing design using nanophotonic neural medium [27].

for heavy data processing, powerful computing, and storage performance [152]. Currently, there are plenty of methods in use for scaling up optical computing including, but not limited to, MZI arrays [153–155] (shown in Figure 2.11(a)(c)(d)), free-space diffraction patterns [23, 156] (shown in Figure 2.11(b)), directioinal couplers [26](shown in Figure 2.12(a)), nanophotonic medium [27, 157] (Figure 2.12(b)), photonic crystal [158], and quantum computing [24], and etc.

The mechanism of optical computation realization is different, resulting in different applications. A photonic crystal is a periodic optical nanostructure with different refractive index to the environment that influence the motion of photons by photonic band-gaps. Photonic crystals can be one, two or three-dimensional and be employed in optical computing and signal processing. Figure 2.11(a) shows that using a mesh of on-chip waveguides, beam couplers and phase shifters, optical computation can be achieved for different applications such as linear matrix operations, quantum information processing and microwave photonics [22]. Figure 2.11(b) describe that using diffractive neural network with compound Huygens' metasurfaces, optical logic operations can be achieved. A monopole prove scans the spatial intensity distribution at the output plane to record the results. Figure 2.11(b) also shows the scanned results with at a certain x and y values [23]. Figure 2.11(c) shows a 15 MZIs integrated photonic network working as a thermo-optical phase shifter network to set the phase of photons in quantum technologies [24]. Mach-Zehnder interferometers, used to measure the relative phase shift variations between two collimated beams derived by splitting light from a single source, can now be used for optical computing and signal processing by using the phase of the light as the encoded information. Figure 2.11(d) shows 56 MZI network that can carry out the linear computation in the deep learning process to realise vowel recognition [25]. Figure 2.12(a) solved the subset sum problem using integrated photonic network accomplished by directional couplers. With the number of waveguide channels representing the addition factors, photons can dissipates into the specifically designed integrated photonic network sufficiently and search for solutions in parallel [26]. Figure 2.12(b) shows digit handwritten pattern recognition by using nanophotonic neural medium [27]. A SiO_2 chip as a host material and numerous inclusions such as air holes accomplish the computation medium shown in Figure 2.12(b). The input light intensity is encoded by the test image converted from 20×20 pixels into a vector. The light enters from the left and then is scattered by inclusions and the output is the energy tistribution on the right side of the medium, illustrating the recognition results. Figure 2.12(c) shows the simulated

optical fields inside the nanophotonic neural medium when the digit ”2” is recognised by two different ”2” samples.

The advantages of diffraction patterns and holographs lay in having a high density in one chip, capacity for fast parallel computing processes, and that all the devices on one chip can be processed simultaneously once the light is shining through the chips. Essentially, the process is finished at the speed at which light can pass through, a feature that is especially suitable for pixel intensive image processing. MZI arrays are preferable for their long-established structural design philosophy, easy to achieve large-scale array fabrication, and stable single device performance when they are scaled up to large matrices. When it comes to photonic crystals, this method can achieve high density computation since it is capable of resolutions down to the nanometre scale [130, 159–161]. The PCM, though not significantly affected by high absorption loss, needs further optimization on material properties. It can also be improved by including changes to the structures of the micro rings or other devices that are of a smaller size and better tunability, that can carry out the computing. Building on this, new forms of architecture, such as those of neuromorphic and reinforcement computing, can also be explored in the future.

Chapter 3

Device preparation and measurement setup

This chapter mainly discusses the fabrication and measurement setup preparation and optimization for getting better measurement results. Based on previous technological development, the device preparation in this thesis continued developing phase-change photonic devices on SiN, and for the first time, developed and optimized phase-change material photonic devices on a silicon platform. Device preparation is divided into two parts, single device preparation by laboratory nanofabrication and large-scale matrix fabrication by collaboration with foundries. The experimental setup includes measurement setup for basic calibration, material calibration, single device switching test, single wavelength large-scale matrix multiplication test, and finally wavelength multiplexing test.

3.1 Device preparation

3.1.1 Single device optimization

The phase-change photonic device consists of a layer of $Ge_2Sb_2Te_5$ (GST) thin film capped by a layer of Indium-Tin-Oxide (ITO) and evanescently coupled to a Si_3N_4 (SiN) or Silicon(Si) photonic waveguide. A typical phase-change photonic device fabrication process includes the following steps (shown in Figure 3.1):

1. Electron beam lithography for pattern transfer and then dry etching for generating SiN or Si waveguides. The fabricated waveguides are shown in Figure 3.1(b). For Si waveguide, SOI substrate is used (Silicon on Insulator)(shown in Figure 3.1). The dry etching recipe is: CHF_3 (40 sccm), SF_6 (15 sccm), Pressure: 20 mTorr, Power:100W for 2 minutes and 30 seconds with the etching rate 48.6 nm/minute.

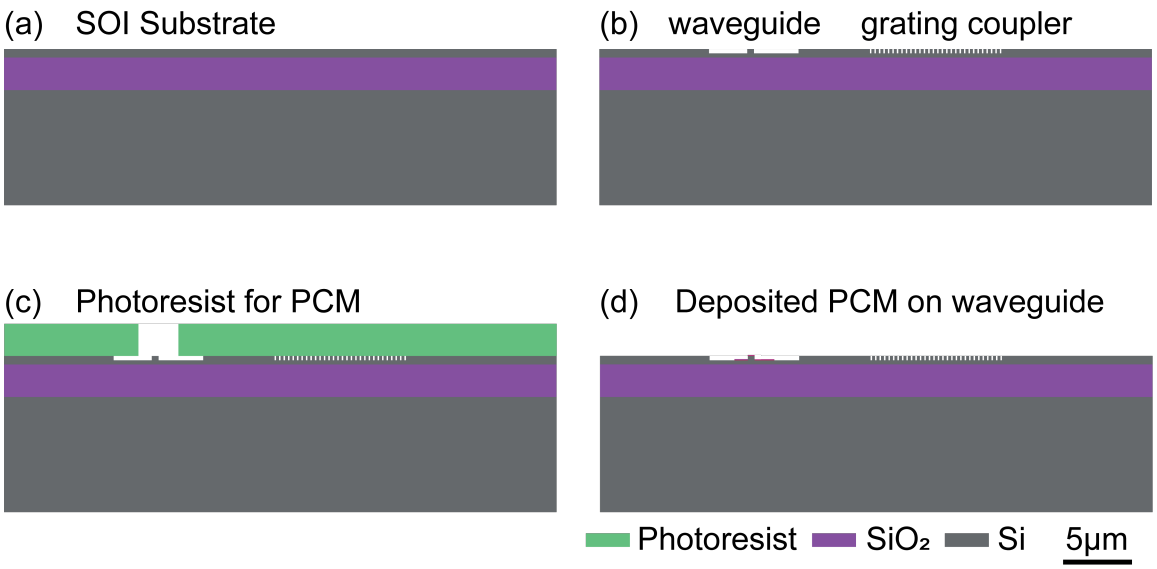


Figure 3.1: Device fabrication process. (a)(b) Ebeam pattern transfer and RIE dry etching to have silicon waveguides and grating couplers. (c)Pattern transfer of window for phase-change materials. (d) Deposited phase-change materials on the waveguide using sputtering technology.

2. An electron beam lithography step is then carried out to open a photoresist window for phase change material deposition (shown in Figure 3.1(c)). A thin film of phase-change materials (e.g. GST) is then deposited on the top of the waveguide with a lift-off process followed by RF sputtering of phase-change materials. (30 W RF power, 5 mTorr Ar atmosphere, and 2×10^{-7} Torr base pressure for GST deposition).

3. After the crucial material deposition, isolation layer to prevent phase-change materials from oxidation or migration such as ZnS-SiO_2, SiO_2, ITO or, Al_2O_3 will be grown by specific methods such as Atomic Layer Deposition (ALD), sputtering or thermal evaporation in order to enhance the interaction with the optical mode (shown in Figure 3.1(d)).

4. If a fully crystallized phase-change material state is needed, a post-sputter annealing step (250°C for 10 minutes for GST) will be used.

SiN phase-change photonic device fabrication process has been developed before this research, and so it is not the project's scope. This project mainly contributes to fabricating phase-change photonic devices on silicon with good performance for the first time. So the following discussion will include the development and optimization of the fabrication process, namely optimization of plain device grating coupler transmission and proximity effect correction to avoid over or underexposure.

Optimization of grating couplers to get the biggest transmitted power

Different methods can be chosen to guide light to the chips. In this thesis, grating couplers are used to couple light from fibre arrays to on-chip photonic components. The higher the transmission signal coupled to the phase-change materials, the easier the switching PCM process will be. As a result, it is necessary to find the appropriate fibres to transfer the highest transmission. The optimization of the structure started with choosing shallowed etched waveguides and then adjusted the period and the fill factor of grating couplers to make the peak coupling wavelength in the telecom wavelength band for data computing and processing applications. The simulated wavelength is 1550 nm. Figure 3.2 (a) and (b) show the simulated mode profiles of shallowed Si waveguides and strip waveguides, from which it is illustrated that with more light coupled inside the waveguides, higher transmission and smaller size can be achieved with shallowed waveguides. So shallowed waveguides are chosen for waveguides in projects in this thesis.

In order to have phase matching conditions and efficient coupling ratios from a optical fibre array to on-chip waveguides, optimized grating couplers for a certain wavelength are needed. According to the phase matching theory [162]:

$$k_i \sin\theta_i + \frac{2\pi m}{p} = \beta \tag{3.1}$$

where k_i is the refractive index of the incident media, and θ_i is the incident angle, $m \in \mathbb{N}$ is the diffraction order. We can get β by $\beta = \frac{2\pi}{\lambda_0} n_{eff}$. And k_i by $k_i = \frac{2\pi}{\lambda_0} n_i$. k_i is the propagation constant inside the waveguide and from the incoming light. n_{eff} is the effective refractive index, and n_i is the group refractive index. Taking $m = 1$ for the first diffraction order and considering air as the incident medium ($n_i = 0$), the period p for the on-chip grating couplers can be obtained from:

$$p = \frac{\lambda_0}{n_{eff} - \sin\theta_i} \tag{3.2}$$

Therefore, The theoretical period for an expected peak wavelength of 1590 nm (to fit the L band laser the author uses) and 1550 nm (for telecom center wavelength) can be calculated through theory. Using this theory, two-dimensional and three-dimensional simulations of suitable periods and fill factors of grating couplers optimization have been done using Lumerical FDTD before experiments are carried out. Figure 3.2(c) and (d) show the optimization simulation of grating couplers. Figure 3.2(c) is the XZ view and Figure 3.2(d) is the perspective view. This is a grating coupler structure on the silicon substrate, with varied periods and fill factors of this

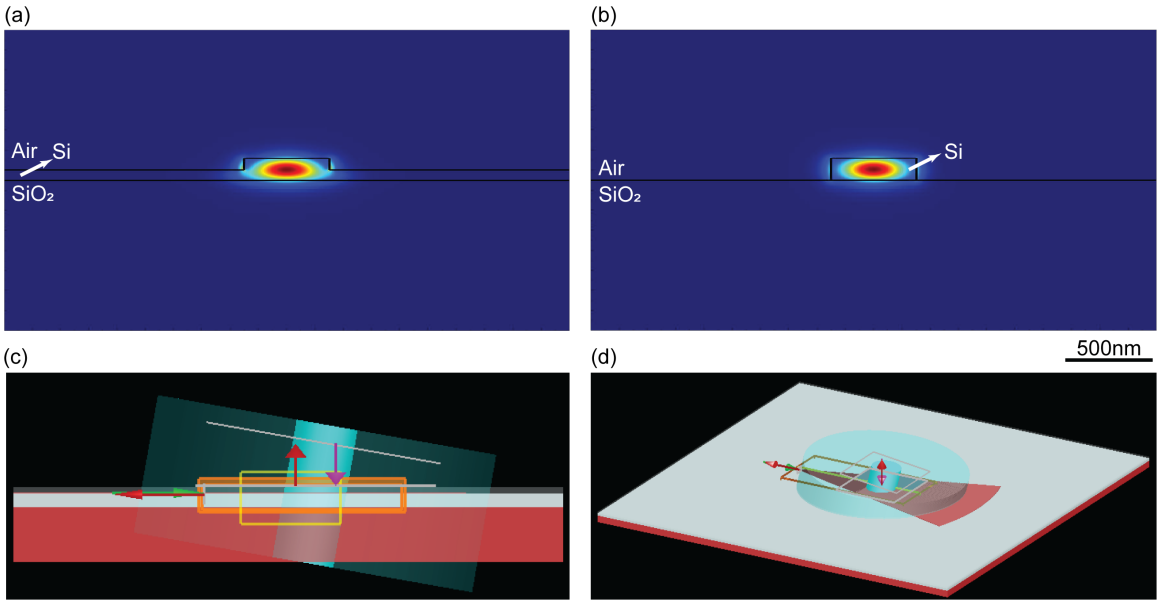


Figure 3.2: Simulated optimization of waveguides and grating couplers. The targetted wavelength is 1550 nm and the targetted mode is TE mode. The boudary condition is perfectly matched layer (PML). Refractive indices are experimentally measured and fit in Oxford. (a)(b)Simulated mode profiles for partially etched waveguides (a) and fully etched waveguides (b). (c) is the XZ view and (d) is the perspective view of the simulation optimization for grating couplers designs. This is a grating coupler structure on the silicon substrate, with varied period and fill factor of this coupler to optimize the transmission performance. The smaller blue cylinder is the fiber core and the bigger blue cylinder is the fiber cladding. The two arrows inside the fiber are the input light source and the two arrows parallel to the waveguide surface are the output coupled light into the waveguide. By varying the period and the fill factor of the coupler, highest output transmission can be found at the signal output port.

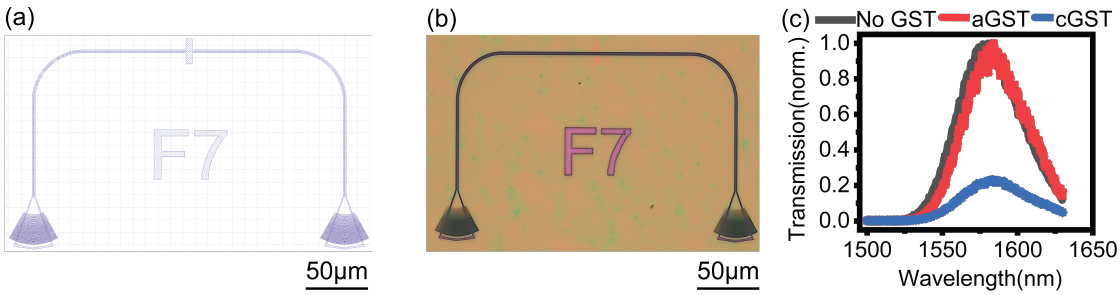


Figure 3.3: Device fabrication process. (a) Pattern designed using python. (b)Fabricated device on SOI platform under an optical microscope. (c)Swept transmission of plain waveguides.

coupler to optimize the transmission performance. The smaller blue cylinder is the fiber core and the bigger blue cylinder is the fiber cladding. The two arrows inside the fiber is the input light source and the two arrows parallel to the waveguide surface is the output coupled light into the waveguide. By varying the period and the fill factor of the coupler, highest output transmission can be found at the signal output port. It is supposed to use period = 0.64 μm and fill factor = 0.88 (unit: 1).

After simulations, actual calibration experiments were carried out to find practical devices. An array of plain waveguides swept the period from 0.6 to 0.8 μm and the fill factor from 0.7 to 0.9 (unit: 1) of waveguides to fit the correct wavelength and tolerant imperfect fabrication process as shown in Figure 3.4(a). Figure 3.3(b) is measured cross section of the shallowed silicon waveguide to show the etching depth (tested by AFM). The targeted etching depth is 120 nm and the experimental depth is 108.7nm, as shown in Figure 3.3(b). Figure 3.3(c) is the corresponding swept transmission spectrum of the best tested device. The final fixed period is 0.64 μm and the fill factor is 0.84 (unit: 1), and the author achieved maximum 40% transmission for a single grating coupler(see Figure 3.4(c)), which is much higher than typical shallowed waveguides available on the market with similar structures (According to the latest IMEC foundry device performance library handbook (ISIPP50G 2.3.0), the peak insertion loss of a shallow etched, one-dimensional and curved grating coupler on a SOI platform in their library is -4.3 dB (confidential)).

Proximity Effect Correction (PEC) to get correct critical dimension

Because of different densities of local pattern arrangement, the dose overlapped with each other leads to patterned areas overexposure or underexposure, increasing the possibility of critical dimensions being off the correct range. PEC (proximity effect

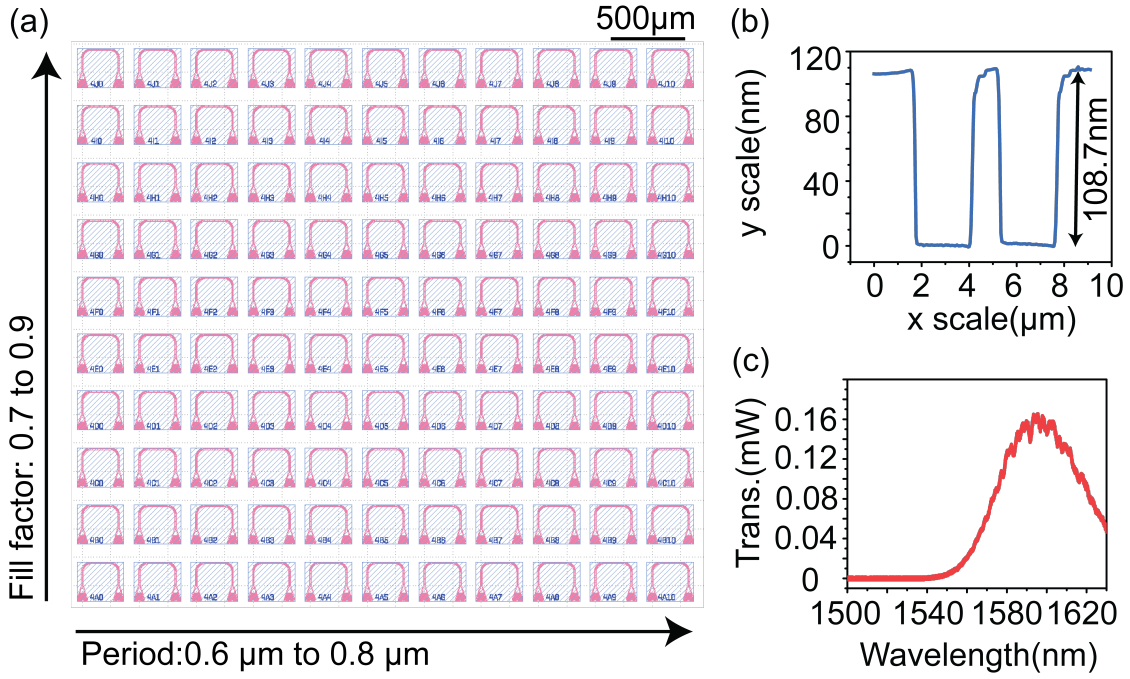


Figure 3.4: Optimization process for the grating coupler on SOI platform. (a) GDS design of swept grating coupler parameters. (b) AFM measurement of the height of the waveguide. (c) The highest transmission optimized for a single device with two grating couplers.

correction methods) is used here to remove this effect, supported by Beamer software to get the critical dimensions for structures such as the gap between slot waveguides and the radius of ring and waveguide width. Figure 3.5 shows strip patterns with 50% fill factor comparison before using PEC and after using PEC. It is critical that the correct dose setting for PEC is applied as a base dose. Several methods are developed to get both quick patterns and precise patterns. For waveguides that require resolution over 150 nm, a larger ebeam lithography current is used to get quick writing speed. For structures like grating couplers that need resolution down to 40 nm, a small ebeam lithography current of 100 pA is used to get precise exposure. The stitching errors are expected to be avoided using a bigger writefield in mode 2 with a small scan step.

3.1.2 Introducing foundry for large-scale fabrication

For a large-scale integrated photonic matrix, one of the most crucial fabrication details to consider is the continuation of large patterns and consistency of identical components. Figure 3.6 shows unsatisfying fabrication problems caused by laboratory-based fabrication. Problems include stitching errors, chip contaminations,

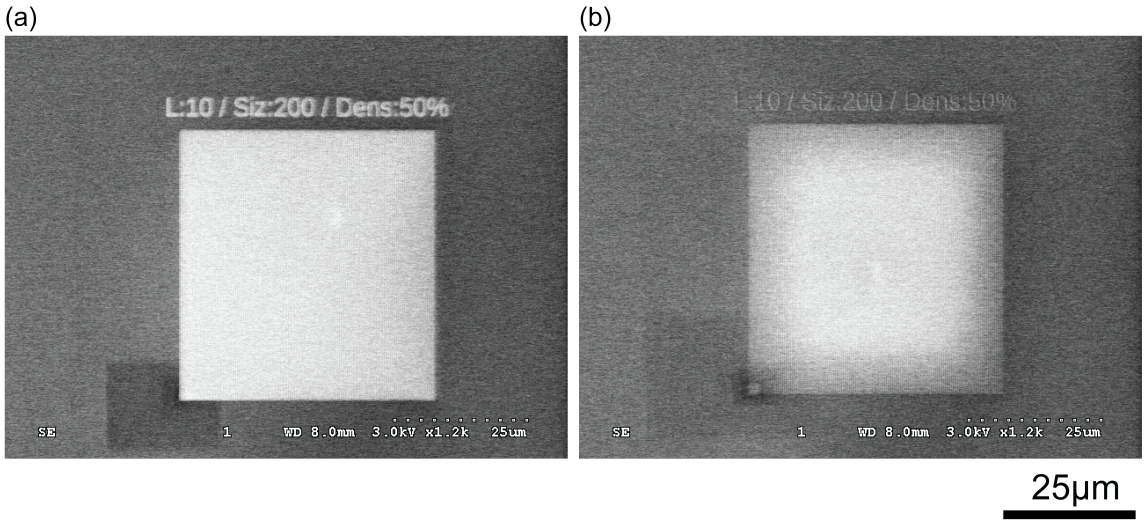


Figure 3.5: SEM images of patterns ebeam lithography with PEC correction (a) and without PEC correction(b).

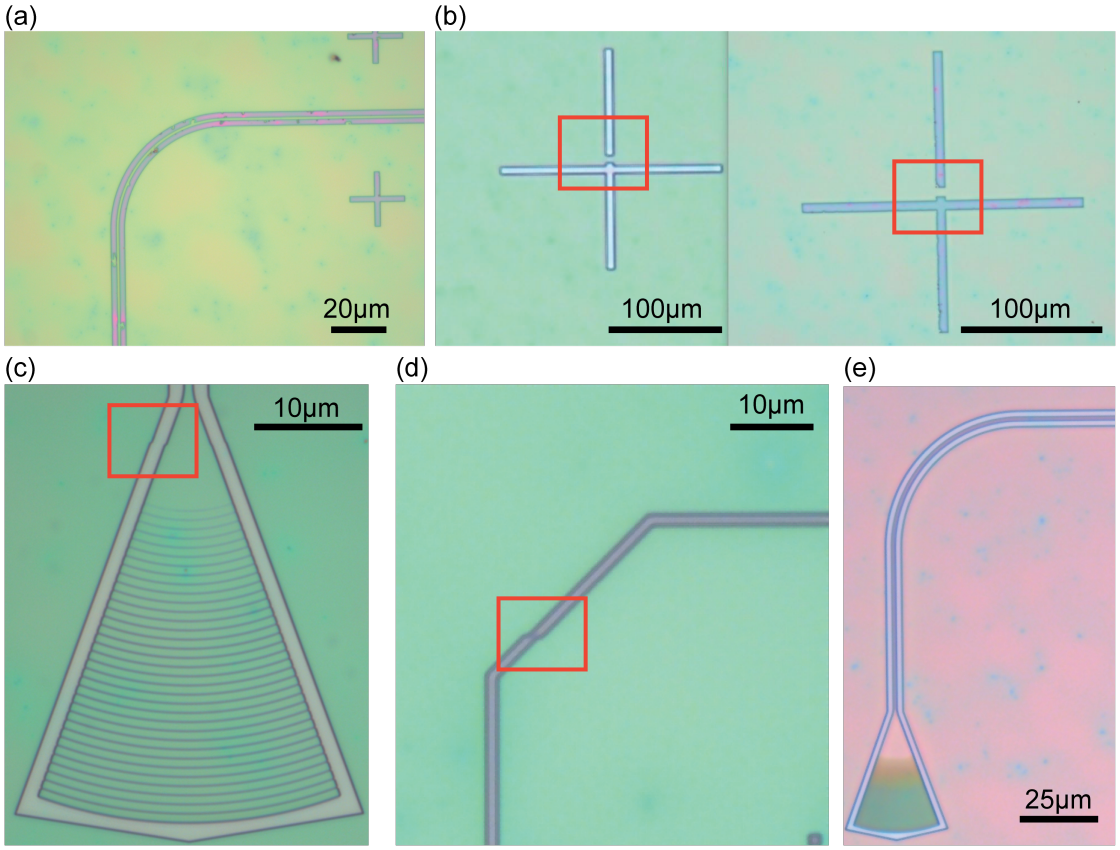


Figure 3.6: Poor laboratory-based fabrication examples. (a)Broken waveguides when unstable etching is carried out. (b)(c)(d) Broken lines (b), misaligned waveguides (c)(d) caused by ebeam stitching errors. (e) Dirty and ununiform surface with dirt introduced during the whole process.

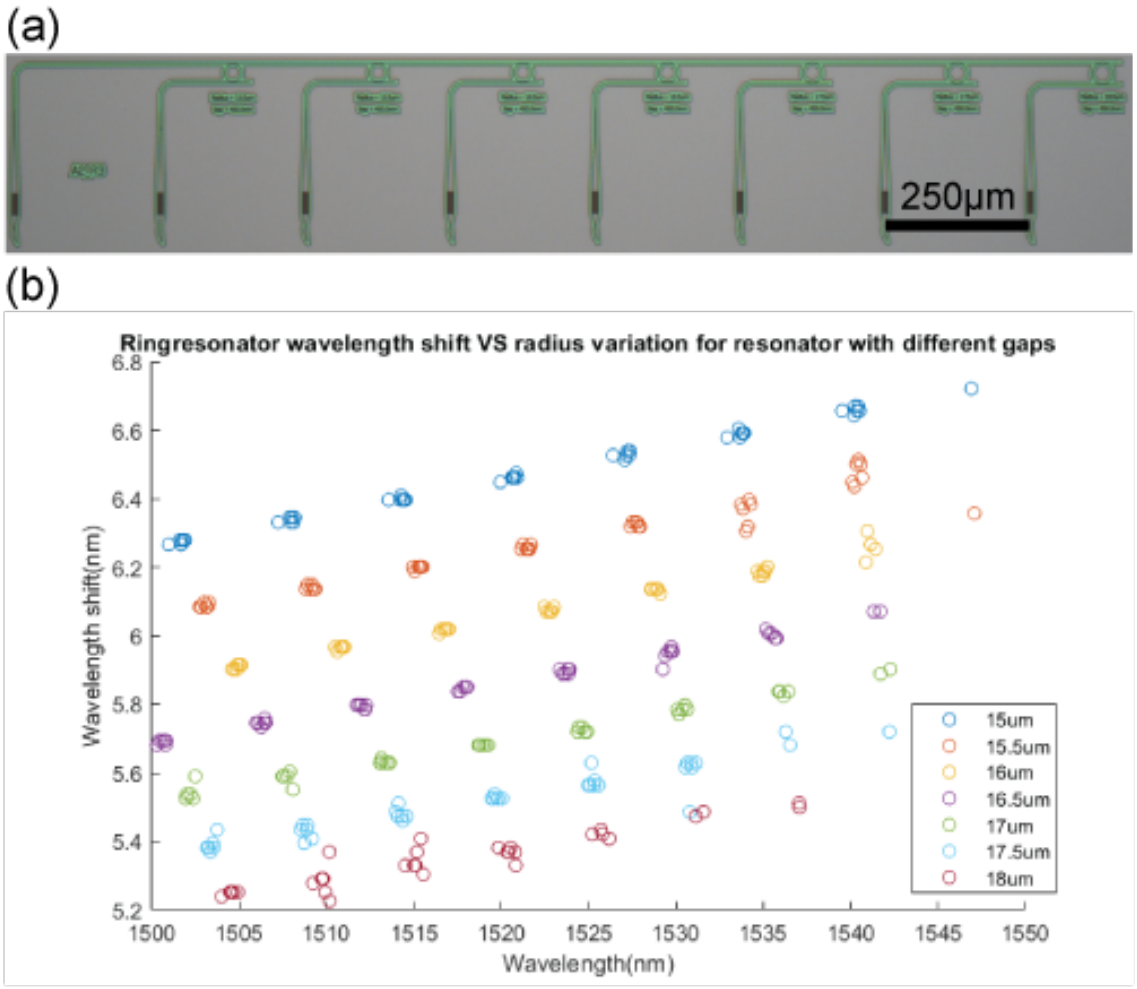


Figure 3.7: Foundry fabricated device examples. (a) Fabricated devices with plenty of microring resonators and the corresponding resonances test in (b).

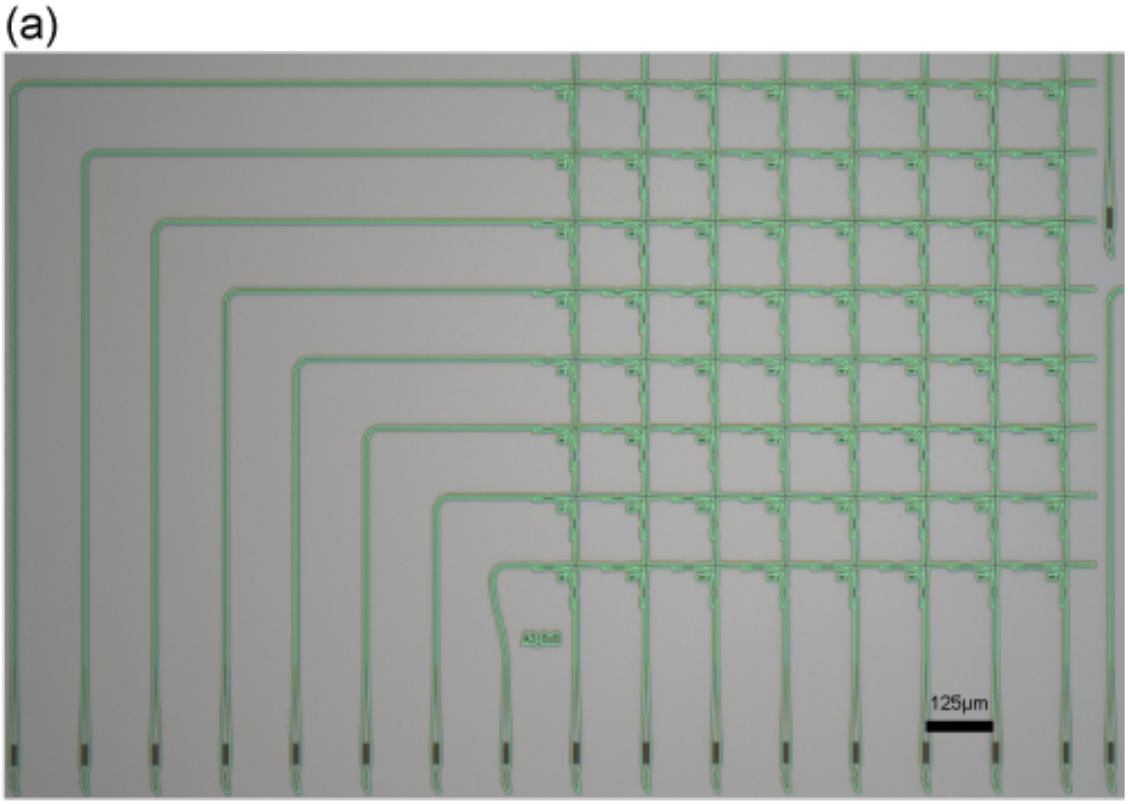


Figure 3.8: Foundry fabricated device examples. (a) Large-scale matrix devices fabricated by the foundry.

and instability of different fabrication runs, most of which cannot be compromised by optimizing the fabrication process. The stitching errors or discontinuation of waveguides and the variations in roughness of the sidewall of microring resonators will reduce the transmission of waveguides on different rows or columns significantly, or fluctuate the performance of identical blocks by changing the resonance wavelength of the same ring resonators, thus reducing the performance of the whole matrix. That leads to the introduction of foundry fabrication because lab-based fabrication can hardly come over these fabrication difficulties. It is thus crucial to do calibration on single devices before applying them to the matrix. Designs for crucial components such as directional couplers, crossings and MMIs have been calibrated and updated through different foundry runs. The detailed calibration process will be discussed in Chapter 6.

Figure 3.7 shows the fabrication chip example from foundry. Figure 3.7 (a) is fabricated microring resonators and (b) is the relative resonances of different devices. With the same dimensions, different devices show high consistency, which can hardly be achieved by laboratory-based fabrication. Figure 3.8 shows a functional 8×8 optical matrix occupying $2 \times 2\ mm^2$ chip size fabricated by foundry, which is hard to be fabricated in the laboratory.

3.2 Experimental setup

There are different setup paradigms for different function-oriented measurements. There are four different measurement setups discussed in this thesis, namely basic device transmission test and spectrum sweep, optical switching test for single devices, electrical switching test for single device and matrix multiplication test for single wavelength, and wavelength multiplexing test. Details of different measurement setups are as follows.

3.2.1 Material calibration and passive transmission measurement

As shown in Figure 3.9, to carry out essential calibrations quickly and conveniently, this transmission and spectrum basic test setup is established. This setup is established by previous DPhils. Probe laser is a continuously tunable laser Santec TSL 550 with wavelength range from 1500 to 1630 nm and resolution 0.001 nm and sweeping speed 100nm/s. From this laser, the light goes through polarization management paddles and then goes to the fibre array and devices, before detected

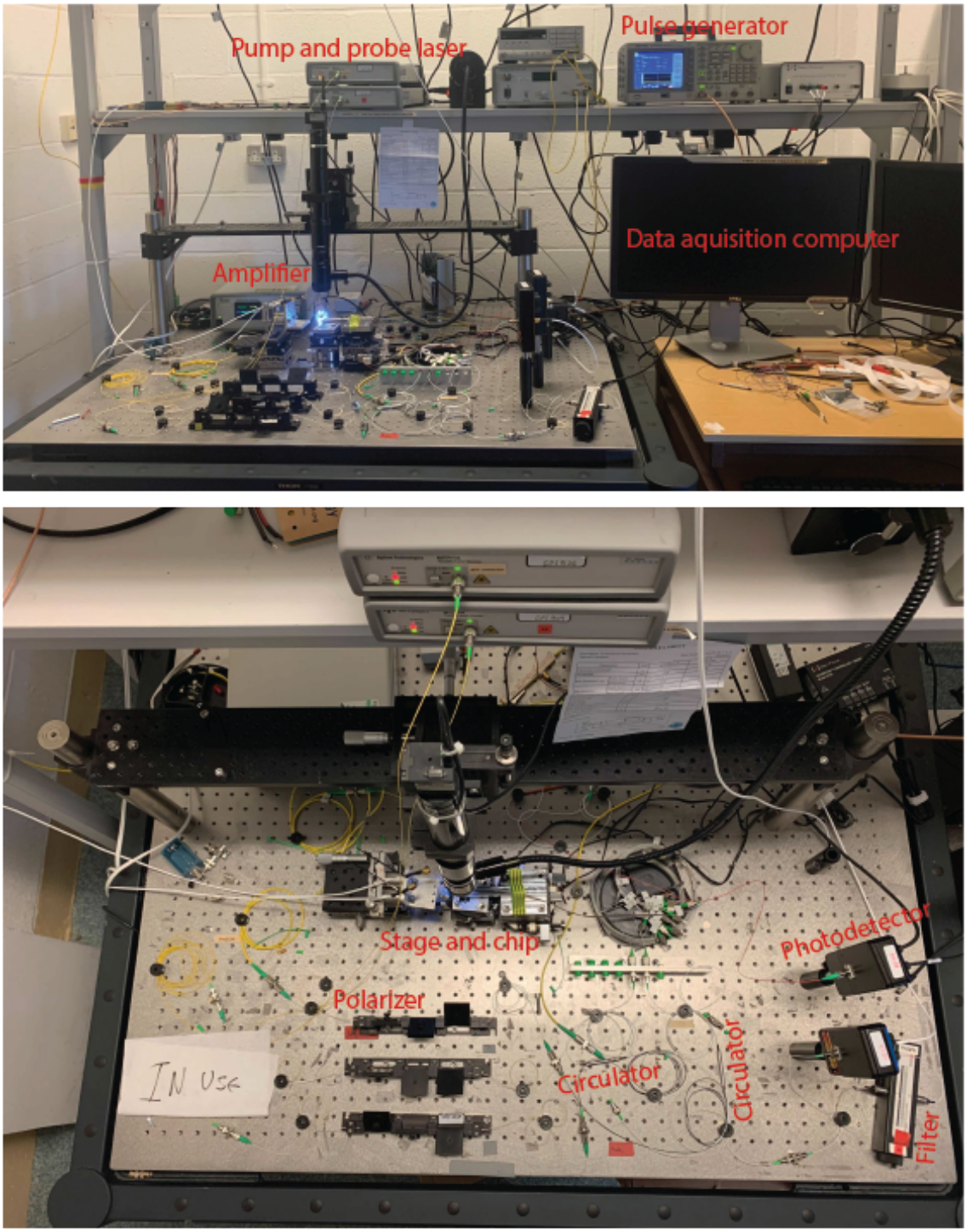


Figure 3.9: Real setup for single device pump/probe experiment.

by 25 KHz and high gain photodetector and transferred to the computer for further data processing, as it is shown in Figure 3.10 (a). The three-paddle polarization controller uses stress to induce birefringence, and then changes the polarization of the single-mode fiber around three independent spools to form three independent fiber wave plates. The amount of birefringence in the fiber is a function of the fiber cladding diameter, the spool diameter, the number of fiber loops, and the wavelength of the light. The required birefringence is caused by the loops in the fiber instead of the twisting of the three fiber blades [163]. This measurement setup can be used to calibrate the phase-change material attenuation and to optimize grating coupler parameters. Similar functions can be realized with a supercontinuum laser source and optical spectrum analyzer (OSA) with a broader wavelength range and higher signal-to-noise ratio (up to 90 dB) as shown in Figure 3.10 (b). A supercontinuum is constructed when a pump beam is sent through a collection of nonlinear processes. Severe broadening of the pump beam happens then with a microsturctured optical fiber [164]. The supercontinuum laser used in this thesis is Whitelase micro from NKT photonics and the bandwidth is from 400 nm to 2000 nm and the output power is 200 mW. It has repetition rate with picosecond pulses up to 30 MHz. There are three reasons to choose this white laser and OSA combination: 1) for wavelength multiplexing processing of matrix multiplication process in this thesis. 2) for future broadband test of the matrix. 3) More accurate test can be carried out with higher signal-to-noise ratio (up to 90 dB). It is thus easier to find a smaller signal and test ring resonators with higher quality factors. The wavelength band of the matrix used in this thesis is from 1540nm to 1560 nm. However, for future broadband parallel signal processing, for example broadband computing from 1500 nm to 1600 nm or from visible wavelength band to near infrared wavelength band, a white laser source is necessary.

3.2.2 Single device optical switching

The optical switching setup includes pump and probe lines (Red line and blue line respectively in Figure 3.11). This setup is established by previous DPhils. The pump line (red line in Figure 3.11) includes a 1590 nm laser source, amplified with an L-band erbium-doped fibre amplifier (EDFA) to switch the state of the GST optically. The probe line (blue line in Figure 3.11) includes a 1610 nm continuous probe laser to monitor the transmission of the light. An arbitrary function generator (Tektronics 100 MHz AFG3102C) is used to send RF pulses to a high-speed electro-optic modulator (EOM) to shape the optical pulses. The nonlinear response of the EOM is

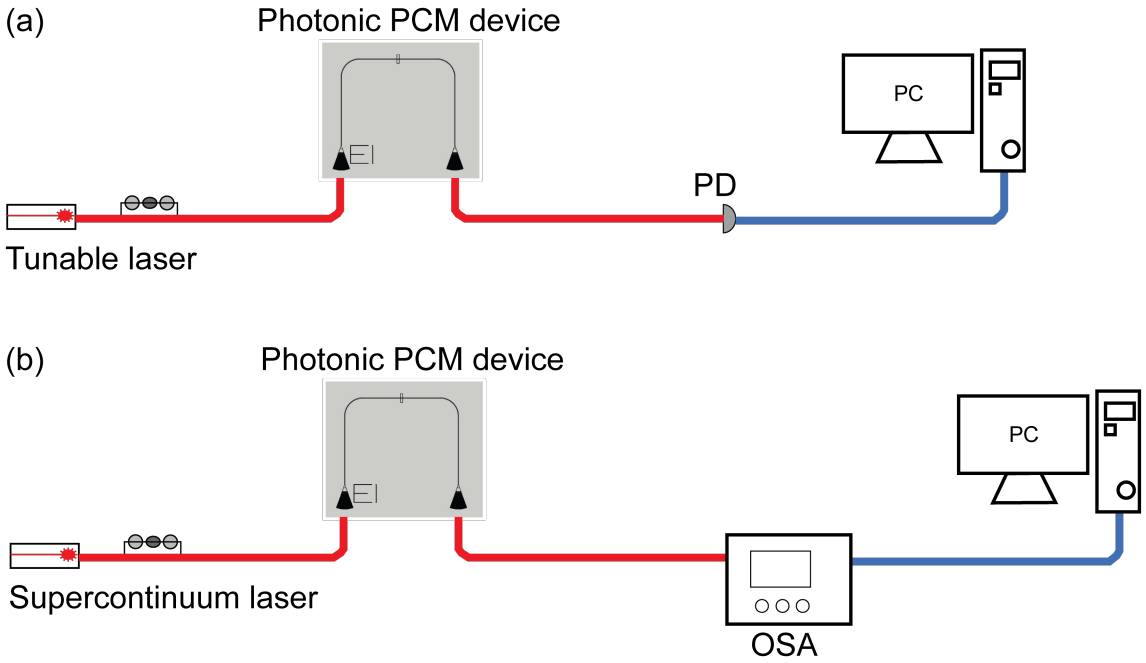


Figure 3.10: Setup for basic transmission and spectrum measurement. (a)Basic setup with tunable laser source and photodetector for data collection. (b)Basic setup with a supercontinuum laser source and OSA(Optical Spectrum Analyser) for data collection.

compensated by the shape of the input RF pulse such that the pulse shape described above can reflect the shape of the input electrical pulses after the EDFA instead of the optical pulses. Optical bandpass filters (BPF) are used in both beam paths to reduce the influence of parasitic wavelengths. At the end of both paths, low-noise-sensitive photodetectors are used to record the dynamic change of the transmission of the light and a fast-speed sampling oscilloscope is used to record the thermo-optical effect of the device when it is excited by writing pulses. With this measurement scheme, phase transitions can be observed in real-time with subnanosecond resolution.

To control the power of the pulses sent to the device, a tunable optical attenuator is used to control the power of the pump seed laser before the EOM. In this way, more control can be guaranteed over the amplitude and repeatability of the pulse power, and 34 levels shown in the next chapter have been achieved.

3.2.3 Matrix measurement: single and multi-wavelength multiplexing

For large-scale matrix measurement, a broadband white laser is used as the laser seed to have multiple channels for different wavelength computations as mentioned in

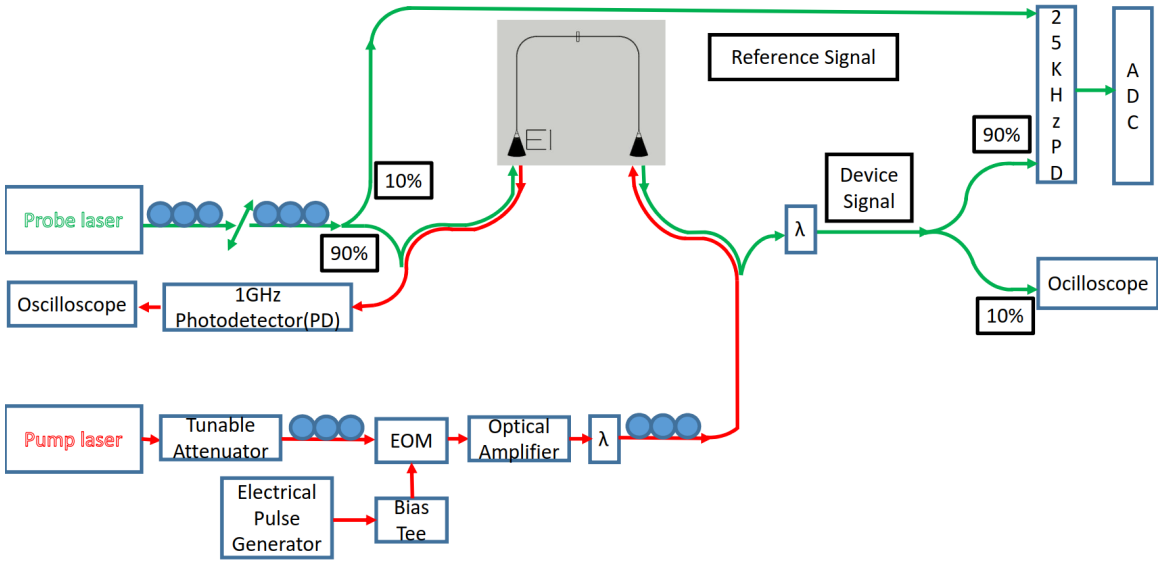


Figure 3.11: Single device pump and probe setup. There are two light paths sharing the same fiber channel: the red light path is pump signal path and the green light path is probe signal path. In the probe channel path, the signal is passing through two polarization management paddles and one in-line polarizer. To reduce the fluctuation of the polarization of the probe seed laser, this in-line fiber polarizer is used to pass linearly polarized light while blocking the orthogonal polarization from the randomly polarized probe light source. After that, the signal is split into two parts: 90% of light go into the device through a 3-port circulator and 10% signal goes to a 25 KHz photodetector and then converted from analog signal to digital signal to the computer. This 10% signal works as a monitor of the probe signal. The other 90% of light go through the device and then filted by a tunable filter to avoid noise signal before going into the 25 KHz photodetector. 90% of the signal goes to the 25 KHz photodetector and the rest goes to a ocilloscope directly to record device fast response in nanosecond scale. The sampling speed of the oscilloscope is 4Gb/s. For the pump signal, a tunable attenuator is arranged after the laser source to control the amplitude of the switching power. One EOM (electro-optical modulator) is used then to add the switching pulse shape from an electrical pulse generator. After the EOM, contineous light is converted into rapid optical pulses to switch the device. The signal then passes through an optical amplifier and a tunable filter to obtain high amplitude optical pulses without noise. And then the pulses go through a polarization management paddle because the grating couplers of the device is polarization-sensitive. After going through the device, the final status of the signal is recorded by a high-speed photodetector (1GHz).

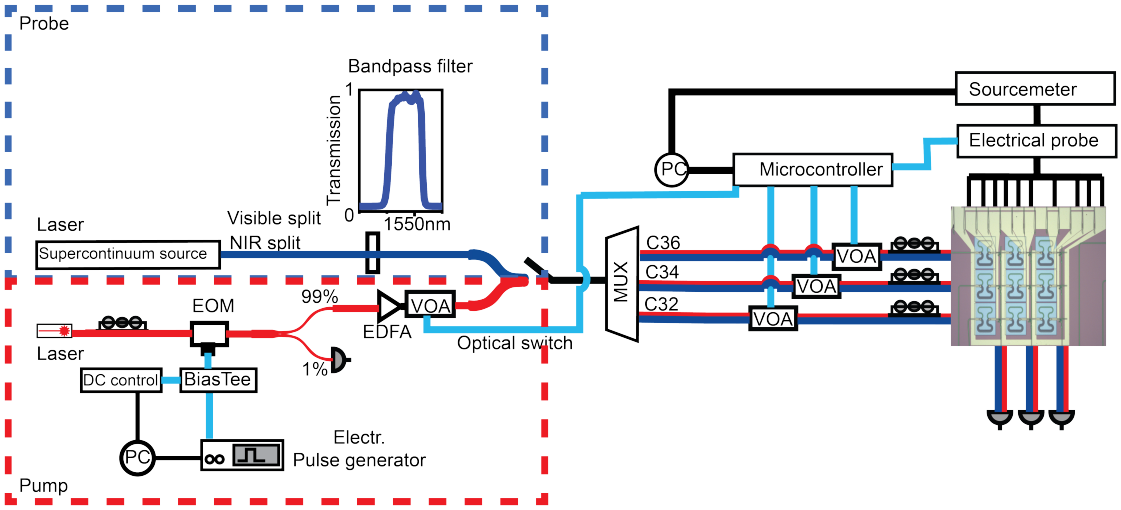


Figure 3.12: Matrix pump and probe setup. The pump line is in red and the probe line is in blue. In the pump line, the polarization management paddle is added before the EOM because EOM is polarization-sensitive. After the EOM, 90 % of the signal goes into the matrix and 10 % of the signal goes to the monitor. EDFA is then used in the pump line to amplify the pump signal to switch phase change materials. The VOA after EDFA is added to completely close this pump path during the computing process. After VOA, there is a 50-50 optical combiner to combine probe line and pump line to the optical matrix. This combiner can be replaced by a optical switch. A demultiplxer is then used to split different wavelength signals to different computing channels of the matrix. One VOA and one polarization management paddle is used before the matrix in each branch to encode input signal and maximize the input power. DWDM ITU-T channel (Dense Wavelength Division Multiplexing International Telecommunication Union Telecommunication Standardization Sector) C36 (1548.51 nm), C34(1550.12 nm), C32(1551.72 nm) is selected to be the computing wavelengths. For the probe line, a supercontinuum source is used to provide multiple wavelengths for wavelength multiplexing computing. Since this supercontinuum laser is from 400 nm to 2000 nm, a splitter after the laser source is used to split near infrared light and visible light. A bandpass filter is then used to filter a wavelength band around 1550 nm. After that the probe signal is sent to 50-50 splitter to the matrix. This matrix setup also has three electrical control parts: a electrical pulse generator to shape the optical switching pulses; a microcontroller to control VOAs to encode input signals and electrical pins to control the phase shifter array in different PCM blocks. Please read Chapter 6 for more detailed explanations for the function of the phase shifter array.

Figure 3.10(b). Figure 3.12 shows the schematic of the matrix measurement setup. This setup is designed and established by the author. First of all, the light passes a notch filter which restricts the wavelength band to be about 20 nm. After this, it goes through a multiplexer and demultiplexer to separate commercialized wavelength DWDM channels around 1550 nm. Here wavelengths 1548nm, 1550nm, 1552nm are chosen. The passing light through the same path is combined with both pump and probe lights to build up such a condensed wavelength multiplexing system. Variable optical attenuators (VOA) are added before the optical matrix to encode different input signals. Polarization management paddles are added after VOA and before the optical matrix because the grating couplers of the matrix is polarization-sensitive. For the pump line, the tunable laser is used to switch devices on different wavelength channels, after amplified by EDFA and going through multiplexers. In order to easily control individual devices and switch them, an electronic modulation MZI phase shifter arrays are added on bus channels to change the splitting ratio between different branch channels to devices, which is shown in Figure 3.12.

3.2.4 Automatic measurement

The automatic measurement system is developed for convenient measurement. The automatic measurement system includes the hardware section and the software section. For the hardware section, to test devices arrays for experiments such as phase-change material mapping and grating coupler sweeping, an automatic stage is used. Figure 3.14 shows the corresponding software interface to control the automatic stage. The coordinates of specific devices are needed before the automatic measurement started. After arriving at a certain device and moving to specific positions of devices, the automatic stage moves around the center of grating couplers to maximize the transmission and find the best position that can couple the biggest transmission. After confirming the device position, a wavelength sweep is carried out, and the corresponding transmission spectrum is recorded.

3.2.5 Software preparation assistant to measurement setup

An automatic switching system is developed to set the state of phase-change materials in a matrix chip using Labview tool, which is shown in Figure 3.15, 3.16 and 3.17. Figure 3.15 shows the main software interface for the matrix measurement. Part 1 is the monitor part which shows the real-time photodetector recordings for all the output channels. There are responsivity and gain settings on the bottom of the

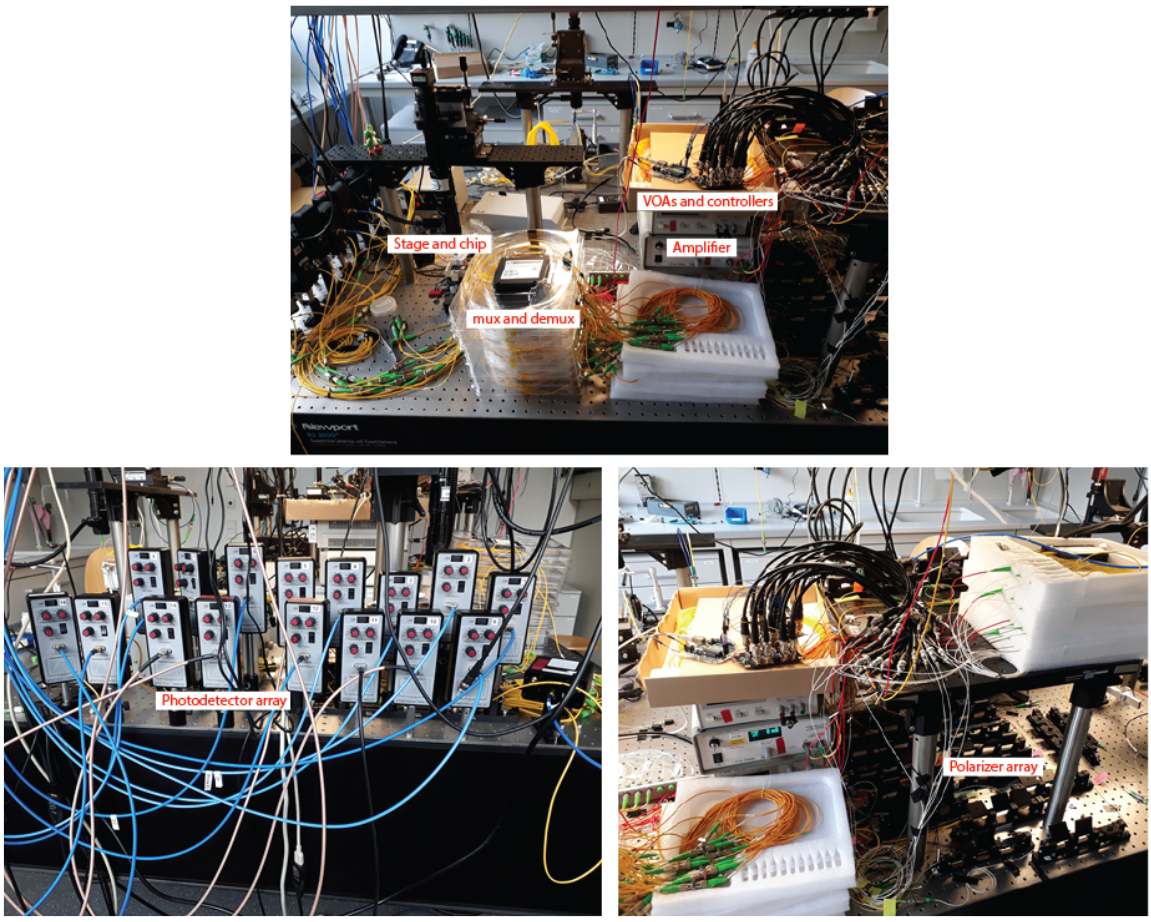


Figure 3.13: Real setup for matrix with wavelength multiplexing functionality.

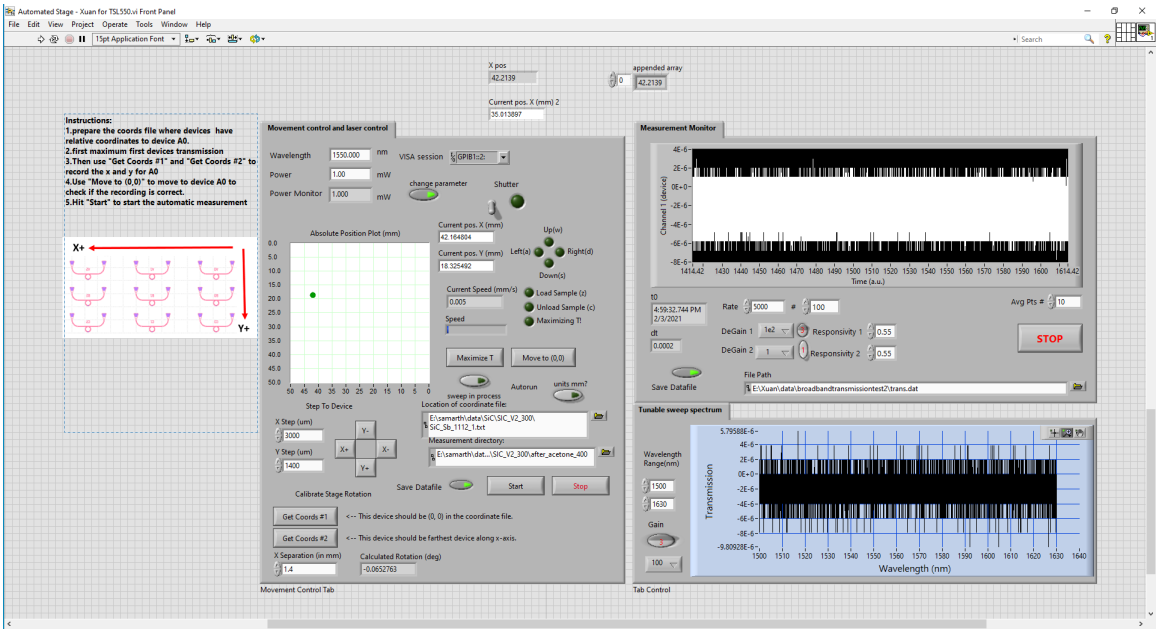


Figure 3.14: Labview interface for automatic measurement (1).

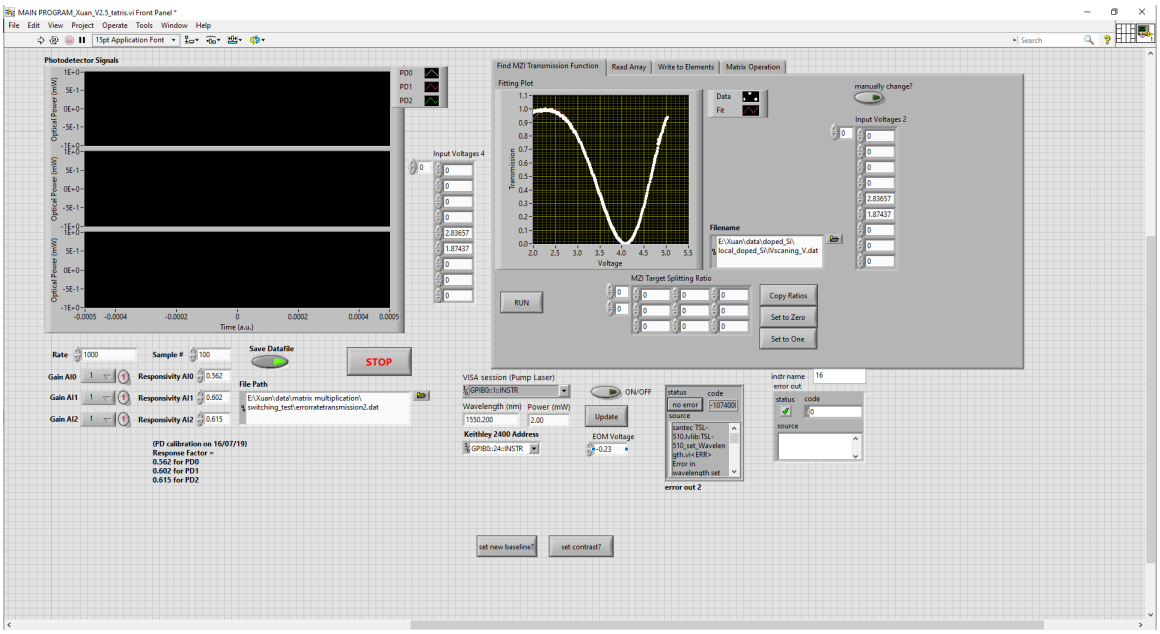


Figure 3.15: Labview interface for automatic measurement (2).

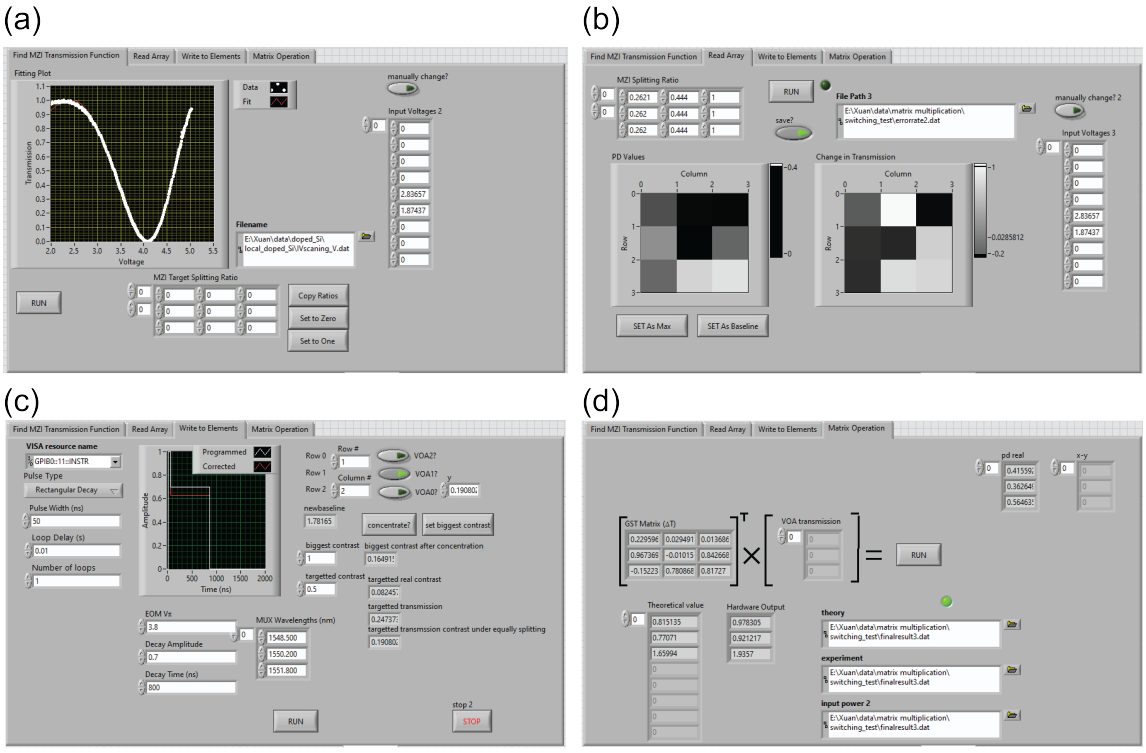


Figure 3.16: Labview interface for automatic measurement (3).

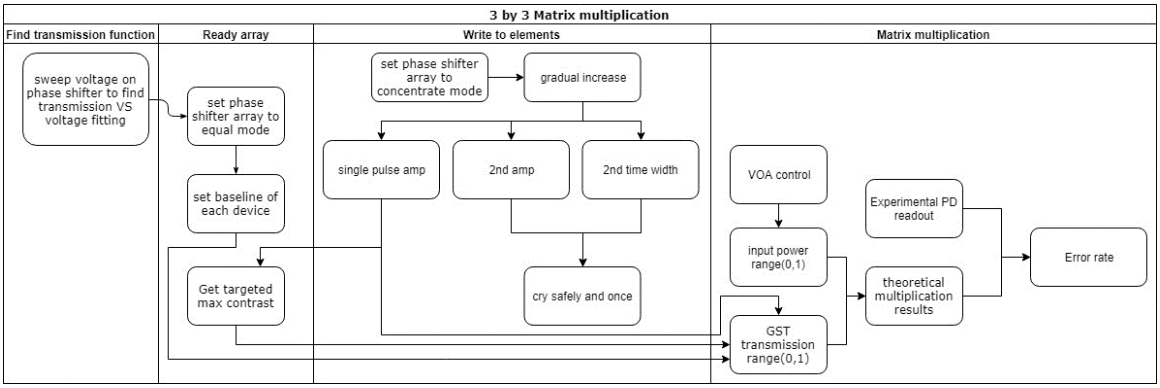


Figure 3.17: Schematic for the software strcuture for the matrix measurement system.

monitors to set the signal to be the correct scale. Part 2 is the control part, including 4 steps when the computing and weights settings are carried out. From Figure 3.17 it can be seen that the whole control panel includes finding transmission function; reading array; writing to elements, and matrix multiplication are corresponding to (a), (b), (c), (d) in Figure 3.16.

The control process starts with finding the MZI transmission function for the phase shifter array of the matrix. The voltage sweeps from 0 V to 10 V to get the cosine curve fitting for each MZI phase shifter. Phase shifters are slightly different from each other due to fabrication tolerance. After this, the relationship between a set voltage and transmission is confirmed. In the second step, different voltages are automatically set according to the fitting curve in step one (Figure 3.16) to have an equal splitting ratio for each device, under which state the status of devices can be recorded as the information in the phase-change material. After the initial status is recorded, step 3 starts. The phase shifter array is switched to the concentrating mode, and the input optical power is concentrated to a particular device to switch it to targeted transmission. After this, step 4 matrix multiplication is carried out. Preprogrammed input signals go through the matrix and multiplied by the new matrix to complete the matrix multiplication. After the first step is finished, the second and third step is carried out continuously and repeatedly to change the state of the matrix. If the matrix is fixed, only step 4 is needed during the calculation process.

Chapter 4

Optimization of single device optical switching performance

The results of this chapter have been peer-reviewed and published in [31].

Using photonics to read and store data becomes an increasingly hot topic because this technology will eliminate the energy consumption needed during optoelectronic conversion in data centers. With multi-level data storage with high accuracy, new computing architectures such as non-von Neumann computing on photonic platforms can be enabled. Towards realizing an optical computing and storage system, this PhD study started from optimizing the performance of a single device. Based on previous researches, the author has successfully achieved several breakthroughs to make the single element more suitable for on-chip, integrated, large scale, high speed and energy efficiency considerations. In this chapter, the author firstly demonstrates an over 5 bits multi-level photonic memory cell with widely used PCM $Ge_2Sb_2Te_5$. Crucially and secondly, for the first time, single pulse modulation without previous knowledge about device status was developed at that time, which improves both energy efficiency and speed. Thirdly, the relationship between pulse parameters and phase change performance during recrystallization and amorphization process is explored to optimize switching performance. Fourthly, the author also dug into the read errors, confidence intervals with increasing distinguished multi-levels and the mechanism behind the relationship between the modulation pulses and the performance. All these conclusions are strongly supported by experimental data with details in the following contents. This work helps to develop photonic memories and show the potential of photonics for novel integrated computing applications.

4.1 Backgroud knowledge

Multi-level cell (MLC) random access memory is a promising direction to solve the well-known non-von Newmann bottleneck. Solutions in this direction includes PCMs [125, 165–167], ferroelectric (FRAM) [168, 169], magnetic random access memory (MRAM) materials, and resistive metal oxide (RRAM) [170–172]. The advantages of PCMs among all of these solutions include high-capacity data storage, long-endurance, high repeatability and good stability and scalability. PCM has significant property contrast with both electrical resistance and optical absorption between crystalline and amorphous states. This unique property makes it an excellent material for multi-level data addressing and retrieval in the optical or electrical domain. Because of the nonlinear relationship between resistance and the WRITE voltage [173], the reinforced Peierls distortion with ageing devices [174], and the random formation of crystalline domain [1, 175].

Accurately control a PCM cell to a particular state is difficult through an electrical programming pulse. Widely used methods at present to improve the accuracy includes the program-and-verify (P&V) [173, 176, 177] iterative method, that is, repeating two steps of modulating the device state and then measuring the resistance until the targeted value is reached. However, this method added extra time and energy consumption to electronic PCM random access memory during the writing process. Additionally, because of the structural relaxation [131, 178–180], the resistance of electronic PCM random access memory devices keep drifting over time. The drift adds extra complexity in distinguishing different resistance states.

On the other hand, because of its big optical contrast between different states and stability over a long time [81], PCMs have already shown great capabilities in the optical domain a long time ago as a role of optical disk binary data storage medium over the recent years. On-chip photonics has extra benefits that electronic PRAM does not have, such as wavelength division multiplexing [181], low cross talk [182], and high bandwidth range [183], which have been demonstrated in recent works that link PCM and photonics. These benefits make it possible to have all-optical multi-level data storage. (up to 8 levels at that time) Additional advantages include better SNR, lower switching energy consumption compared with current widely used optical storage technologies [10, 93, 94, 135, 184]. By combining different PCM memory devices and modulating them simultaneously, in-memory computing can be enabled. Applications that have been realized up to now includes abacus-like arithmetic computing multiplication, addition, and subtraction [94], and matrix-vector multiplication [185].

Integrated photonic devices with PCM is a promising and developing area. Nevertheless, there were some obstacles, including restricted levels ($\leq$ 10 unique levels) and thousands of pulses are needed in order to crystalline the phase change optical cell to a specific state, a mixture of crystalline and amorphous state or a fully crystalline state at the final stage [186]. These obstacles increase the time consumption and energy consumption of the whole system.

Consequently, the author developed a single pulse programming method to efficiently modulate a multi-level photonic device. A single device with 34 arbitrary modulation levels has been developed, and the status can maintain stability and repeatability. Instead of using thousands of pulses, only one pulse can accomplish both amorphization and crystallization in less than 250 ns for both directions. The relationship between pulse parameters and the phase change process is explored and serves to further optimization of the single device modulation method.

4.2 Experimental, device and theoretical preparation

4.2.1 Experimental Setup

Figure 3.11 in Chapter 3 shows the schematic of the measurement setup for this experiment. The pump circuit (red line) and probe circuit (green line) are separated from each other, and light travels in opposite directions using circulators and optical filters to get more explicit monitoring power and reduce interference. The probe laser (usually a tunable laser) goes through polarization controller paddles with an in-line polarizer in between to calibrate the polarization of light. After that, the light goes through a beam splitter and 10% power are split into the photodetector to work as a reference signal to remove dynamic environmental drifts. The other 90% power passes the memory cell in order to test the state of the cell. The probe signal is down to 0.1 mW in order to reduce drifts because of thermo-optical effects. The thermo-optic effect means that the refractive index of a material changes with the response to temperature [187]. Both silicon waveguides and phase change material on them have this effect.

This project can be improved further by using better photodetectors with lower noise and higher power sensitivity to catch more accurate and reconfigurable multi-levels. The pump pulse shape is modulated by EOM controlled by an electrical pulse generator through a bias tee.

4.2.2 Device structure consideration

Figure 4.1 shows the device structures designed for experiments in this chapter. There are two types of devices. The first type of devices is one device with both arms split by a 50/50 Y splitter shown in (a) and (b): one branch works as a reference arm and another as the experimental arm. However, the pump power reduced a half before accessing the PCM because of the Y splitter. As a result, the second type of device structure in Figure 4.1 (c) and (d) was designed and fabricated. It is a set of devices that each device array has 5 simple waveguides with 4 identical length PCM strips shown in Figure 4.1 (c) for functionality, repeatability test and fabrication tolerance. Each array has another plain waveguide without PCM as a reference device.

The authors decided to continue with the already successfully demonstrated SiN platform for all devices for simplicity of experiments. Since changing the substrate has a significant influence on the performance of devices, the author has carried out systematic work and performed a detailed comparison of different substrates in the next chapter.

The author improved grating coupler parameters by sweeping grating coupler parameters for the period and fill factors. The author optimized the smoothness of the surface of waveguides using O_2 plasma and the reflow fabrication process. PCM's thin-film quality was improved by controlling the sputtering process more precisely and slower. These help reduce the signal fluctuation of devices and improve the signal-to-noise ratio to make different levels more distinguishable.

To make use of GST on its significant contrast wavelength range and be compatible with the current optical operating system, the author chose the L telecom wavelength band as the switching and monitoring wavelength range.

In order to avoid oxidation of GST during the switching process (the melting temperature is up to 890 Kelvin) in the atmosphere, the author chose ITO, which is transparent in the telecom wavelength range, to work as a capping layer.

Because both the thickness and stoichiometric coefficients of GST can make a difference to refractive index [188] and then leads to attenuation to the waveguides, the author keeps the same sputtering parameters for both device deposition and thin film deposition for ellipsometry test.

Considering all the factors listed above, the author finally chose a strip GST of 4 μm length alongside the waveguide direction, 10 nm thickness and 10 μm width to cover the whole waveguide with 10 nm ITO capping layer on a single SiN waveguide as the platform for multi-level experiments in this chapter.

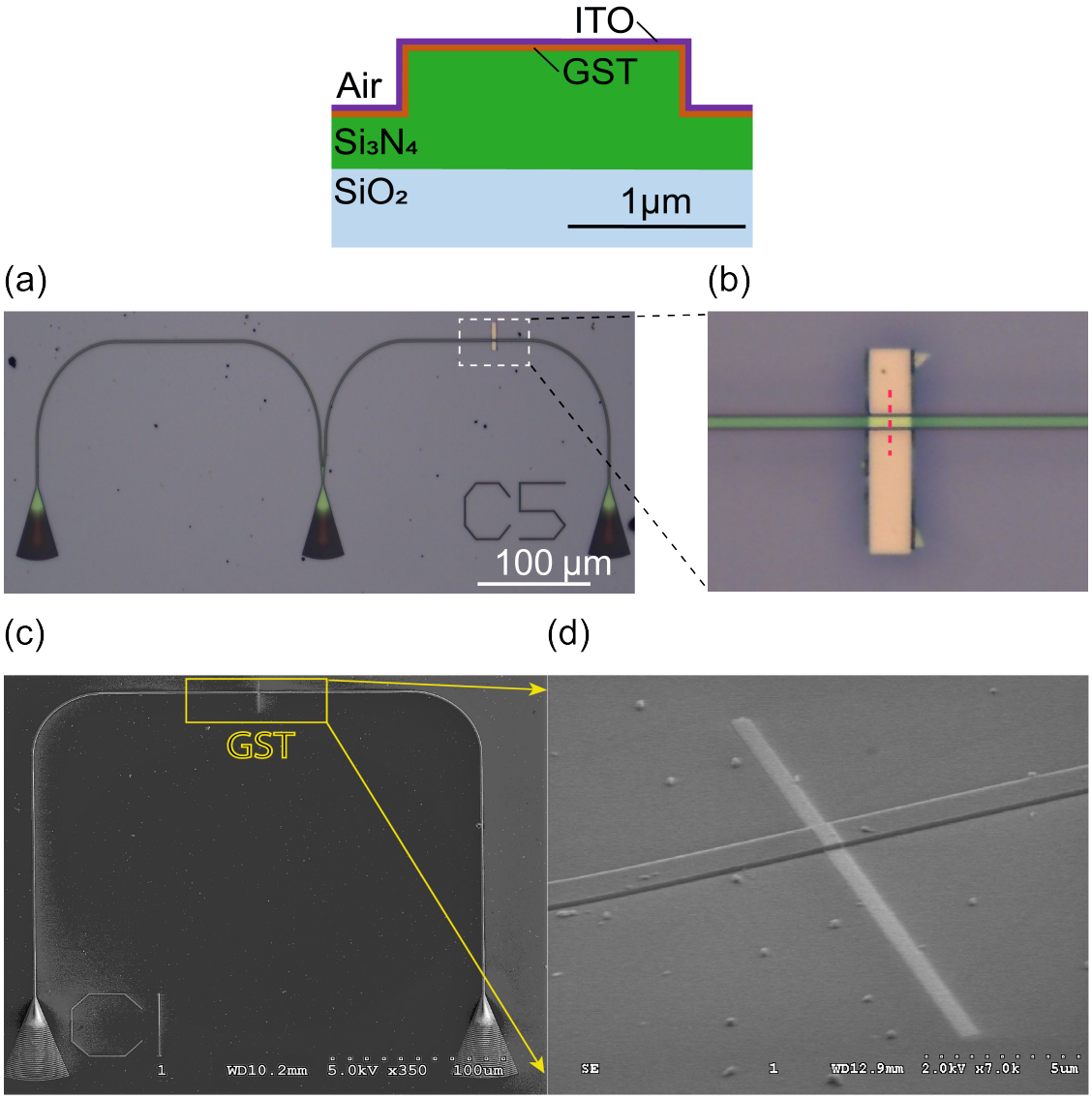


Figure 4.1: Structure of tested devices in experiments. The schematic on the top is the cross-section of the functional material area (the cross-section position is with a red dashed line highlighted in (b)). On the Si_3N_4 partially etched waveguides, there is a 10 nm GST covered by a 10 nm Indium Tin Oxide (ITO) capping layer. (a) An optical image of the device used for multi-level experiments. The device with 50/50 Y splitters combines two simple straight waveguides: the left waveguide works as a reference waveguide, the right waveguide has functional material deposited on it with zoomed-in figure (b). (c)An SEM image of a simpler device structure also used in this experiments with only one straight waveguide. (d) An SEM image of PCM on the waveguide with 30 degrees tiled capture angle.

As-deposited GST is used for amorphous state, and the state after hot plate annealing at 250 degree for 10 minutes is used as GST crystalline state.

4.2.3 Simulation for Switching Process

Simulation of light propagation under different states of GST was carried out before experiments. The mode profiles simulation results of light propagation of both the amorphous state and the crystalline state of GST are shown in Figure 4.2 (c) and (d) specifically. The mode profiles are calculated with Lumerical Mode solutions. With this two-dimensional Finite Difference Eigenmode (FDE) solver, it is possible to get effective refractive indices and the mode profiles of the waveguide with different phase change materials. The targetted wavelength is 1550 nm and the targetted mode is TE mode. The boudary condition is perfectly matched layer (PML). The straight waveguide is directly built in the software. Refractive indices of different materials are measured exprimentally by a ellipsometer and a fitting model. During the simulations carried out in this thesis, Lumerical FDTD and Mode solutions are used for optical field simulation and Lumerical Device solution is used for thermal field simulation. As a result, during the dynamic switching process, the photonic dynamics and thermal dynamics happen respectively. In the future, multiphsics simulation can be carried out with Comsol to get more accurate simulation results. The mode profiles show a big difference between the crystalline state and the amorphous state of GST because of the big refractive index difference (more detailed information in Chapter 5). The evanescent coupling to GST is much stronger with the crystalline state, causing more propagation absorption loss and higher insertion loss at the interface due to mismatching modes between waveguides and functional areas.

After that, the author carried out FDTD and Device simulations to show the optical and thermal dynamics during the switching process with pulses. The simulation of the dynamic switching process using a programming optical pulse on a 2-μm-long strip GST on waveguide is carried out using finite element method (FEM) finite-difference time-domain (FDTD), as it is shown in Figure 4.2(b). The geometry is built according to the experimental fabrication results. An optical source is then generated in Lumerical FDTD with the specific device structures. After that, the light source is transferred into Lumerical Device simulation software to add the influence of the temperature changes with specific pulses and the switching consequence or the device states. During simulations along the propagation direction, asymmetric boundry condition is used along this direction to reduce the computing complexity.

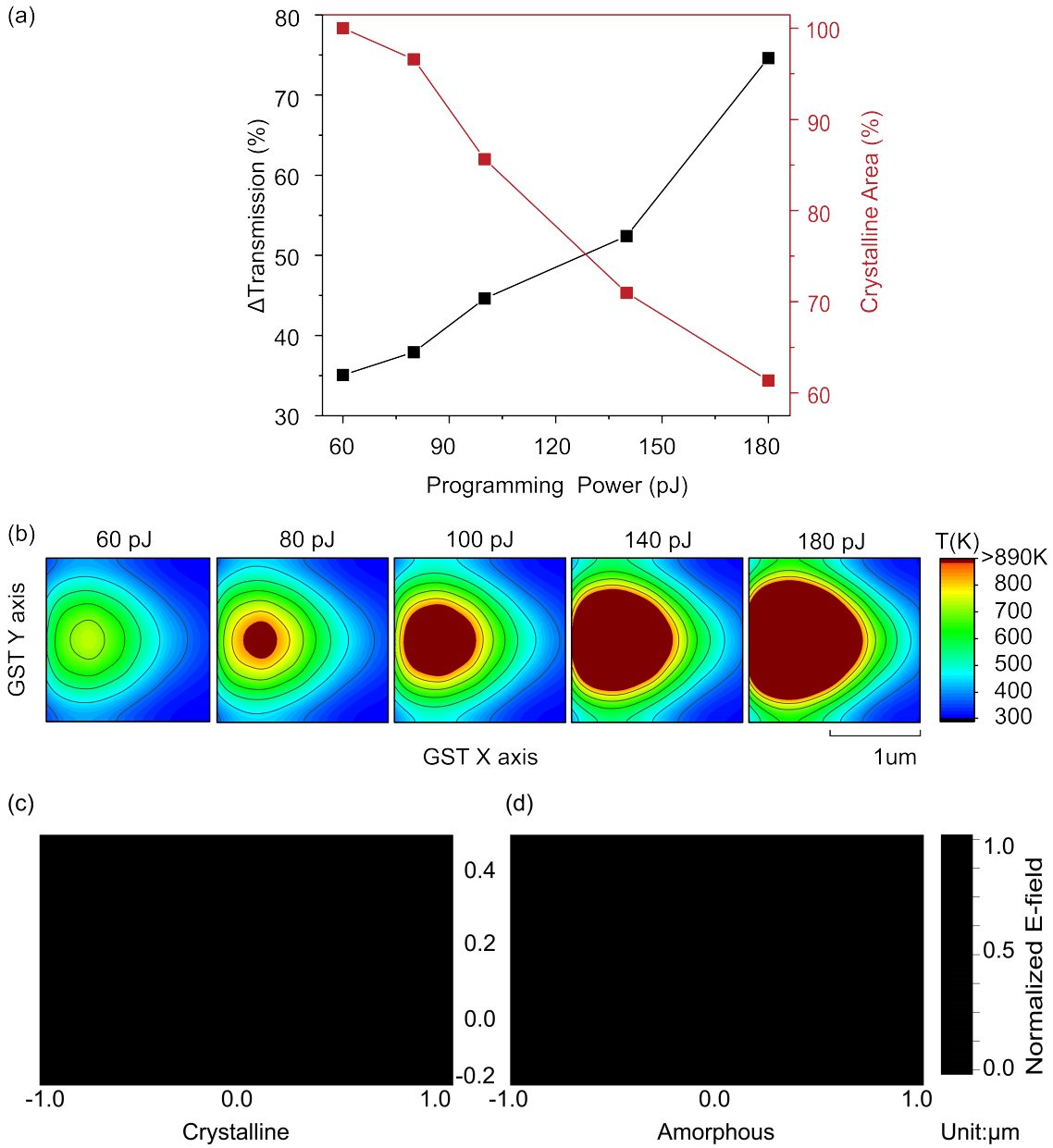


Figure 4.2: Simulation for different power and corresponding temperature distribution, transmission contrast and estimated crystalline area of a device. (a) shows the transmission contrast between amorphous and crystalline state, as the crystalline area becomes bigger and bigger because of the increasing programming power. The transmission change is normalised to the initial transmission state of the device. The crystalline area is normalised to the whole area of the phase change material in this simulation. (b) shows the corresponding temperature distribution on the GST cross-section on the waveguide with sending different programming power pulses. The area filled with dark red color is the area where the temperature went over 890 K. This area is defined as crystalline area because the melting temperature of GST is 890 K, the area over 890 K (filled with dark red color in Figure (b)) is expected to be melt and switched to a crystalline state after cooling down to room temperature. (c) Mode profiles on the cross-section for both crystalline state (c) and amorphous state (d).

It can be illustrated from the Figure 4.2 (a)(b) simulation that when the phase of GST changes from crystalline to amorphous (verse visa), which can be tuned by increasing power, light propagation changes a lot. Furthermore, its ability to light absorption changes as well. With increasing power, the area of amorphous GST becomes larger (Figure 4.2)(a), and the transmission becomes higher than using less power. The author uses refractive indices of different materials from [168]. The increase of the pulse power enables the phase change from an amorphous state to a crystalline state, thus the growth of the amorphous region and the transmission increases accordingly. The temperature distribution at the center of the GST strip after programming pulses is shown in Figure 4.2(b).

The highlighted region with dark red in Figure 4.2 is where the temperature of this material goes over 890 K, which is the melting temperature of GST (measured by Yamada et al. [189]). These regions become amorphous states after sending different power of pulses. The dynamic changes of optical, thermal and nucleation domain in the device during the crystallization process are much more complicated than the amorphization process and require coherent multi-physical domain simulations. Consequently, the author targets understanding the crystallization process by empirical techniques rather than theoretical simulations. The author also found in Figure 4.2(b) that the highest temperature of the device is slightly after the GST starting point, which agrees with the near-field coupling fact that the device needs a transfer range from plain waveguide to the field of combination of SiN and GST.

From Figure 4.2 it can be seen that with increased power, the area that goes over melting temperature increases accordingly, resulting in the increased amorphization area and increased transmission. However, it is hard to achieve 100 % crystallization because the huge attenuation of GST will prevent the amorphization/crystallization of later device and the separation of optical and thermal simulation leads to the inaccuracy of simulation. As a result, a similar simulation is worth being carried out again with Comsol multiphysics, where the optical domain and thermal domain can be combined.

4.2.4 Mechanism exploration

Because of different and dramatic changes in absorption capability between amorphous and crystalline GST, the light transmission that goes through the waveguide covered by PCMs (GST in this chapter) is easily tuned according to the different status of GST. As a result, the transmission can be regarded as information. A fully amorphous state is information status ”0”, and a fully crystalline state is information

status "1". If the programming power to the PCM portion is precisely controlled, leading to a mixture of the amorphous and crystalline parts, the transmission will sit between a fully amorphous state and a fully crystalline state to represent different intermediate statuses. In that case, up to 34 information status is demonstrated here by dual-pulse precise manipulation method.

In Figure 4.3, the author illustrates the schematic of the dual-pulse manipulation method of the transmission state of the $Ge_2Sb_2Te_5$ (GST) PCM. A 20 ns rectangular WRITE pulse is used to control the composition of amorphous versus crystalline material, thus determining the final transmission state of the device. Because this pulse is short in period and high in power intensity, GST can be heated up rapidly to go over melting temperature and rapidly cool down below crystalline temperature to change to an amorphous state from the initial crystalline state. In order to return the GST material to the started crystalline state, a double-step fixed ERASE pulse is used regardless of the current state of the PCM photonic device. The same short pulse with high power is used at the first step to melt the whole device to erase previous state influence, and then a longer pulse with relatively more minor power is used to help GST slowly cool down below the crystallization temperature to reform the ordered crystalline structure.

4.3 Experiments

4.3.1 5 bits distinguished levels achievement

First of all, high storage intensity capability is demonstrated by storing 34 unique transmission levels in only one PCM photonic device. The 34 levels modulation is shown in Figure 4.4. A dual-pulse modulation scheme is used to realize both amorphization as programming and crystallization as erasing the memory cell. Figure 4.1(c) shows the cross-section material layer structure of a functional memory device. Based on SiO_2 substrate and 330 nm SiN device layer, the light is confined in the SiN waveguide, and GST is deposited on the top of waveguides with the ITO cover to isolate GST from air to avoid oxidation. A pulse of 50 ns width with arbitrary amplitude is used to achieve random programming levels, and another fixed double-step pulse with 50 ns, same amplitude as amorphization as the first step and 200 ns, 50% amplitude as the second step is used to return to the initial state of this memory cell.

The highest storage density of one device here is 34 levels, and this number is restricted during this experiment to two factors: the biggest absolute contrast this

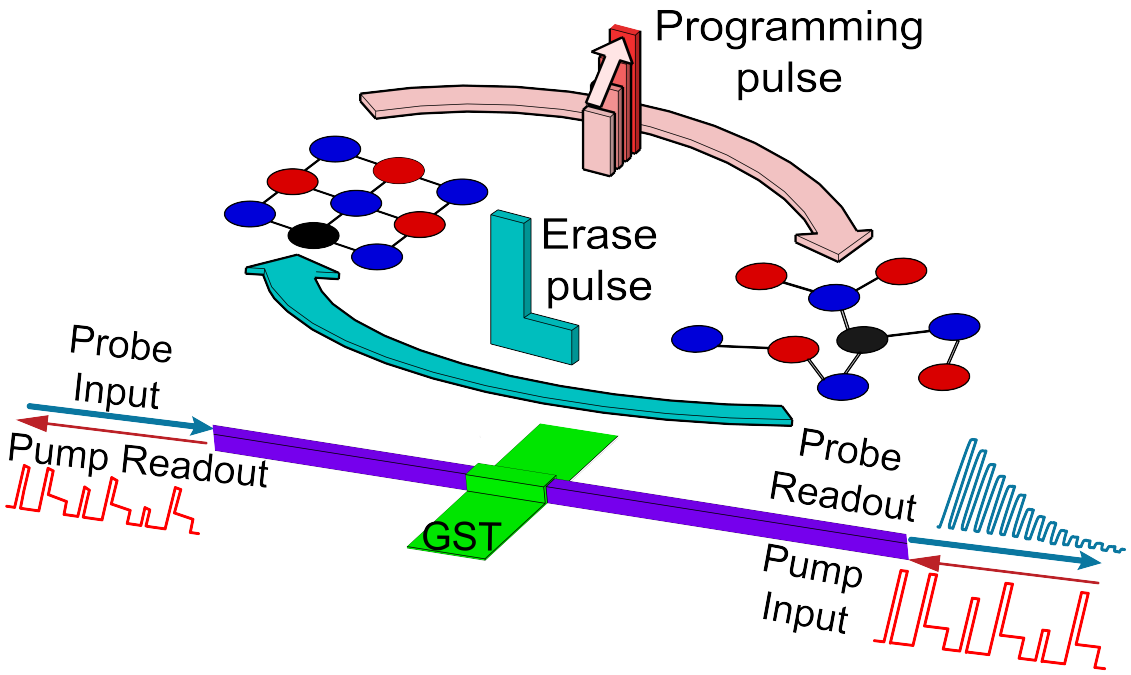


Figure 4.3: Schematic of switching process. Two light waves go through the waveguide with opposite directions: pump pulses (from right to left on the plot) and probe continuous light (from left to right on the plot). Rectangular pulses (programming pulses) are used for amorphization and double-step pulses (erase pulses) are used for crystallization.

device can achieve and the smallest absolute contrast that the device can switch and the monitor can detect. With optimized grating couplers, high absolute transmission contrast is guaranteed with this device. Near 30 % relative experimental biggest contrast between amorphous and crystalline states of devices has been tested with this device. The number of levels is yet limited by the smallest switching contrast that the monitor can detect in order to distinguish different levels from noises and to guarantee the storage accuracy. The discussion of accuracy confidence intervals of different levels will be discussed later in Figure 4.10.

In order to precisely control the pump power, instead of directly modulating the laser or the optical amplifier, the author uses variable optical attenuators (VOAs) before the device to have linear increasing pump pulses. The response of the VOA is calibrated before use. Figure 4.3 shows the schematic of the switching process. With this VOA, this work can achieve different levels of attenuation of the input pulses, thus the final status of devices.

The specific switching steps are as follows:

1. Rectangular pulses are used with varied power controlled by VOA for pumping. The author fixed the maximum import power with VOA fully open and then tuned the VOA range between 0 and 1. Firstly, the author tested the threshold importing power of switching with a certain VOA value and then split power into expected level numbers to achieve different final amorphous states.

2. After each amorphization pulse is tuned by VOA, a double-step crystallization pulse is used to erase the device to the same baseline to test the repeatability of a single amorphization pulse.

3. The power of the amorphization pulses is linearly increased as shown in Figure 4.4 (a) and the same sequence is repeated 10 times, and the repeatability performance is shown in Figure 4.4 (c).

A low-pass filter filters the output transmission after devices to obtain a high-quality output signal without higher frequency. GST material itself is questioned to have an ageing problem in literature [174]. As a consequence, the duration property is also tested to evaluate the ageing performance. The continuous transmission performance is shown in Figure 4.4 for over 8 hours with high stability. It was demonstrated that this non-volatility can maintain over months in integrated photonic circuitry [10] and more than ten years in traditional optical disk storage devices [81].

In order to evaluate the cyclability performance of the device with high data density simultaneously, all the different levels have been repeatedly written and erased 10 times and the data distribution is shown in Figure 4.4(b). The standard deviation

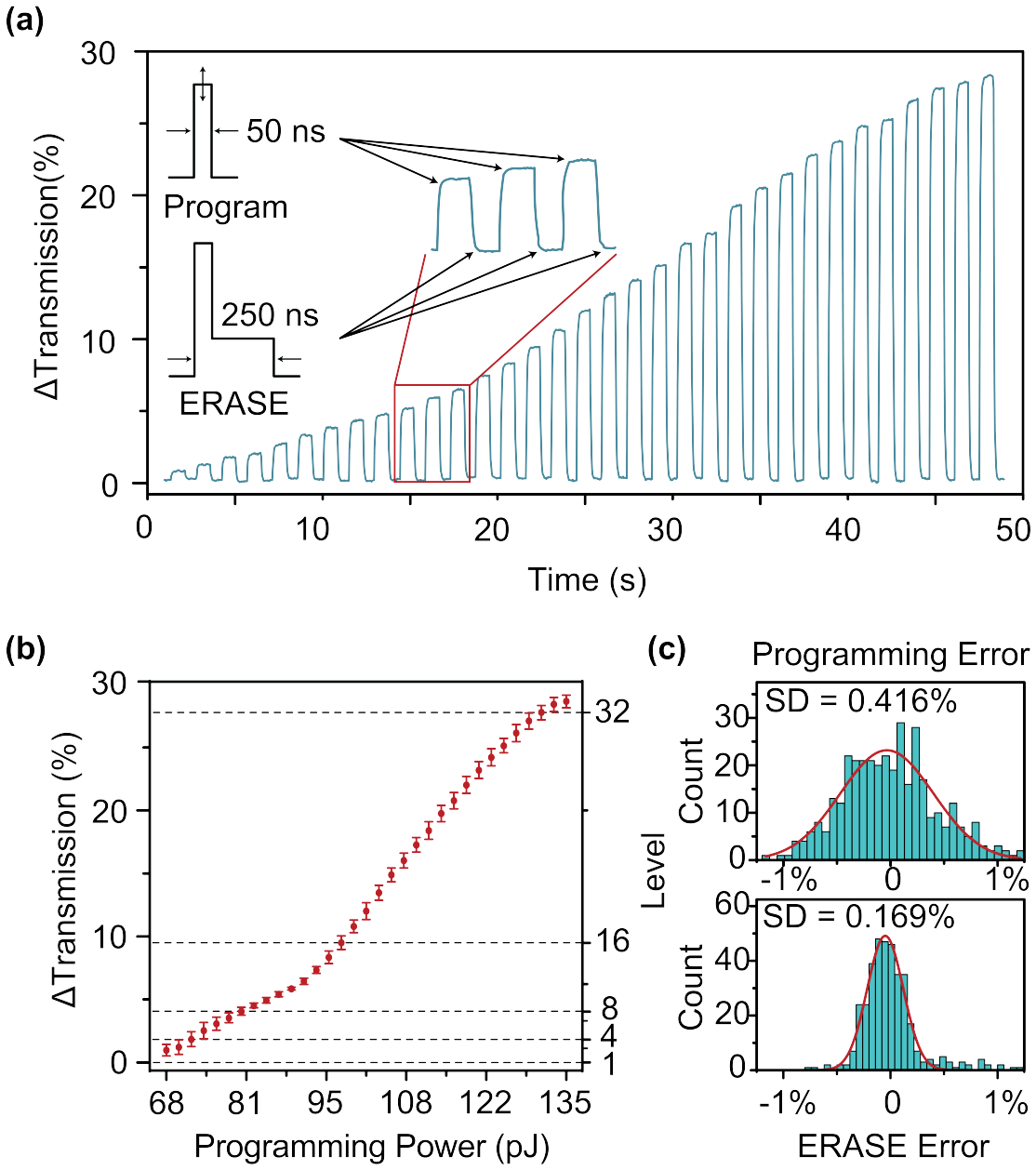


Figure 4.4: Multi-level performance with the dual-pulse programming method. (a) The transmission response of one iteration of 34 individual levels achieved by monotonically increasing the amplitude of the programming pulses. The length of the PCM device used is 4 μm. The transmission change is normalised to the initial transmission state of the device. (b) After 10 write and erase cycles, the average transmission of each individual level and standard deviation are recorded in (b). The transmission change is normalised to the initial transmission state of the device. (c) Histogram plots the difference between the desired transmission level and the actual transmission level (b). A red line shows Gaussian fits to the error distribution in this plot. The error rate is normalised to the average value of each specific device level.

for different levels is down under 0.5%, and thus, the repeatable capability of the photonic phase-change devices is confirmed. The mechanical and thermal drift is difficult to avoid in the experiments, although further improvements can be carried out by minimizing the polarization controller's fluctuations and reducing the noise generated by the optical amplifier.

4.3.2 Dual-Pulse, Multi-level Operation

Secondly, a dual-pulse, multi-level crystallization method is developed to switch the PCM device, as shown in Figure 4.5(a). By varying the amplitude or the time duration of the second step of the pulse, the ERASE/Crystallization operation can be carried out. It is easier to crystallize an amorphous device with a double-step pulse than previous methods. The possible reason may be that the first step of this pulse helps to melt the device to the liquid state. The liquid state is easier to convert to the crystalline state, compared with the amorphous state. Different parameters of ERASE pulse shapes are sent to the device to see the final state differences of the memory device. Both the amplitude and time width of the second step of the double-step pulse is adjusted. The performance of the device is shown in Figure 4.5. For both cases, the first step of the ERASE pulse keeps the same as a 50 ns pulse at a fixed amplitude, the same amplitude as it is used to amorphize the device. When it comes to varying the second step's amplitude, the second step's width is fixed at 200 ns. It can be observed from Figure 4.5(b) that for a low amplitude lower than 0.2 (normalized to the first step of the pulse), the device transmission changes is relatively small. The response of the device become near-linear after the 0.2 thresholds and reaches the maximum contrast and fully crystalline state at an amplitude slightly less than 0.4. The non-linearity across the whole modulation range shows the importance of the threshold amplitude to the recrystallization process. The pulse amplitude determines the highest temperature during the recrystallization process, which decides whether it can go over the crystallization temperature of GST and trigger the recrystallization process. Once the process is triggered, the recrystallization process started and became quicker with higher amplitude and corresponding higher temperature and thus more significant contrast when the process finishes.

On the other hand, for the time width modulation, the amplitude of the second step has been confirmed beforehand to make sure that the highest temperature can go over the crystallization temperature of the material. Consequently, the crystallization process only depends on the time duration and becomes linear as pulse width increases. The linearity of the dynamic phase change can be seen in Figure 4.5(c).

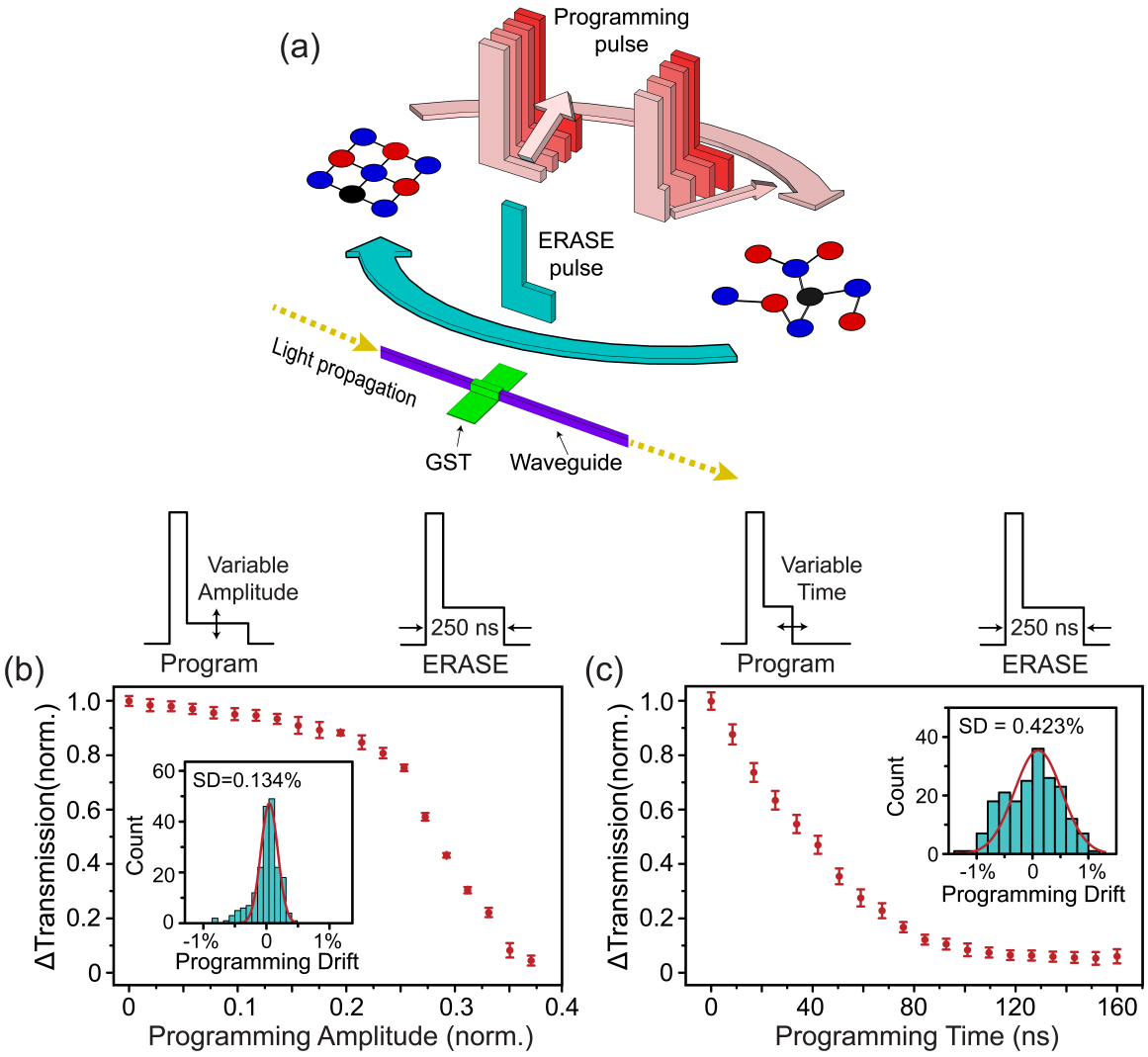


Figure 4.5: Transmission performance of final states of a PCM photonic device using different double-step programming methods. (a) A schematic of the experiment where the double-step programming pulse trailing end varies in both amplitude and time. (b) The transmission performance of a PCM device with increasing amplitude modulation. Once the relative amplitude exceeds 0.2 of the first pulse, recrystallization starts to occur much more rapidly because the temperature is now over crystalline temperature. The inserted figure is the total deviation distribution of different levels caused by amplitude modulation. (c) Transmission performance of PCM devices for double-step programming pulses using time width modulation of the trailing end. The increasing of the time width leads to more area of GST being amorphized. The inserted figure is the total deviation distribution of time width modulation. The transmission change in (b) and (c) is normalised to the initial transmission state of the device. The error rate is normalised to the average value of each specific device level.

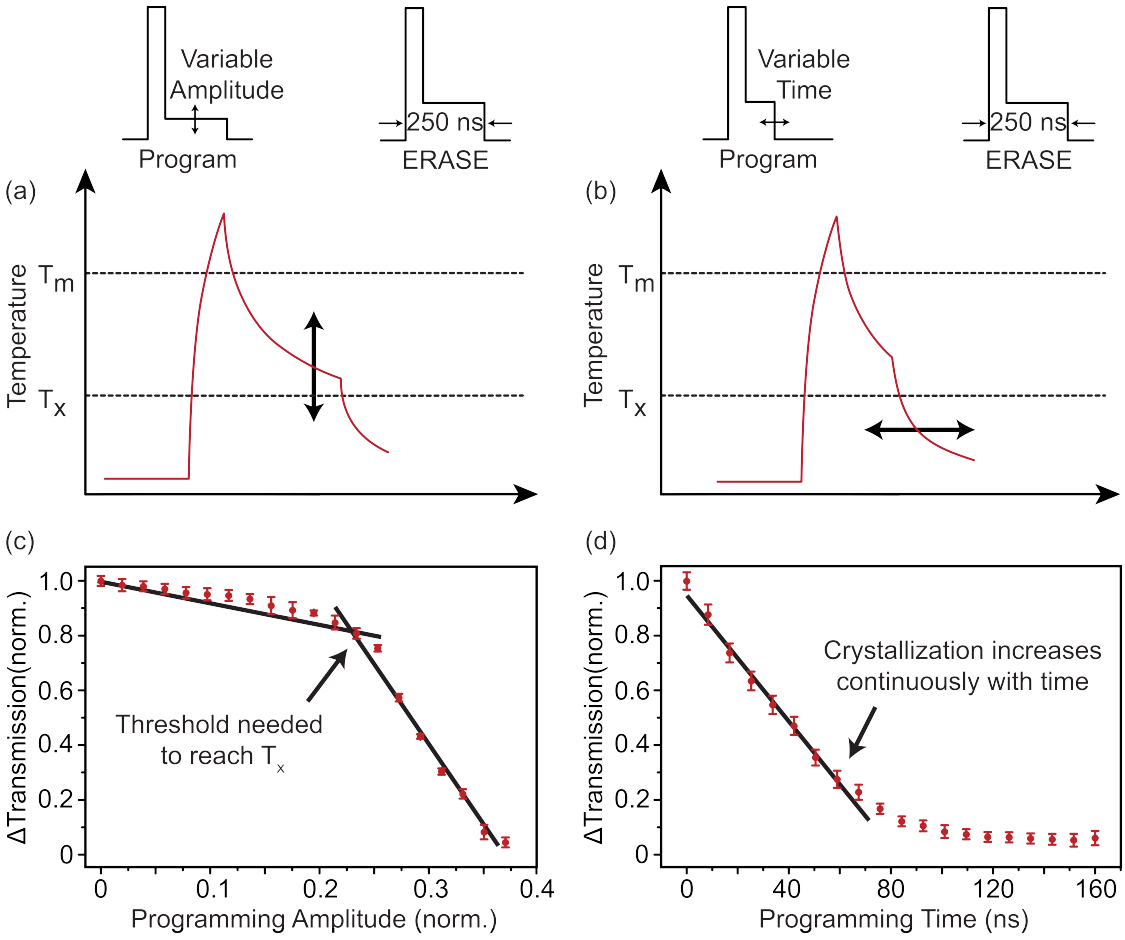


Figure 4.6: Temperature changes ((a)(b)) because of the two different modulation methods variation and the corresponding transmission contrast changes ((c)(d)). (a)(c) Changes of amplitude variation method. (b)(d) Changes of time width variation method.

At the end of the modulation region, both amplitude modulation and time width modulation show gradual saturation when the parameter increases, illustrating that the fully crystalline state is achieved. The repeatability of both modulation methods has been tested, and the error distribution is shown in the insets of Figure 4.5(b) and Figure 4.5(c).

Figure 4.6 shows a more explicit comparison between these two modulation methods in the point of view of temperature changes in order to figure out the different performance of these two modulation methods. It is estimated from the transmission change tendency that with the variation of amplitude method, the initial power with lower amplitude is not enough to reach the crystallization temperature (shown in Figure 4.6(a)). That is why the crystallization speed is relatively slow, according to

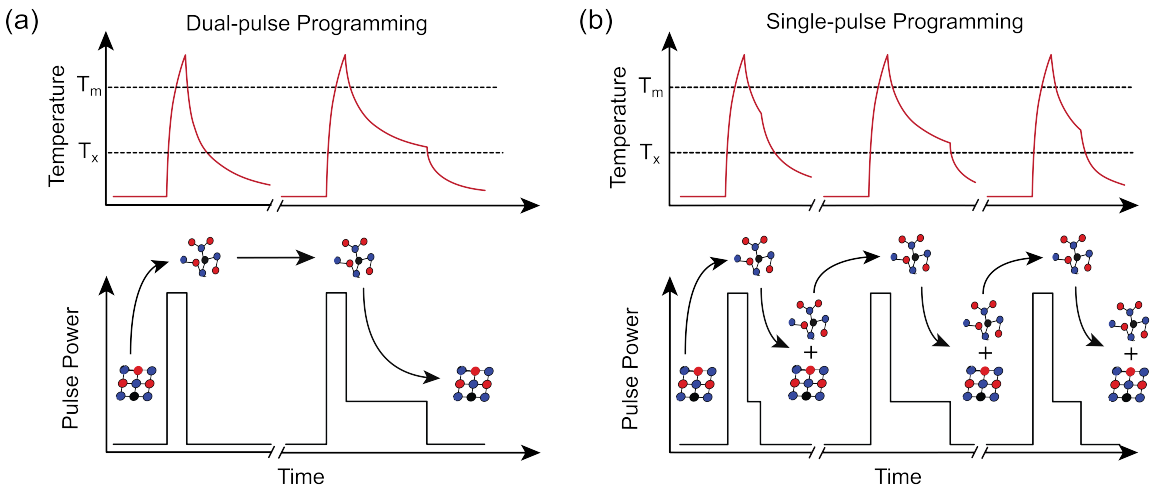


Figure 4.7: (a) Schematic of the physical mechanism for the dual-pulse programming and recrystallization processes. The temperature change in the upper plot illustrates the dynamics of the material while pulses are added. An ERASE pulse is needed to reach the initial state after each programming pulse. (b) Temperature changes and schematic of the method to achieve single-pulse double step programming. The initial high amplitude portion of the double-step pulse with the duration of 50 ns serves to erase the memory of former states by bringing the PCM above its melting temperature before recrystallization.

Figure 4.6(c). However, after the amplitude arrives at a certain threshold, the final temperature of the heating process goes over the crystalline temperature. Thus, the crystallization speed started to increase dramatically, although the increased speed of the adding power did not change.

On the other hand, the circumstance with the time width modulation method is different. With that method, the fixed amplitude is above the threshold of reaching a final heating temperature which is higher than the crystalline temperature at the beginning (shown in Figure 4.6(b)). The higher temperature helps the modulation start with a high crystallization speed (shown in Figure 4.6(d)). This observation gives the author a preference for choosing the time width modulation instead of the amplitude modulation method to have a faster and more stable modulation performance.

4.3.3 Arbitrary Modulation

Another advantage of the double-step pulse modulation is that arbitrary state modulation can be achieved regardless of the former state of the memory cell. Traditional methods usually recrystallize the photonic device back to the initial crystalline state before it is set to a new memory state (shown in Figure 4.7). Instead, the

method in this thesis is a double-step pulse as described above with variation of time width or amplitude of the second step (shown in Figure 4.7(b)).

It is possible to use the double-step pulse to have a different status. To accomplish this process, as it is shown in Figure 4.7(a), the device is firstly switched from a fully crystalline state to a mixture state of amorphous and crystalline with a targeted most prominent contrast. After the switching range is confirmed, as it is shown in Figure 4.7(b), in order to improve the accuracy of individual levels and reduce time and energy consumption, all the different levels can be set with double-step pulses, with a slight adjustment of the shape of the pulse. The first step of the double-step is a 50 ns rectangular pulse, which can achieve amorphization with targeted most significant contrast. The function of the first step is to help GST go over melting temperature and erase all the former states. The function of the second step is to maintain the temperature of GST PCM superior to the crystallization temperature. Thus it can accomplish the crystallization process. The time width of the second step decides the portion of the crystalline state out of the whole material at the final stage or the final state of the device.

Arbitrary states modulation is demonstrated in Figure 4.8. Only a single double-step pulse is sent to the device at each state changing point. The upper subplot of Figure 4.8(a) shows the different time width of the second step of double-step pulses sent to the device, which is the only difference between different modulation pulses. It can be illustrated from this figure that the device can be smoothly switched from high-to-low and low-to-high states regardless of the former material state. The stability and reliability performance is demonstrated by 200 randomly assigned pulses and corresponding transmission state distribution in Figure 4.8(b). The standard distribution is shown in the inset of Figure 4.8(a) and is 0.482%.

The arbitrary amplitude modulation is also tested in Figure 4.9. LabVIEW program is used to control the amplitude precisely and randomly before sending it to memory cells. From Figure 4.9, the arbitrary amplitude modulation can be achieved, but the linearity and stability are worse than time width modulation. These experimental results can firmly support the temperature hypothesis in Figure 4.6.

4.4 Repeatability, switching speed discussion

4.4.1 Repeatability investigation

The repeatability of the devices that can be precisely set has been tested with WRITE/ERASE pulse pair. As shown in Figure 4.4(a), 34 distinguished levels can be

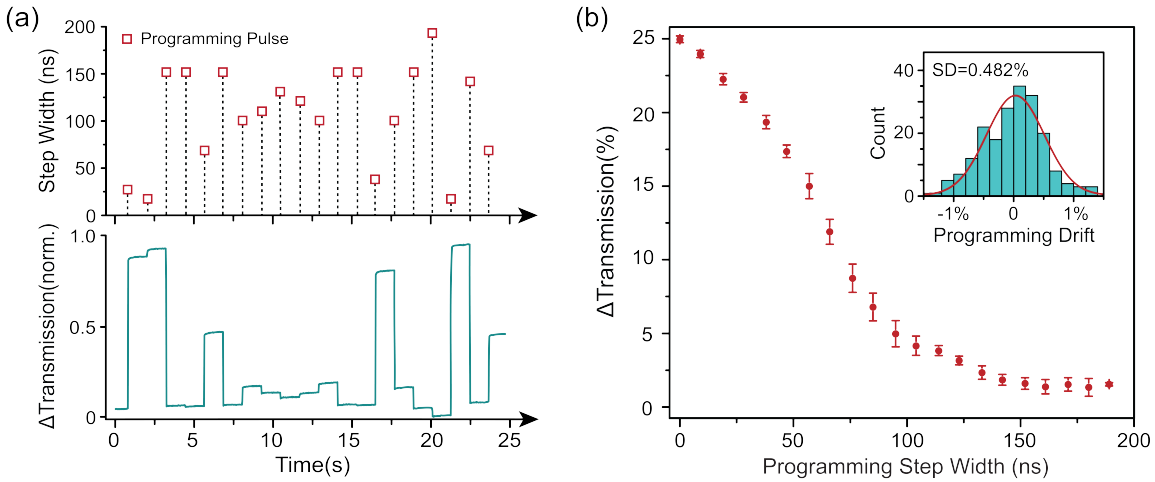


Figure 4.8: Arbitrary modulation using the time width modulation method. (a) Multiple double-step programming pulses (upper figure) of random durations are sent to the device and the corresponding transmission performance (lower figure). The device can switch to a certain transmission level without knowing the previous state of the device. (b) Transmission performance and standard deviation distribution of random programming with duration modulation. The inserted plot is the error bar distribution of different levels.The transmission change in (a) and (b) is normalised to the initial transmission state of the device. The error rate is normalised to the average value of each specific device level.

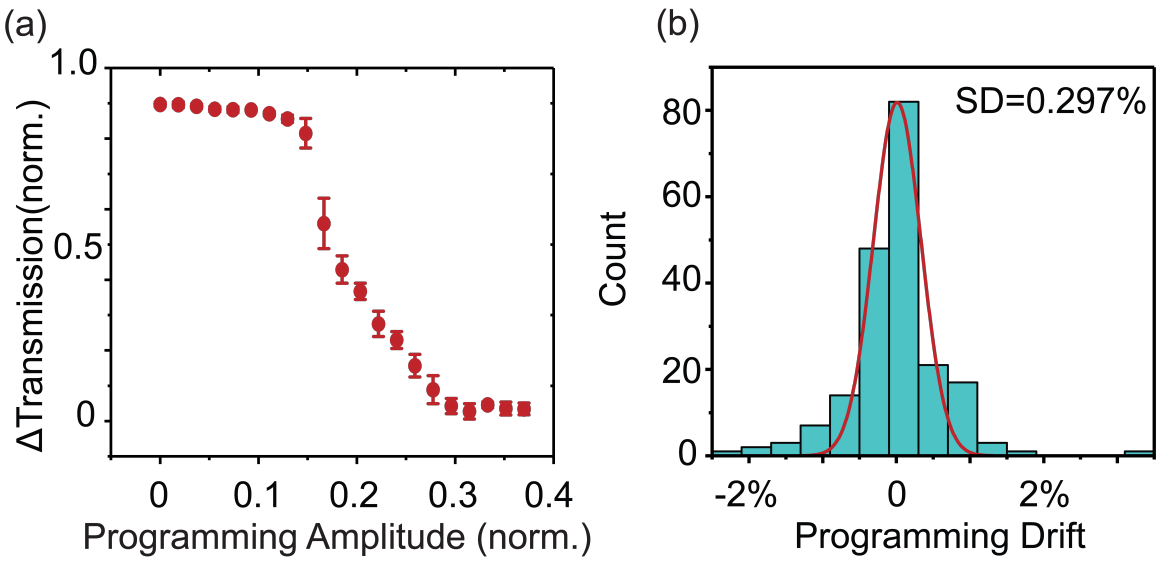


Figure 4.9: Arbitrary modulation using the arbitrary programmed amplitude of the second step of pulses. (a) Transmission levels and standard deviation distribution of random amplitude programming. (b) Error bar distribution of levels in the left plot. The transmission change in (a) and (b) is normalised to the initial transmission state of the device. The error rate is normalised to the average value of each specific device level.

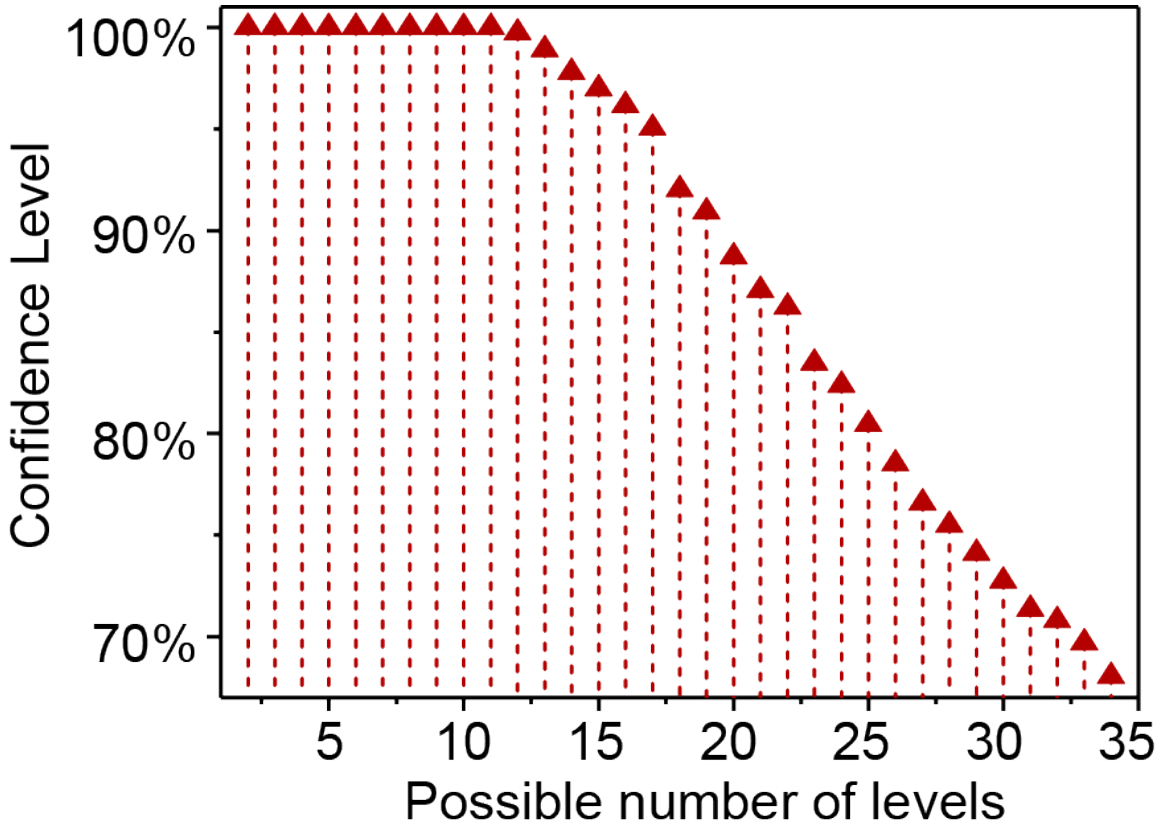


Figure 4.10: The relationship between confidence intervals and the number of distinguished levels.

achieved and resolved from levels nearby without problems after the device stabilized. However, Figure 4.4(b), Figure 4.8(b), and Figure 4.9(a) also illustrates non-negligible overlaps between levels when the data density is increasing with one single device. PCM itself is demonstrated to be stable over 10 years under room temperature. Thus, this problem is expected to be attributed to variations between different programming pulses and influence from environmental fluctuations to the system.

As a consequence, the relationship between the degree of confidence and non-overlapping multi-states is illustrated in Figure 4.10 with a negative correlation. With the current limits of the experimental setup and the environment, up to 11 levels of distinguishment can be achieved with 100% accuracy. The data density can be increased near twice, to 19 levels in a single cell with a cost of only 10% accuracy loss. 26 levels can be achieved with 80% accuracy, and about 70% accuracy can still be achieved with the highest data density 34 levels.

4.4.2 Switching speed investigation

In order to test the maximum possible speed of data retrieval and addressing the integrated photonic memory, the probe transmission is monitored while the programming and ERASE pulse are sent to the device sequentially with the variation of the time interval between pulses. The results of the data addressing and retrieval test are shown in Figure 4.11.

The time interval between the programming pulse and the ERASE pulse varies between 50 ns and 1 μs. There is an initial dip at each transmission level directly after pump pulse, which is probably because of the increased absorption by free carrier absorption and thermo-optical effects according to literature [14, 187, 190] where these effects are deeply studied. After the WRITE pulse ends, free carrier absorption lasts and decays for tens of femtoseconds. On the other hand, the thermo-optical effect lasts for hundreds of nanoseconds because GST material needs to get thermal equilibrium with the surrounding environment, including waveguides and substrates. Both of these effects increase the waiting time between different programming pulses and thus reduce the switching frequency.

According to the tested results, the smallest time interval is expected to be approximately 200 ns for the amorphization process and 500 ns for the crystallization process. This performance is much better than previous multi-level memory cells in literature [177, 191–193] where the switching frequency is about tens of kHz. The most significant difference between this method and previous demonstrations is that

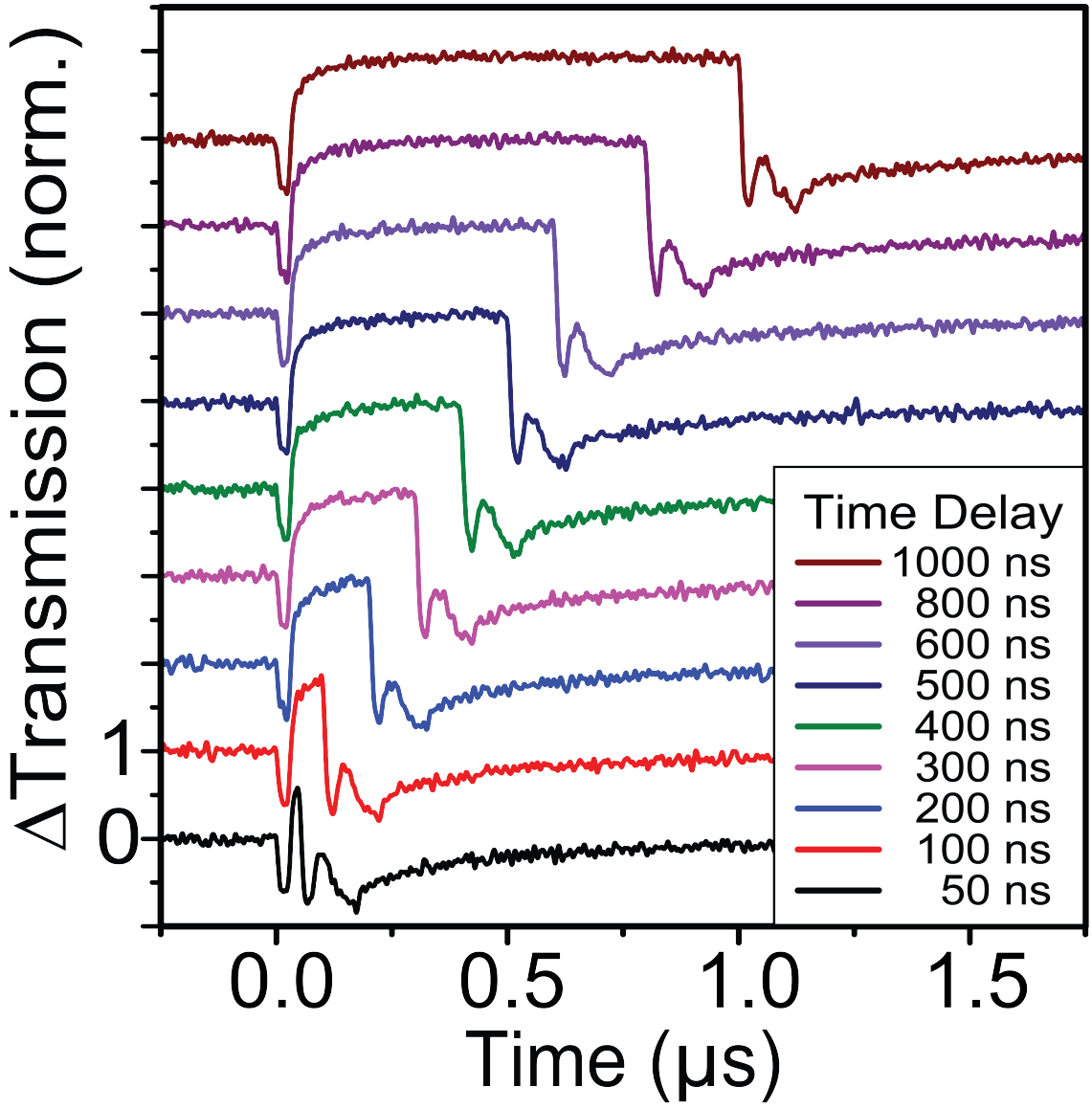


Figure 4.11: Cooling time test between amorphization and recrystallization pulses. Cooling time is the delay between two programming pulses when the device recovers to a stable state after the phase switch. As the cooling time increases, the GST transmission can saturate to a stable value because of the thermo-optical effect.

the method in this chapter does not require current device state feedback to set a desired level.

The optimized amorphization process of GST itself can be as short as several picoseconds [194], and less than 1 ns for crystallization process for GST [195]. Optical pulses with picosecond or femtosecond time width have been demonstrated to switch the state of GST to change the absorption of the material [194, 196, 197]. As a consequence, further investigation can be carried out in terms of using much shorter pulses to set the state of the memory cell [186, 198], which can reduce the thermal decay by 200 ns as it is shown in Figure 4.11.

Previous demonstrations of crystallization of GST-integrated optical memory cells need thousands of pulses to achieve a fully crystalline state [94, 184, 185]. As a consequence, the typical energy consumption for a crystallization process is about 10 nm and the typical time consumption of one crystallization process is about 4 μs respectively [94]. The work in this chapter helps to reduce the energy cost by more than an order of magnitude in both energy (680 pJ) and time (250 ns) domains with the double-step programming and ERASE pulses. Frankly speaking, the features of low drift, programming pulse shapes and multi-level memory cells have been demonstrated separately in literature [173, 199, 200]. However, what should be emphasized here is that this work combined all of these advantages onto the same photonic phase change device. The first time in the world when this work was published, all-optical, stable and reliable memory cells with over 34 distinguishable levels on integrated photonic platforms have been demonstrated, and energy and time efficiency were improved by one order of magnitude.

4.5 Conclusion

In conclusion, this chapter explored research in three different aspects. First of all, up to 34-multi-level data states have been accommodated in one single memory cell, which is recorded high compared with what had been done before in the MLC area. Secondly, a new modulation method to control phase-change photonic memory devices has been developed to reduce energy consumption and time consumption by about one magnitude compared with the previous methods. Thirdly, with the exploration and the optimization of the modulation method, arbitrary level modulation with high accuracy has been achieved irrespective of former device states. By changing the shape of a single pulse, the temperature of GST can be programmed precisely; thus, the phase change process can be tuned precisely, and so as the final

state of the device. The shape of the pulse is accurately controlled by splitting one pulse into several pieces and controlling each piece's time width and amplitude individually. Thanks to the electronic arbitrary pulse generator, this modification does not add an extra burden to the whole modulation process. This method is flexible, reliable and easy to realize. The drift of the device state over time is much lower than its electronic counterparts. These results are essential milestones in the process of realizing integrated photonic computing applications such as in-memory computing [201] and neuromorphic computing [135] with high throughput speed and low energy consumption.

Chapter 5

Si and SiN platforms performance comparison for computing applications

The results of this chapter have been peer-reviewed and published in [32].

In the age of big data, higher demand has been raised for the speed, energy consumption and performance of other aspects of data processing systems. Photonic computing is a crucial solution to the gap between processing vast volumes of data and the weak data processing capability of current computing and storage systems. Photonic computing network is superior to electronic counterparts because of its advantages, including wide bandwidth for data processing and storage, high data throughput rate, low energy consumption and signal latency. By introducing phase change materials (PCMs) into the integrated photonic platform, the computing system gains exceptional co-locating computing and storage advantages at the same position. The architecture of in-memory computing has the potential to break the well-known von-Newmann bottleneck. Although various photonic designs have been demonstrated with Si or SiN platform, the complete understanding of such platforms has been elusive. This chapter provides a thorough comparison of the performance of phase change photonic devices with both Si and SiN platforms for the consideration of computation. These experimental results depict that Si shows significant advantages for systematical integration, data density and phase change speed.

On the other hand, it lost the competition in terms of energy efficiency. Furthermore, the single pulse modulation enabled by double-step pulses shown in the previous chapter is also demonstrated with the silicon platform. Functions such as memory retention, multilevel data addressing and retrieval are demonstrated as well.

Work in this chapter demonstrated the capability of efficient phase change photonic in-memory computing on the Si platform.

5.1 Material and device structure comparison

The principle of Dennard scaling [202] and well-known von Neumann bottlenecks [203, 204] raise a high demand for a high-performance computing system, where silicon photonics can have superior advantages to CMOS electronics. Excellent features of photonic data processing such as wide bandwidth, parallel processing, tera bites level processing speed, and low crosstalk make it promising compared to electrical processing [10]. Integrated photonic platforms including SiN, GeSi, III-V semiconductors, [181, 205, 206], have been used for developing crucial photonic components, such as lasers [207], modulators [208], switches [209], filters [210], multiplexers [211, 212], photodetectors [213–217] and memory cells. Silicon photonic platform is the dominant platform. Owing to silicon's unique property to work as a semiconductor material, silicon waveguides can be developed into thermal heaters by doping certain areas and thus can accumulate broader applications [218]. Other features that offer a potential path to commercialize silicon photonics include high compatibility with other integrated photonic components, fabless manufacturing process and large-scale Si photonic integrated circuits (PICs).

Today, the mechanisms of modulating photonic signals on silicon platforms include free-carrier dispersion effects and thermo-optical effects. Both of these mechanisms are energy-consuming and require continuous voltage biasing [219–221]. However, the addition of PCMs offers the non-volatility feature to the photonic data addressing and retrieval system. For example, $Ge_2Sb_2Te_5$ (GST), one typical kind of phase-change materials, stores the information of light through coupling evanescently to photonic waveguides [10, 14].

Significant progress has been made in advanced optical communication/computing applications such as the exploration of volatility and non-volatility properties of integrated PCM photonic devices and the improvement of the storages density of a single cell to over 5 bits [31, 132]. There are also single device researches including electro-optical hybrid devices [134, 222, 223], reconfigurable optical micro-ring resonators [224, 225], and optical switches [226–230]. In the aspect of photonic computing architectures, scientific explorations include logical computations [136, 231], accumulative addition [94] and multiplication [185]. Plenty of researches are carried out in the area of the artificial neural network simultaneously, including optical synapses [135]

and the latest research, deep-learning neurosynaptic networks for image recognition [232]. During recent years, GST has been employed to develop new types of phase change photonic devices on silicon platforms [20, 228, 233]. Therefore, Si and SiN, as two dominant integrated photonic platforms with distinct optical properties, can fit for both linear and non-linear applications. The notable differences in thermal and electrical conductivity between these platforms lead to distinct operational dynamics in the phase change material photonic cells. Consequently, a detailed comparison between these two platforms helps deeper understanding and more proper usage of these platforms.

In this chapter, the differences between phase change photonic cells on Si and SiN platforms are explored, highlighting their strengths and shortages. Thanks to the higher mode confinement, silicon is superior to SiN in integration, speed and device footprint. On the other hand, SiN owns excellent energy efficiencies due to its lower thermal conductivity. This chapter mainly focuses on the device performance in the C (1530-1565nm) and L (1565-1625nm) wavelength bands since these bands are the dominant bands for data transport, although most of the analysis is suitable to wider applications. The following experimental results can work as an excellent platform reference for developing this rising field, integrated phase change photonics.

5.1.1 Material analysis

The refractive indices are compared in Figure 5.1. Figure 5.1(a) shows the real refractive index while Figure 5.1(b) shows the extinction coefficients (in log10 scale) of Si, stoichiometric SiN (grown via LPCVD), and GST with different statuses measured with ellipsometry. The ellipsometry wavelength range is between 250nm and 1690nm. In the C and L band, the optical contrast of GST between the crystalline and amorphous states is the most significant in the whole range. The choice of C and L band is after considering the application of integrated optical computing and storage systems, too. Figure 5.1(a) shows that the real part of the refractive index of Si is much larger than that of SiN, which causes stronger optical mode confinement within Si waveguides. Stronger confinement induces a more compact integration, with trade-offs of unwanted sensitivities to sidewall roughness and geometric variation. Consequently, it is more crucial for silicon photonics to carry out necessary tolerance analysis and calibration of fabrication processes than for SiN devices.

Crucially, the contrast of the optical indices between Si and GST is less significant than that of SiN at telecommunication wavelengths. On the one hand, such similarity contributes to lower scattering losses at the interface between GST and

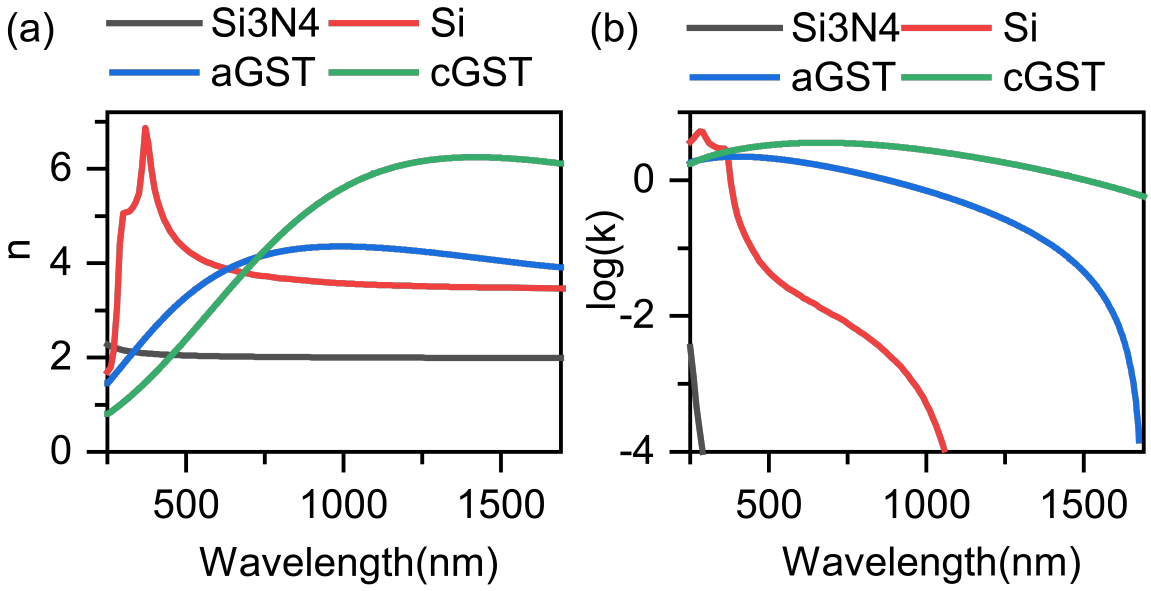


Figure 5.1: Optical refractive indices of both amorphous and crystalline states of Si, SiN, and GST materials measured by ellipsometry: (a) real part and (b) imaginary part of refractive indices respectively.

silicon waveguides (see Figure 5.2). This feature was applied to develop tunable dielectric metasurfaces [234]. Meanwhile, this also leads to weaker evanescent field coupling and, consequently, the less significant dynamic modulation. Figure 5.1(b) shows nearly negligible values of imaginary parts of both Si and SiN in the telecommunication wavelength bands. Consequently, Si has the propagation losses of 0.1-0.5 dB/cm and for SiN the value is 0.04-1.37 dB/cm [3]. SiN material has a markedly wider spectral range of transparency, covering the wavelength from the visible band to the infrared wavelength band, compared with silicon. Wider wavelength ranges make it possible to develop visible phase-change photonics as the optical indices difference of two states of GST is also more notable.

In conclusion, applications and spectral regions of interest determine the type of proper substrates.

5.1.2 Mechanism and simulation

The mode profiles and light propagation profiles of phase change photonic cells are simulated using the ellipsometry measurement data of optical indices of GST, Si, and SiN. The GST strip on the top of waveguides is 10-nm-thick and 4-μm-long. Figure 5.2(a), together with Figure 5.2(b), shows E profiles at cross-section of silicon waveguides with phase change materials and their SiN counterparts. The targetted

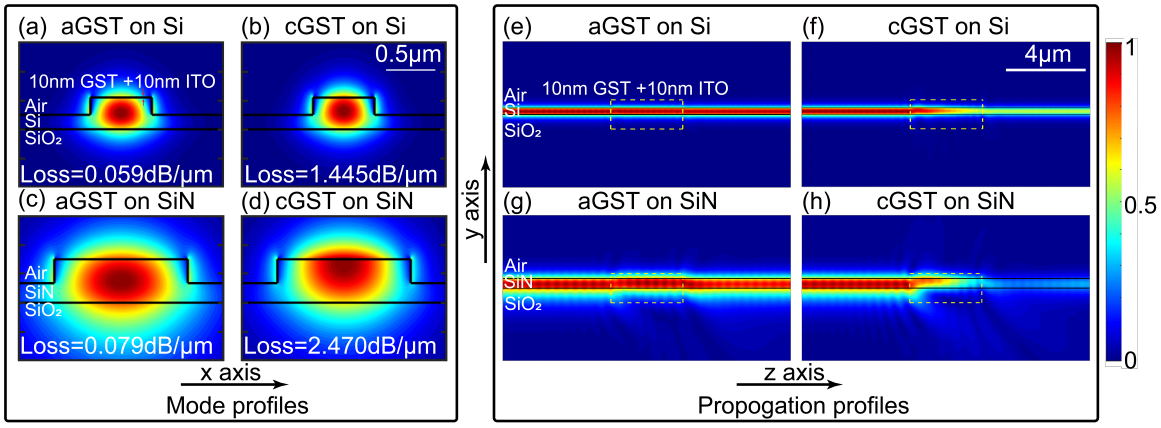


Figure 5.2: The simulation of eigenmode profiles and propagation mode profiles of the fundamental TE mode inside Si and SiN waveguides with GST. Eigenmodes in waveguides describe electromagnetic fields that are invariant in their intensity profile as they propagate along the fibre [28]. The 2D eigenmode profiles of Si waveguides with amorphous (a) and crystalline GST (b) and their SiN counterparts (c) and (d) are shown, with a significant electrical field distribution change because of GST. The propagation modes are guided along the propagation direction and depends on the waveguide structure as shown in (e)-(h). (e) and (f) illustrates simulated propagation profiles of the fundamental TE mode with 4 μm amorphous (e) and crystalline GST (f) on top of the waveguide. (g) and (h) are SiN counterparts. Light as an electromagnetic wave can have different formats within the waveguide, such as TE mode (E field is perpendicular to the propagation direction) and TM mode (E field is perpendicular to the propagation direction).

wavelength is 1550 nm and the targetted mode is TE mode. The boudary condition is perfectly matched layer (PML). Figure 5.2(e) and Figure 5.2(f) depict the propagation mode profiles of this device. Figures 5.3 (c)(d)(g)(h) illustrate mode profiles for SiN substrates accordingly. SiN platforms are widely used in the literature [10, 94, 135, 224]. Similarly to the previous chapter, during simulations along the propagation direction, asymmetric boundry condition is used along this direction to reduce the computing complexity. The smaller contrast of refractive indices between GST and Si is observed to cause lower losses from reflection and scattering, while SiN causes better matching of optical modes between bare waveguides and the PCMs. Bigger refractive index contrast between silicon and air contributes to a denser waveguide structure due to higher confinement of the fundamental TE mode inside the waveguide, with a width of 500 nm instead of 1.3 μm SiN. Stronger confined modes inside silicon waveguides also lead to lower evanescent coupling to the GST. This feature leads to lower propagation loss in amorphous and crystalline states than GST on SiN substrates.

The estimation of propagation loss coefficient is carried out using the following formula:

$$\alpha = \frac{4\pi Im(n_{eff})}{\lambda} \tag{5.1}$$

Where n_{eff} is the simulation results of complex effective refractive indices. The definition of propagation loss coefficient comes from

$$P_L = P_0 e^{-\alpha L} \tag{5.2}$$

where P_0 (unit: W) is the initial power, P_L (unit: W) is the power after the propagation distance L (unit: m) and the power decays in proportion to $e^{-\alpha L}$. The unit of α is dB/m. It is expected to see transmission contrast between the amorphous and crystalline state of GST with a length of 4-μm is 95% (amorphous, 0.059 dB/μm) and 26% (crystalline, 1.445 dB/μm). These results agree with the experimental results in Figure 5.3(d), where the transmission of the same length of GST device reduces from 96% to 23% normalized by straight waveguides. Due to the lower propagation loss on silicon substrates, longer devices of GST are necessary than SiN to have a greater optical contrast between amorphous and crystalline states.

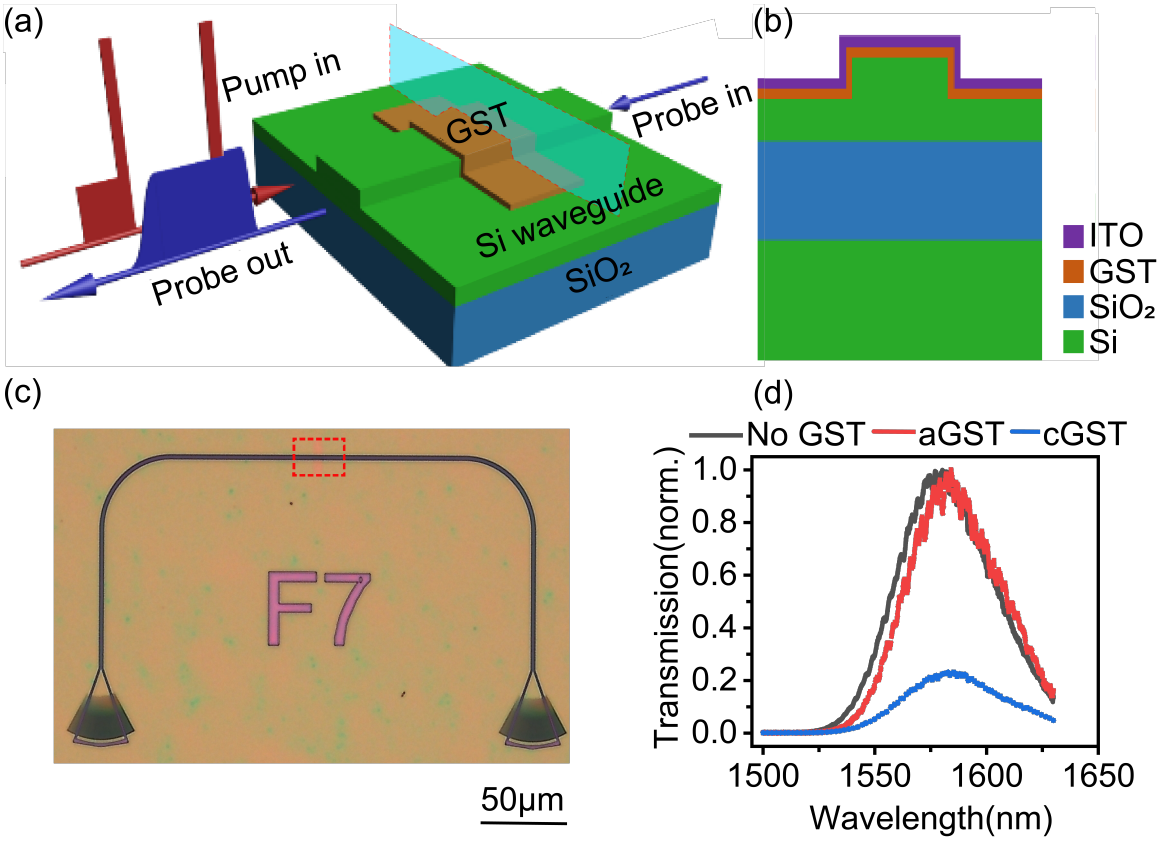


Figure 5.3: The design of the device and fabricated device static performance. (a) A schematic of the applicable device and (b) cross-sectional view of phase change photonic devices on silicon substrates. (c) The optical image of a GST photonic device. GST is highlighted by the red dashed square. (d) Transmission spectrum comparison between a straight waveguide, a waveguide with amorphous GST and thermal annealed crystalline GST, normalized by the transmission of the straight waveguide.

5.1.3 Device and experimental setup preparation

Device design and fabrication

The silicon substrate structure is an SOI structure, a 220 nm device layer on the top of a 3μm buried oxide layer. The device is shown in Figure 5.3 where the phase change material (GST) is evanescently coupled to the optical mode of the Si waveguide. Consequently, this device can carry out optical WRITE, READ and ERASE operations. EBL and dry RIE etching are used to fabricate partially etched waveguides (120 nm etch depth). The RF sputtering technology is used to deposit a 10 nm applicable layer of GST with the protection cover of a 10 nm of Indium-Tin-Oxide (ITO) on the top of the waveguide (2×10^{-6} Torr base pressure, 5 mTorr Ar atmosphere, and 30 W RF power).

The device architecture of a phase change photonic cell is shown in Figure 5.3(a) together with the cross-section structure shown in Figure 5.3(b). Figure 5.3(c) shows the optical image of a phase change photonic cell with a red dash square highlighting the position of GST. This device is fabricated on a silicon substrate. Light is coupled into the waveguide through grating couplers with the optimized transmission efficiency of 40% for a single grating coupler shown in Chapter 3. The transmission spectrums shown in Figure 5.3(d) include that of a bare silicon waveguide (black curve), the same waveguide with as-deposited amorphous GST with a length of 4 μm (red curve), and the crystalline state of that device after thermal annealing (blue curve). The thermal annealing happens on a hot plate at 250 °C for 10 minutes. The crystallization process introduces significantly increased propagation loss because of the absorption of GST. While amorphous GST allows 95% light to pass through the waveguide, the transmission decreases to about 25% of the input power after passing through a 4-μm-long crystalline state GST. This measurement is carried out before GST deposition, after GST deposition and after hot plate annealing on the same device.

The author further fabricated different lengths of devices, including 1,2,4,6 μm devices shown in Figure 5.4. The aim is to figure out the relationship between different lengths of devices and the performance regarding energy consumption, switching contrast between different states, etc. Performance comparison for different lengths of devices are also discussed in detail in the following section 5.4.

Measurement Setup

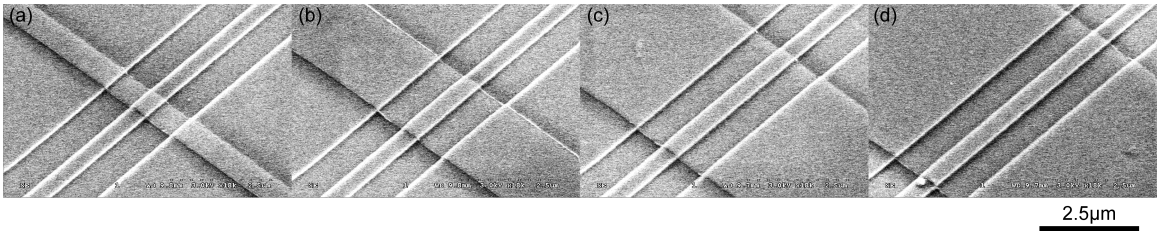


Figure 5.4: SEM images of different lengths of GST on top of waveguides. (a)1 μm GST. (b)2 μm GST. (c)4 μm GST. (d)6 μm GST.

The measurement setup is a typical pump-probe setup. The pump light is generated by an L band laser source fixed at the wavelength of 1590 nm. The light is then amplified by an erbium-doped fiber amplifier (EDFA) to ensure that the power is sufficient to optically switch the state of the GST. For the probe light, a continuous probe laser at 1610 nm is chosen to read the optical signal continuously. The pump pulses are turned into different shapes, including rectangular shapes and triangular shapes, using a signal generator with arbitrary function shapes (Tektronics 100 MHz AFG3102C). This pulse generator can modulate a high-speed electro-optic modulator (EOM) through RF pulses. The non-linear response of the EOM is compensated by the shape of the input RF pulse.

As a consequence, the pulse shapes described above reflect the shape of the optical pump pulse after the EDFA rather than the input electrical pulse. Parasitic optical signals at unwanted wavelengths are removed by optical bandpass filters in both pump and probe beam paths. For the long-term monitoring of probe signals, low-noise sensitive photodetectors are chosen for high-quality readout, and ultrafast photodetectors are chosen for capturing the thermo-optical effect of the device when the dynamic phase change happens, together with a high-speed sampling oscilloscope. With this measurement configuration, the phase transitions below sub-nanosecond can be monitored in real-time. A tunable optical attenuator is added to the pump circuit before the EOM, aiming at controlling the amplitude of pulses sent to devices. Furthermore, to stabilize the polarization of the probe laser, an in-line fiber polarizer is applied after the laser in addition to a polarization controller. To improve the measurement accuracy further, a reference signal line and a corresponding photodetector can be applied to eliminate any possible noise signal arising from thermal fluctuations or polarization drift, to name a few, generated from the setup.

5.2 Demonstration of single pulse modulation on SOI platform

Amorphization

Reaching any arbitrary states from any initial state is possible with a single-shot pulse on the silicon platform using amorphization or crystallization modulation in a similar manner to the one on a SiN platform [31]. Single rectangular pulses with varying amplitudes (illustrated by red color varying from light to dark) are applied to devices for phase transitions, and a double-step pulse is employed to erase the device back to the initial state. Figure 5.5(b) shows the transmission response with non-volatile, multilevel operations of the tested devices. The transmission recordings of one completed cycle of multilevel states setting are shown here. The pulse width is 25 ns. With the same pulse sequence, the device was programmed over 400 cycles. The author plotted the final state of the device as a function of amorphization amplitude and the programming error as shown in Figure 5.5(c) and (d). The histogram of different levels and standard deviation are shown in Figure 5.5 (c). The standard deviation is down to 0.687 %. The relationship between the switched transmission contrast and the pump power is shown in Figure 5.5 (d).

Crystallization

The author further explored the crystallization process. In previous literature, multiple pulses (19 to be precise) with energies ranging from 370 to 600 pJ were required with total programming energy of 9.5 nJ and a duration of 3.8 ms. Other similar approaches are developed with ultrafast pulses [19, 135, 235] but those required multiple recrystallization pulses of decreasing amplitude to reach the desired intermediate states. Double-step crystallization pulses are used in this chapter to modulate the state of the devices, as shown in Figure 5.6(a). Recrystallization pulses are shown as blue color from light to dark for different time widths of the second step. With the increase of the duration of the second step of crystallization pulses, the transmission decreases and the material is gradually crystallized. Arbitrary multilevel modulation is also achieved with using the same device as demonstrated in Figure 5.7 (a). Figure 5.7 (b) and (c) show the deviation distribution of stair time width programming and arbitrary time width programming separately. It can be observed that the standard deviation of stair programming modulation is 0.3%, noted as much smaller compared with 0.9% of arbitrary programming. Further experiments are needed to be carried out to improve the stability and reliability of arbitrary programming.

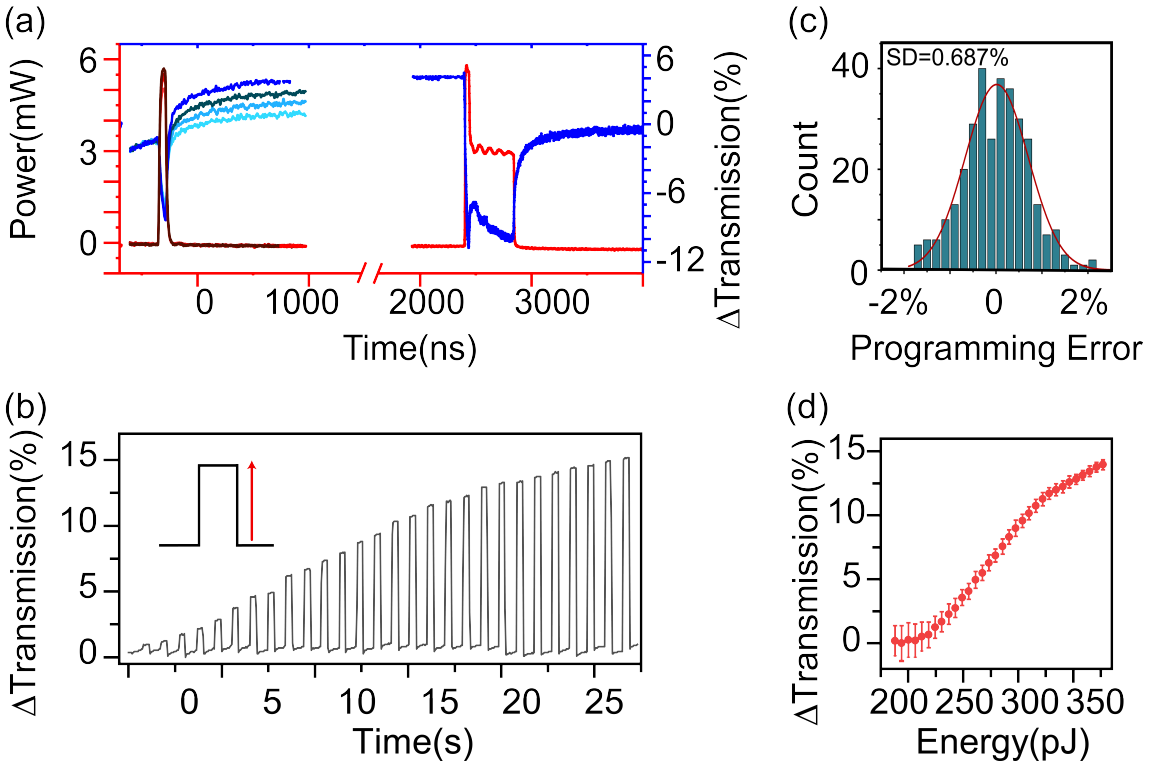


Figure 5.5: Single pulse amplitude modulation for GST amorphization on Si waveguides. (a) Pulses shapes (red curves) and corresponding transmission changes (blue curves) with pulse amplitude modulation for amorphization/programming and crystallization/erasing. (b)In a longer time scale, independent multilevel states with pulse amplitude modulation. (c) Total deviation distribution of different levels of programming pulse amplitudes. The standard deviation of different levels is 0.687%. (d) Separate errorbar distribution for each level of programming pulse amplitudes. The transmission change in (a),(b) and (d) is normalised to the initial transmission state of the device. The initial transmission state shows big fluctuation in (d) and even shows lower transmission than the initial crystalline state. There are two possible reasons. Firstly, the initial state may not be fully crstalline state but get more crystallization during the switching process. Secondly, the crystallization pulse may damage the device a bit and the small switching energy cannot guarantee to fully crystalline the device during each switching process. The error rate in (d) is normalised to the average value of each specific device level.

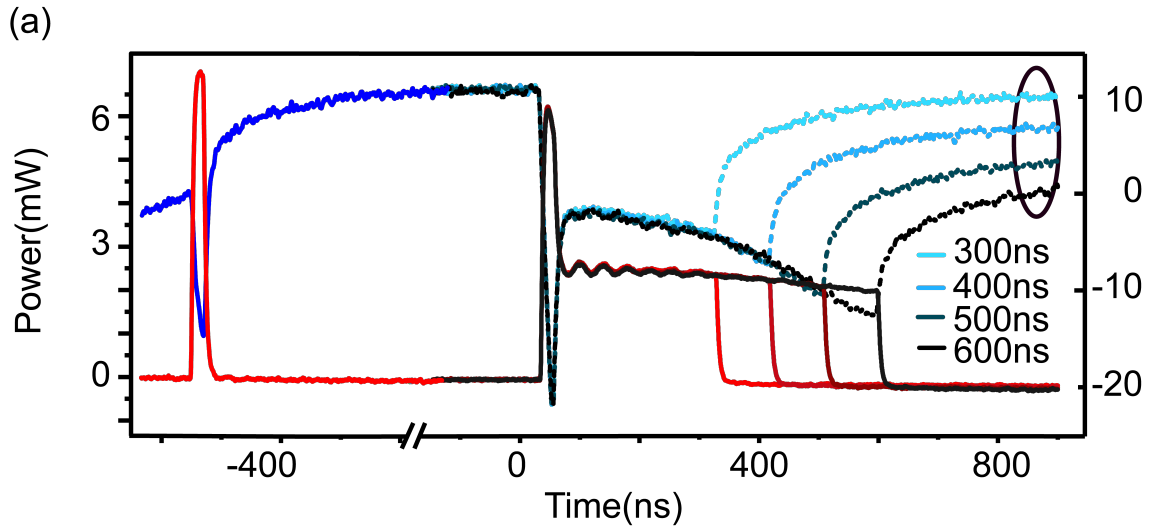


Figure 5.6: Double step modulation for crystallization process. (a) Pump pulses (red curves) and corresponding transmission changes (blue curves) with different second step time width modulation. From light color to dark color, the time width of the second step of crystallization pulses increases, and the corresponding transmission contrast changes increase. The transmission change is normalised to the initial transmission state of the device.

5.3 Analysis of dynamic response while switching phase

5.3.1 Dynamic response while amorphization

Comparison analysis of thermal and optical properties during the amorphization operation is demonstrated for both waveguide platforms. The transmission response in real-time of the amorphization process corresponds to a short pump pulse with the variation of amplitude and pulse width illustrated in Figure 5.8. Figure 5.8(a) depicts the spatial distribution of temperature after a 10 mW amorphization pulse was sent to the device. The black dot shows the position of the maximum temperature. Simulations were carried out to illustrate the thermal changes inside this phase change photonic cell when the phase transition happens from crystalline to amorphous states. The temperature changes inside the GST strip were plotted to describe the dynamic process before and after a 20 ns pulse was sent to the device. The amplitude of the amorphization pulse varies from 2 to 10 mW in Figure 5.8(b). The dynamic changes of the temperature happen at this black dot in Figure 5.8(a). Both devices on Si and SiN platforms were simulated, shown in solid and dashed lines, respectively. It can be illustrated that the temperature of GST on the Si waveguide rises quicker but

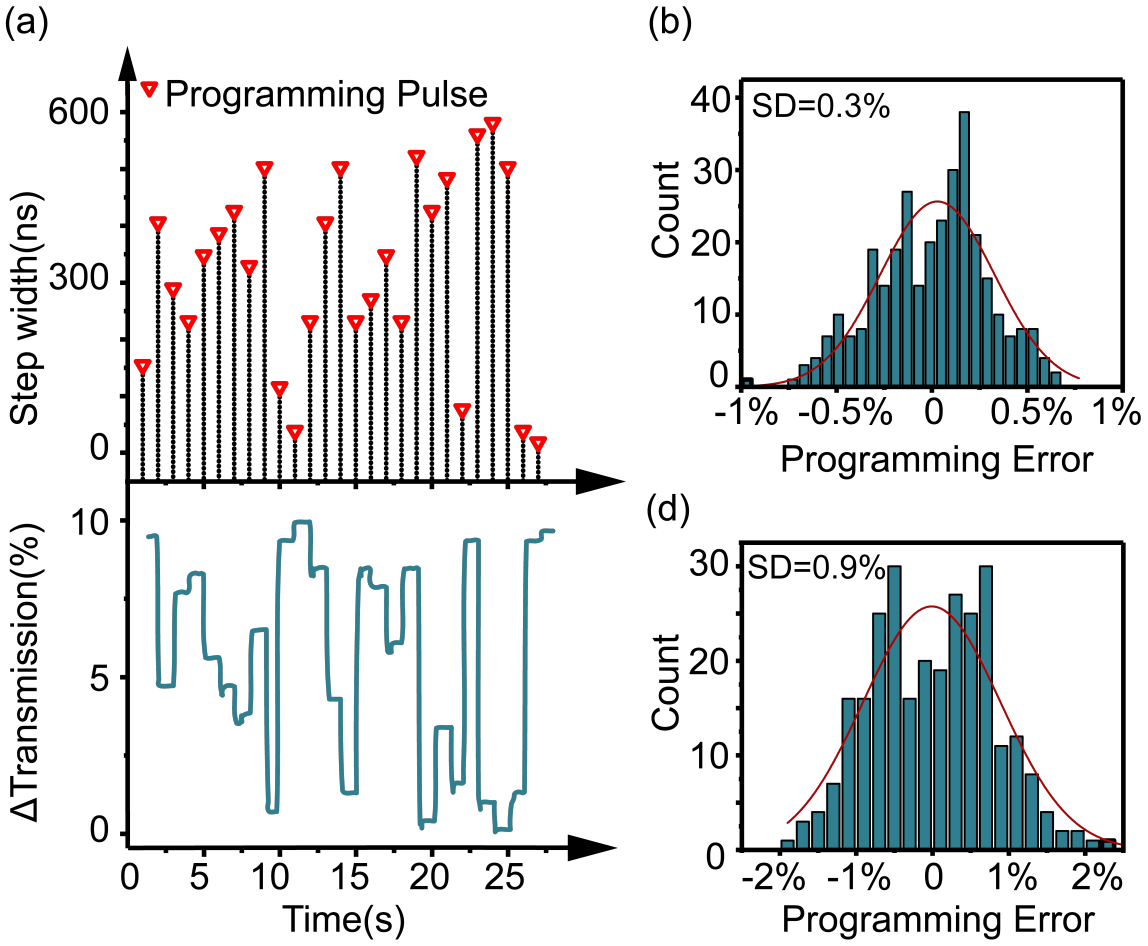


Figure 5.7: Double step modulation for crystallization process. (a) Arbitrary second step time width modulation. The upper plot is the different time widths of programming pulses, and the lower plot is the corresponding transmission changes. (b) Total deviation distribution of different levels of programmed second step time width. The standard deviation of different levels is 0.3%. (c) Total deviation distribution of different levels of randomly programming second step time width. The standard deviation of different levels is 0.9%. The transmission change in (a) is normalised to the initial transmission state of the device. The error rate in (b) is normalised to the average value of each specific device level.

peaks at a lower temperature than that of SiN. The geometry of the device and the thermal properties play an important role in this difference. More compact GST-Si waveguides lead to a more concentrated heating process; meanwhile, higher thermal conductivity of silicon makes it difficult to accumulate energy and thus saturate at a lower temperature. The thermal conductivities for both silicon and SiN material are as the following (bulk material data from [236]):

$$\begin{aligned} \kappa_{Si} &= 148W \cdot m^{-1} \cdot K^{-1} \\ \kappa_{Si_3N_4} &= 43W \cdot m^{-1} \cdot K^{-1} \end{aligned} \tag{5.3}$$

Quicker response of heat dissipation is thus experienced in Si than SiN, resulting in a lower saturation temperature on the same optical power volume condition. Further improvement can be carried out by changing the partially etched silicon slab layer into a fully etched strip layer, as that is a large source of heat dissipation. On the other hand, quicker heat dissipation help reducing the cooling time between different operations, which is advantageous when pump pulses have a shorter duration but a high amplitude. Experimental results in Figure 5.8(c) strongly support the simulation results. GST on Si consumes four times more energy than SiN in order to achieve similar transmission contrast.

5.3.2 Dynamic response while crystallization

Similarly to the amorphization process, the author also recorded the pulse shapes and optical response of the crystallization process in Figure 5.9(a) and Figure 5.9(b). The author used double-step pulses to carry out the crystallization process, with varied amplitude and time width of the second step to control the final device phase state (23.5 mW with varied time width from 300 ns to 600 ns). The initial step is 25 ns and 58.75 mW, followed by the long tail or second step. 4-μm-long devices on top of a silicon waveguide are used. Figure 5.9(a) shows the pulse shape and Figure 5.9(b) is corresponding device transmission responses.

Transmission changes are a reflection of the temperature of the device on a scale. It shows from this plot that the first step pulse gives the device a sharp temperature increase to melt the whole material to a melting state, and with the disappearance of the first step pulse, the temperature rapidly decreased and then slowly increased. This is because the heating process with the second pulse is longer than the first step, but the temperature increase is limited by the amplitude of the second step. After the disappearance of the second step, the device's temperature drops slowly and gives the material a different time length to recover back to a specific amorphous-crystalline

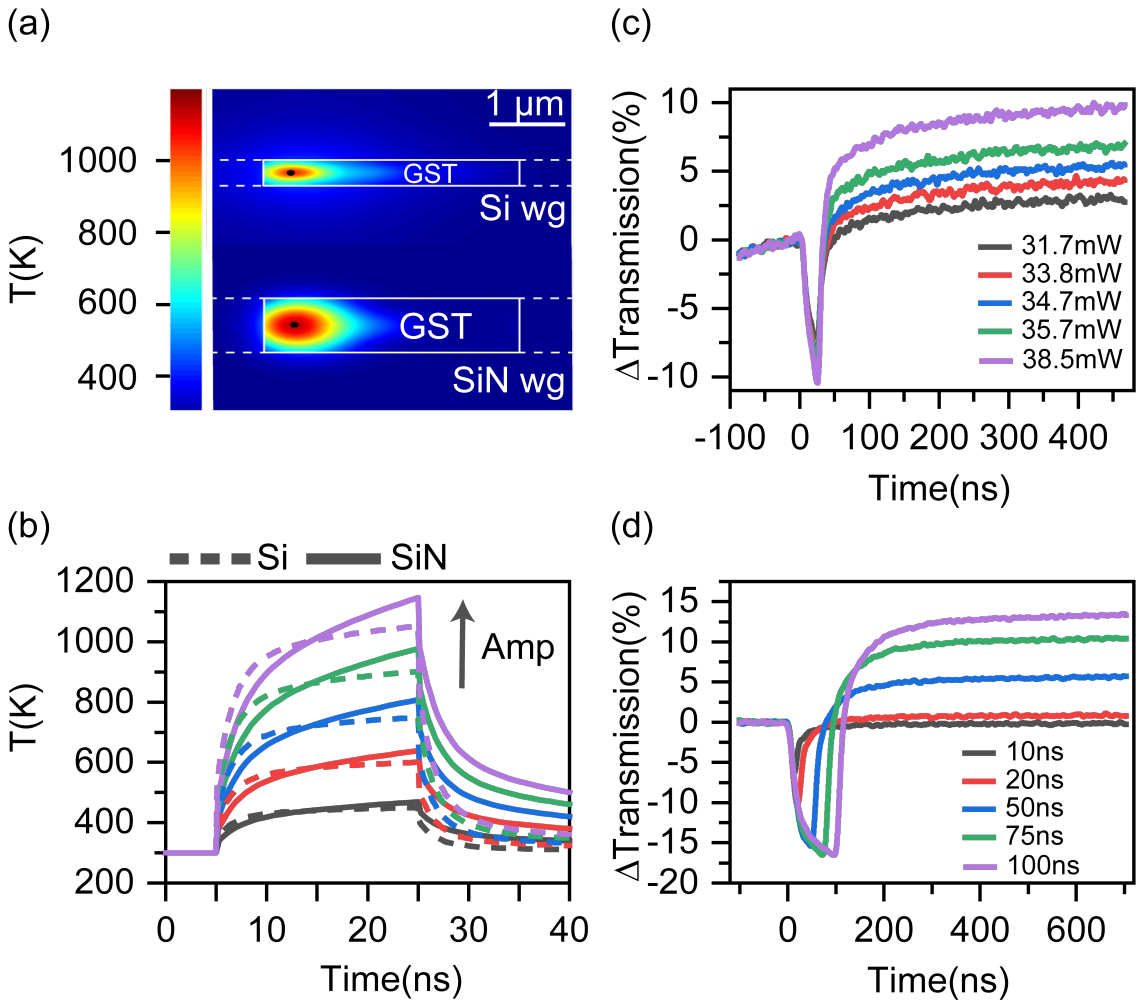


Figure 5.8: The mechanism investigation of the amorphization process through both simulations and experiments. (a) Temperature distribution maps from the top view for a 4-μm-long GST on top of a 500 nm Si waveguide and 1.3 μm SiN waveguide with an amorphization pulse with a 10mW amplitude and a 20ns duration. The position with the highest temperature is labelled with a black dot. (b) The simulation demonstration of the relationship between pump power and temperature changes for both Si and SiN devices. The pulse duration is fixed at 20 ns while the amplitude varies from 2 to 10 mW with the step of 2. (c) (d) are experimental transmission response of thermo-optical effect taken with a high-speed photodetector to the pump pulse changes: amplitude variation (c) and time width variation (d). The transmission change in (c) and (d) is normalised to the initial transmission state of the device.

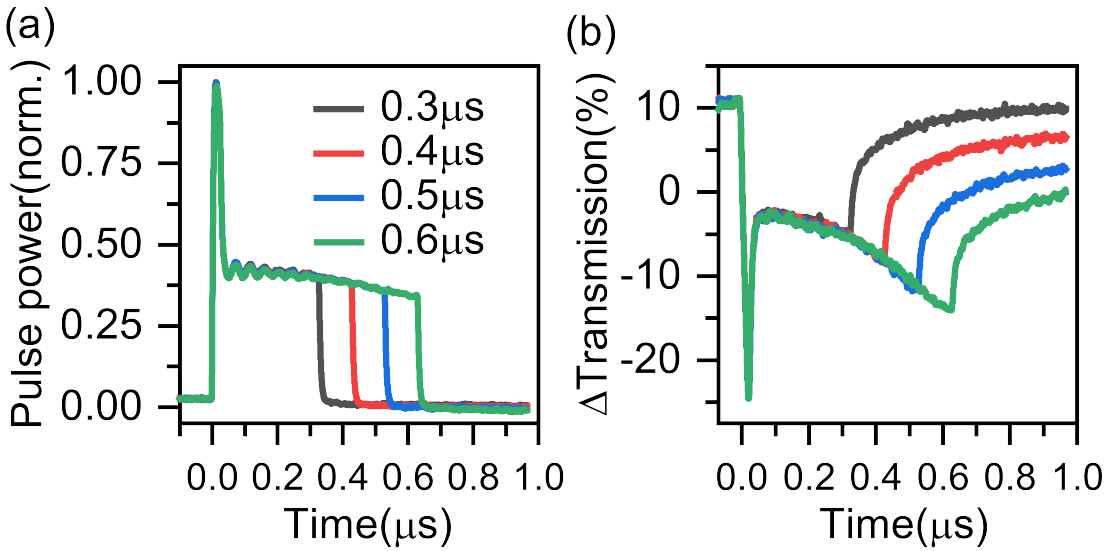


Figure 5.9: Mechanism investigation of crystallization process through experimental demonstrations. (a) Recordings of crystallization pulses with the variation of time width of the second step and (b) device corresponding transmission readout. This modulation method is double-step crystallization time width modulation with a fixed first step of 25 ns and 300-600 ns for the second step time width variation. The pulse power in (a) is normalised to the range of (0,1) to show the relationship between the peak amplitude and the second step pulse. The transmission change in (b) is normalised to the initial transmission state of the device.

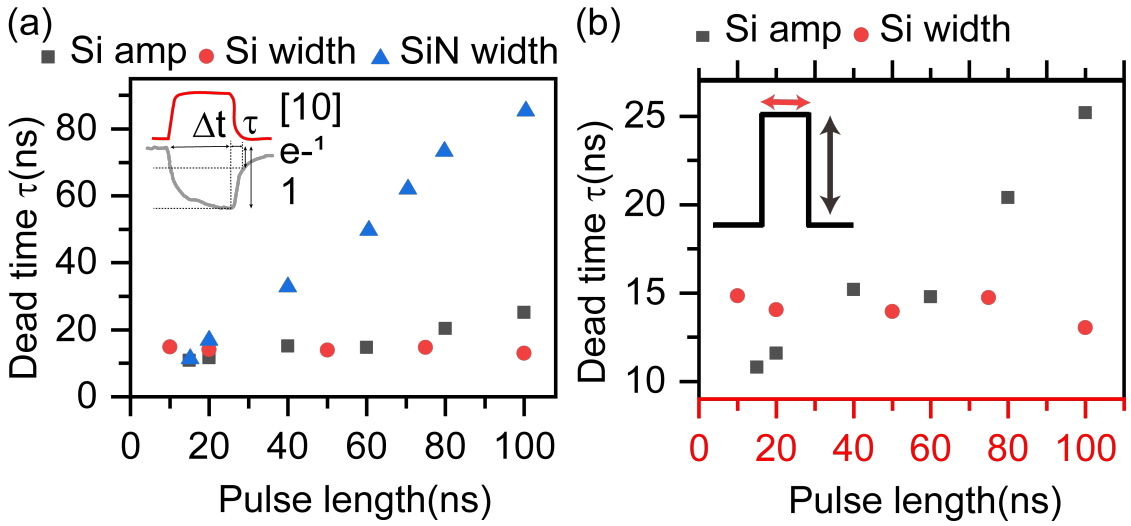


Figure 5.10: (a) Dead time (definition from [10]) comparison for both Si and SiN devices. The modulation methods of amplitude modulation and time width modulation are also compared. The data of SiN devices is from [10] for comparison. (b) is zoomed-in dead time comparison between these two modulation methods on Si waveguides in order to emphasize the difference.

mixture state. The more time it takes to recover, the lower temperature it will end with and the more crystalline it will be.

5.4 Performance comparison

5.4.1 Switching speed

Figure 5.8(c) and (d) shows the transmission response of GST-on-waveguide device as a result of thermo-optical effects. A single pulse with a fixed duration of 20 ns with varied amplitude was sent to the device for amorphization. The strong thermo-optical effects in both GST and silicon [237] leads to a positive correlation between the device temperature, and then refractive indices, and then a delay dead time in programming before the device can reach equilibrium state. The data in Figure 5.8(c) and (d) is used to carry out the calculation of dead time of different switching methods shown in Figure 5.10 (a) and (b). However, more experiments should be repeated in the future to test the stability of this dead time test. The dead time $t_{deadtime}$ was defined as the time duration for the transmitted light passing through a waveguide to launch up from the lowest transmission point $T_{finalstate}$ to a specific transmission point $\frac{1}{e} \cdot T_{finalstate}$ from [10]:

$$t_{deadtime} = t_{\frac{1}{e} \cdot T_{finalstate}} - t_{T_{finalstate}} \tag{5.4}$$

The dead time determines the shortest time required between different programming operations in computing and memory applications. Experiments are carried out to collect silicon device results and compare that with the data of its SiN counterparts from [10]. The dead time for devices with silicon waveguides is only one-fourth shorter than SiN devices because of the significantly higher thermal conductivity and more compact footprint for quicker heat dissipation, shown in Figure 5.10(a). Consequently, faster write-read operations make silicon GST devices suitable for programming pulses shorter than 20 ns. Different modulation methods also make a non-negligible difference to the dead time, shown in Figure 5.10(b). The variation of the amplitude of the single rectangular pulse with fixed time duration is shown with black dots, and the variation of the duration of the pulse is shown with red dots. The increase of dead time is proportional to the increase of the pulse amplitude, while it is hardly affected by the pulse duration. The possible reason is that GST reaches thermal equilibrium with pulses greater than 10 ns, supported by simulations in Figure 5.8(b). Thus, a constant dead time is observed with pulses whose duration is greater than 10 ns and the amplitude is fixed.

5.4.2 Switching threshold and energy consumption

The energy consumption is then discussed in this section. The energy switching threshold for amorphization for different lengths of GST is illustrated in Figure 5.11. Figure 5.11(a) depicts a heat map of energy consumption and a bar chart of transmission changes for a silicon waveguide with 2-μm-long and 4-μm-long crystalline GST on top, respectively. Longer devices have a lower energy switching threshold and a more significant switching contrast with the same energy consumption (shown in Figure 5.11(b)). This conclusion agrees well with experimental observations with SiN devices in [11]. In order to achieve similar transmission contrasts, silicon waveguides cost greater energy consumption due to its higher thermal conductivity than SiN devices, shown in Figure 5.11(c). The switching performance of GST on top of SiN waveguides is plotted in Figure 5.11(c) as a comparison to silicon counterparts. Unfortunately, there is no 4-μm-long device tested before, so the data of 5-μm-long devices is chosen (the closest device dimension in the literature). More accurate experiments can be carried out for further development to figure out the energy consumption with, for example, ultrafast pulses and other substrates.

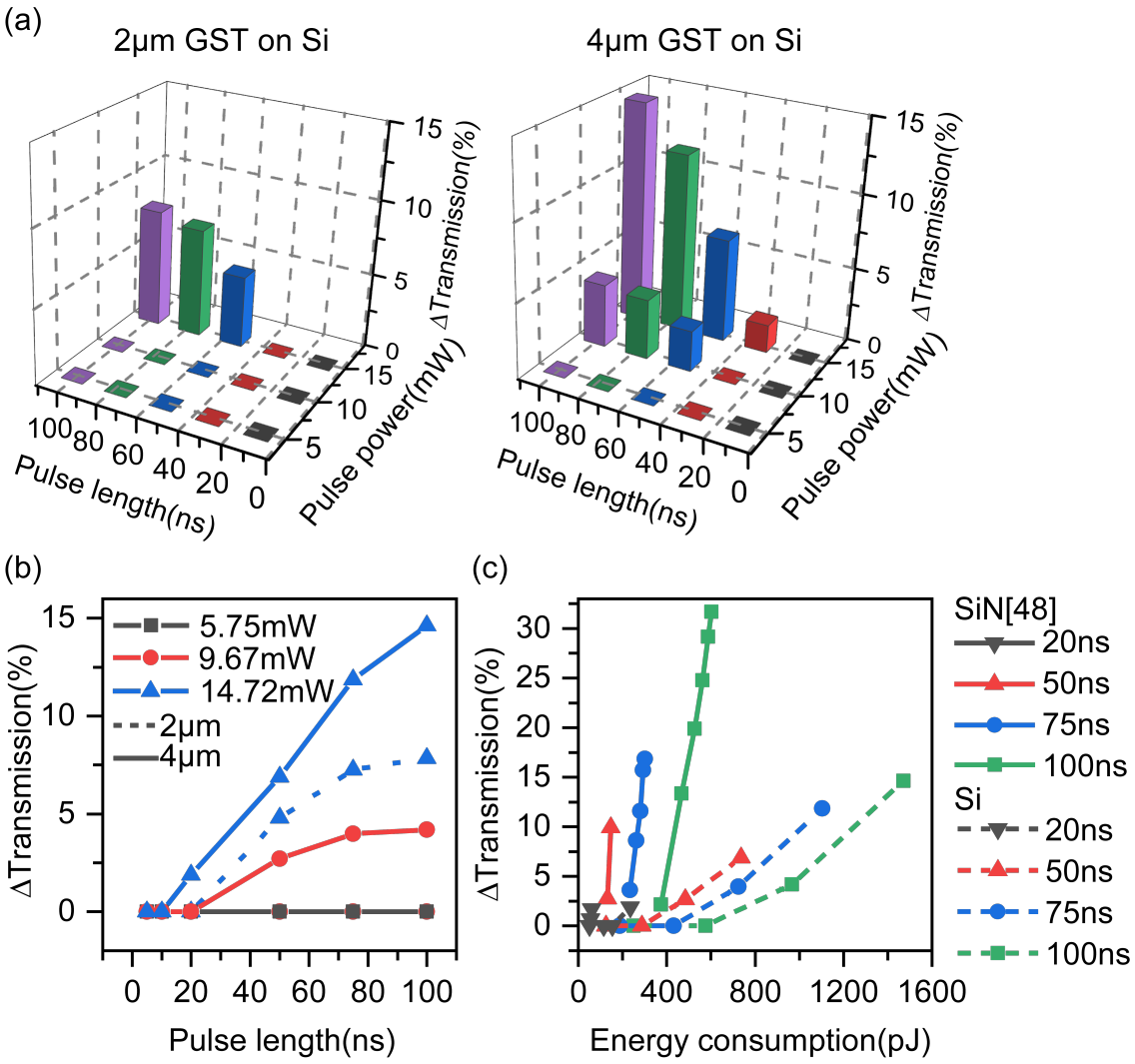


Figure 5.11: Relationship between switching parameters (including the substrate materials and the length of phase change material GST), optical transmitted contrast between states, and energy consumption. Phase change photonic devices with 2 μm (length along propagation direction) applicable GST and 4 μm applicable GST are depicted with a solid line and dashed line separately. (a) is three-dimensional maps for switching parameters and corresponding transmission contrasts for 2 μm and 4 μm devices separately. (b) The relationship between transmission contrasts and the duration of pump pulses varied from 5 ns to 100 ns and the length of the device is between 2 μm and 4 μm. (c) The correlation between energy consumption and the choice of substrates (Si or SiN) and duration of pulses. Notably, the length of GST is 4 μm on Si and 5 μm on the SiN device from [11]. The duration of pulses varies from 20 ns to 100 ns. Every data point is on average of 300 repeated measurements. The transmission change in (b) and (c) is normalised to the initial transmission state of the device.

5.5 Conclusion

Table 5.1: Silicon versus SiN integrated photonic devices performance comparison

Waveguide Type	Si	SiN
Refractive index at 1550 nm	$3.478 + 0\,i$	$1.9894 + 0\,i$
Refractive index at 470 nm	$4.491 + 0.76\,i$	$2.049 + 0\,i$
Thermal conductivity(W $\cdot m^{-1} \cdot K^{-1}$)	148	43
Footprint of the GST cell(applicable part: thickness × length × lateral size)(um^3)	$0.01 \times 4 \times 0.45$	$0.01 \times 4 \times 1.3$
Propagation loss(GST amorphous)(dB/um)	0.059	0.079
Propagation loss(GST crystalline)(dB/um)	1.445	2.470
switching dead time with 10 nm pump pulse (ns)	10	10
switching dead time with 100 nm pump pulse (ns)	13	87
Smallest non-volatile amorphization energy (pJ)	388.4	42[4]

The summary of the experimental evaluation of the critical trade-offs between Si and SiN substrates is shown in Table 5.1. Different platforms and their material properties lead to differences in device footprint and optical properties, thus differences in density, speed and energy consumption of an optical computing system. Si substrate enables a denser footprint and high time efficiency in amorphization process than SiN substrate. Nevertheless, the silicon substrate makes the device energy-hungry, simultaneously due to its rapid heat dissipation from the Si slab. Using strip waveguides instead of rib waveguides, as mentioned before, may overcome this shortage. Moreover, SiN is preferred by applications in the visible and near-infrared spectral regions, whereas Si platform with denser architecture is more suitable for data addressing, retrieval, and in-memory computing applications [185] with advantageous scalability in system operations.

Advantages of the silicon platform include:

a) good compatibility with existing CMOS foundry fabrication capabilities and other integrated electronic and optical components to establish an optoelectronic hybrid computing and storage system;

b) high data writing and erasing speed and excellent heat dissipation;

c) dense footprint;

d) low propagation loss in the telecom wavelength regions.

Although disadvantages of this platform, such as energy consumption, are non-negligible, recent researches that combine silicon and SiN platforms show a promising future to make full use of the advantages of both platforms while eliminating their shortages.

In conclusion, differences of key properties of Si and SiN platforms in aspect to operational energy consumption, time consumption and footprint are reported in this chapter. The stability of single-shot double-step modulation of silicon devices is then

summarised. Up-to-date device performances are discussed. Thanks to its higher mode confinement and greater thermal conductivity, silicon is clearly advantageous over SiN regarding speed, integration and system scalability. All-optical systems may be more suitable for SiN platforms where the wavelength range can be broader, and the energy consumption is more efficient than the silicon platform.

Chapter 6

Demonstration of a Large Scale Optical Computing System

The results of this chapter have been peer-reviewed and published in [238].

6.1 Motivation

As current computing systems struggle to meet the ever-changing needs of data exploration and processing, researchers are focusing on developing the next generation of computational productivity tools. Newer tools that are being explored include quantum computing [239], optical computing [240], electronic non-volatile in-memory computing [241] and even DNA computing tools [242]. Of these methods, optical computing stands out due to the mature techniques it utilizes compared with other new computing techniques as well as its many beneficial features such as wavelength division multiplexing (WDM), high computation speed, and low energy consumption. The potential of this technology has garnered wide attention and has led to its swift development and optimization on several fronts. Due to its high density and ultrafast computing speed, free-space optics have been explored for the application of matrix multiplication and Fourier transformation [156, 243]. Other areas of development include integrated neuromorphic computing [217, 244] with phase change materials, optical computational networks with volatile phase shifters [25], and spatial light modulator networks enabled by holography [245] or photonic crystals [246]. However, despite its great potential, optical computing networks still have shortcomings that must be addressed. First, most of these networks are volatile, which leads to the consumption of unnecessary amounts of energy during the computation process. Second, if approached using a non-CMOS compatible fabrication process, then foundry technology development is necessary, wider applications are restricted and

it is more challenging to merge into current electronic computing systems. Third, advanced and more efficient computation architecture formats, such as neuromorphic computing, are still being explored further.

While the format and architecture of optical computing have long been a point of research focus, they still remain in an early stage of development. Several different computing structures have been explored such as recurrent computing[247, 248], convolution computing [12, 249–251], neuromorphic computing [244], among others. Although it has significant potential for improving computing speed and reducing energy consumption, optical computing networks need further development to enhance the capability of current computational systems.

In this chapter, an integrated easy-programmable, non-volatile in-memory computing optical network core that can carry out machine learning tasks such as pattern recognition and natural language processing is developed. In this computing core, phase change photonic computing cells [201] work as the basic components that enable the in-memory computing capability. Directional couplers are used in order to guide light to different computation channels inside this network. This method is used for its easy fabrication and scalability. Thermal phase shifters are used in this network to obtain simple programming capabilities for individual devices. All of the above features are included in this core. The computation capability is demonstrated by the rotation matrix calculation and small pattern recognition. The advantage of this type of core is its capability for parallel tasks processing with exceptionally low computational energy consumption. To show the further potential scalibility of this optical basic core, this project also carried out a simulation of a bigger computation system with cascaded cores.

This non-volatile, energy-efficient optical core makes the easier scalability of optical networks possible. This in turn allows the network to carry out much more complex machine learning tasks such as physical system simulations, big data analytics, or complicated system decision optimization. The addition of wavelength multiplexing has the potential to carry out parallel processing through up to 10000 channels with different photonic generation methods [252, 253]. We believe this easily programmable, and CMOS compatible optical core has the potential to accelerate the development of current computational systems.

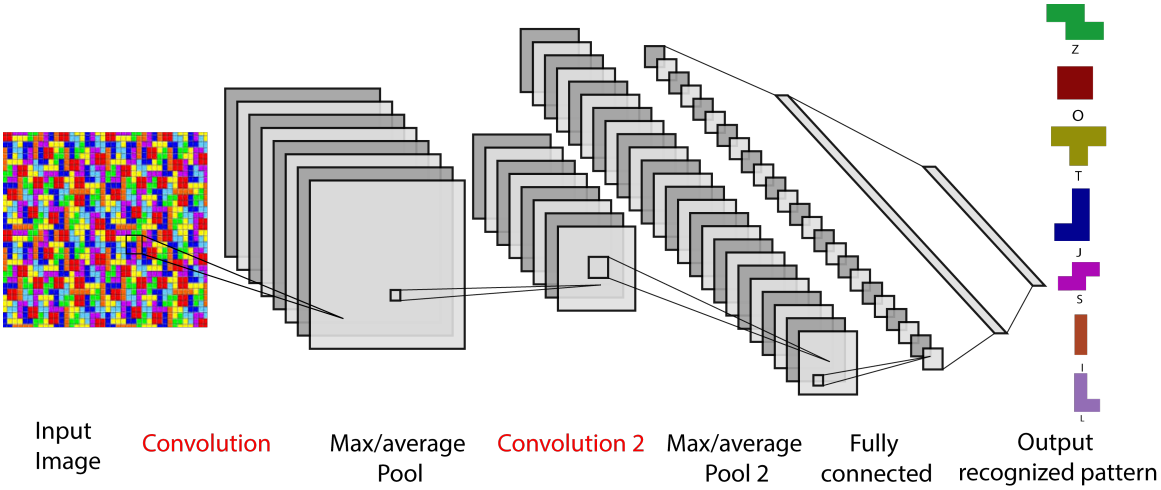


Figure 6.1: Optical hardware acceleration in a typical CNN neural network

6.2 Mechanism

Figure 6.1 shows the schematic of a complex convolutional neural network system. A convolutional neural network is a class of artificial neural network. A convolutional neural network system normally consists of a input layer, one or multiple convolution layers, pooling layers and one fully-connected layer. The convolution layers carry out linear convolutions and then generate a feature map. A nonlinear operation such as ReLU is after convolution operations and then the results contribute to the next pooling layer. In this particular figure, both convolution layers can be carried out by a photonic PCM computing matrix which is highlighted in red. The photonic integration to this system will improve the computing speed by making good use of parallel processing of optical matrix and reduce the energy consumption by introducing phase change materials. The other layers are computed through software.

$$\begin{bmatrix} Y_1 \\ Y_2 \\ \vdots \\ Y_n \end{bmatrix} = \begin{bmatrix} G_{11} & G_{12} & \cdots & G_{1n} \\ G_{21} & G_{22} & \cdots & G_{2n} \\ \vdots & \vdots & \ddots & \vdots \\ G_{n1} & G_{n2} & \cdots & G_{nn} \end{bmatrix} \times \begin{bmatrix} X_1 \\ X_2 \\ \vdots \\ X_n \end{bmatrix} \tag{6.1}$$

For matrix multiplication, the convolution kernel weight settings are encoded in a phase change photonic matrix (G_{11} - G_{nn} in Equation 6.1). The input signal is pre-processed and flattened into vectors (X_1-X_n in Equation 6.1) and then imported into the optical matrix. In this import process, the input signal in the form of vectors is multiplied by the convolution kernel, which is a column of a matrix. The

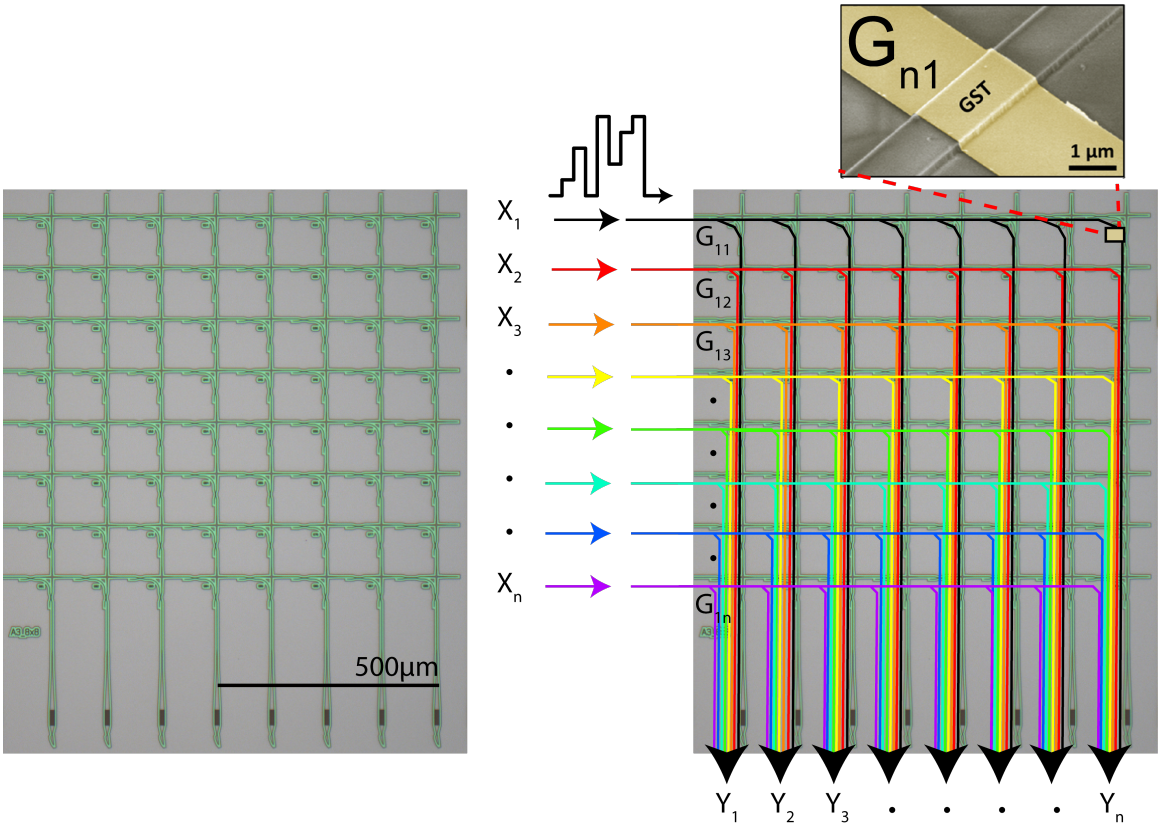


Figure 6.2: Optical image of an 8×8 photonic phase change matrix. In this figure, phase change material devices are deposited on each block of the matrix shown in the inserted figure, working as the weight $G_{11} - G_{nn}$. Different input signals $X_1 - X_n$ can be input into different branches with the amplitude encoded with information. The output signal $Y_1 - Y_n$ is the matrix multiplication results as shown in Equation 6.1.

output signal is the multiplied result of the convolution computation process (Y_1-Y_n in Equation 6.1). This concept has been described in a previous publication using a 1 × 2 matrix [201] on a silicon nitride platform. Here, the author scales up the computation capability to an 8 × 8 phase change matrix on a silicon platform (Optical image of matrix in Figure 6.2) to give a proof-of-concept. The optical image in Figure 6.2 explains it clearly. Different input signals with different wavelengths are encoded in advance with different information. These input signals then go through different row waveguides, identical powers are split into each column, they are added together in the same column, and finally recorded in the output to complete the vector-vector multiplication process. All the columns together make up the matrix multiplication. The number of columns decides the number of vector-vector multiplications that can be carried out simultaneously.

The phase state of the phase change material (PCM) functions as the weight of the convolution layer in the network. The fully crystalline state (low transmission) represents a state "-1" and the fully amorphous state (high transmission) represents state "1". The mixture of amorphous and crystalline states represent values between "-1" and "1". They are multiplied by the input power, which is normalized to [0,1] as the other multiplication factor and modulated by variable optical attenuators. Consequently, the output signal is normalized to the range of [-1,1].

6.3 Development of the matrix structure

Considering a bigger matrix such as a 3 × 3 matrix, it is hard to manage the fabrication of the whole structure. It can require up to a scale of several millimeters with reliable repeatability of identical devices. In this thesis, the author turned to foundries for help with fabrication. In a foundry-aided fabrication process, the author optimized different functional components used in the optical matrix before submitting the final design to a foundry.

Figure 6.3 shows the design of a foundry-aided matrix chip: Block (a) is individual calibration blocks for different directional couplers which use MZI to work as a calibration tool, (b) is the simple calibration for MZIs themselves, (c) is calibration for loss of crossings, (d) is calibration devices for phase shifters, (e) is calibration for on-chip multiplexers, and (f) is experimental matrix devices with matrices ranging in size from 3 × 3 to 8 × 8. The following sections list the optimization process and final performance of critical components, and (g) is a directional coupler calibration with Y splitters.

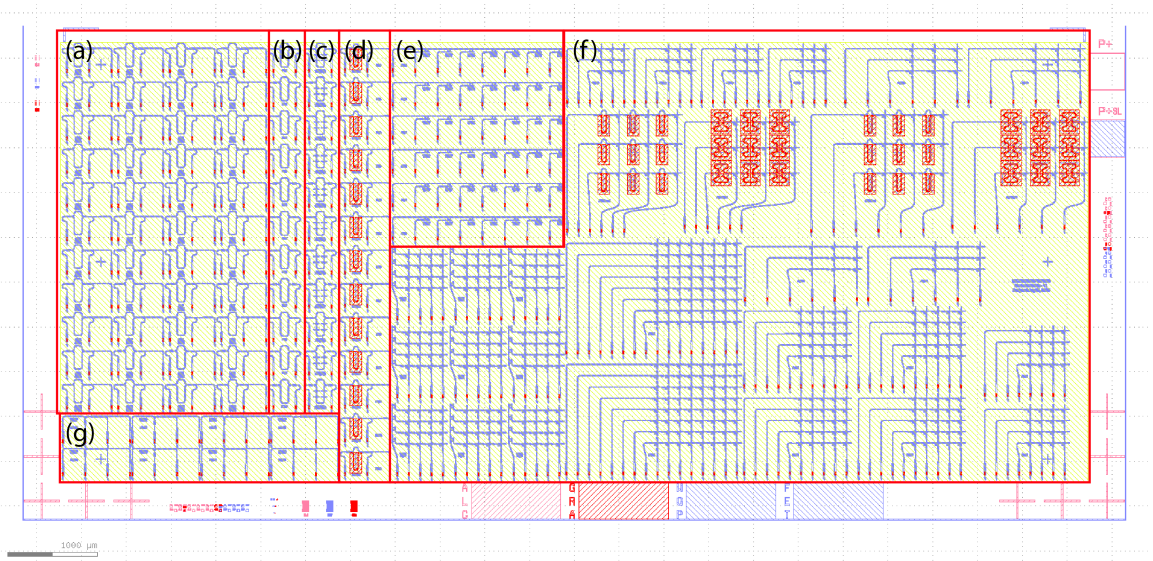


Figure 6.3: Outlook of foundry-aided matrix chip. Different blocks have different functions.

6.3.1 Single components: design, optimization, and test

The unique characteristic of photonic matrix multiplication with phase change materials is that the calculation can be completed simply with light flow. This works by sending light through this PCM photonic matrix, which results in the calculation of the output power. The matrix is composed of several components including PCM devices ($Ge_2Sb_2Te_5$ or GST here) (Figure 6.4(a)), directional couplers (Figure 6.4(b)), and crossings (Figure 6.4(d)). In the matrix design that is used for demonstration in this thesis, thermal phase shifters (Figure 6.4(e)) are used for easier modulation of single components. The design of crossings is optimized to reduce the propagation loss when different waveguides inevitably meet each other. The coupling efficiency of the directional couplers is designed to have equal splitting power for different rows. The phase shifters are used to tune the splitting ratio of different horizontal branches to set a certain device's weight without affecting other components and to adjust for the splitting ratio offset due to fabrication offsets. The PCM cells will record the weights of neural network kernels or set the other vector values in a multiplication process.

Directional couplers

Light can only travel in a straight line, so directional couplers and bent waveguides are used to couple light from the bus input channel to each computing block,

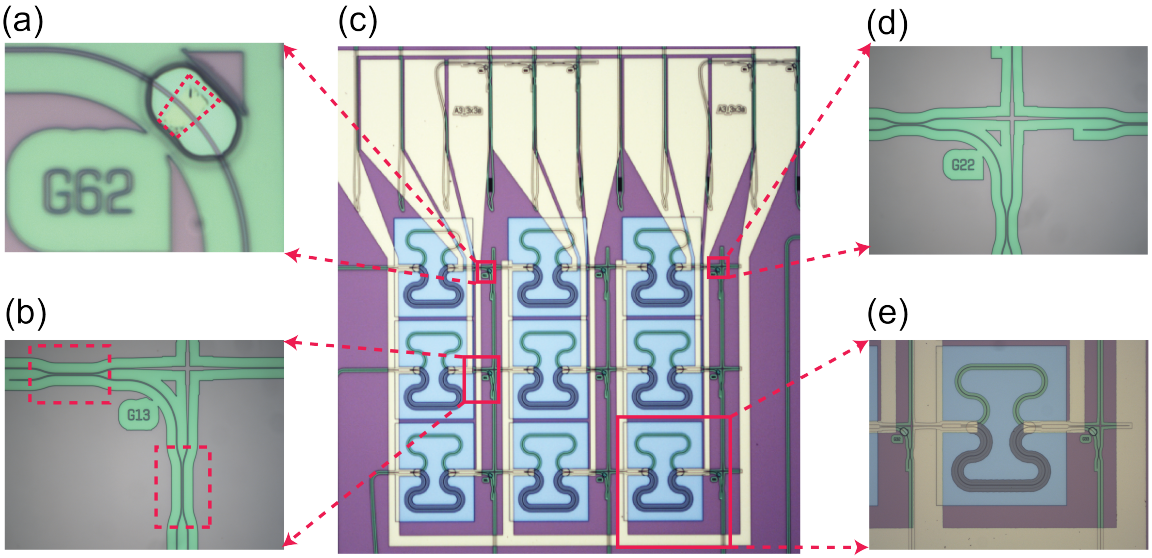


Figure 6.4: An image of a phase change photonic matrix and enlarged images of critical single components in the matrix. (a) 10 nm thin film of phase change material (GST here) on top of the waveguide. (b) Directional couplers that couple light from the bus row waveguides to single block and from block back to the bus column waveguides. (c) The outlook of the whole phase change photonic matrix. (d) Crossings inside the photonic network, and (e) thermal phase shifter in each block for adjusting the splitting ratio for different blocks.

direct them through PCM computing components, and then couple back to the bus output channels. In a photonic matrix, the input light signal is supposed to be equally split between each computing node despite the light from branches going through different numbers of directional couplers and crossings. The matrix is designed to be an arrayed structure with input and output arranged in different directions to manage the density. For this reason, directional couplers with different splitting ratios are calibrated as individual components and before being applied to the matrix. Directional couplers in a matrix include two different types of couplers: 1) input directional couplers before a PCM block that split power into the device section; and 2) output directional couplers after a PCM block multiplication that carry the accumulation out to the bus waveguides. The propagation loss, the coupling loss of directional couplers and the crossing loss all affect the propagating light intensity. If all of these factors are ignored, the ideal splitting ratio calculation format can be simply expressed as following:

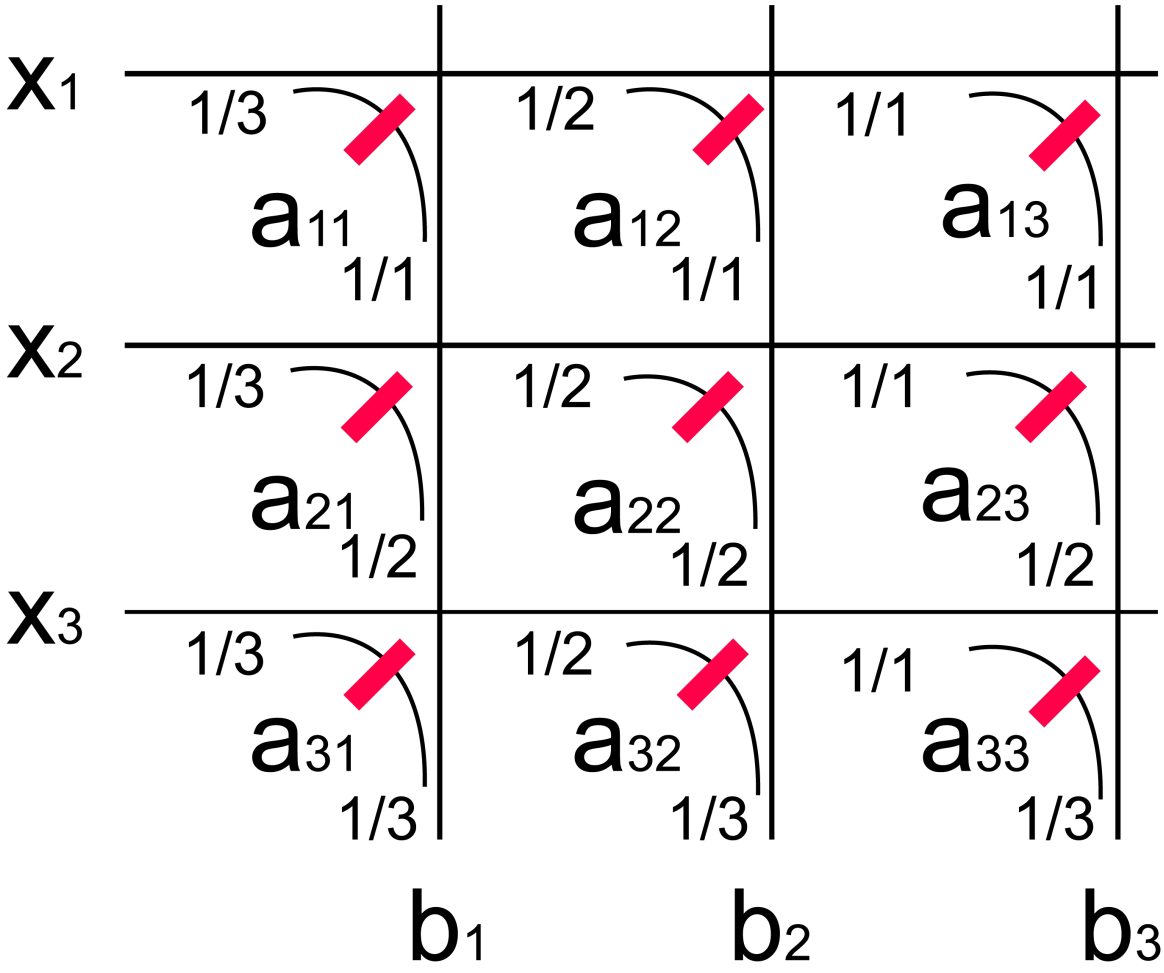


Figure 6.5: Schematic of calculated splitting ratio of directional coupler according to Equation 6.2

$$Ratio_{ideal} = \begin{cases} \dfrac{1}{n+1-j}, & DC_{input}, \\ \dfrac{1}{j}, & DC_{output}. \end{cases} \tag{6.2}$$

As a result, the splitting ratios of specific directional couplers for a 3×3 matrix are shown in Figure 6.5. However, considering the imperfection of the fabrication process, the loss of the silicon-on-insulator(SOI) waveguides and crossings are non-negligible and needs to be considered in the matrix.

Figure 6.6 shows the calibration devices of directional couplers. According to the coupling mode theory, the coupling ratio of a directional coupler is related to both the coupling gap and the coupling length. For a 500 nm partially etched silicon waveguide that is experiencing an increase of coupling length, the coupling ratio

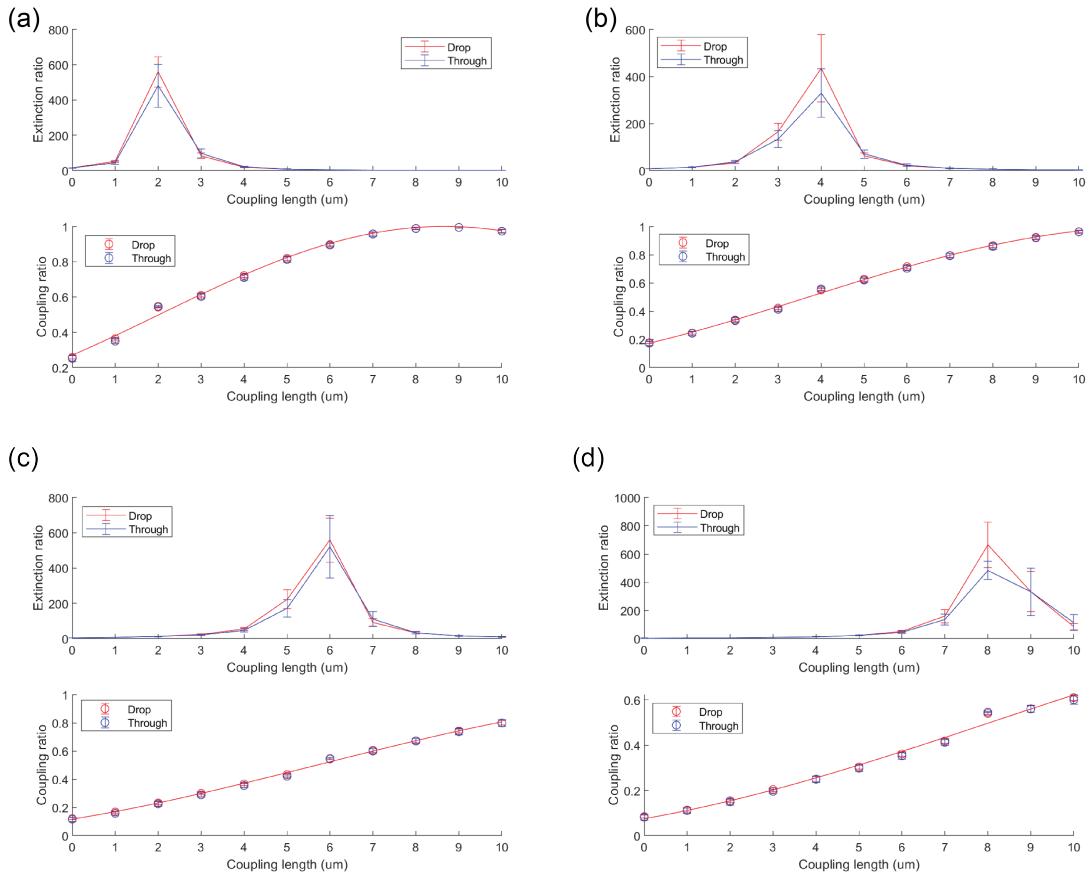


Figure 6.6: Calibration of directional coupler coupling ratio. Directional couplers with different coupling gap: 300 nm (a), 350 nm (b), 400 nm (c), 450 nm (d) with coupling length variation from 1 μm to 10 μm is fabricated and measured. The extiction ratio, coupling ratio and fitting coupling ratio curve are shown in this figure.

follows the following fitting equation:

$$Transmission = \sin^2(\frac{\pi \cdot x \cdot a}{1.55} + b) \tag{6.3}$$

The gap of the coupler is varied with 300 nm, 350 nm, 400 nm, and 450 nm, respectively in Figure 6.6 (a), (b), (c), and (d) with the coupling length changing from 1 μm to 10 μm. Good agreement between the fitted curve and the experimental data guarantees the accuracy of the specific coupling ratio needed in the matrix. An example of this is the splitting ratio in Figure 6.5. The final gap width was confirmed to be 300 nm.

Crossings

Crossings are an essential components to the network. The optimization of crossings is meant to reduce transmission loss. The author confirmed the final design after carrying out several FDTD simulations. Figure 6.7 shows the experimental data for optimization. The initial design of the crossings is shown in Figure 6.7 (b), where the center of the crossing is made up of two MMI structures. An experimental crossings calibration was carried out with MZI calibration structure shown in Figure 6.7 (a). After varying the length of MMI, the extinction ratio and transmission percentage per crossing bar was then measured in Figure 6.7 (c) and (d) separately. Thus, the optimized crossing bar structure was confirmed and applied to the larger matrix.

Thermal phase shifters

Another important component of the matrix is thermal phase shifters. Switching a single device inside a matrix is hard to achieve, especially those devices that are far from the input. MZI-structured metal phase shifters were used in this experiment to tune the splitting ratio. 200 nm thick Nichrome was used for the metal heater layer. 1 μm of SiO_2 was used as the isolation layer between the metal alloy and the waveguide layer. Figure 6.4 (e) shows the optical image of thermal phase shifters on each block device. The phase shifters are used to tune the splitting ratio of different horizontal bus channels. They are also used to concentrate optical power on a certain device by thermally changing the phase of one arm of MZI. This is done to switch a specific device back and forth without affecting the other devices during the process of setting network weights. The phase shifter has two output paths, one leads to the GST within that device block, and the other leads to the next device block. When one device is switched or the weights of the network are changed, it will concentrate power on a certain GST device to change the states accordingly

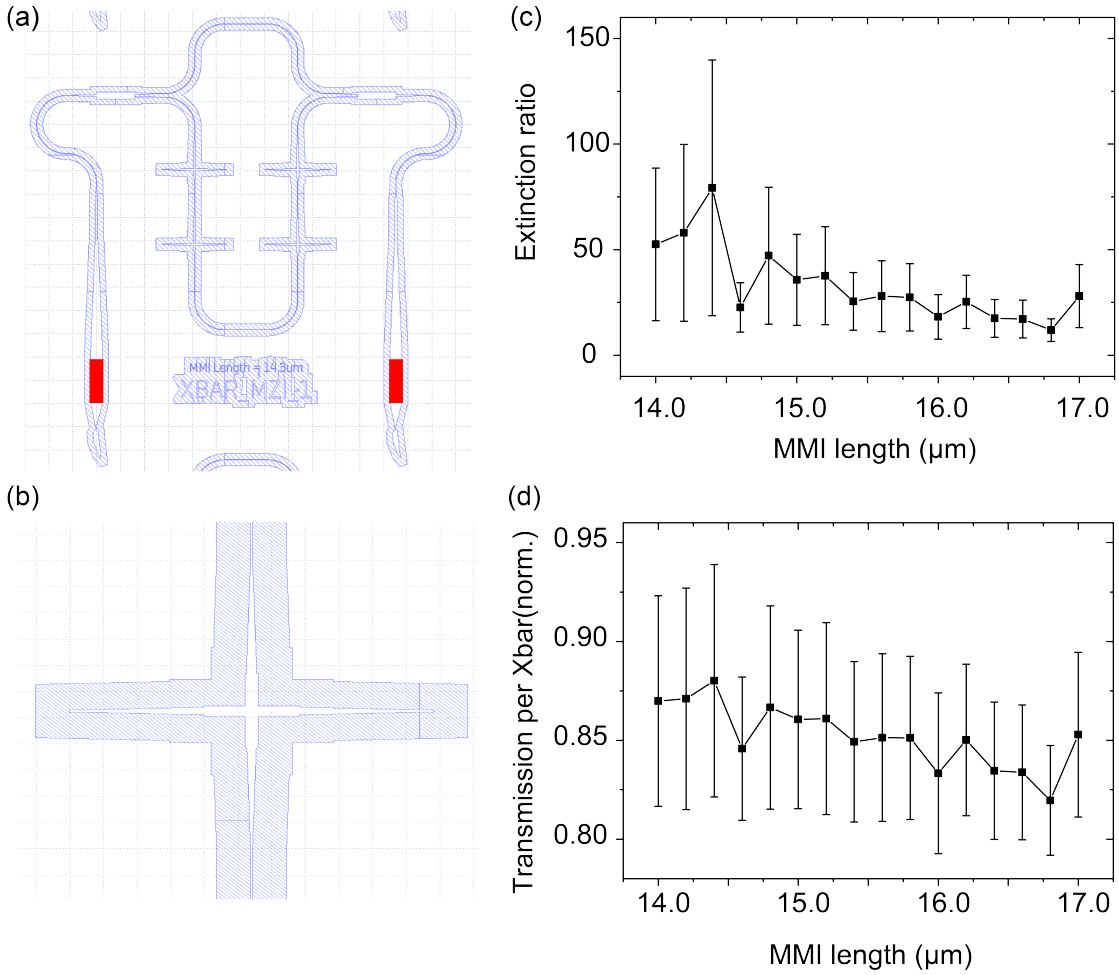


Figure 6.7: Calibration and optimization of the crossing bar structure. (a) Calibration devices used in the optimization process. One calibration device is composed of one MZI with four identical crossing bars on one arm of it. (b) A enlarged plot of one crossing bar. (c) Measurement result of extinction ratio of different crossings with variation of MMI length. (d) Measurement results of transmission per crossing bar of different crossings with the variation of MMI lengths.

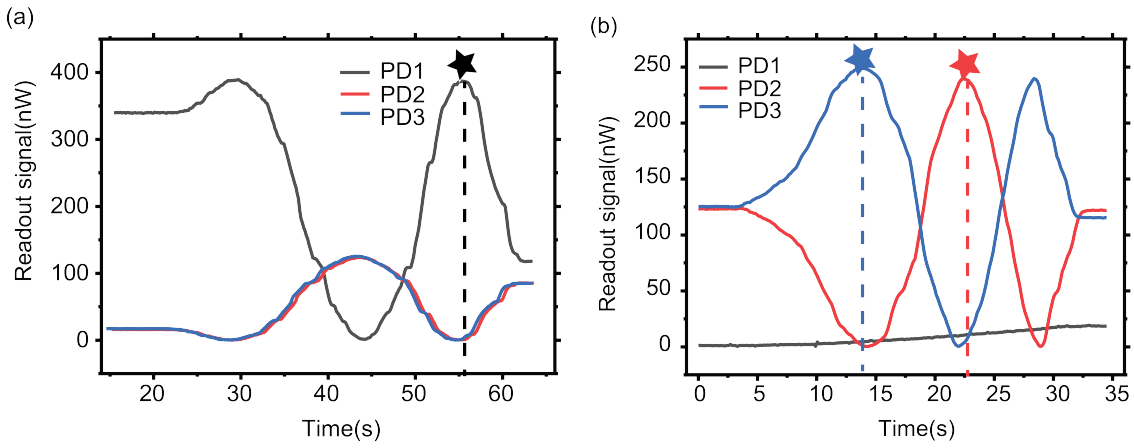


Figure 6.8: Performance of phase shifters of Row 1, Colomn 1,2 and 3 in the matrix. (a) Power concentrates on device of Row 1 Column 1 (black star point). (b) Power concentrates on device of Row 1 Column 2 (red star point) and Row 1 Column 3 (blue star point).

without leaking power to other devices. Instead of using a directional coupler to give a fixed splitting ratio, a balanced MZI along with a directional coupler structure is used before bus waveguide channels and branch waveguide channels. This leads to an active adjustable splitting ratio. Phase shifters adjust the light splitting ratio in one row. The dynamic adjustment range of phase shifters is shown in Figure 6.8. This figure specifically uses the experimental performance of phase shifters in Row 1, Column 1,2 and 3 when the voltage is applied to these phase shifter sweeps. When the power is concentrated in the phase shifter of Row 1 Column 1 (black line in Figure 6.8 (a) at a specific voltage sweeping point, the input power can be concentrated on a Column 1 device while the power of Column 2, and 3 is near zero. (represented as star point in Figure 6.8 (a)). Similarly, at the red star point in Figure 6.8 (b), the input power is concentrated in a Column 2 device. At the blue star point in Figure 6.8 (b), input power is concentrated on a Column 3 device. In this way, the input power can be concentrated on individual devices and switch them most efficiently without affecting other devices.

High amplitude power over a short time frame is sent to a device to amorphize GST and double-step pulse [31] is sent to crystalline GST. When it is carrying out the photonic computation, the phase shifter array is adjusted to equally split the energy. The specific 3×3 matrix in Figure 6.8 (c), which is used to carry out all the experiments in this work, has 3 inputs and 3 outputs, 9 phase shifters, 9 crossings, 18 directional couplers and 9 GST computing devices.

This figure shows that an extinction ratio of over 20 dB extinction ratio is achieved with a heater that has a voltage smaller than 10 V. When the setting weights process is carried out, the input power is amplified and then concentrated on individual devices one by one. This switches each device to its desirable state. When the computation process is carried out, all the splitting ratios are set to an equal splitting ratio. The author used two ways to set the voltage of phase shifters. They can be manually set for quick adjustments, or they can be automatically set by using the fitting curve of MZI interference changes.

6.3.2 Weights definition from (-1,1) to the real transmission

As mentioned in previous chapters, tests have been performed to compare how different lengths, switching powers, and platforms affect the transmission contrast of waveguides coated by GST (shown in Figure 5.11). These tests explored the performances of 2 μm and 4 μm long GST devices on both SiN and SOI platforms with pulse widths from 20 to 100 ns switching pulses. The results shows that optical contrast while switching between amorphous and crystalline states is near-linear along with the power increase and an increase in the device size. Doubling the length of GST gives approximately double the contrast. Furthermore, the contrast of GST on an SOI platform is approximate a quarter compared to its performance on a SiN platform.

The contrast needed in the matrix should be big enough to improve the signal-to-noise ratio. This in turn will improve the overall accuracy of the matrix. However, as it is shown in Figure 5.11, considering the loss of GST in both amorphous and crystalline states (demonstrated in [184]), it is preferable to use small GST patches to reduce the loss of the matrix and thus have a larger matrix size. Considering the factors of overall matrix performance, computational accuracy, and energy expenditure, 4 μm x 5 μm x 10 nm GST was chosen as the PCM volume in the matrix. Thanks to the usage of phase shifters, the switching contrast performance of one device inside the matrix is similar to what has been tested in individual single devices. Figure 6.4 (a) shows an enlarged single computing unit which has an active phase change material (PCM) device, occupying an area of 4 μm $\times$ 5 μm on the waveguides.

6.3.3 Experimental setup

Figure 3.12 shows the experimental setup. There are two light paths: a pump path for setting the weights of the matrix which is shown in red and a probe path for

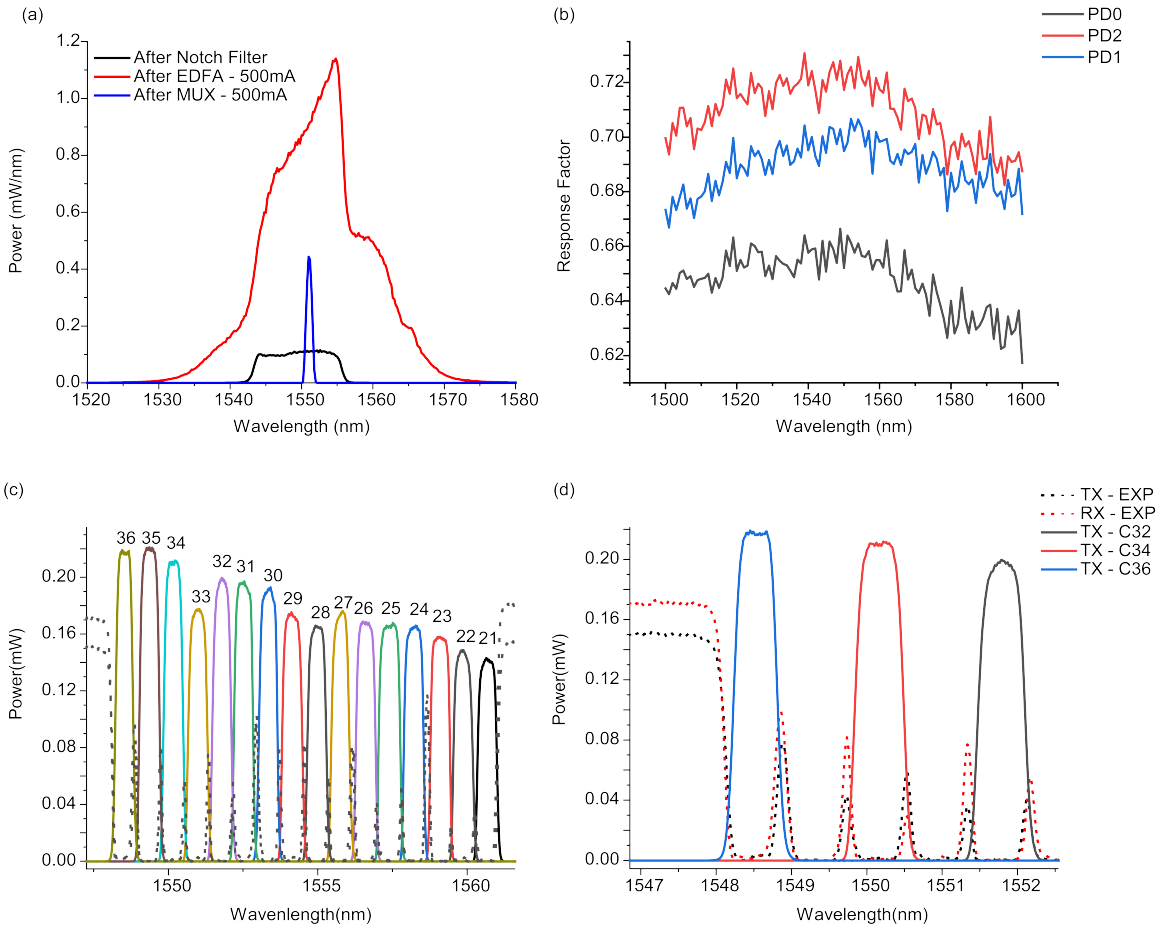


Figure 6.9: Different components in the matrix experimental setup calibration before the real experiments. (a) The output of supercontinuum laser after notch filter (black), EDFA (red) and mux (blue). (b) Response of different photodetectors. (c) Response of different outputs of the multiplexer. (d) The response of specific multiplexer channels used in the matrix experiments.

carrying out the matrix multiplication which is shown in dark blue. For the pump path, a tunable laser in the telecom wavelength band was used to selectively set the weights of devices in different rows. The amplitude and the width of optical pulses are modulated by EOM and amplified by EDFA before sending to devices that set the weights of GST. Commercial multiplexers and demultiplexers were used in this experiment. The wavelength bandwidth was 2 nm per channel as shown in Figure 6.9.

Several parts needed to be calibrated before the real experiments were carried out. Figure 6.9 shows the calibrated results of equipment before conducting the real experiments. Figure 6.9 (a) is the figure of the calibration results from the supercontinuum laser source. To split a channel of light source from a wideband

light source, a notch filter is first used. This filters out a small wavelength range of light power of around 1550 nm which is shown as a black line in the plot. After going through the filter, EDFA is used to amplify this range of light. The center wavelength of EDFA is also 1550 nm. This limited wavelength range improves the efficiency of EDFA amplification. Subsequently, the multiplexer filters this narrower range of light source, which is then ready to be input into the photonic matrix. It can be seen in the plot that the power of the light source before the photonic matrix is around 0.4 mW/nm, which is the probe power used in the experiment. The pump power is amplified further by the EDFA.

Figure 6.9 (b) shows the calibration of different photodetectors. Different photodetectors differ slightly in the response of light sources throughout and entire wavelength range. This can be seen in the read-out of the test. In the experiments, the relevant response factors are set up separately based on different photodetectors.

The wavelength is set to 1548 nm (C36), 1550 nm (C34) or 1552 nm (C32) based on the device in each row (shown in Figure 6.9 (d)). For the probe path, the computing wavelength is set to commercial DWDM channels. After passing through a bandpass filter and off-chip multiplexer (MUX), light at certain wavelengths were filtered to specific rows in the photonic matrix to carry out calculations in the different rows. In the figure below, C36 refers to the top row, C34 to the second row and C32 to the bottom row. Figure 6.9 (c) is the multiplexer output of all of its channels. Figure 6.9 (d) is the output of channels used in these experiments.

Before the multiplication processed by the PCM on the top of the waveguides, different input information is encoded using electrically controlled variable optical attenuators (VOA). Next, the matrix multiplication process is conducted by coupling light through the directional coupler which is then modulated by GST on the top of the waveguides. After that, the light is coupled into the vertical output by another directional coupler. Afterwards, off-chip demultiplexers and photodetectors pick certain wavelengths to obtain the calculation read-out. The output signals are then captured by photodetectors as the hardware calculation results. Thermal phase shifters are controlled by an electrical signal modulated by Arduino software.

6.4 Demonstration of the Application

6.4.1 Demonstrating 1: Calculation of the 3D rotation matrix

To show the reconfigurable capability of a photonic matrix, the 3 × 3 matrix is set to three different kinds of rotation matrices that rotate a cube with different colors on different surfaces (Figure 6.10). 3D modeling is widely useful in many applications such as face recognition security systems, VR computer game construction and mimicking rebuilding of the physical world. It is hard and high energy-consuming work which is mostly achieved by GPU or FPGA hardware acceleration technology [78, 254].

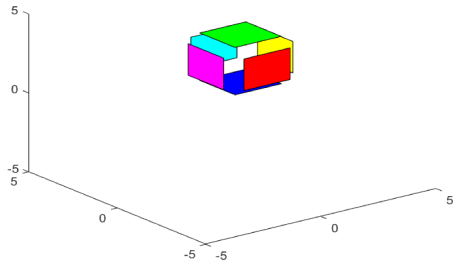
However, this work will demonstrate how a photonic matrix can make it easy to achieve arbitrary angle rotation at ultra-fast speeds. The rotation of a 3D image here is realised by rotating the three dimensional vertices of the object and then connecting the rotated vertices together to get the rotated image. In principle, a three dimensional object can be rotated in any direction with any angle multiplied by a predefined 3 × 3 rotation matrix. The author uses 3 rotation matrices to rotate a unit cube 90 degree along the x, y, and z axes. The corresponding rotation matrix is shown in Table 6.1.

Table 6.1: table

$\begin{bmatrix} 1 & 0 & 0 \\ 0 & 0 & -1 \\ 0 & 1 & 0 \end{bmatrix}$	$\begin{bmatrix} 0 & 0 & 1 \\ 0 & 1 & 0 \\ -1 & 0 & 0 \end{bmatrix}$	$\begin{bmatrix} 0 & -1 & 0 \\ 1 & 0 & 0 \\ 0 & 0 & 1 \end{bmatrix}$
90° x axis rotation matrix	90° y axis rotation matrix	90° z axis rotation matrix

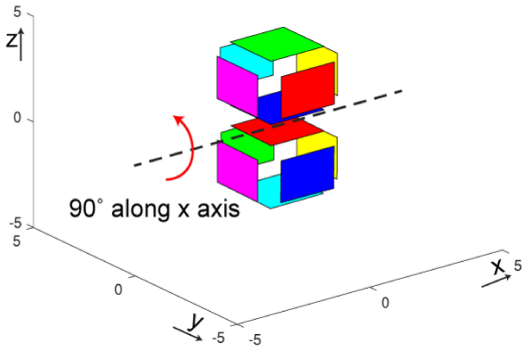
Figure 6.10 shows how the author uses the photonic matrix to realize the rotation of a three-dimensional cube. The value of the rotation matrix is set to the photonic matrix. Figure 6.10(a)-(d) shows a completed process of rotating a three-dimensional cube. Each step illustrates the state of the photonic matrix and the rotation results. The input signals are the x,y,z coordinates of the vertices of the 3D image. The state of phase change material is defined as before. The fully crystalline state is -1, the fully amorphous state is 1, and the middle state is 0.

Figure 6.10(a) shows that the initial states of all GST units are set to the middle state, or state 0. The corresponding cube image shows the initial position of this cube as well as the initial position of the differently colored surfaces.



(a) Start/initial state

0.0006	-0.0001	-0.0013
-0.001	0.0001	-0.0007
0.0013	0.0014	0.0041

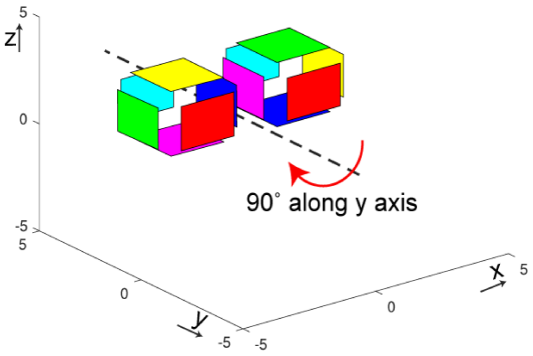


(b) 90° x rotation

1.001	0.001	-0.0013
0.001	0.001	-0.9901
0.0013	1.001	0.001

(c) 90° y rotation

0.0006	0.001	1.0013
0.001	1.0001	-0.0007
-0.9913	0.0014	0.001



(d) 90° z rotation

0.0006	-0.9927	-0.0013
1.001	0.0001	-0.0007
0.0013	0.0014	0.9941

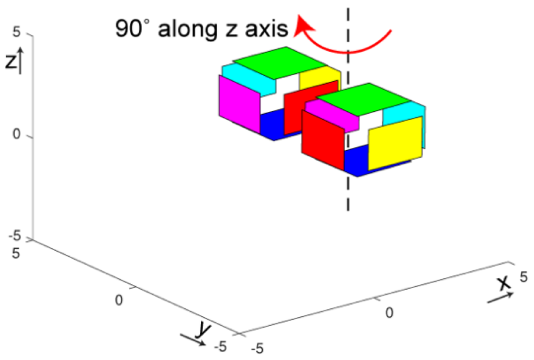


Figure 6.10: Hardware realization of rotation matrix demonstration using rotating a three dimensional cube as an example. (a) The initial photonic matrix state and corresponding cube outlooking in a coordinate system. (b) The state of photonic matrix and corresponding cube outlooking after 90° x axis rotation. (c) The state of photonic matrix and corresponding cube outlooking after 90° y axis rotation. (d) The state of photonic matrix and corresponding cube outlooking after 90° z axis rotation.

To show the reconfiguration capability of photonic matrices, the same matrix is reset to three different combinations of weights (Figure 6.10(b),(c),(d)) to realize the rotation of a 3D object alongside the x, y, and z axes, respectively.

To see all the surfaces of the same cube, surface overlap is avoided by not connecting the surfaces to one another. Tables in each figure show the GST states when the matrix carries out the function of rotating input objects. The original cube is at position (0,0,0) and rotates to (0,0,-5) which is 90° alongside the x axis. Different color surfaces are rotated with the cube accordingly. Similarly, the same cube is rotated 90° alongside the x axis (Figure 6.10(b)), 90° alongside the y axis (Figure 6.10(c)), and 90° alongside z axis (Figure 6.10(d)) using another rotation matrix. In this calculation, all the x,y, and z coordinates of vertices are first normalized to 0-1. This makes them suitable to process through the photonic matrix. Then each individual vertex is sent through the matrix in an (x,y, and z) format and receives the rotated data through the output signal. After that, the anti-normalization procedure recovers the 3D model to its intrinsic size and relocated position. All the rotated cubes are replotted using the rotated datasets. A cube is rather simple since it only contains 6 surfaces with 8 vertices. All the vertices that make up this model were collected and input into the photonic rotation matrix. After recovering data and replotting, the second models are reconstructed as 3D images after rotation. This is a rather simple demonstration of a rotation matrix. Further improvements can be made like using more complex models such as human bodies, developing the architecture, using more precise methods such as locally increasing sampling rate, and adapting averaging methods which can help to get higher resolution results.

6.4.2 Demonstration 2: small pattern recognition

To demonstrate the functionality of phase change photonic matrices, the author demonstrates a simple pattern recognition application using a single layer perceptron network. This network's linear calculation part is carried out by a phase change photonic matrix with a single wavelength in this thesis. Figure 6.11 shows the schematic of the neural network structure used in this application. $x_1 \cdots x_m$ is the input layer, multiplied by the weights matrix and then added together. The result then goes through the activation function layer, or nonlinear layer, and then the output results are received. The linear part highlighted in red is carried out by a 3×3 phase change matrix.

As it is shown in Figure 6.12, the aim of this specific perceptron neural network is to recognize randomly generated 3×3 pixel patterns in Figure 6.12(b) in a 1 kB

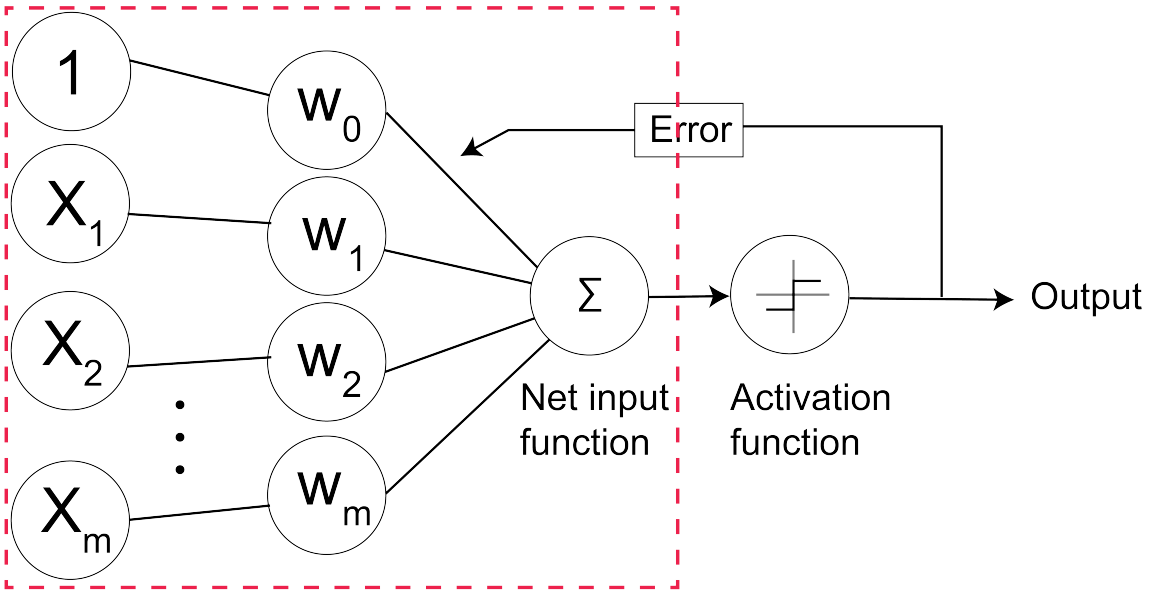


Figure 6.11: Schematic of matrix multiplication application: single layer perceptron neural network. Red highlighted part is carried out by the phase change photonic matrix hardware. Others are calculated by computer.

background plot in Figure 6.9(a). Figure 6.12(a) is a randomly generated 1 kB pixel picture with binary data. Figure 6.12(b) is composed of three targeted patterns which can be recognized from Figure 6.12(a).

The matrix computation process is divided into three steps: weights setting, input signal encoding, and computing and signal sampling. The first step of the weights setting is shown in Figure 6.13. These targeted patterns need to be set beforehand as the weights of the layer in the matrix via PCM states (G_{nn} in Figure 6.13(a)). Here it is assumed that black pixels represent the fully crystalline state "1" and white pixels represent the fully amorphous state "-1". The target patterns are randomly chosen. Figure 6.13(b) shows the targeted patterns and corresponding digital matrix that will be programmed as weights in the network.

The second step is input signal encoding. There must be VOA in each channel before inputting signals into the matrix, as shown in Figure 6.14. With a fixed input power, VOA is used to modulate the signal from 0 to 1 times input power, representing different input signals. To simplify the experiments, the input signal only has 0 and 1 for the binary data.

In the third and final step, the 3 × 3 photonic matrix then works as a matching window to go through the whole background image. The input image information is encoded as input data by modulating VOA attenuation ratios. The image is then sent

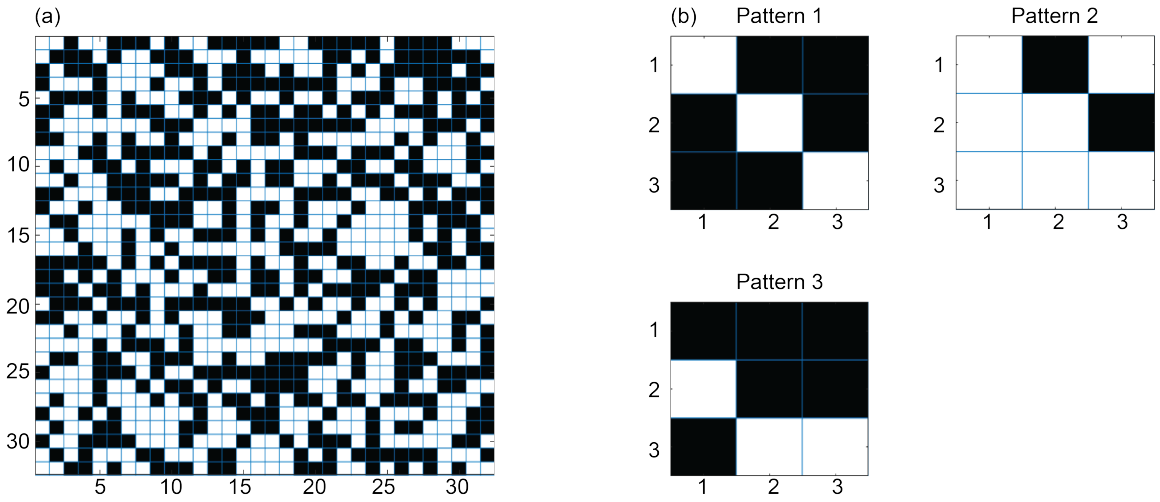


Figure 6.12: Input background signal (a) and targeted patterns that need to be recognized from the background (b).

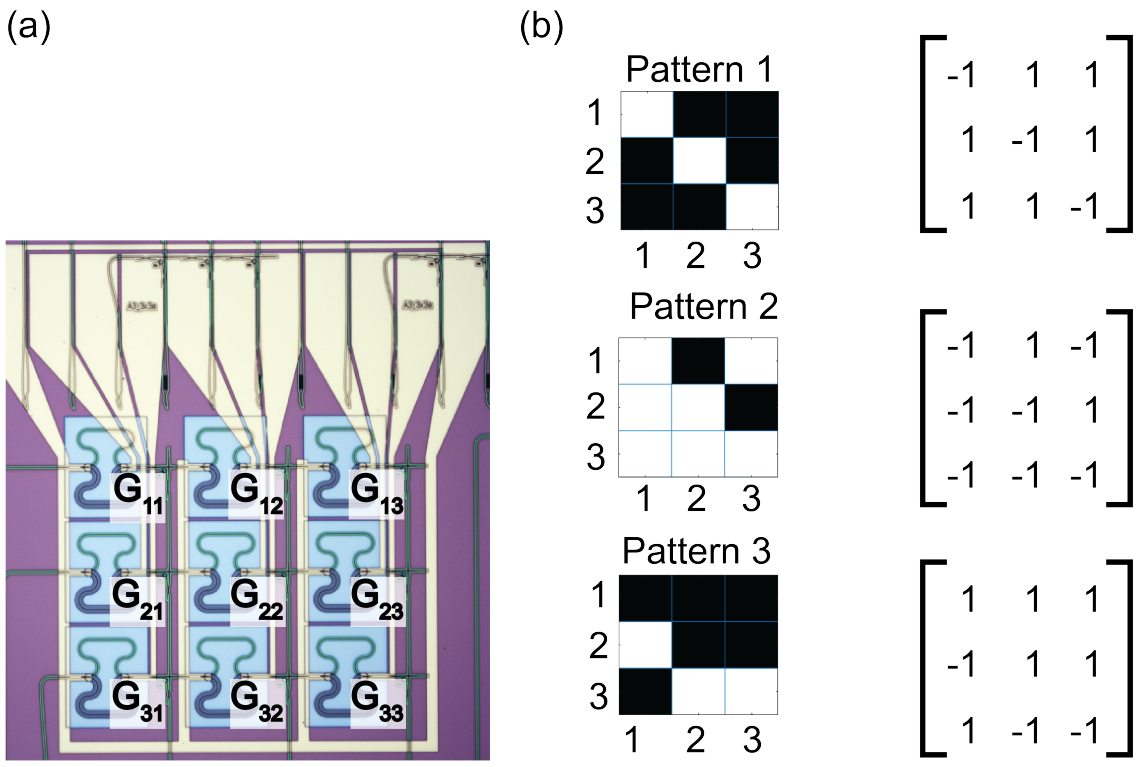


Figure 6.13: Step 1: weights setting step. (a) 3 × 3 phase change matrix used to carry out matrix computation in this application. (b) Randomly generated targeted patterns and corresponding digital matrix that will be programmed as weights.

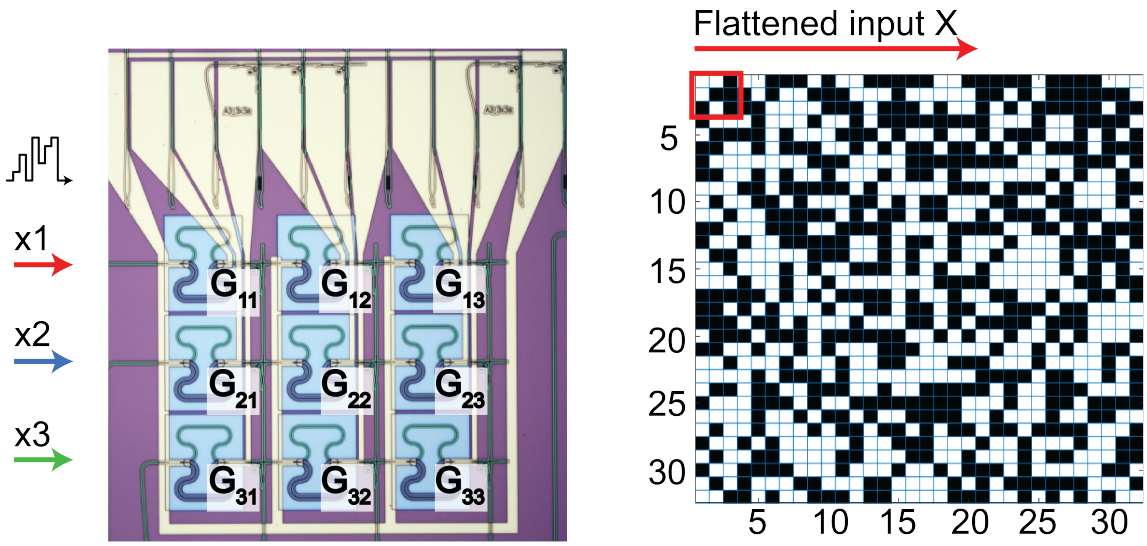


Figure 6.14: Step 2: Input signal encoding step. The input signals are divided into 3×3 blocks and flattened to 1×9 vectors before sending to the matrix. And then the moving window goes through the whole matrix so that all the background pixels are encoded and input to the matrix.

through the matrix. A moving window is used to encode data in a 3×3 manner. It is then flattened into a 1×9 vector before being input into the matrix. As the matching matrix moves, the entirety of the background information is input into the matrix for the calculation. The calculation results can be read out by the photodetectors at the output of each grating coupler channel.

Figure 6.15 shows the comparison of hardware computation results in yellow and software computation results in blue plotted on the same graph. These results match the target pattern 1,2, and 3 which have different matching window positions inside the background plot. The brightest part in a heat map is the part that represents the most matching patterns, or where the pattern is recognized. Positions in the background are shown in Figure 6.15 (d) with red square highlighting. It can be seen from Figure 6.15 (b) that the experimental results agree with the simulation results. Those positions include all targeted patterns in the background plots. Figure 6.15 (c) is a heat map showing experimental convolution calculation results of these three target patterns in the input image. The brightest part in the heat map is the highest calculation value where the pattern is recognized. This is highlighted by red squares in Figure 6.15 (d). These results agree with the position of the target patterns. All of these results are demonstrated with single wavelength, but wavelength multiplexing, as shown in Figure 6.16, can be carried out to improve the computing efficiency, with

the help of multiplexers and filters. With three channels sharing the same waveguide channel, the computing density can be improved by three times.

6.5 Future optimization

To explore the scaling potential of the optical phase change matrix, the author investigated the limitations of matrix size based on two optimized designs shown in Figure 6.17. Figure 6.17 (a) and (b) show two different designs of unit cells in the large-scale matrix multiplication system. The unit cell in Figure 6.17(a) consists of two directional couplers and one waveguide crossing. Power split power from a single input channel to a single output channel gradually decreases below the noise level. At the same time, the dimensions of the matrix increase with unavoidable accumulated losses from crossings and couplers. The coupling coefficients of waveguide couplers in each row and column are calculated by:

$$\kappa_i = \kappa_{i+1} \times \frac{\eta_x}{1 + \kappa_{i+1} \times \eta_x} \tag{6.4}$$

where κ_i and κ_{i+1} are coupling coefficients of couplers in the i_{th} and $(i+1)_{th}$ row and column, respectively. ηx is transmission happening at a waveguide crossing, so as to equally split the power of light from any input port to any output port.

The unit cell in Figure 6.17 consists of one waveguide coupler, one add-drop ring resonator, and one waveguide crossing. The coupling coefficients of waveguide couplers in each row are defined based on the above equation. They equally split the light power before passing through the GST, which is represented as yellow rectangle in Figure 6.17 (a) and (b). A ring resonator drops the split light into the output channel. The 3dB bandwidth ($\Delta\lambda$) of a ring is set as 0.1 nm, and the free spectral range (FSR) of the ring is 20 nm. The wavelength seperation between two adjacent input channels is 20/(N-1) (unit: nm), where N is the dimension of the matrix system. The transmission function of a ring follows a Lorenz function:

$$T = 1 - \frac{1}{1 + (\frac{\lambda - \lambda_0}{\frac{\delta\lambda}{2}})^2} \tag{6.5}$$

where λ_0 is the resonant wavelength. Figure 6.17(c) shows estimates of matrix dimensions versus the power of light being routed without absorption of GST from

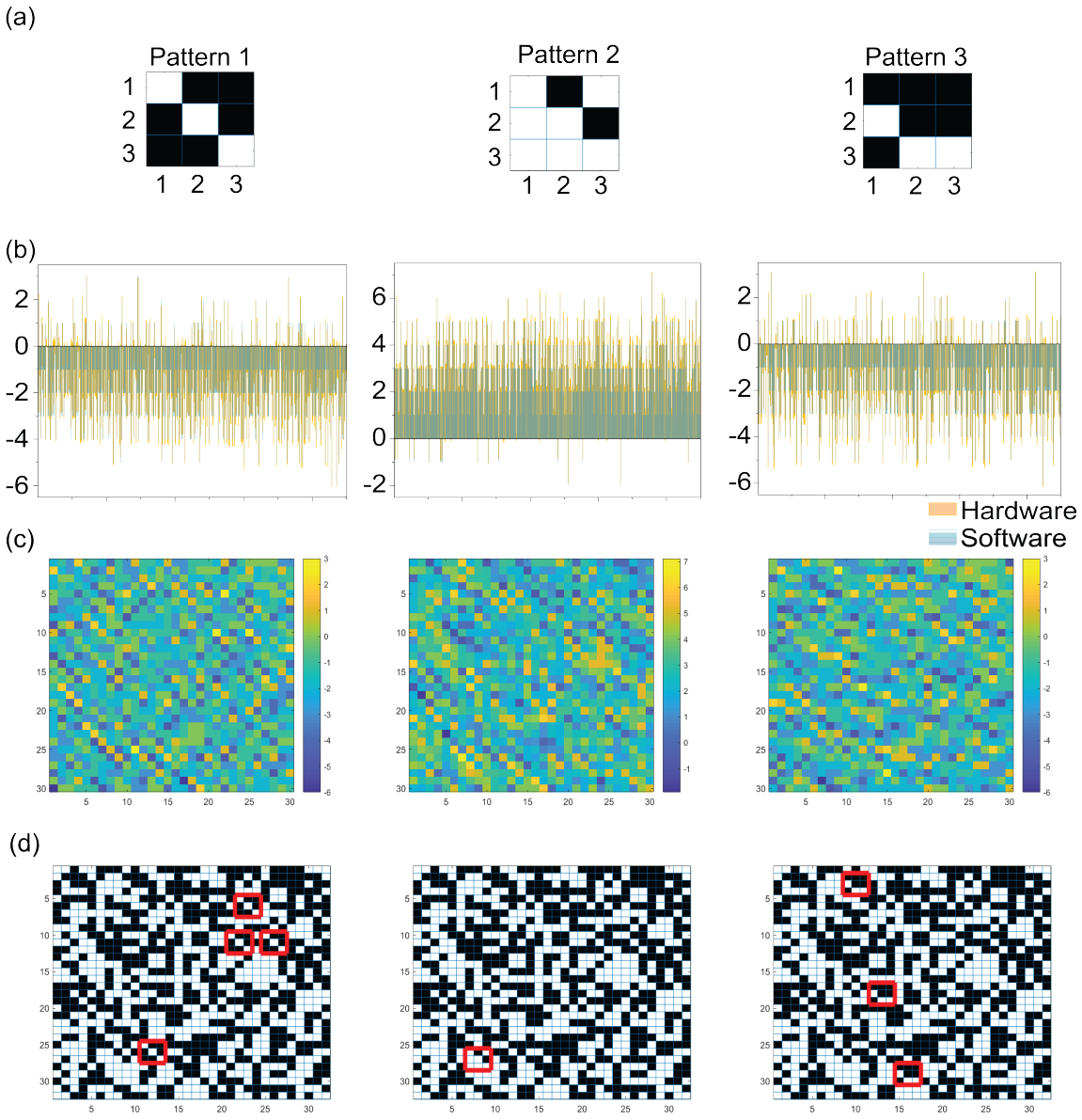


Figure 6.15: Hardware computation results of pattern recognition. (a) Targeted patterns. (b) Hardware computation (in yellow) and software computation results (in blue) comparison of the whole background plot. (c) Heat map of computation results. (d) Original input plot with the red highlighted square of recognized patterns' positions, which agrees with the targeted pattern shapes.

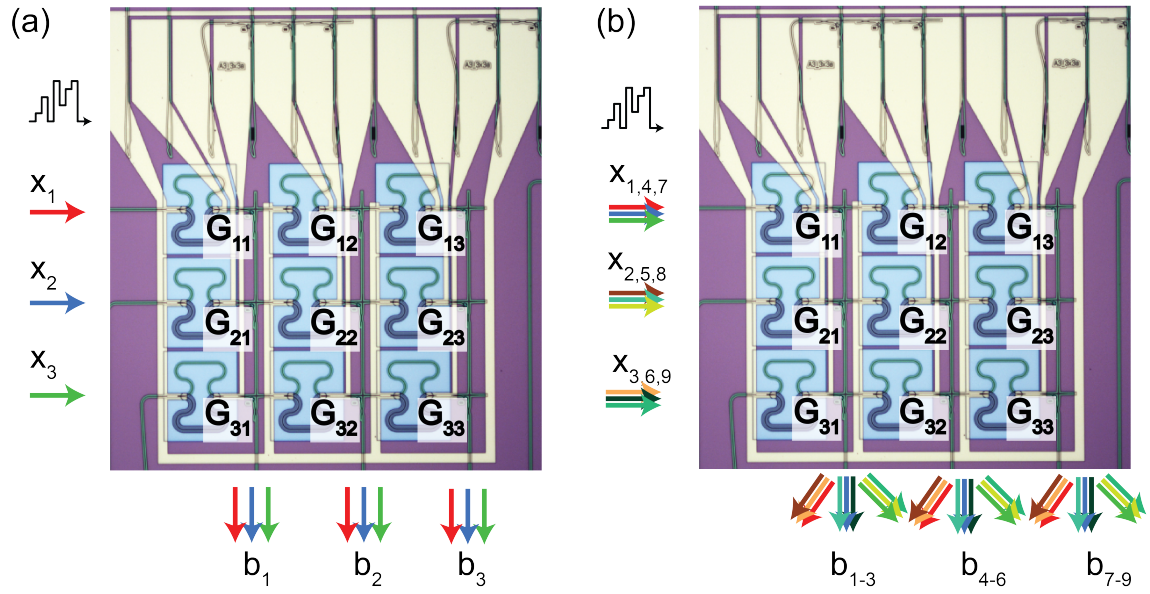


Figure 6.16: Schematic of wavelength multiplexing computation. (a) is the single wavelength computation mode. (b) is the wavelength multiplexing mode. There are 3 parallel computing channels in each input waveguide in this plot.

one input port to another with the power of 0 dBm. Despite the many benefits, photonic devices are limited by their fabrication process. They have an intrinsically larger footprint compared with their electronic counterparts, and there are significant physical limitations of photonic diffraction and reflection in telecom wavelength bands. Weighing the benefits of this efficient computation with its large amount of energy consumed, it is not wise to infinitely extend the size of a photonic matrix. Taking that into consideration, the author simulated these limitations that might post challenges to scaling up a single photonic computing matrix core to larger dimensions. Considering the limited sensitivity of photodetectors at -120 dBm, the estimated dimensions of a matrix could be 450 $\times$ 450 and 494 $\times$ 494 for matrix systems with unit cells as shown in Figure 6.17 (a) and (b), respectively.

6.6 Conclusion

The author demonstrated a phase change photonic matrix core which can carry out matrix vector multiplication on a silicon platform. The author demonstrated its computational functionality by carrying out random pattern recognition and the author explored the dimensional potential of this matrix based on current experimental data. The phase change optical computation core has advantages such as parallel

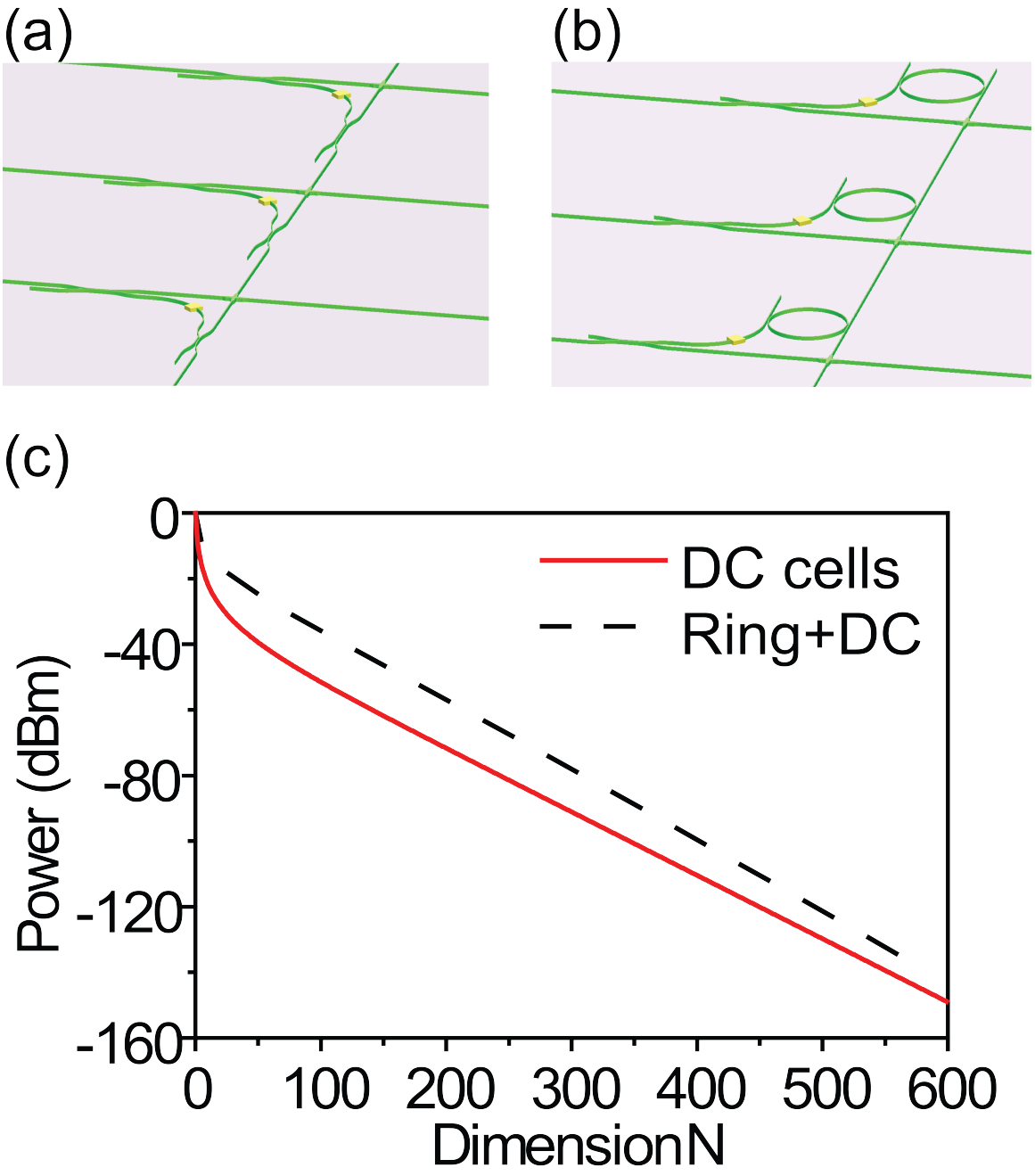


Figure 6.17: Scaling up simulation.(a) Single device block design of directional couplers. (b) Single device block design of one directional coupler and one ring resonator. (c) Simulation of estimated scaling up limit on the condition of current photodetector sensitivity with the above two structures.

computing, low crosstalk, and low energy consumption. In addition, a Si platform enables easy integration of the matrix with on-chip lasers, photodetectors, and other important optical components to build all-optical computation systems. This work serves as a prototype for future practical large-scale optical computing systems for machine learning and matrix multiplication applications.

Chapter 7

Conclusion and Outlook

In this thesis, the author first optimized the phase-change single device on modulation methods and explained the mechanism behind the switching methods. Up to 34 levels of storage information states have been tested with an excellent standard deviation of individual levels. An arbitrary method of addressing levels method has been discovered, optimized, and analyzed to better control these functional cells. The new controlling method is more energy- and time-efficient than previous methods.

Afterwards, a comparison between different platforms is carried out in different areas, including switching contrast, energy cost and switching speed. Devices on SiN and SOI platforms have been fabricated and compared through material optical properties and devices, modelling results and experimental measurements. The SiN platform has a more energy-efficient and broader wavelength range, while devices on the SOI platform have quicker speed, smaller size, and are more compatible with other optical components in an optical processing system. Different platforms should be used according to different applications.

After optimizing both single-device performances and choosing the most suitable platform, the author turned to the realization of big matrices. Before the final matrix experiments, many calibrations and pretests for matrices were carried out, including optimizing optical connections, phase modulations, and directional couplers for adjusting the splitting ratio of bus waveguides and branch waveguides. Two application demonstrations were carried out to test the performance of this matrix, including the rotation matrix for pure matrix multiplication applications and working as the linear part of a single-perception neural network.

However, many future developments can be accomplished.

7.1 New material exploration

The first area that can be explored is the material domain. The phase-change material used in this thesis is $Ge_2Sb_2Te_5$ which is a commonly used phase-change material used for a long time and is easy to control. However, the PCM family is a huge system, and optical properties vary because of different elemental composition. $Ge_2Sb_2Te_5$ is widely used and stable. However, it brings high absorption to optical circuitry, limiting its usage on a bigger matrix scale. In addition, the contrast between amorphous and crystalline states of GST is less significant with SOI waveguide than SiN waveguide, according to research in Chapter 5, which may limit the performance of phase-change photonic computing tool on SOI platform. Switching to a different phase-change material could be able to solve this problem. The first material that can help solve this problem is Sb_2S_3, one kind of phase-change material with moderate optical contrast and near-zero optical absorption. The low loss property makes it easy to carry out optical computation without energy consumption, making this material very promising. Further exploration of this material is valuable for low loss photonic computing systems.

Another phase-change material that is worth trying is $Ag_3In_4Sb_{76}Te_{17}$(AIST). AIST is a material that has bigger contrast than GST, and it is more stable and started to be used as the material for CD-ROM several decades ago. It can win the competition in optical contrast, which helps to increase the accuracy in matrix multiplication. It also has wide applications in the metasurface area, considering the significant contrast in the real part of the refractive index.

Another promising phase-change material is $Ge_2Sb_2Se_4Te_1$. $Ge_2Sb_2Se_4Te_1$ has lower loss than $Ge_2Sb_2Te_5$ and higher contrast of phase shift between an amorphous and crystalline state than Sb_2S_3. Furthermore, it could, in the future, be applied to a mid-infrared wavelength range and metasurface domain.

In addition, a material sweep that varies elemental composition and optical properties could be carried out with different phase-change materials. Consequently, new features or new phase-change materials may be discovered. Similarly, the mechanism

or tendency of optical property changes may be discovered to guide future research into the optical properties of the phase-change material family.

7.2 Higher speed, larger scale and lower cost

Pursuing a computation and storage system aims for higher speed, a larger scale computing size, and lower energy costs. The higher speed modulators should be considered in the matrix multiplication. A balance needs to be considered between the switching contrast and switching speed. The switching contrast delays the recovery or dead time. A bigger matrix scale and the limiting parameters need to be considered. Cascaded ring resonators can add on-chip multiplexers to the computing system, which improves the system's efficiency. Other on-chip elements such as on-chip lasers, on-chip modulators and on-chip photodetectors can improve the speed of the computing system. Therefore, electrical modulation or electrical switching should make use of a broader range of phase-change material family.

7.3 More efficient computing structures for suitable applications

In addition to matrix multiplication, there are other types of architecture used in optical computing and storage. Computing architecture, for example, includes reservoir computing, inverse design computing, holography computing and more. Among the various computing methods, it is difficult to tell which architecture is superior and could lead to a breakthrough of optical computing development, as further developments need to be made. Different computing methods have specific strengths and should be applied where they can be utilized best.

7.4 Challenges to be overcome for larger-scale optical networks

Optical computing neural networks produce numerous benefits, such as increased computing speed, no time response limits, and no electromagnetic interference or

crosstalk. However, some challenges need to be overcome in order to develop optical computing neural networks. Firstly, integrated optical circuits need to be large enough to accommodate optical mode propagation due to the intrinsic physical mechanism. Optical circuits cannot be as small as electrical circuits, which have transistors with several nanometers. Furthermore, the current popular and widely used logic computing system in electronics cannot be directly used in optical analogue systems and requires electrical-optical conversion. The crosstalk with input signals also needs to be suppressed and isolated to get a higher signal-to-noise ratio [153].

Chapter 8

Publications, patents and conferences

8.1 Patents

1. Zhou, W., **Li X.**, Bhaskaran, H "Photonic field-programmable coupler arrays (FPCAs) based on the phase-only Sb2S3-SOI phase-change photonic waveguide platform for photonic routing" (under filing)

2. Rios, C., Youngblood, N., Cheng, Z., **Li X.**, Pernice, W. H. P., Wright, C. D., Bhaskaran, H "Scalable matrix-vector multiplication using phase-change materials on integrated photonic circuits"(Filed: Nov 2018)

8.2 Publications

Journal articles

1. **Xuan Li**, Nathan Youngblood, Wen Zhou, Johannes Feldmann, Jacob Swett, Samarth Aggarwal, A. Sebastian, C. David Wright, Wolfram Pernice, Harish Bhaskaran, "On-chip Phase Change Optical Matrix Multiplication Core", 2020 IEEE International Electron Devices Meeting (***IEDM 2020***), pp.7.5.1-7.5.4 (2020).

2. **Xuan Li**, N. Youngblood, Z. Cheng, S. G. C. Carrillo, E. Gemo, C. D. Wright, W. H. Pernice, and H. Bhaskaran "Experimental investigation of silicon and silicon nitride platforms for phase change photonic in-memory computing", ***Optica*** 7, 3 (2020).

3. **Xuan Li**, N. Youngblood, C. Rios, Z. Cheng, C. D. Wright, W. H. Pernice, and H. Bhaskaran "Fast and reliable storage using a 5 bit, nonvolatile photonic memory cell", ***Optica*** 6, 1 (2019).

4. N. Farmakidis, N. Youngblood, **Xuan Li**, J. Tan, J. L. Swett, Z. Cheng, C. David Wright, W. H. P. Pernice, and H. Bhaskaran, "Plasmonic Nanogap Enhanced Phase-Change Devices with Dual Electrical-Optical Functionality", ***Science Advances*** (2019), Vol. 5, eaaw2687.

5. J. Feldmann, N. Youngblood, **Xuan Li**, C. D. Wright, H. Bhaskaran, and W. H. P. Pernice, "Integrated 256 Cell Photonic Phase-Change Memory with 512-Bit Capacity," ***IEEE J. Sel. Top. Quantum Electron.*** 26, 1-7 (2020).

6. S. G. C. Carrillo, E. Gemo, **Xuan Li**, N. Youngblood, A. Katumba, P. Bienstman, W. Pernice, H. Bhaskaran, and C. D. Wright, "Behavioral modeling of integrated phase-change photonic devices for neuromorphic computing applications," ***APL Mater.*** 7, 091113 (2019).

7. Johannes Feldmann , Helge Gehring , Nathan Youngblood , Maxim Karpov , **Xuan Li** , Manuel Le Gallo , Xin Fu , Anton Lukashchuk , Arslan Raja , Junqiu Liu , C David Wright , Abu Sebastian , Tobias Kippenberg , Harish Bhaskaran, "Parallel convolution processing using an integrated photonic tensor core", ***Nature*** 589, 52–58 (2021).

8. C. D. Wright, H. Bhaskaran, W. H. P. Pernice, S. G. C. Carrillo, E. Gemo, A. Baldycheva, Z. Cheng, **Xuan Li**, C. Rios, N. Youngblood, J. Feldmann, N. Gruhler, and M. Stegmaier, "Integrated Phase-Change Photonics: A Strategy for Merging Communication and Computing," in 2019 Optical Fiber Communications Conference and Exhibition. (***OFC 2019***) Proceedings (Institute of Electrical and Electronics Engineers Inc., 2019), p. M1D.3.

9. N. Youngblood, Z. Cheng, N. Farmakidis, **Xuan Li**, J. Tan, and H. Bhaskaran, "Phase change photonics for brain-inspired computing (Conference Presentation)," in Micro- and Nanotechnology Sensors, Systems, and Applications XI, M. S. Islam and T. George, eds. (***SPIE 2019***), Vol. 10982, p. 24.

10. T. Chen, Y. Lu, Y. Sheng, Y. Shu, **Xuan Li**, R. J. Chang, H. Bhaskaran, and J. H. Warner, "Ultrathin All-2D Lateral Graphene/GaS/Graphene UV Photodetectors by Direct CVD Growth," ***ACS Appl. Mater. Interfaces*** 11, 48172–48178 (2019).

Conference presentations

1. **Xuan Li**, et al. Oral presentation "On-chip Phase Change Optical Matrix Multiplication Core", 67th International Electronic Device Meeting. (2020)

2. **Xuan Li**, et al. Poster presentation and ***Best Poster Award Nominee***. "Comparison between Silicon and Silicon Nitride Platform for Non-volatile Phase Change Photonic In-Memory Computing", MRS Fall Meeting 2020, 2020.11.27-2020.12.4.

3. **Xuan Li**, ***Organizer*** and poster presenter at MME photonics 2019, Oxford. 2019.8.22-24.

4. Xuan Li, poster presentation: "Matrix multiplication by phase change photonic in-memory computing", The next generation of cloud computing. Microsoft Cambridge Institute Workshop. 2019.10.25-26

5. **Xuan Li**, Oral presentation "Stable and Repeatable Multilevel Storage Using Phase Change Photonics. MRS Fall Meeting 2018, Hynes Convention Center, Boston, Massachusetts, United States, 2018.11.25 – 2018.11.30

6. **Xuan Li**, Oral presentation and ***Excellent Paper Award***: "Multilevel Phase-change Optical Memory on a Silicon Photonics Platform", LIMIS, Changsha, China, 2018.11.11 – 2018.11.13

7. **Xuan Li**, ***Best Student Presentation Award, 1st place***, "All optical, Waveguide-Integrated Memory". 2nd International Symposium on Doped Amorphous Chalcogenides and Devices, Lake District, UK, 2018.5.2-2018.5.5

8. **Xuan Li**, ***Selected Speaker***, "Photonic Computing and Storage", Oxfest 7th Annual Symposium, Oxford, UK, 2018.2.24

Newspaper articles

1. **Xuan Li**, Yifu Ding, Nathan Youngblood, "Is photonics the end of the CPU?" The Oxford Students, Vol. 87, 4(2019).

References

[1] Alexander V. Kolobov, Paul Fons, Anatoly I. Frenkel, Alexei L. Ankudinov, Junji Tominaga, and Tomoya Uruga. Understanding the phase-change mechanism of rewritable optical media. *Nature Materials*, 3(10):703–708, oct 2004.

[2] Amir H. Hosseinnia, Amir H. Atabaki, Ali A. Eftekhar, and Ali Adibi. High-quality silicon on silicon nitride integrated optical platform with an octave-spanning adiabatic interlayer coupler. *Optics Express*, 23(23):30297, nov 2015.

[3] Pascual Muñoz, Gloria Micó, Luis A. Bru, Daniel Pastor, Daniel Pérez, José David Doménech, Juan Fernández, Rocío Baños, Bernardo Gargallo, Rubén Alemany, Ana M. Sánchez, Josep M. Cirera, Roser Mas, and Carlos Domínguez. Silicon Nitride Photonic Integration Platforms for Visible, Near-Infrared and Mid-Infrared Applications. *Sensors*, 17(9):2088, sep 2017.

[4] Timo Aalto, Matteo Cherchi, Mikko Harjanne, Srivathsa Bhat, Paivi Heimala, Fei Sun, Markku Kapulainen, Tomi Hassinen, and Tapani Vehmas. Open-Access 3-μm SOI Waveguide Platform for Dense Photonic Integrated Circuits. *IEEE Journal of Selected Topics in Quantum Electronics*, 25(5):1–9, sep 2019.

[5] IMEC. SILICON NITRIDE PHOTONIC INTEGRATED CIRCUIT PROTOTYPING AND SMALL VOLUME PRODUCTION. Technical report.

[6] Meint Smit, Kevin Williams, and Jos Van Der Tol. Past, present, and future of InP-based photonic integration. *APL Photonics*, 4(5):050901, may 2019.

[7] Ziyang Zhang, David Felipe, Vasilis Katopodis, Panos Groumas, Christos Kouloumentas, Hercules Avramopoulos, Jean Yves Dupuy, Agnieszka Konczykowska, Alberto Dede, Antonio Beretta, Antonello Vannucci, Giulio Cangini, Raluca Dinu, Detlef Schmidt, Martin Moehrle, Patrick Runge, Jung Han Choi, Heinz Gunter Bach, Norbert Grote, Norbert Keil, and Martin Schell. Hybrid photonic integration on a polymer platform. *Photonics*, 2(3):1005–1026, sep 2015.

[8] Xiaoning Zhang, Jun Qiu, Xingcan Li, Junming Zhao, and Linhua Liu. Complex refractive indices measurements of polymers in visible and near-infrared bands. *Applied Optics*, 59(8):2337, mar 2020.

[9] Wen Sun, Bin Gao, Miaofang Chi, Qiangfei Xia, J Joshua Yang, He Qian, and Huaqiang Wu. Understanding memristive switching via in situ characterization and device modeling. *Nature Communications*, 10(1):3453, 2019.

[10] Carlos Rios, Matthias Stegmaier, Peiman Hosseini, Di Wang, Torsten Scherer, C. David Wright, Harish Bhaskaran, and Wolfram H.P. Pernice. Integrated all-photonic non-volatile multi-level memory. *Nature Photonics*, 9(11):725–732, 2015.

[11] Carlos Rios, Matthias Stegmaier, Zengguang Cheng, Nathan Youngblood, C. David Wright, Wolfram H. P. Pernice, and Harish Bhaskaran. Controlled switching of phase-change materials by evanescent-field coupling in integrated photonics [Invited]. *Optical Materials Express*, 8(9):2455, sep 2018.

[12] J. Feldmann, N. Youngblood, M. Karpov, H. Gehring, X. Li, M. L. Gallo, X. Fu, A. Lukashchuk, A. S. Raja, J. Liu, C. D. Wright, A. Sebastian, T. J. Kippenberg, W. H.P. Pernice, and H. Bhaskaran. Parallel convolutional processing using an integrated photonic tensor core. *Nature*, 589(7840):52–58, feb 2021.

[13] E. Petronijevic and C. Sibilia. Thin films of phase change materials for light control of metamaterials in the optical and infrared spectral domain. *Optical and Quantum Electronics*, 52(2):110, feb 2020.

[14] Miquel Rudé, Josselin Pello, Robert E. Simpson, Johann Osmond, Gunther Roelkens, Jos J.G.M. Van Der Tol, and Valerio Pruneri. Optical switching at 1.55 μm in silicon racetrack resonators using phase change materials. *Applied Physics Letters*, 103(14):141119, 2013.

[15] Changming Wu, Heshan Yu, Huan Li, Xiaohang Zhang, Ichiro Takeuchi, and Mo Li. Low-Loss Integrated Photonic Switch Using Subwavelength Patterned Phase Change Material. *ACS Photonics*, 6(1):87–92, jan 2019.

[16] Hossein Taghinejad, Sajjad Abdollahramezani, Ali A. Eftekhar, Tianren Fan, Amir H. Hosseinnia, Omid Hemmatyar, Ali Eshaghian Dorche, Alexander Gallmon, and Ali Adibi. ITO-based microheaters for reversible multi-stage switching

of phase-change materials: towards miniaturized beyond-binary reconfigurable integrated photonics. *Optics Express*, 29(13):20449, jun 2021.

[17] Yegang Lu, Matthias Stegmaier, Pavan Nukala, Marco A. Giambra, Simone Ferrari, Alessandro Busacca, Wolfram H.P. Pernice, and Ritesh Agarwal. Mixed-mode operation of hybrid phase-change nanophotonic circuits. *Nano Letters*, 17(1):150–155, 2017.

[18] Carlos Ríos, Yifei Zhang, Mikhail Shalaginov, Skylar Deckoff-Jones, Haozhe Wang, Sensong An, Hualiang Zhang, Myungkoo Kang, Kathleen A. Richardson, Christopher Roberts, Jeffrey Chou, Vladimir Liberman, Steven A. Vitale, Jing Kong, Tian Gu, and Juejun Hu. Multi-level Electro-thermal Switching of Optical Phase-Change Materials Using Graphene. *Advanced photonic research*, 2(1):2000034, jan 2020.

[19] Nikolaos Farmakidis, Nathan Youngblood, Xuan Li, James Tan, Jacob L. Swett, Zengguang Cheng, C. David Wright, Wolfram H.P. Pernice, and Harish Bhaskaran. Plasmonic nanogap enhanced phase-change devices with dual electrical-optical functionality. *Science Advances*, 5(11):eaaw2687, nov 2019.

[20] Hanyu Zhang, Linjie Zhou, Liangjun Lu, Jian Xu, Ningning Wang, Hao Hu, B. M.Azizur Rahman, Zhiping Zhou, and Jianping Chen. Miniature Multilevel Optical Memristive Switch Using Phase Change Material. *ACS Photonics*, 6(9):2205–2212, 2019.

[21] Jiajiu Zheng, Zhuoran Fang, Changming Wu, Shifeng Zhu, Peipeng Xu, Jonathan K. Doylend, Sanchit Deshmukh, Eric Pop, Scott Dunham, Mo Li, and Arka Majumdar. Nonvolatile Electrically Reconfigurable Integrated Photonic Switch Enabled by a Silicon PIN Diode Heater. *Advanced Materials*, 32(31):2001218, aug 2020.

[22] Wim Bogaerts, Daniel Pérez, José Capmany, David A.B. Miller, Joyce Poon, Dirk Englund, Francesco Morichetti, and Andrea Melloni. Programmable photonic circuits. *Nature*, 586(7828):207–216, oct 2020.

[23] Chao Qian, Xiaobin Lin, Xiaobin Lin, Jian Xu, Yang Sun, Erping Li, Baile Zhang, and Hongsheng Chen. Performing optical logic operations by a diffractive neural network. *Light: Science and Applications*, 9(1):1–7, dec 2020.

[24] Jacques Carolan, Christopher Harrold, Chris Sparrow, Enrique Martín-López, Nicholas J. Russell, Joshua W. Silverstone, Peter J. Shadbolt, Nobuyuki Matsuda, Manabu Oguma, Mikitaka Itoh, Graham D. Marshall, Mark G. Thompson, Jonathan C.F. Matthews, Toshikazu Hashimoto, Jeremy L. O'Brien, and Anthony Laing. Universal linear optics. *Science*, 349(6249):711–716, aug 2015.

[25] Yichen Shen, Nicholas C. Harris, Scott Skirlo, Mihika Prabhu, Tom Baehr-Jones, Michael Hochberg, Xin Sun, Shijie Zhao, Hugo Larochelle, Dirk Englund, and Marin Soljačić. Deep learning with coherent nanophotonic circuits. *Nature Photonics*, 11(7):441–446, jul 2017.

[26] Xiao Yun Xu, Xuan Lun Huang, Zhan Ming Li, Jun Gao, Zhi Qiang Jiao, Yao Wang, Ruo Jing Ren, H. P. Zhang, and Xian Min Jin. A scalable photonic computer solving the subset sum problem. *Science Advances*, 6(5):eaay5853, jan 2020.

[27] Erfan Khoram, Ang Chen, Dianjing Liu, Lei Ying, Qiqi Wang, Ming Yuan, and Zongfu Yu. Nanophotonic media for artificial neural inference. *Photonics Research*, 7(8):823, aug 2019.

[28] M. Mazilu, J. Baumgartl, S. Kosmeier, and K. Dholakia. Optical Eigenmodes; exploiting the quadratic nature of the light-matter interaction. *Optics Express*, 19(2):933, jan 2011.

[29] John Von Neumann and Michael D. Godfrey. First Draft of a Report on the EDVAC. *IEEE Annals of the History of Computing*, 15(4):27–75, 1993.

[30] Daniele Ielmini and Andrea L. Lacaita. Phase change materials in non-volatile storage, dec 2011.

[31] Xuan Li, Nathan Youngblood, Carlos Ríos, Zengguang Cheng, C. David Wright, Wolfram HP Pernice, and Harish Bhaskaran. Fast and reliable storage using a 5 bit, nonvolatile photonic memory cell. *Optica*, 6(1):1, jan 2019.

[32] Xuan Li, Nathan Youngblood, Zengguang Cheng, Santiago Garcia-Cuevas Carrillo, Emanuele Gemo, Wolfram H. P. Pernice, C. David Wright, and Harish Bhaskaran. Experimental investigation of silicon and silicon nitride platforms for phase-change photonic in-memory computing. *Optica*, 7(3):218, mar 2020.

[33] Xuan Li, Nathan Youngblood, Wen Zhou, Johannes Feldmann, Jacob Swett, Samarth Aggarwal, A. Sebastian, C. David Wright, Wolfram Pernice, and Harish Bhaskaran. On-chip phase change optical matrix multiplication core. In *Technical Digest - International Electron Devices Meeting, IEDM*, volume 2020-Decem, pages 7.5.1–7.5.4. Institute of Electrical and Electronics Engineers Inc., dec 2020.

[34] J. E. Bowers, J. T. Bovington, A. Y. Liu, and A. C. Gossard. A path to 300 mm hybrid silicon photonic integrated circuits. In *Optical Fiber Communication Conference, OFC 2014*, pages 1–3. Optical Society of America (OSA), mar 2014.

[35] Tin Komljenovic, Michael Davenport, Jared Hulme, Alan Y. Liu, Christos T. Santis, Alexander Spott, Sudharsanan Srinivasan, Eric J. Stanton, Chong Zhang, and John E. Bowers. Heterogeneous silicon photonic integrated circuits. *Journal of Lightwave Technology*, 34(1):20–35, jan 2016.

[36] Yifan Qi and Yang Li. Integrated lithium niobate photonics. *Nanophotonics*, 9(6):1287–1320, jun 2020.

[37] Meint Smit, Xaveer Leijtens, Huub Ambrosius, Erwin Bente, Jos Van Der Tol, Barry Smalbrugge, Tjibbe De Vries, Erik Jan Geluk, Jeroen Bolk, Rene Van Veldhoven, Luc Augustin, Peter Thijs, Domenico D'Agostino, Hadi Rabbani, Katarzyna Lawniczuk, Stanislaw Stopinski, Saeed Tahvili, Antonio Corradi, Emil Kleijn, Dzmitry Dzibrou, Manuela Felicetti, Elton Bitincka, Valentina Moskalenko, Jing Zhao, Rui Santos, Giovanni Gilardi, Weiming Yao, Kevin Williams, Patty Stabile, Piet Kuindersma, Josselin Pello, Srivathsa Bhat, Yuqing Jiao, Dominik Heiss, Gunther Roelkens, Mike Wale, Paul Firth, Francisco Soares, Norbert Grote, Martin Schell, Helene Debregeas, Mohand Achouche, Jean Louis Gentner, Arjen Bakker, Twan Korthorst, Dominic Gallagher, Andrew Dabbs, Andrea Melloni, Francesco Morichetti, Daniele Melati, Adrian Wonfor, Richard Penty, Ronald Broeke, Bob Musk, and Dave Robbins. An introduction to InP-based generic integration technology. *Semiconductor Science and Technology*, 29(8):83001, aug 2014.

[38] Mohammad J. Bereyhi and Tobias J. Kippenberg. Nanofabrication meets open science. *Nature Nanotechnology*, 16(8):850–852, jul 2021.

[39] Kerstin Wörhoff, René G. Heideman, Arne Leinse, and Marcel Hoekman. TriPleX: A versatile dielectric photonic platform. *Advanced Optical Technologies*, 4(2):189–207, apr 2015.

[40] Pisu Jiang and Krishna C. Balram. Suspended gallium arsenide platform for building large scale photonic integrated circuits: passive devices. *Optics Express*, 28(8):12262, apr 2020.

[41] Laurent Vivien, Charles Baudot, Frédéric Bœuf, Bertrand Szelag, Carlos Alonso-Ramos, Daniel Benedikovic, Delphine Marris-Morini, Eric Cassan, Sylvain Guerber, Maurin Douix, Léopold Virot, Philippe Rodriguez, Fabrice Nemouchi, Christophe Jany, Badhise Ben Bakir, Xavier Le Roux, D. Perez-Galacho, Mathias Berciano, Guillaume Marcaud, Ismael Charlet, L. Deniel, Christian Lafforgue, Jian Hao Zhang, Samuel Serna, P. Damas, Phuong T. Do, Dorian Doser, Jocelyn Durel, Elodie Ghegin, Vladyslav Vakarin, Joan Manel Ramirez, Stéphane Monfray, Sébastien Cremer, E. Duran Valdeiglesias, Loic Sanchez, Franck Fournel, Pierre Brianceau, and K. Hassan. Building blocks of silicon photonics. *Semiconductors and Semimetals*, 101:1–41, jan 2019.

[42] SungWon Chung, Makoto Nakai, and Hossein Hashemi. Low-power thermo-optic silicon modulator for large-scale photonic integrated systems. *Optics Express*, 27(9):13430, apr 2019.

[43] Daniel J. Blumenthal, René Heideman, Douwe Geuzebroek, Arne Leinse, and Chris Roeloffzen. Silicon Nitride in Silicon Photonics. In *Proceedings of the IEEE*, volume 106, pages 2209–2231, dec 2018.

[44] Luc M. Augustin, Rui Santos, Erik Den Haan, Steven Kleijn, Peter J.A. Thijs, Sylwester Latkowski, Dan Zhao, Weiming Yao, Jeroen Bolk, Huub Ambrosius, Sergei Mingaleev, André Richter, Arjen Bakker, and Twan Korthorst. InP-Based Generic Foundry Platform for Photonic Integrated Circuits. *IEEE Journal of Selected Topics in Quantum Electronics*, 24(1):1–10, jan 2018.

[45] Christof P. Dietrich, Andrea Fiore, Mark G. Thompson, Martin Kamp, and Sven Höfling. GaAs integrated quantum photonics: Towards compact and multi-functional quantum photonic integrated circuits. *Laser and Photonics Reviews*, 10(6):870–894, nov 2016.

[46] Hakan Inan, Muhammet Poyraz, Fatih Inci, Mark A. Lifson, Murat Baday, Brian T. Cunningham, and Utkan Demirci. Photonic crystals: Emerging biosensors and their promise for point-of-care applications. *Chemical Society Reviews*, 46(2):366–388, jan 2017.

[47] J. Gonzalo Wangüemert-Pérez, Abdelfettah Hadij-ElHouati, Alejandro Sánchez-Postigo, Jonas Leuermann, Dan Xia Xu, Pavel Cheben, Alejandro Ortega-Moñux, Robert Halir, and Íñigo Molina-Fernández. Subwavelength structures for silicon photonics biosensing. *Optics and Laser Technology*, 109:437–448, jan 2019.

[48] Hai Hu, Xiaoxia Yang, Feng Zhai, Debo Hu, Ruina Liu, Kaihui Liu, Zhipei Sun, and Qing Dai. Far-field nanoscale infrared spectroscopy of vibrational fingerprints of molecules with graphene plasmons. *Nature Communications*, 7(1):1–8, jul 2016.

[49] Oliver A. Williams, Michael Daenen, and Ken Haenen. Biological applications of nanocrystalline diamond. In *Materials Research Society Symposium Proceedings*, volume 956, pages 121–125. Springer, jan 2007.

[50] P. A. Nistor and P. W. May. Diamond thin films: Giving biomedical applications a new shine. *Journal of the Royal Society Interface*, 14(134):1–15, sep 2017.

[51] Christopher R. Doerr. Silicon photonic integration in telecommunications. *Frontiers in Physics*, 3:37, aug 2015.

[52] Dirk Taillaert, Roel Baets, Pieter Dumon, Wim Bogaerts, Dries Van Thourhout, Bert Luyssaert, Vincent Wiaux, Stephan Beckx, and Johan Wouters. Silicon-on-Insulator platform for integrated wavelength-selective components. In *Proceedings of WFOPC2005 - 4th IEEE/LEOS Workshop on Fibres and Optical Passive Components*, volume 2005, pages 115–120. IEEE Computer Society, 2005.

[53] Nahum Izhaky, Michael T. Morse, Sean Koehl, Oded Cohen, Doron Rubin, Assia Barkai, Gadi Sarid, Rami Cohen, and Mario J. Paniccia. Development of CMOS-compatible integrated silicon photonics devices. *IEEE Journal on Selected Topics in Quantum Electronics*, 12(6):1688–1697, nov 2006.

[54] Sarvagya Dwivedi, T. Van Vaerenbergh, Alfonso Ruocco, Thijs Spuesens, Peter Bienstman, Pieter Dumon, and Wim Bogaerts. Measurements of effective refractive index of SOI waveguides using interferometers. In *Integrated Photonics Research, Silicon and Nanophotonics, IPRSN 2015*, page 371. Optical Society of America (OSA), jun 2015.

[55] Jared F. Bauters, Martijn J. R. Heck, Demis D. John, Jonathon S. Barton, Christiaan M. Bruinink, Arne Leinse, René G. Heideman, Daniel J. Blumenthal, and John E. Bowers. Planar waveguides with less than 01 dB/m propagation loss fabricated with wafer bonding. *Optics Express*, 19(24):24090, nov 2011.

[56] L. Shen, Y. Jiao, W. Yao, Z. Cao, J. P. van Engelen, G. Roelkens, M. K. Smit, and J. J. G. M. van der Tol. High-bandwidth uni-traveling carrier waveguide photodetector on an InP-membrane-on-silicon platform. *Optics Express*, 24(8):8290, apr 2016.

[57] Keiichi Matsumoto, Junya Kishikawa, Tetsuo Nishiyama, Yuya Onuki, and Kazuhiko Shimomura. Novel integration method for III-V semiconductor devices on silicon platform. *Japanese Journal of Applied Physics*, 55(11):112201, nov 2016.

[58] Muhammad Rodlin Billah, Matthias Blaicher, Tobias Hoose, Philipp Immanuel Dietrich, Pablo Marin-Palomo, Nicole Lindenmann, Aleksandar Nesic, Andreas Hofmann, Ute Troppenz, Martin Moehrle, Sebastian Randel, Wolfgang Freude, and Christian Koos. Hybrid integration of silicon photonics circuits and InP lasers by photonic wire bonding. *Optica*, 5(7):876–883, feb 2018.

[59] N. Grote, N. Keil, C. Zawadzki, W. Brinker, D. De Felipe, and Z. Zhang. Polymer photonic integration platform: Technology and components. In *Technical Digest - 2012 17th Opto-Electronics and Communications Conference, OECC 2012*, pages 285–286, 2012.

[60] Xingyu Zhang, Amir Hosseini, Xiaohui Lin, Harish Subbaraman, and Ray T. Chen. Polymer-based hybrid-integrated photonic devices for silicon on-chip modulation and board-level optical interconnects. *IEEE Journal on Selected Topics in Quantum Electronics*, 19(6):196–210, 2013.

[61] Shota Tsuneyasu, Ryota Takahashi, Haruki Minami, Kazuki Nakamura, and Norihisa Kobayashi. Ultrafast Response in AC-Driven Electrochemiluminescent Cell Using Electrochemically Active DNA/Ru(bpy)32+ Hybrid Film with Mesoscopic Structures. *Scientific Reports*, 7(1):8525, dec 2017.

[62] Kentaro Tanaka and Yoshio Okahata. A DNA-lipid complex in organic media and formation of an aligned cast film. *Journal of the American Chemical Society*, 118(44):10679–10683, jan 1996.

[63] Andrew J. Steckl. DNA - A new material for photonics? *Nature Photonics*, 1(1):3–5, jan 2007.

[64] Hao Yan, Xlaoping Zhang, Zhlyong Shen, and Nadrian C. Seeman. A robust DNA mechanical device controlled by hybridization topology. *Nature*, 415(6867):62–65, jan 2002.

[65] Lee Carroll, Jun Su Lee, Carmelo Scarcella, Kamil Gradkowski, Matthieu Duperron, Huihui Lu, Yan Zhao, Cormac Eason, Padraic Morrissey, Marc Rensing, Sean Collins, How Yuan Hwang, and Peter O'Brien. Photonic packaging: Transforming silicon photonic integrated circuits into photonic devices. *Applied Sciences (Switzerland)*, 6(12):426, dec 2016.

[66] Tymon Barwicz, Ted W. Lichoulas, Yoichi Taira, Yves Martin, Shotaro Takenobu, Alexander Janta-Polczynski, Hidetoshi Numata, Eddie L. Kimbrell, Jae Woong Nah, Bo Peng, Darrell Childers, Robert Leidy, Marwan Khater, Swetha Kamlapurkar, Elaine Cyr, Sebastian Engelmann, Paul Fortier, and Nicolas Boyer. Automated, high-throughput photonic packaging. *Optical Fiber Technology*, 44:24–35, aug 2018.

[67] Francis Agyenim, Philip Eames, and Mervyn Smyth. Experimental study on the melting and solidification behaviour of a medium temperature phase change storage material (Erythritol) system augmented with fins to power a LiBr/H2O absorption cooling system. *Renewable Energy*, 36(1):108–117, jan 2011.

[68] Michael C. Floros, Kayden L.C. Kaller, Kosheela D. Poopalam, and Suresh S. Narine. Lipid derived diamide phase change materials for high temperature thermal energy storage. *Solar Energy*, 139:23–28, dec 2016.

[69] Atul Sharma, V. V. Tyagi, C. R. Chen, and D. Buddhi. Review on thermal energy storage with phase change materials and applications. *Renewable and Sustainable Energy Reviews*, 13(2):318–345, feb 2009.

[70] Murat Kenisarin and Khamid Mahkamov. Solar energy storage using phase change materials. *Renewable and Sustainable Energy Reviews*, 11(9):1913–1965, dec 2007.

[71] Kashif Iqbal, Asfandyar Khan, Danmei Sun, Munir Ashraf, Abdur Rehman, Faiza Safdar, Abdul Basit, and Hafiz Shahzad Maqsood. Phase change materials, their synthesis and application in textiles—a review. *Journal of the Textile Institute*, 110(4):625–638, apr 2019.

[72] K Gawron and J. Schröder. Properties of some salt hydrates for latent heat storage. *International Journal of Energy Research*, 1(4):351–363, jan 1977.

[73] M Wuttig, H Bhaskaran, and T Taubner. Phase-change materials for non-volatile photonic applications. *Nature Photonics*, 11(8):465–476, 2017.

[74] J. Feinleib, J. Deneufville, S. C. Moss, and S. R. Ovshinsky. Rapid reversible light-induced crystallization of amorphous semiconductors. *Applied Physics Letters*, 18(6):254–257, mar 1971.

[75] Joaquin Faneca, Thalía Domínguez Bucio, Frederic Y. Gardes, and Anna Baldycheva. O-band N-rich silicon nitride MZI based on GST. *Applied Physics Letters*, 116(9):093502, mar 2020.

[76] Carlos Ríos, Yifei Zhang, Mikhail Y. Shalaginov, Skylar Deckoff-Jones, Haozhe Wang, Sensong An, Hualiang Zhang, Myungkoo Kang, Kathleen A. Richardson, Christopher Roberts, Jeffrey B. Chou, Vladimir Liberman, Steven A. Vitale, Jing Kong, Tian Gu, and Juejun Hu. Multi-Level Electro-Thermal Switching of Optical Phase-Change Materials Using Graphene. *Advanced Photonics Research*, 2(1):2000034, jan 2021.

[77] Wen Dong Song, Lu Ping Shi, Xiang Shui Miao, and Chong Tow Chong. Synthesis and characteristics of a phase-change magnetic material. *Advanced Materials*, 20(12):2394–2397, jun 2008.

[78] Manar Abu Talib, Sohaib Majzoub, Qassim Nasir, and Dina Jamal. A systematic literature review on hardware implementation of artificial intelligence algorithms. *Journal of Supercomputing*, 77(2):1897–1938, feb 2021.

[79] Xuan Li, Nathan Youngblood, Carlos Ríos, Zengguang Cheng, C. David Wright, Wolfram HP Pernice, and Harish Bhaskaran. Fast and reliable storage using a 5 bit, nonvolatile photonic memory cell. *Optica*, 6(1):1, 2019.

[80] Lei Wang, Liang Tu, and Jing Wen. Application of phase-change materials in memory taxonomy. *Science and Technology of Advanced Materials*, 18(1):406–429, 2017.

[81] Matthias Wuttig and Noboru Yamada. Phase-change materials for rewriteable data storage. *Nature Materials*, 6(11):824–832, 2007.

[82] Jochen Hellmig, Andrei V. Mijiritskii, Herman J. Borg, Kateřina Musialková, and Piet Vromans. Dual-layer blu-ray disc based on fast-growth phase-change materials. *Japanese Journal of Applied Physics, Part 1: Regular Papers and Short Notes and Review Papers*, 42(2 B):848–851, feb 2003.

[83] S. Ismail-Beigi. Methods and Materials: CDs and DVDs, 2021.

[84] Santiago García Cuevas Carrillo, Liam Trimby, Yat Yin Au, V. Karthik Nagareddy, Gerardo Rodriguez-Hernandez, Peiman Hosseini, Carlos Ríos, Harish Bhaskaran, and C. David Wright. A Nonvolatile Phase-Change Metamaterial Color Display. *Advanced Optical Materials*, 7(18):1801782, sep 2019.

[85] Wikipedia. GeSbTe - Wikipedia.

[86] Martin Salinga, Egidio Carria, Andreas Kaldenbach, Manuel Bornhöfft, Julia Benke, Joachim Mayer, and Matthias Wuttig. Measurement of crystal growth velocity in a melt-quenched phase-change material. *Nature Communications*, 4(1):1–8, aug 2013.

[87] Romain Parize, Thomas Cossuet, Odette Chaix-Pluchery, Hervé Roussel, Estelle Appert, and Vincent Consonni. In situ analysis of the crystallization process of Sb2S3 thin films by Raman scattering and X-ray diffraction. *Materials and Design*, 121:1–10, may 2017.

[88] E. Černošková, R. Todorov, Z. Černošek, J. Holubová, and L. Beneš. Thermal properties and the structure of amorphous Sb 2 Se 3 thin film. *Journal of Thermal Analysis and Calorimetry*, 118(1):105–110, sep 2014.

[89] A. S. Rogachev, S. G. Vadchenko, and A. S. Shchukin. SHS reaction and explosive crystallization in thin films: Resemblance and distinction. *International Journal of Self-Propagating High-Temperature Synthesis*, 26(1):44–48, jan 2017.

[90] M. M. Abdel-Aziz. Effect of thallium on the crystallization kinetics of the chalcogenide glasses GeSe2 and GeSe4. *Journal of Thermal Analysis and Calorimetry*, 79(3):709–714, feb 2005.

[91] Hao Wang, Tianqi Guo, Yuan Xue, Shilong Lv, Dongning Yao, Zhiguo Zhou, Sannian Song, and Zhitang Song. The phase change memory features high-temperature characteristic based on Ge-Sb-Se-Te alloys. *Materials Letters*, 254:182–185, nov 2019.

[92] Jianmin Wang, Lei Wang, and Jun Liu. Overview of Phase-Change Materials Based Photonic Devices. *IEEE Access*, 8:121211–121245, 2020.

[93] Matthias Stegmaier, Carlos Ríos, Harish Bhaskaran, C. David Wright, and Wolfram H.P. Pernice. Nonvolatile All-Optical 1 $\times$ 2 Switch for Chipscale Photonic Networks. *Advanced Optical Materials*, 5(1):1600346, jan 2017.

[94] J. Feldmann, M. Stegmaier, N. Gruhler, C. Riós, H. Bhaskaran, C. D. Wright, and W. H.P. Pernice. Calculating with light using a chip-scale all-optical abacus. *Nature Communications*, 8(1):1–8, 2017.

[95] Johannes Feldmann, Nathan Youngblood, Xuan Li, C. David Wright, Harish Bhaskaran, and Wolfram H.P. Pernice. Integrated 256 Cell Photonic Phase-Change Memory with 512-Bit Capacity. *IEEE Journal of Selected Topics in Quantum Electronics*, 26(2):1–7, mar 2020.

[96] Qihang Zhang, Yifei Zhang, Junying Li, Richard Soref, Tian Gu, and Juejun Hu. Broadband nonvolatile photonic switching based on optical phase change materials: beyond the classical figure-of-merit. *Optics Letters*, 43(1):94, jan 2018.

[97] Dazeng Feng, Shirong Liao, Hong Liang, Joan Fong, Bhavin Bijlani, Roshanak Shafiiha, B. Jonathan Luff, Ying Luo, Jack Cunningham, Ashok V. Krishnamoorthy, and Mehdi Asghari. High speed GeSi electro-absorption modulator at 1550 nm wavelength on SOI waveguide. *Optics Express*, 20(20):22224, sep 2012.

[98] Ahmad B. Ayoub and Mohamed A. Swillam. High-performance optical modulator using ultra-thin silicon waveguide in SOI technology. In Marek Osiński, Yasuhiko Arakawa, and Bernd Witzigmann, editors, *Physics and Simulation of Optoelectronic Devices XXVI*, volume 10526, page 79. SPIE-Intl Soc Optical Eng, feb 2018.

[99] Nicolas Bosq, Nathanaël Guigo, Jacques Persello, and Nicolas Sbirrazzuoli. Melt and glass crystallization of PDMS and PDMS silica nanocomposites. *Physical Chemistry Chemical Physics*, 16(17):7830–7840, 2014.

[100] Wikipedia. Poly(methyl methacrylate) - Wikipedia.

[101] W. N. Dos Santos, J. A. De Sousa, and R. Gregorio. Thermal conductivity behaviour of polymers around glass transition and crystalline melting temperatures. *Polymer Testing*, 32(5):987–994, 2013.

[102] J. P. Jog. Crystallization of Polyethyleneterephthalate. *Journal of Macromolecular Science, Part C*, 35(3):531–553, 1995.

[103] James W. Summers. The melting temperature (or not melting) of poly(vinyl chloride). *Journal of Vinyl and Additive Technology*, 14(3):105–109, sep 2008.

[104] Mohammad Jawaid, Rachid Bouhfid, and Abou el Kacem Qaiss. *Functionalized graphene nanocomposites and their derivatives: Synthesis, processing and applications*. Elsevier, nov 2018.

[105] Sten Seifert and Patrick Runge. Revised refractive index and absorption of In_1-xGa_xAs_yP_1-y lattice-matched to InP in transparent and absorption IR-region. *Optical Materials Express*, 6(2):629, feb 2016.

[106] Katsumi Nakatsuhara, Tetsuya Mizumoto, Eiji Takahashi, Sainul Hossain, Yoshikazu Saka, Byong-Jin Ma, and Yoshiaki Nakano. All-optical switching in a distributed-feedback GaInAsP waveguide. *Applied Optics*, 38(18):3911, jun 1999.

[107] Shayan Saeidi, Payman Rasekh, Kashif M. Awan, Alperen Tüğen, Mikko J. Huttunen, and Ksenia Dolgaleva. Demonstration of optical nonlinearity in InGaAsP/InP passive waveguides. *Optical Materials*, 84:524–530, jun 2018.

[108] Junting Liu, Hongkun Nie, Bingzheng Yan, Kejian Yang, He Yang, Vladislav Khayrudinov, Harri Lipsanen, Baitao Zhang, and Jingliang He. Nonlinear optical absorption properties of InP nanowires and applications as a saturable absorber. *Photonics Research*, 8(6):1035, jun 2020.

[109] Brian Slovick, Lucas Zipp, and Srini Krishnamurthy. Indium phosphide metasurface with enhanced nonlinear absorption. *Scientific Reports*, 7(1):1–7, sep 2017.

[110] L. Mandelkern, G. M. Stack, and P. J.M. Mathieu. MELTING TEMPERATURE OF POLYMERS: THEORETICAL AND EXPERIMENTAL. In *Analytical Calorimetry*, volume 5, pages 223–237. Plenum Press, 1984.

[111] Jacek Dudowicz, Karl F. Freed, and Jack F. Douglas. The glass transition temperature of polymer melts. *Journal of Physical Chemistry B*, 109(45):21285–21292, nov 2005.

[112] Yang Yang Li, Frédérique Cunin, Jamie R. Link, Ting Gao, Ronald E. Betts, Sarah H. Reiver, Vicki Chin, Sangeeta N. Bhatia, and Michael J. Sailor. Polymer replicas of photonic porous silicon for sensing and drug delivery applications. *Science*, 299(5615):2045–2047, mar 2003.

[113] Tomoyuki Yokota, Peter Zalar, Martin Kaltenbrunner, Hiroaki Jinno, Naoji Matsuhisa, Hiroki Kitanosako, Yutaro Tachibana, Wakako Yukita, Mari Koizumi, and Takao Someya. Ultraflexible organic photonic skin. *Science Advances*, 2(4):e1501856, apr 2016.

[114] Raquel Vaz, Manuela F. Frasco, and M. Goreti F. Sales. Photonics in nature and bioinspired designs: Sustainable approaches for a colourful world. *Nanoscale Advances*, 2(11):5106–5129, nov 2020.

[115] Ari Novack, Matt Streshinsky, Ran Ding, Yang Liu, Andy Eu Jin Lim, Guo Qiang Lo, Tom Baehr-Jones, and Michael Hochberg. Progress in silicon platforms for integrated optics. *Nanophotonics*, 3(4-5):205–214, aug 2014.

[116] Meint Smit, Kevin Williams, and Jos Van Der Tol. Past, present, and future of InP-based photonic integration. *APL Photonics*, 4(5):050901, may 2019.

[117] Adel A.M. Saleh and Jane M. Simmons. All-optical networkingevolution, benefits, challenges, and future vision. In *Proceedings of the IEEE*, volume 100, pages 1105–1117. Institute of Electrical and Electronics Engineers Inc., 2012.

[118] Daniel Kilper, K. Guan, K. Hinton, and R. Ayre. Energy challenges in current and future optical transmission networks. In *Proceedings of the IEEE*, volume 100, pages 1168–1187. Institute of Electrical and Electronics Engineers Inc., 2012.

[119] Zheng Zhao, Zheng Wang, Zhoufeng Ying, Shounak Dhar, Ray T. Chen, and David Z. Pan. Logic synthesis for energy-efficient photonic integrated circuits. In *Proceedings of the Asia and South Pacific Design Automation Conference, ASP-DAC*, volume 2018-Janua, pages 355–360. Institute of Electrical and Electronics Engineers Inc., feb 2018.

[120] Tamara L. Troy and Suresh N. Thennadil. Optical properties of human skin in the near infrared wavelength range of 1000 to 2200 nm. *Journal of Biomedical Optics*, 6(2):167, 2001.

[121] Bowei Dong, Yanqin Yang, Qiongfeng Shi, Siyu Xu, Zhongda Sun, Shiyang Zhu, Zixuan Zhang, Dim Lee Kwong, Guangya Zhou, Kah Wee Ang, and Chengkuo Lee. Wearable Triboelectric-Human-Machine Interface (THMI) Using Robust Nanophotonic Readout. *ACS Nano*, 14(7):8915–8930, jul 2020.

[122] Patrick Nalepka, Maurice Lamb, Rachel W. Kallen, Kevin Shockley, Anthony Chemero, Elliot Saltzman, and Michael J. Richardson. Human social motor solutions for human–machine interaction in dynamical task contexts. *Proceedings of the National Academy of Sciences of the United States of America*, 116(4):1437–1446, jan 2019.

[123] Caerwyn Ash, Michael Dubec, Kelvin Donne, and Tim Bashford. Effect of wavelength and beam width on penetration in light-tissue interaction using computational methods. *Lasers in Medical Science*, 32(8):1909–1918, nov 2017.

[124] Sujay B. Desai, Surabhi R. Madhvapathy, Angada B. Sachid, Juan Pablo Llinas, Qingxiao Wang, Geun Ho Ahn, Gregory Pitner, Moon J. Kim, Jeffrey Bokor, Chenming Hu, H. S.Philip Wong, and Ali Javey. MoS2 transistors with 1-nanometer gate lengths. *Science*, 354(6308):99–102, oct 2016.

[125] Benjamin C. Lee, Engin Ipek, Onur Mutlu, and Doug Burger. Architecting phase change memory as a scalable dram alternative. *ACM SIGARCH Computer Architecture News*, 37(3):2, 2009.

[126] J. Joshua Yang, Dmitri B Strukov, and Duncan R Stewart. Memristive devices for computing. *Nature Nanotechnology*, 8(1):13–24, 2013.

[127] Jean Pierre Gaspard. Structure of covalently bonded materials: From the Peierls distortion to Phase-Change Materials. *Comptes Rendus Physique*, 17(3-4):389–405, mar 2016.

[128] Saikat Mukhopadhyay, Jifeng Sun, Alaska Subedi, Theo Siegrist, and David J. Singh. Competing covalent and ionic bonding in Ge-Sb-Te phase change materials. *Scientific Reports*, 6(1):1–9, may 2016.

[129] Won Jun Yang, Hanjin Park, Da Sol Kim, Taewoo Ha, Seung Jong Park, Min Ahn, Jae Hoon Kim, Young Kyun Kwon, and Mann Ho Cho. Phase-change like process through bond switching in distorted and resonantly bonded crystal. *Scientific Reports*, 9(1):1–11, dec 2019.

[130] Min Zhu, Oana Cojocaru-Mirédin, Antonio M. Mio, Jens Keutgen, Michael Küpers, Yuan Yu, Ju Young Cho, Richard Dronskowski, and Matthias Wuttig. Unique Bond Breaking in Crystalline Phase Change Materials and the Quest for Metavalent Bonding. *Advanced Materials*, 30(18):1706735, may 2018.

[131] Wabe W Koelmans, Abu Sebastian, Vara Prasad Jonnalagadda, Daniel Krebs, Laurent Dellmann, and Evangelos Eleftheriou. Projected phase-change memory devices. *Nature Communications*, 6:8181, 2015.

[132] Nathan Youngblood, Carlos Ríos, Emanuele Gemo, Johannes Feldmann, Zengguang Cheng, Anna Baldycheva, Wolfram HP Pernice, C. David Wright, and Harish Bhaskaran. Tunable Volatility of Ge 2 Sb 2 Te 5 in Integrated Photonics. *Advanced Functional Materials*, 29(11):1807571, jan 2019.

[133] Daiki Tanaka, Yuya Shoji, Masashi Kuwahara, Xiaomin Wang, Kenji Kintaka, Hitoshi Kawashima, Tatsuya Toyosaki, Yuichiro Ikuma, and Hiroyuki Tsuda. Ultra-small, self-holding, optical gate switch using Ge_2Sb_2Te_5 with a multi-mode Si waveguide. *Optics Express*, 20(9):10283, apr 2012.

[134] Shuai Wen, Yun Meng, Minghui Jiang, and Yang Wang. Multi-level coding-recoding by ultrafast phase transition on Ge2Sb2Te5 thin films. *Scientific Reports*, 8(1):4979, dec 2018.

[135] Zengguang Cheng, Carlos Ríos, Wolfram H.P. Pernice, C. David Wright, and Harish Bhaskaran. On-chip photonic synapse. *Science Advances*, 3(9):1–7, 2017.

[136] Zengguang Cheng, Carlos Ríos, Nathan Youngblood, C. David Wright, Wolfram H.P. Pernice, and Harish Bhaskaran. Device-Level Photonic Memories and Logic Applications Using Phase-Change Materials. *Advanced Materials*, 30(32):1802435, aug 2018.

[137] V. Weidenhof, N. Pirch, I. Friedrich, S. Ziegler, and M. Wuttig. Minimum time for laser induced amorphization of Ge2Sb2Te5 films. *Journal of Applied Physics*, 88(2):657–664, jul 2000.

[138] Sébastien Cueff, Arnaud Taute, Antoine Bourgade, Julien Lumeau, Stephane Monfray, Qinghua Song, Patrice Genevet, Brice Devif, Xavier Letartre, and Lotfi Berguiga. Reconfigurable Flat Optics with Programmable Reflection Amplitude Using Lithography-Free Phase-Change Material Ultra-Thin Films. *Advanced Optical Materials*, 9(2):2001291, jan 2021.

[139] Judson D. Ryckman, V. Diez-Blanco, Joyeeta Nag, Robert E. Marvel, B. K. Choi, Richard F. Haglund, and Sharon M. Weiss. Photothermal optical modulation of ultra-compact hybrid Si-VO_2 ring resonators. *Optics Express*, 20(12):13215, jun 2012.

[140] Ryan M. Briggs, Imogen M. Pryce, and Harry A. Atwater. Compact silicon photonic waveguide modulator based on the vanadium dioxide metal-insulator phase transition. *Optics Express*, 18(11):11192, may 2010.

[141] H. Gehring, M. Blaicher, W. Hartmann, P. Varytis, K. Busch, M. Wegener, and W. H.P. Pernice. Low-loss fiber-to-chip couplers with ultrawide optical bandwidth. *APL Photonics*, 4(1):010801, jan 2019.

[142] Jerome Michon, Sarah Geiger, Lan Li, Claudia Goncalves, Hongtao Lin, Kathleen Richardson, Xinqiao Jia, and Juejun Hu. A 3-D Integrated Photonics Platform with Deterministic Geometry Control. In *Conference Proceedings - Lasers and Electro-Optics Society Annual Meeting-LEOS*, volume 2020-May, pages 194–201. Institute of Electrical and Electronics Engineers Inc., may 2020.

[143] Tetsuya Miki and Hideki Ishio. Viabilities of the Wavelength-Division-Multiplexing Transmission System Over an Optical Fiber Cable. *IEEE Transactions on Communications*, 26(7):1082–1087, 1978.

[144] Ajay K. Sharma, R. K. Sinha, and R. A. Agarwala. Wavelength division multiplexing systems and networks. *IETE Technical Review (Institution of Electronics and Telecommunication Engineers, India)*, 15(4):235–250, 1998.

[145] Alan E. Willner. Vector-mode multiplexing brings an additional approach for capacity growth in optical fibers. *Light: Science and Applications*, 7(3):18002, mar 2018.

[146] Jie Liu, Guoxuan Zhu, Junwei Zhang, Yuanhui Wen, Xiong Wu, Yanfeng Zhang, Yujie Chen, Xinlun Cai, Zhaohui Li, Ziyang Hu, Jiangbo Zhu, and Siyuan Yu. Mode division multiplexing based on ring core optical fibers. *IEEE Journal of Quantum Electronics*, 54(5):1–18, oct 2018.

[147] Joel Carpenter and Timothy D. Wilkinson. All optical mode-multiplexing using holography and multimode fiber couplers. *Journal of Lightwave Technology*, 30(12):1978–1984, jun 2012.

[148] Haichun Liu, Muthu K.G. Jayakumar, Kai Huang, Zi Wang, Xiang Zheng, Hans Ågren, and Yong Zhang. Phase angle encoded upconversion luminescent nanocrystals for multiplexing applications. *Nanoscale*, 9(4):1676–1686, jan 2017.

[149] Christopher M. Collier, Michael Wiltshire, Jacqueline Nichols, Brandon Born, Emily L. Landry, and Jonathan F. Holzman. Nonlinear dual-phase multiplexing in digital microfluidic architectures. *Micromachines*, 2(4):369–384, sep 2011.

[150] Wen Chen. Multiple-wavelength double random phase encoding with CCD-plane sparse-phase multiplexing for optical information verification. *Applied Optics*, 54(36):10711, dec 2015.

[151] Yurii A. Vlasov and Sharee J. McNab. Losses in single-mode silicon-on-insulator strip waveguides and bends. *Optics Express*, 12(8):1622, apr 2004.

[152] Jian Wang and Yun Long. On-chip silicon photonic signaling and processing: a review. *Science Bulletin*, 63(19):1267–1310, oct 2018.

[153] V. Sasikala, • K Chitra, and K. Chitra. All optical switching and associated technologies: a review. *Journal of Optics (India)*, 47(3):307–317, sep 2018.

[154] Wim Bogaerts and Abdul Rahim. Programmable Photonics: An Opportunity for an Accessible Large-Volume PIC Ecosystem. *IEEE Journal of Selected Topics in Quantum Electronics*, 26(5):1–17, sep 2020.

[155] Yichen Shen, Nicholas C. Harris, Scott Skirlo, Mihika Prabhu, Tom Baehr-Jones, Michael Hochberg, Xin Sun, Shijie Zhao, Hugo Larochelle, Dirk Englund, and Marin Soljačić. Deep learning with coherent nanophotonic circuits. *Nature Photonics*, 11(7):441–446, jul 2017.

[156] Xing Lin, Yair Rivenson, Nezih T. Yardimci, Muhammed Veli, Yi Luo, Mona Jarrahi, and Aydogan Ozcan. All-optical machine learning using diffractive deep neural networks. *Science*, 361(6406):1004–1008, sep 2018.

[157] Nasim Mohammadi Estakhri, Brian Edwards, and Nader Engheta. Inverse-designed metastructures that solve equations. *Science*, 363(6433):1333–1338, mar 2019.

[158] Zhen Chai, Xiaoyong Hu, Feifan Wang, Xinxiang Niu, Jingya Xie, and Qihuang Gong. Ultrafast All-Optical Switching. *Advanced Optical Materials*, 5(7):1600665, 2017.

[159] J. D. Joannopoulos, Pierre R. Villeneuve, and Shanhui Fan. Photonic crystals: Putting a new twist on light, mar 1997.

[160] Masaya Notomi. Manipulating light with strongly modulated photonic crystals. *Reports on Progress in Physics*, 73(9):096501, sep 2010.

[161] Jeevan Jot Singh, Divya Dhawan, and Neena Gupta. All-optical photonic crystal logic gates for optical computing: an extensive review. *Optical Engineering*, 59(11):110901, nov 2020.

[162] Amnon Yariv and Pochi Yeh. *Photonics: optical electronics in modern communications (the oxford series in electrical and computer engineering)*. 2006.

[163] Donald K. Wilson. Polarization control aids fiber component testing. *Laser Focus World*, 33(1):1, 1997.

[164] Wikipedia. Explanation of Supercontinuum.

[165] Ferdinando Bedeschi, Rich Fackenthal, Claudio Resta, Enzo Michele Donze, Meenatchi Jagasivamani, Egidio Cassiodoro Buda, Fabio Pellizzer, David W. Chow, Alessandro Cabrini, Giacomo Matteo Angelo Calvi, Roberto Faravelli, Andrea Fantini, Guido Torelli, Duane Mills, Roberto Gastaldi, and Giulio Casagrande. A bipolar-selected phase change memory featuring multi-level cell storage. In *IEEE Journal of Solid-State Circuits*, volume 44, pages 217–227, jan 2009.

[166] Moinuddin K. Qureshi, Vijayalakshmi Srinivasan, and Jude A. Rivers. Scalable high performance main memory system using phase-change memory technology. *ACM SIGARCH Computer Architecture News*, 37(3):24, jun 2009.

[167] Ping Zhou, Bo Zhao, Jun Yang, and Youtao Zhang. A durable and energy efficient main memory using phase change memory technology. In *Proceedings - International Symposium on Computer Architecture*, volume 37, pages 14–23, New York, New York, USA, 2009. ACM Press.

[168] Hiroshi Ishiwara. FeFET and ferroelectric random access memories. In *Multifunctional Oxide Heterostructures*, volume 9780199584, pages 7619–7627. oct 2012.

[169] Yoshihiro Arimoto and Hiroshi Ishiwara. Current Status of Ferroelectric Random-Access Memory. *MRS Bulletin*, 29(11):823–828, nov 2004.

[170] Naoki Nishimura, Tadahiko Hirai, Akio Koganei, Takashi Ikeda, Kazuhisa Okano, Yoshinobu Sekiguchi, and Yoshiyuki Osada. Magnetic tunnel junction device with perpendicular magnetization films for high-density magnetic random access memory. *Journal of Applied Physics*, 91(8):5246–5249, apr 2002.

[171] Saied Tehrani, Jon M. Slaughter, Mark DeHerrera, Brad N. Engel, Nicholas D. Rizzo, John Salter, Mark Durlam, Renu W. Dave, Jason Janesky, Brian Butcher, Ken Smith, and Greg Grynkewich. Magnetoresistive random access memory using magnetic tunnel junctions. In *Proceedings of the IEEE*, volume 91, pages 703–712, may 2003.

[172] S. S. P. Parkin, K. P. Roche, M. G. Samant, P. M. Rice, R. B. Beyers, R. E. Scheuerlein, E. J. O'Sullivan, S. L. Brown, J. Bucchigano, D. W. Abraham, Yu Lu, M. Rooks, P. L. Trouilloud, R. A. Wanner, and W. J. Gallagher.

Exchange-biased magnetic tunnel junctions and application to nonvolatile magnetic random access memory (invited). *Journal of Applied Physics*, 85(8):5828–5833, apr 1999.

[173] Abu Sebastian, Tomas Tuma, Nikolaos Papandreou, Manuel Le Gallo, Lukas Kull, Thomas Parnell, and Evangelos Eleftheriou. Temporal correlation detection using computational phase-change memory. *Nature Communications*, 8(1):1115, dec 2017.

[174] Jean Yves Raty, Wei Zhang, Jennifer Luckas, Chao Chen, Riccardo Mazzarello, Christophe Bichara, and Matthias Wuttig. Aging mechanisms in amorphous phase-change materials. *Nature Communications*, 6(1):7467, dec 2015.

[175] Lei Jiang, Bo Zhao, Youtao Zhang, Jun Yang, and Bruce R. Childers. Improving write operations in MLC phase change memory. In *Proceedings - International Symposium on High-Performance Computer Architecture*, pages 201–210. IEEE, feb 2012.

[176] A. Cabrini, S. Braga, A. Manetto, and G. Torelli. Voltage-driven multilevel programming in phase change memories. In *Proceedings of the 2009 IEEE International Workshop on Memory Technology, Design, and Testing, MTDT 2009*, pages 3–6. IEEE, aug 2009.

[177] Miao Hu, Catherine E. Graves, Can Li, Yunning Li, Ning Ge, Eric Montgomery, Noraica Davila, Hao Jiang, R. Stanley Williams, J. Joshua Yang, Qiangfei Xia, and John Paul Strachan. Memristor-Based Analog Computation and Neural Network Classification with a Dot Product Engine. *Advanced Materials*, 30(9):1–10, 2018.

[178] I. V. Karpov, M. Mitra, D. Kau, G. Spadini, Y. A. Kryukov, and V. G. Karpov. Fundamental drift of parameters in chalcogenide phase change memory. *Journal of Applied Physics*, 102(12):124503, dec 2007.

[179] Daniele Ielmini, Andrea L. Lacaita, and Davide Mantegazza. Recovery and drift dynamics of resistance and threshold voltages in phase-change memories. *IEEE Transactions on Electron Devices*, 54(2):308–315, feb 2007.

[180] N. Papandreou, H. Pozidis, T. Mittelholzer, G. F. Close, M. Breitwisch, C. Lam, and E. Eleftheriou. Drift-tolerant multilevel phase-change memory. Technical report, may 2011.

[181] Mario Paniccia. Integrating silicon photonics. *Nature Photonics*, 4(8):498–499, aug 2010.

[182] H. John Caulfield and Shlomi Dolev. Why future supercomputing requires optics. *Nature Photonics*, 4(5):261–263, 2010.

[183] Mehdi Asghari and Ashok V. Krishnamoorthy. Silicon photonics: Energy-efficient communication. *Nature Photonics*, 5(5):268–270, may 2011.

[184] Carlos Rios, Peiman Hosseini, C. David Wright, Harish Bhaskaran, and Wolfram H.P. Pernice. On-chip photonic memory elements employing phase-change materials. *Advanced Materials*, 26(9):1372–1377, 2014.

[185] Carlos Ríos, Nathan Youngblood, Zengguang Cheng, Manuel Le Gallo, Wolfram H. P. Pernice, C. David Wright, Abu Sebastian, Harish Bhaskaran, Manuel Le Gallo, Wolfram H. P. Pernice, C. David Wright, Abu Sebastian, and Harish Bhaskaran. In-memory computing on a photonic platform. *Science Advances*, 5(2):eaau5759, feb 2018.

[186] Y. Liu, M. M. Aziz, A. Shalini, C. D. Wright, and R. J. Hicken. Crystallization of Ge2Sb2Te5 films by amplified femtosecond optical pulses. *Journal of Applied Physics*, 112(12):123526, 2012.

[187] Matthias Stegmaier, Carlos RÍos, Harish Bhaskaran, and Wolfram H.P. Pernice. Thermo-optical Effect in Phase-Change Nanophotonics. *ACS Photonics*, 3(5):828–835, 2016.

[188] Kostiantyn Shportko, Stephan Kremers, Michael Woda, Dominic Lencer, John Robertson, and Matthias Wuttig. Resonant bonding in crystalline phase-change materials. *Nature Materials*, 7(8):653–658, jul 2008.

[189] Noboru Yamada, Eiji Ohno, Kenichi Nishiuchi, Nobuo Akahira, and Masatoshi Takao. Rapid-phase transitions of GeTe-Sb2Te3 pseudobinary amorphous thin films for an optical disk memory. *Journal of Applied Physics*, 69(5):2849–2856, mar 1991.

[190] Richard A. Soref and Brian R. Bennett. Electrooptical effects in silicon, jan 1987.

[191] W. Kim, S. Menzel, D. J. Wouters, R. Waser, and V. Rana. 3-Bit Multilevel Switching by Deep Reset Phenomenon in Pt/W/TaOX/Pt-ReRAM Devices. *IEEE Electron Device Letters*, 37(5):564–567, may 2016.

[192] Jian Liu, Huafeng Yang, Zhongyuan Ma, Kunji Chen, Xinxin Zhang, Xinfan Huang, and Shunri Oda. Characteristics of multilevel storage and switching dynamics in resistive switching cell of Al2O3/HfO2/Al2O3 sandwich structure. *Journal of Physics D: Applied Physics*, 51(2):025102, jan 2018.

[193] Meng Fan Chang, Chia Chen Kuo, Shyh Shyuan Sheu, Chorng Jung Lin, Ya Chin King, Frederick T. Chen, Tzu Kun Ku, Ming Jinn Tsai, Jui Jen Wu, and Yue Der Chih. Area-efficient embedded resistive RAM (ReRAM) macros using logic-process vertical-parasitic-BJT (VPBJT) switches and read-disturb-free temperature-aware current-mode read scheme. *IEEE Journal of Solid-State Circuits*, 49(4):908–916, apr 2014.

[194] Lutz Waldecker, Timothy A. Miller, Miquel Rudé, Roman Bertoni, Johann Osmond, Valerio Pruneri, Robert E. Simpson, Ralph Ernstorfer, and Simon Wall. Time-domain separation of optical properties from structural transitions in resonantly bonded materials. *Nature Materials*, 14(10):991–995, oct 2015.

[195] Feng Rao, Keyuan Ding, Yuxing Zhou, Yonghui Zheng, Mengjiao Xia, Shilong Lv, Zhitang Song, Songlin Feng, Ider Ronneberger, Riccardo Mazzarello, Wei Zhang, and Evan Ma. Reducing the stochasticity of crystal nucleation to enable subnanosecond memory writing. *Science*, 358(6369):1423–1427, nov 2017.

[196] Y Liu, M M Aziz, A Shalini, C D Wright, and R J Hicken. Crystallization of Ge2Sb2Te5 films by amplified femtosecond optical pulses. *Journal of Applied Physics*, 112(12):3168, 2012.

[197] C. David Wright, Yanwei Liu, Krisztian I. Kohary, Mustafa M. Aziz, and Robert J. Hicken. Arithmetic and biologically-inspired computing using phase-change materials. *Advanced Materials*, 23(30):3408–3413, aug 2011.

[198] Ke Zhang, Simian Li, Guangfei Liang, Huan Huang, Yang Wang, Tianshu Lai, and Yiqun Wu. Different crystallization processes of as-deposited amorphous Ge 2Sb 2Te 5 films on nano- and picosecond single laser pulse irradiation. *Physica B: Condensed Matter*, 407(13):2447–2450, jul 2012.

[199] Y. Wang, D. Cai, Y. Chen, Y. Wang, H. Wei, R. Huo, X. Chen, and Z. Song. Optimizing Set Performance for Phase Change Memory with Dual Pulses Set Method. *ECS Solid State Letters*, 4(7):Q32–Q35, 2015.

[200] Abu Sebastian, Manuel Le Gallo, and Daniel Krebs. Crystal growth within a phase change memory cell. *Nature Communications*, 5:4314, 2014.

[201] Carlos Ríos, Nathan Youngblood, Zengguang Cheng, Manuel Le Gallo, Wolfram H. P. Pernice, C. David Wright, Abu Sebastian, and Harish Bhaskaran. In-memory computing on a photonic platform. *Science Advances*, 5(2):eaau5759, feb 2019.

[202] Gordon E Moore. Cramming More Components onto Integrated Circuits. *Electronics*, 38(8):114–117, 1965.

[203] Michael P. Frank. The physical limits of computing. *Computing in Science and Engineering*, 4(3):16–26, may 2002.

[204] Igor L Markov. Limits on fundamental limits to computation. *Nature*, 512(7513):147–154, 2014.

[205] Richard Soref. Silicon photonics: A review of recent literature, 2010.

[206] Lukas Chrostowski, Hossam Shoman, Mustafa Hammood, Han Yun, Jaspreet Jhoja, Enxiao Luan, Stephen Lin, Ajay Mistry, Donald Witt, Nicolas A. F. Jaeger, Sudip Shekhar, Hasitha Jayatilleka, Philippe Jean, Simon B.-de Villers, Jonathan Cauchon, Wei Shi, Cameron Horvath, Jocelyn N. Westwood-Bachman, Kevin Setzer, Mirwais Aktary, N. Shane Patrick, Richard J. Bojko, Amin Khavasi, Xu Wang, Thomas Ferreira de Lima, Alexander N. Tait, Paul R. Prucnal, David E. Hagan, Doris Stevanovic, and Andy P. Knights. Silicon Photonic Circuit Design Using Rapid Prototyping Foundry Process Design Kits. *IEEE Journal of Selected Topics in Quantum Electronics*, 25(5):1–26, 2019.

[207] Avi Klein, Gilad Masri, Hamootal Duadi, Kfir Sulimany, Ohad Lib, Hadar Steinberg, Stanislav A. Kolpakov, and Moti Fridman. Ultrafast rogue wave patterns in fiber lasers. *Optica*, 5(7):774, jul 2018.

[208] Cheng Wang, Mian Zhang, Xi Chen, Maxime Bertrand, Amirhassan Shams-Ansari, Sethumadhavan Chandrasekhar, Peter Winzer, and Marko Lončar. Integrated lithium niobate electro-optic modulators operating at CMOS-compatible voltages. *Nature*, 562(7725):101–104, oct 2018.

[209] Tae Joon Seok, Kyungmok Kwon, Johannes Henriksson, Jianheng Luo, and Ming C. Wu. Wafer-scale silicon photonic switches beyond die size limit. *Optica*, 6(4):490, apr 2019.

[210] Emir Salih Magden, Nanxi Li, Manan Raval, Christopher V. Poulton, Alfonso Ruocco, Neetesh Singh, Diedrik Vermeulen, Erich P. Ippen, Leslie A. Kolodziejski, and Michael R. Watts. Transmissive silicon photonic dichroic filters with spectrally selective waveguides. *Nature Communications*, 9(1):3009, dec 2018.

[211] Peter J Winzer, David T Neilson, and Andrew R Chraplyvy. Fiber-optic transmission and networking: the previous 20 and the next 20 years [Invited]. *Optics Express*, 26(18):24190, 2018.

[212] Huifu Xiao, Zilong Liu, Xu Han, Jianhong Yang, Guanghui Ren, Arnan Mitchell, and Yonghui Tian. On-chip reconfigurable and scalable optical mode multiplexer/demultiplexer based on three-waveguide-coupling structure. *Optics Express*, 26(17):22366, 2018.

[213] Meixin Feng, Jin Wang, Rui Zhou, Qian Sun, Hongwei Gao, Yu Zhou, Jianxun Liu, Yingnan Huang, Shuming Zhang, Masao Ikeda, Huaibing Wang, Yuantao Zhang, Yongjin Wang, and Hui Yang. On-Chip Integration of GaN-Based Laser, Modulator, and Photodetector Grown on Si. *IEEE Journal of Selected Topics in Quantum Electronics*, 24(6):1–5, nov 2018.

[214] Yannick Salamin, Ping Ma, Benedikt Baeuerle, Alexandros Emboras, Yuriy Fedoryshyn, Wolfgang Heni, Bojun Cheng, Arne Josten, and Juerg Leuthold. 100 GHz Plasmonic Photodetector. *ACS Photonics*, 5(8):3291–3297, aug 2018.

[215] Chenran Ye, Ke Liu, Richard A Soref, and Volker J Sorger. A compact plasmonic MOS-based 2×2 electro-optic switch. *Nanophotonics*, 4(1):261–268, 2015.

[216] Bo Wen Jia, Kian Hua Tan, Wan Khai Loke, Satrio Wicaksono, and Soon Fatt Yoon. Integration of an InSb photodetector on Si via heteroepitaxy for the mid-infrared wavelength region. *Optics Express*, 26(6):7227, mar 2018.

[217] Bob Zheng, Hangqi Zhao, Ben Cerjan, Sadegh Yazdi, Emilie Ringe, Peter Nordlander, and Naomi J. Halas. A room-temperature mid-infrared photodetector for on-chip molecular vibrational spectroscopy. *Applied Physics Letters*, 113(10):101105, sep 2018.

[218] Hanyu Zhang, Linjie Zhou, Jian Xu, Ningning Wang, Hao Hu, Liangjun Lu, B. M.A. Rahman, and Jianping Chen. Nonvolatile waveguide transmission tuning with electrically-driven ultra-small GST phase-change material. *Science Bulletin*, 64(11):782–789, may 2019.

[219] Alexander N. Tait, Thomas Ferreira De Lima, Mitchell A. Nahmias, Heidi B. Miller, Hsuan Tung Peng, Bhavin J. Shastri, and Paul R. Prucnal. Silicon Photonic Modulator Neuron. *Physical Review Applied*, 11(6):064043, jun 2019.

[220] Kan Wu, Chaoshi Guo, Hao Wang, Xiaoyan Zhang, Jun Wang, and Jianping Chen. All-optical phase shifter and switch near 1550nm using tungsten disulfide (WS_2) deposited tapered fiber. *Optics Express*, 25(15):17639, jul 2017.

[221] Yan Li, Weiwei Chen, Tingge Dai, and Pengjun Wang. Nonvolatile integrated optical phase shifter with flash memory technology. *Applied Physics Express*, 12(10):102005, oct 2019.

[222] Carlota Ruiz de Galarreta, Ivan Sinev, Arseny M. Alexeev, Pavel Trofimov, Konstantin Ladutenko, Santiago Garcia-Cuevas Carrillo, Emanuele Gemo, Anna Baldycheva, Jacopo Bertolotti, and C. David Wright. Reconfigurable multilevel control of hybrid all-dielectric phase-change metasurfaces. *Optica*, 7(5):476, may 2020.

[223] Gerardo Rodriguez-Hernandez, Peiman Hosseini, Carlos Ríos, C. David Wright, and Harish Bhaskaran. Mixed-Mode Electro-Optical Operation of Ge2Sb2Te5 Nanoscale Crossbar Devices. *Advanced Electronic Materials*, 3(8):1700079, aug 2017.

[224] Jan von Keitz, Johannes Feldmann, Nico Gruhler, Carlos Ríos, David Wright, Harish Bhaskaran, Wolfram H. P. Pernice, C. David Wright, Harish Bhaskaran, and Wolfram H. P. Pernice. Reconfigurable Nanophotonic Cavities with Nonvolatile Response. *ACS Photonics*, 5(11):4644–4649, nov 2018.

[225] Kengo Nozaki, Akihiko Shinya, Shinji Matsuo, Yasumasa Suzaki, Toru Segawa, Tomonari Sato, Yoshihiro Kawaguchi, Ryo Takahashi, and Masaya Notomi. Ultralow-power all-optical RAM based on nanocavities. *Nature Photonics*, 6(4):248–252, apr 2012.

[226] Zeqin Lu, Han Yun, Yun Wang, Zhitian Chen, Fan Zhang, Nicolas A. F. Jaeger, and Lukas Chrostowski. Broadband silicon photonic directional coupler using asymmetric-waveguide based phase control. *Optics Express*, 23(3):3795, feb 2015.

[227] Alexander V. Kolobov, Paul Fons, Junji Tominaga, and Stanford R. Ovshinsky. Vacancy-mediated three-center four-electron bonds in GeTe-Sb2Te3 phase-change memory alloys. 87(16):165206, apr 2013.

[228] Jiajiu Zheng, Amey Khanolkar, Peipeng Xu, Shane Colburn, Sanchit Deshmukh, Jason Myers, Jesse Frantz, Eric Pop, Joshua Hendrickson, Jonathan Doylend, Nicholas Boechler, and Arka Majumdar. Non-volatile quasi-continuously programmable silicon photonics using phase-change materials (Conference Presentation). In Graham T. Reed and Andrew P. Knights, editors, *Silicon Photonics XIV*, volume 10923, page 28. SPIE, mar 2019.

[229] Jiajiu Zheng, Amey Khanolkar, Peipeng Xu, Shane Colburn, Sanchit Deshmukh, Jason Myers, Jesse Frantz, Eric Pop, Joshua Hendrickson, Jonathan Doylend, Nicholas Boechler, and Arka Majumdar. GST-on-silicon hybrid nanophotonic integrated circuits: a non-volatile quasi-continuously reprogrammable platform. *Optical Materials Express*, 8(6):1551, jun 2018.

[230] Peipeng Xu, Jiajiu Zheng, Jonathan K Doylend, and Arka Majumdar. Low-Loss and Broadband Nonvolatile Phase-Change Directional Coupler Switches. *ACS Photonics*, 6(2):553–557, 2019.

[231] Jianwei Wang, Stefano Paesani, Yunhong Ding, Raffaele Santagati, Paul Skrzypczyk, Alexia Salavrakos, Jordi Tura, Remigiusz Augusiak, Laura Mančinska, Davide Bacco, Damien Bonneau, Joshua W. Silverstone, Qihuang Gong, Antonio Acín, Karsten Rottwitt, Leif K. Oxenløwe, Jeremy L. O'Brien, Anthony Laing, and Mark G. Thompson. Multidimensional quantum entanglement with large-scale integrated optics. *Science*, 360(6386):285–291, apr 2018.

[232] J. Feldmann, N. Youngblood, C. D. Wright, H. Bhaskaran, and W. H.P. Pernice. All-optical spiking neurosynaptic networks with self-learning capabilities. *Nature*, 569(7755):208–214, may 2019.

[233] Eilam Yalon, Isha M. Datye, Jeong Sun Moon, Kyung Ah Son, Kangmu Lee, and Eric Pop. Energy-Efficient Indirectly Heated Phase Change RF Switch. *IEEE Electron Device Letters*, 40(3):455–458, mar 2019.

[234] Wright CD. Alexeev AM, Ruiz De Galarreta C, Garcia-Cuevas Carrillo S, Sinev IS, Samusev AK, Gemo E, Nagareddy VK, Au Y-Y. Tunable Dielectric Metadevices Enabled by Phase-Change Materials. Technical report, 2017.

[235] Miquel Rude Rude, Robert E. Simpson, Romain Quidant, Valerio Pruneri, Jan Renger, Miquel Rudé, Robert E. Simpson, Romain Quidant, Valerio Pruneri, and Jan Renger. Active Control of Surface Plasmon Waveguides with a Phase Change Material. *ACS Photonics*, 2(6):669–674, jun 2015.

[236] AZO Materials. Properties: Silicon Nitride (Si3N4) Properties and Applications, 2015.

[237] Carlos Ríos, Nathan Youngblood, Zengguang Cheng, Manuel Le Gallo, Wolfram H. P. Pernice, C. David Wright, Abu Sebastian, and Harish Bhaskaran. In-memory computing on a photonic platform. *Science Advances*, 5(2):eaau5759, feb 2018.

[238] Xuan Li, Nathan Youngblood, Wen Zhou, Johannes Feldmann, Jacob Swett, Samarth Aggarwal, A. Sebastian, C. David Wright, Wolfram Pernice, and Harish Bhaskaran. On-chip phase change optical matrix multiplication core. In *Technical Digest - International Electron Devices Meeting, IEDM*, volume 2020-Decem, pages 7.5.1–7.5.4. Institute of Electrical and Electronics Engineers Inc., dec 2020.

[239] Frank Arute, Kunal Arya, Ryan Babbush, Dave Bacon, Joseph C. Bardin, Rami Barends, Rupak Biswas, Sergio Boixo, Fernando G.S.L. Brandao, David A. Buell, Brian Burkett, Yu Chen, Zijun Chen, Ben Chiaro, Roberto Collins, William Courtney, Andrew Dunsworth, Edward Farhi, Brooks Foxen, Austin Fowler, Craig Gidney, Marissa Giustina, Rob Graff, Keith Guerin, Steve Habegger, Matthew P. Harrigan, Michael J. Hartmann, Alan Ho, Markus Hoffmann, Trent Huang, Travis S. Humble, Sergei V. Isakov, Evan Jeffrey, Zhang Jiang, Dvir Kafri, Kostyantyn Kechedzhi, Julian Kelly, Paul V. Klimov, Sergey Knysh, Alexander Korotkov, Fedor Kostritsa, David Landhuis, Mike Lindmark, Erik Lucero, Dmitry Lyakh, Salvatore Mandrà, Jarrod R. McClean, Matthew McEwen, Anthony Megrant, Xiao Mi, Kristel Michielsen, Masoud Mohseni, Josh Mutus, Ofer Naaman, Matthew Neeley, Charles Neill, Murphy Yuezhen Niu, Eric Ostby, Andre Petukhov, John C. Platt, Chris Quintana, Eleanor G. Rieffel, Pedram Roushan, Nicholas C. Rubin, Daniel Sank, Kevin J. Satzinger,

Vadim Smelyanskiy, Kevin J. Sung, Matthew D. Trevithick, Amit Vainsencher, Benjamin Villalonga, Theodore White, Z. Jamie Yao, Ping Yeh, Adam Zalcman, Hartmut Neven, and John M. Martinis. Quantum supremacy using a programmable superconducting processor. *Nature*, 574(7779):505–510, oct 2019.

[240] Mitchell A. Nahmias, Thomas Ferreira De Lima, Alexander N. Tait, Hsuan Tung Peng, Bhavin J. Shastri, and Paul R. Prucnal. Photonic Multiply-Accumulate Operations for Neural Networks. *IEEE Journal of Selected Topics in Quantum Electronics*, 26(1), 2020.

[241] Fuxi Cai, Justin M. Correll, Seung Hwan Lee, Yong Lim, Vishishtha Bothra, Zhengya Zhang, Michael P. Flynn, and Wei D. Lu. A fully integrated reprogrammable memristor–CMOS system for efficient multiply–accumulate operations. *Nature Electronics*, 2(7):290–299, jul 2019.

[242] Fei Wang, Hui Lv, Qian Li, Jiang Li, Xueli Zhang, Jiye Shi, Lihua Wang, and Chunhai Fan. Implementing digital computing with DNA-based switching circuits. *Nature Communications*, 11(1):121, dec 2020.

[243] Tyler W. Hughes, Momchil Minkov, Ian A.D. Williamson, and Shanhui Fan. Adjoint Method and Inverse Design for Nonlinear Nanophotonic Devices. *ACS Photonics*, 5(12):4781–4787, dec 2018.

[244] J. Feldmann, N. Youngblood, C. D. Wright, H. Bhaskaran, and W. H.P. Pernice. All-optical spiking neurosynaptic networks with self-learning capabilities. *Nature*, 569(7755):208–214, may 2019.

[245] Ying Zuo, Bohan Li, Yujun Zhao, Yue Jiang, You-Chiuan Chen, Peng Chen, Gyu-Boong Jo, Junwei Liu, and Shengwang Du. All-optical neural network with nonlinear activation functions. *Optica*, 6(9):1132, sep 2019.

[246] Kan Yao, Rohit Unni, and Yuebing Zheng. Intelligent Nanophotonics: Merging Photonics and Artificial Intelligence at the Nanoscale. *Nanophotonics*, 8(3):339–366, mar 2019.

[247] Y. Paquot, F. Duport, A. Smerieri, J. Dambre, B. Schrauwen, M. Haelterman, and S. Massar. Optoelectronic reservoir computing. *Scientific Reports*, 2:287, 2012.

[248] François Duport, Bendix Schneider, Anteo Smerieri, Marc Haelterman, and Serge Massar. All-optical reservoir computing. *Optics Express*, 20(20):22783, sep 2012.

[249] Jonathan K. George, Hani Nejadriahi, and Volker J. Sorger. Towards on-chip optical FFTs for convolutional neural networks. In *2017 IEEE International Conference on Rebooting Computing, ICRC 2017 - Proceedings*, volume 2017-Janua, pages 1–4. Institute of Electrical and Electronics Engineers Inc., nov 2017.

[250] Takahito Tanimura, Takeshi Hoshida, Tomoyuki Kato, Shigeki Watanabe, and Hiroyuki Morikawa. Convolutional neural network-based optical performance monitoring for optical transport networks. *Journal of Optical Communications and Networking*, 11(1):A52–A59, 2019.

[251] Xingyuan Xu, Mengxi Tan, Bill Corcoran, Jiayang Wu, Andreas Boes, Thach G. Nguyen, Sai T. Chu, Brent E. Little, Damien G. Hicks, Roberto Morandotti, Arnan Mitchell, and David J. Moss. 11 TOPS photonic convolutional accelerator for optical neural networks. *Nature*, 589(7840):44–51, jan 2021.

[252] Eiichi Kuramochi, Kengo Nozaki, Akihiko Shinya, Koji Takeda, Tomonari Sato, Shinji Matsuo, Hideaki Taniyama, Hisashi Sumikura, and Masaya Notomi. Large-scale integration of wavelength-addressable all-optical memories on a photonic crystal chip. *Nature Photonics*, 8(6):474–481, jun 2014.

[253] Julien Mandon, Guy Guelachvili, and Nathalie Picqué. Fourier transform spectroscopy with a laser frequency comb. *Nature Photonics*, 3(2):99–102, feb 2009.

[254] Mohammadreza Najafi, Kaiwen Zhang, Mohammad Sadoghi, and Hans Arno Jacobsen. Hardware Acceleration Landscape for Distributed Real-Time Analytics: Virtues and Limitations. In *Proceedings - International Conference on Distributed Computing Systems*, pages 1938–1948. Institute of Electrical and Electronics Engineers Inc., jul 2017.